ABSTRACT

Title of Dissertation: LIGHT ACTIVATABLE PURE PORPHYRIN NANOPARTICLES FOR THE PHOTODYNAMIC OPENING OF THE BLOOD-BRAIN BARRIER AND GLIOBLASTOMA TREATMENT

Collin Thomas Inglut,
Doctor of Philosophy, 2022

Dissertation directed by: Assistant Professor, Huang Chiao Huang,
Fischell Department of Bioengineering

Glioblastoma (GBM) consistently recurs due to infiltrating cancer cells that cannot be removed by surgery and chemotherapy. The diffusive nature of GBM makes complete surgical resection unsafe, and the intact blood-brain barrier (BBB) prevents the penetration and accumulation of nearly all chemotherapy in infiltrative GBM cells. Existing BBB opening strategies are often associated with increased risk of edema, hemorrhage, or neurotoxicity and thus have limited clinical success. Photodynamic therapy (PDT) is a photochemistry-based treatment modality that has shown promise in treating GBM and opening the BBB in the clinic. In fact, a single adjunctive dose of PDT has been shown to add as much as 18 months to patient survival. However, the full potential of PDT is limited by the light activation depth of the 'gold standard' pro-drug photosensitizer, 5-aminolevulinic acid (5-ALA). In addition, large doses of PDT can result in edema and neurotoxicity. To address these issues, our lab has developed a photodynamic

priming (PDP) strategy using the verteporfin (VP) photosensitizer, which operates at low optical energy to enhance intratumoral drug accumulation without damaging the healthy brain tissues. Unfortunately, VP is hydrophobic and requires liposomal encapsulation for intravenous administration, which can alter the photosensitizers cellular pharmaceutics. Here, we develop and compare a novel carrier-free pure-photosensitizer nanoparticle to a clinically relevant liposomal formulation.

This dissertation covers a complementary, four-pronged approach to enhance drug delivery to brain tumors and treat GBM: (1) Understand the photoactivation depth of clinically relevant photosensitizers in the rodent brain for the targeting of infiltrative GBM cells. (2) Explore the mechanisms of photochemistry-induced BBB opening. (3) Engineer light-activable nanotechnology that can open the BBB, improve drug delivery, and eradicate GBM cells. And (4) develop a high-throughput model to examine the BBB integrity and efflux transporter function. The central hypothesis of this dissertation is the delivery of photoactivatable pure-photosensitizer nanoparticles can eradicate GBM cells and enhance drug delivery to microscopic GBM tumors.

LIGHT ACTIVATABLE PURE PORPHYRIN NANOPARTICLES FOR THE PHOTODYNAMIC OPENING OF THE BLOOD-BRAIN BARRIER AND GLIOBLASTOMA TREATMENT

by

Collin Thomas Inglut

Dissertation submitted to the Faculty of the Graduate School of the
University of Maryland, College Park, in partial fulfillment
of the requirements for the degree of
Doctor of Philosophy
2022

Advisory Committee:
Assistant Professor, Huang Chiao Huang, Chair
Associate Professor, Giuliano Scarcelli
Associate Professor, Kimberly M. Stroka
Professor, Xiaoming (Shawn) He
Principal Investigator, Michael M. Gottesman
Professor, Lawrence C. Washington

Dedication

In memory of Jennie Revezzo and Donald J. Inglut, Sr.

Acknowledgements

There are so many people I would like to thank for making this dissertation possible and for supporting me during my time at the University of Maryland.

First, I would like to thank my advisor, Dr. Huang Chiao (Joe) Huang. His support, drive, and dedication to my learning, has helped me become the best student, scientist, and engineer I could be. I am grateful for all his guidance over the past five years, and I am thankful to be one of his first Ph.D. students. Thank you, Joe, for truly caring about me, both inside and outside of lab.

Next, I would like to thank all my lab-mates. First, Barry Liang, who has been by my side in lab since day one. Your devotion to science has been an inspiration. I am thankful for all the help you have offered me throughout our Huang Lab journey. Going on trips to Sushi Para with you were always the best. Thank you, Aaron Sorrin, for your team player attitude. Your writing and grammar help is unmatched and truly appreciated. Our weekly hangouts during lockdown, watching Tiger King, will be missed. Thank you, Brandon Gaitan, for the constant support, help with my research, and positive outlook. The fancy steak dinners, cigars on the roof, and horse betting, were some of my favorite nights in DC. Our very long days in the dark room will not be missed. Thank you all for being amazing lab mates and friends. This work wouldn't have been possible without help from everyone in lab.

I would also like to acknowledge several peers and post docs who have helped me with collaborative projects. Thank you, Dr. Kelsey Gray, Dr. Nina Connelly, Dr. Joanna Thomas, Jill Stabile, and Daniel Najafali. Working and learning with you all has been a pleasure.

I offer my sincere appreciation to my other advisor and mentor at the NIH, Dr. Michael Gottesman and Dr. Rob Robey. Your guidance has helped me become a better scientist and critical thinker. I am grateful for the support and your valuable insight into my work over the last two years. I deeply enjoyed my time at the NIH with you both.

Thank you, Fischell Department of Bioengineering staff, for your day-to-day help with graduate school requirements. I would especially like to thank Bill Churma, for always going out of his way to lend a helping hand and listening to my problems.

I would like to recognize several friends who have constantly supported me during this journey. Thank you to Danial Song, Samm Stewert, Barry Liang, Brandon Gaitan, Aaron Sorrin, and Joey Biasi. And a special thank you to my girlfriend, Isabel Guterman, who supported me through one of the hardest points in my life. Thank you for always listening to me, caring for me, and helping me relax. I am so grateful for your endless love, patience, and encouragement.

Finally, my entire family deserves a huge thank you. My grandparents, Donald and Anna, who gave me huge financial support during all my schooling and who always believed in me. My hard-working dad and uncle, Don and Tom, who helped install their work ethic in me, and who supported and guided me through life. Thank you, Tommy, for fixing my car 4 times during grad school when it broke down. And my sister, Jessa, who always helped me when times were tough.

And a final shout out to my cat Papaya, who was always there to sit on my lap (and my laptop) while I worked from home. You helped me more than you could know. And to my favorite band, Blink-182, who I listened to on repeat, for five years, while performing experiments. *The tour is over, I've survived.*

Table of Contents

† These chapters were taken or adapted from C.T Inglut's previously published manuscripts. Specific citations and permission from the publishers are included in footnotes at the beginning of each chapter.

List of Tables

List of Figures

List of Abbreviations

16:0 Lyso-PC – 16:0 lysophosphocholine

ABC – ATP-binding cassette

ALA – aminolevulinic acid

ABCB1- ATP Binding Cassette Subfamily B Member 1

ABCG2 – ATP binding cassette subfamily G member 2

BBB – blood-brain barrier

CPT-cAMP – 8-(4-chlorophenylthio) adenosine-3',5'-cyclic monophosphate sodium

DOPE – dioleoylphosphatidylethanolamine

DOTAP – N-(2,3-Dioleoyloxy-1-propyl)trimethylammonium methyl sulfate

DSPE-PEG – distearoylphosphoethanolamine-polyethylene-glycol

EGFR – epidermal growth factor receptor

FCCP – carbonilcyanide p-triflouromethoxyphenylhydrazone

FDA – United States Food and Drug Administration

FGR – fluorescence-guided resection

FITC-dextran – fluorescein isothiocyanate–dextran

GBM – glioblastoma

H&E – haematoxylin and eosin

HBMECs – human brain microvascular endothelial cells

HSR – hypersensitivity reactions

IC_{50} – half-maximal inhibition concentration

IL – interleukin

JAnaP – Junction Analyzer Program

LD_{50} – median lethal dose

MGMT – O6-methylguanine methyl transferase

MMP – metalloproteinase proteins

MPS – mononuclear phagocyte system

MTT – (4,5-dimethylthiazol-2-yl)-2,5-diphenyltetrazolium bromide

PBS – phosphate buffered saline

PC – phosphatidylcholine

PDP – Photodynamic priming

PDT – photodynamic therapy

PE – phosphatidylethanolamine

PEG – polyethylene glycol

PpIX – protoporphyrin IX

PS – phosphatidylserine

RIPA – radioimmunoprecipitation assay

ROS – reactive oxygen species

SOSG – singlet oxygen sensor green

SEM – standard error of the mean

TAMs – tumor-associated macrophages

TEM – transmission electron microscopy

TMRE – tetramethylrhodamine ethyl ester

TMZ – temozolomide

VE-cadherin – vascular endothelial cadherin

VP – verteporfin

ZO-1 – zonula occluden-1

Chapter 1. Introduction

Glioblastoma (GBM) is the most common and deadly brain cancer. It is characterized by highly infiltrative cells that invade away from the primary tumor and into the healthy brain. Patients with GBM have a near 100% recurrence rate, with 80% of the tumors recurring within 1-2 cm of the original tumor edge [1, 2]. GBM is typically treated with surgical resection followed by chemotherapy and radiation to eradicate the residual invasive cells [3]. However, complete surgical resection of GBM is near impossible and unsafe. In addition, most patients will experience resistance to chemotherapy or discontinue maintenance treatment due to complications [4, 5]. While the systemic toxicity of chemotherapy can be reduced by nanoparticle systems [6], they do not effectively transverse the intact blood-brain barrier (BBB), diminishing their treatment efficacy [7].

Several strategies have been developed to disrupt the continuous tight junction network that joins the adjacent endothelial cells for enhanced drug delivery, including the infusion of hyperosmolar solutions and focused ultrasound [8]. However, these methods are not yet universally available in the clinic due to a number of limitations, such as lack of selectivity or healthy tissue damage [8-11]. Moreover, many of these strategies focus on endothelial tight junction disassociation and do not account for BBB closing nor their cytotoxicity on the other supportive cells, including astrocytes and neurons [8].

Photodynamic therapy (PDT) has shown promise in opening the BBB and treating the deadliest brain cancer in adults- GBM. In fact, a single adjunctive dose of PDT has been shown to add up to 18 additional months to patients' lives [12].

Traditionally, PDT involves the high optical energy (80-300 J/cm^2) activation of non-cytotoxic photosensitizers to generate reactive oxygen species that can kill cancer cells [13]. PDT requires careful optimization as high doses within the brain can induce edema and neurotoxicity [14-20]. Photodynamic priming (PDP), a subtherapeutic dose of PDT, using the verteporfin (VP) photosensitizer can modulate the vasculature and enhance intratumoral chemotherapy accumulation without damaging the surrounding healthy tissues [19]. However, VP is insoluble in water and requires a drug delivery vehicle. The current gold standard for delivering VP to patients is Visudyne, a Food and Drug Administration (FDA) approved liposome [21]. Still, liposomes can limit cancer cell uptake, which may diminish treatment efficacy. It is also well recognized there are many immunological and toxicological considerations for the design and use of liposomal drugs [6]. A pure-drug carrier-free nanoparticle of VP that resembles the free-form version of VP could be ideal for PDP and GBM treatment.

1.1 Objective and Significance

The **overall objective** of this dissertation is to examine how photochemistry can be leveraged to **enhance drug delivery to the brain** and ultimately improve the **treatment efficacy for the deadliest brain cancer,** GBM. We accomplished this goal by engineering a novel drug delivery system and repurposing a traditional photochemistry-based treatment modality, PDT. We then applied these tools to understand the mechanisms behind inducing GBM cell death and BBB modulation. The **significance** of this dissertation lies in: (**1**) A unique photodynamic priming strategy, fundamentally different from the conventional GBM treatment, to selectively open the BBB for enhanced delivery of therapeutics; (**2**) The development of a pure-

drug carrier-free nanoparticle of the hydrophobic photosensitizer VP; (**3**) It focuses on the underlying cause of recurrence for the most common and lethal brain tumor, the infiltrative GBM cells beyond the margins of surgical resection.

1.2 Approach and Innovation

This dissertation focuses on engineering a drug delivery system and designing a photochemistry-based treatment strategy that can be readily inserted into the existing clinical workflow for GBM. We will first examine the photosensitization reaction efficiency and activation depth of two clinically relevant photosensitizers in an ex vivo rodent brain model. We will investigate how to better deliver the hydrophobic photosensitizer VP to patients by engineering and thoroughly characterizing multiple nanoparticle systems, including biomolecule-VP conjugates, Liposomal VP, and a pure-drug carrier-free nanoparticle of VP. We seek to understand how the different nanoparticle systems induce GBM cell death and determine their treatment efficacy compared to the free-form photosensitizer, which cannot be used clinically. We will further explore how the sub-cytotoxic PDT can open the BBB for the delivery of therapeutics to the infiltrative GBM cells beyond the surgical margins and examine the impact on healthy brain tissues. The **central innovative elements** of this dissertation are:

1) Sub-cytotoxic Photodynamic Priming to Modulate the Blood-brain Barrier

The concept of using the VP photosensitizer, which has a longer excitation wavelength (690 nm), over the clinical ‘gold standard’ and ‘tumor cell-targeted’ prodrug aminolevulinic acid (ALA)-induced protoporphyrin IX (PpIX; 635 nm), to open the BBB is new [22]. The deeper penetrating light/ photosensitizer activation and

the ability to target the vasculature (on-demand and based on the selected drug-light interval) will allow for a more selective and effective opening. The spatiotemporal nature of PDT, confining light to the specified treatment areas, can also reduce normal tissue damage [23]. Mechanistically, we will examine how sub-cytotoxic PDT, known as priming, modulates the cell-cell junctions within brain endothelial cells for enhanced drug delivery. We will investigate the efficacy of VP- and ALA-mediated BBB opening in rodents.

2) A Pure-drug, Carrier-free Formulation of the verteporfin Photosensitizer

Liposomes hold great potential as drug delivery vehicles due to their biocompatibility and modular properties [24, 25], coupled with the significant advantage of attenuating the risk of systemic toxicity from the encapsulated chemotherapy agent [26-28]. However, there are still several drawbacks that limit their range of applications. Some of the biggest drawbacks of liposomes are the "Accelerated Blood Clearance Phenomenon", the redirection of the therapeutic payload to mononuclear phagocyte system containing organs (i.e., liver and spleen), and the diminished cellular uptake [29]. Repeated injections of pegylated liposomes can lose their "stealth" ability and are more quickly cleared from the blood due to the abundant secretion of anti-PEG IgM, IgE, and immunoglobulin G, followed by the opsonization of C protein fragments (complement activation), and finally uptake by macrophages [30-43]. To minimize the patient's exposure to liposomes, we engineered a pure-drug, carrier-free formulation of VP, termed NanoVP. Analysis revealed NanoVP had superior in vitro and in vivo cancer treatment efficacy compared to a liposomal formulation that represents the current gold standard. We further examined the

mechanisms of cancer cell death for different drug delivery systems of VP, including our novel NanoVP system.

1.3 Summary and Dissertation Outline

This dissertation is organized as follows: **Chapter 2** provides an overview of GBM, the BBB, and PDT. This chapter focuses on current treatments for GBM while highlighting our understanding of why the disease is so deadly; The infiltration GBM cells that invade outwards into the healthy brain and the defense mechanisms of the BBB that limit drug penetration into the brain. An overview of PDT is provided with a focus on how it is currently applied in the clinic for GBM treatment and the barriers that need to be overcome for it to be more effective. **Chapter 3** explores the activation depth of two clinically relevant photosensitizers in the rodent brain. Here, singlet oxygen production capabilities are correlated with photosensitizer photobleaching to determine the ideal photosensitizer for PDT treatment of GBM. **Chapter 4** examines the mechanisms governing photochemistry-induced BBB opening. Non-optimized and high doses of PDT within the brain can result in healthy tissue damage. In this chapter, we examine the impact of sublethal PDT doses on human brain microvasculature endothelial cells and cell-cell junction maturity. We further examine the ability to deliver nanoparticles past the endothelial cells in a transwell model. **Chapter 5** focuses on developing VP-biomolecule conjugates for PDT treatment. The three VP-biomolecule conjugates are thoroughly characterized *in situ* and *in vitro* to determine the impact of covalent conjugation on VPs photochemical properties and PDT efficacy. **Chapter 6** investigates the immunological and toxicological considerations for the design of liposomes. While the advantages of liposomes are well understood, this

chapter explains the several drawbacks that limit their range of clinical applications. We aim to shed light on key considerations that should be factored into the design and clinical use of liposomal formulations. **Chapter 7** spotlights the development of a pure-drug carrier-free nanoparticle of VP. This chapter covers synthesis methods and examines the novel nanoparticle's photochemical properties in storage and physiologically relevant environments. This chapter further explores the biomedical applications of the pure-drug nanoparticle *in vitro* and *in vivo*. PDT efficacy is examined within a subcutaneous GBM mouse model and the degree of photochemistry-induced BBB opening is determined using an intracranial rat model. Two clinically relevant photosensitizer formulations are used for comparison. **Chapter 8** focuses on developing a transgenic zebrafish model for studying BBB integrity and drug efflux transporter function. A high throughput cell-based assay is developed to determine if luciferase substrates are also substrates for the zebrafish drug transporters present at the BBB.

Chapter 2. Background

2.1 Glioblastoma

GBM is the most common and deadly brain tumor, accounting for more than 77% of all primary malignant tumors of the central nervous system. There are approximately 12,000 new cases annually in the US [1, 2]. The survival rates remain almost unchanged in decades, with the median survival being 14-16 months and the 5-year survival rate under 5%. Patient survival without treatment is only 6 months [1, 2]. Even with the world's best healthcare and medical treatments at his disposal, the late Senator John McCain succumbed to the disease in August 2018 after battling it for 13 months.

2.1.1 Standard of Care

GBM recurrence is nearly universal due to the inability of the current treatment to remove and eradicate the entire cancerous cell population (**Figure 2.1**) [44, 45]. Current first-line treatment includes maximal surgical resection followed by chemotherapy (temozolomide, TMZ, 75 mg/m^2 daily) and radiation (~1.8 Gy daily, ~30 fractions total) for 6 weeks, followed by 6 months of adjuvant chemotherapy (TMZ, 150 mg/m^2 for 5 days every 28 days) [3]. Surgery is performed to remove the bulk of the primary tumor; however, because the tumor preferentially invades the healthy brain tissue along myelinated fibers in white matter tracts and blood vessels, complete surgical removal is unsafe [46-49]. In fact, studies have shown primary tumor size is not correlated with survival outcomes [50], but rather if the location of the tumor is near a major white matter tract (e.g., the cortico-spinal tract and the anterior thalamic radiation) [51].

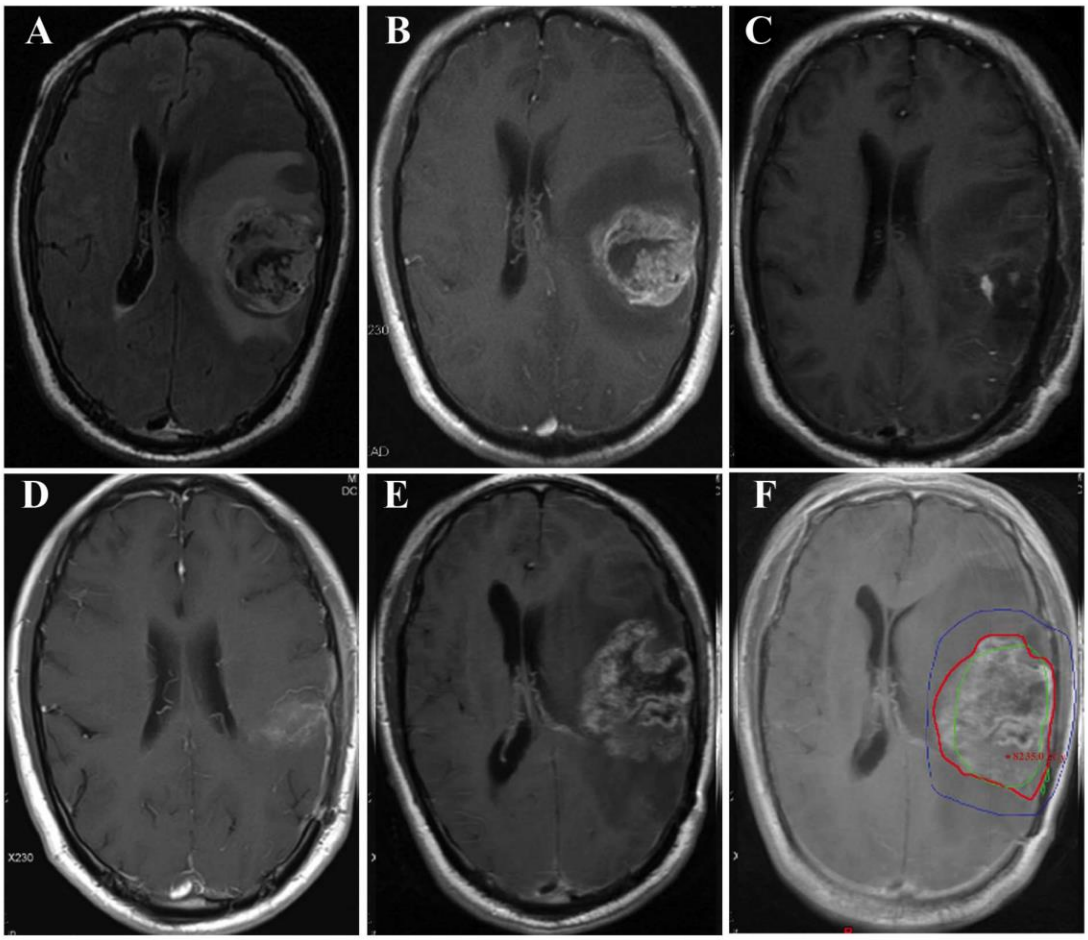

Figure 2.1 Magnetic Resonance Images of Glioblastoma Recurrence. (a) Fluid-attenuated inversion recovery image prior to treatment. (b) Post-contrast T1-weighted image prior to treatment. (c) Post-contrast T1-weighted image post-surgery. (d) post-contrast T1-weighted image after the completion of radiotherapy. (e) Post-contrast T1-weighted image at 10 months after diagnosis. (f) Post-contrast T1-weighted image at recurrence was fused with the planning computed tomography image, revealing local recurrence. The blue line indicates the 54-Gy IDL, the green line indicates the 60-Gy IDL and the red line marks the tumor recurrence volume. IDL, isodose line. *Reprinted from Zhou et al., Recurrence patterns in patients with high-grade glioma following temozolomide-based chemoradiotherapy. Mol Clin Oncol 5(2): 289-294. 2016. Permission obtained from Spandidos-publications.*

The chemotherapy TMZ is used to eradicate the remaining infiltrative cancerous cells after surgery. TMZ is a DNA alkylating agent that induces cell cycle arrest at G2/M by delivering a methyl group to purine bases of DNA [52]. However, approximately 50-55% of newly treated patients will have insignificant or no response, known as intrinsic drug resistance, and about 40% will later develop resistance to the

therapy, known as acquired drug resistance [4, 5]. The DNA repair protein O6-methylguanine methyl transferase (MGMT) removes the added methyl groups from the O6 position of guanine in DNA, stopping eventual DNA strand breaks [53]. The upregulation of this resistance mechanism is correlated with a worse patient prognosis and lower median patient survival [54-56]. For example, patients with methylated MGMT promotors (i.e., decrease in MGMT protein) had a 2-year survival rate of 49%, while patients with unmethylated MGMT promotors had a 2-year survival rate of 15% [54].

Large doses of TMZ are required to reach therapeutic levels in the brain and treatment GBM as only 17.8 ± 13.3% can cross the intact BBB [57]. One method to combat drug resistance and the high expression of MGMT is to increase the dose of TMZ. When MGMT repairs the alkylated DNA, it becomes irreversibly inactivated when the alkyl group is transferred to the cysteine moiety in its active site. Dose escalation has the potential to increase the rate of DNA alkylation and outpace the rate of MGMT protein synthesis [53]. However, dose-escalation studies have shown to induce hematologic toxicity. In one study that examined an alternative dosing schedule with an increased amount of TMZ (regimen:7-days-on/7-days-off,150 mg/m^2/day), ~38% of patients required a dose reduction due to thrombocytopenia and/or neutropenia [58]. Moreover, hematologic toxicity is not uncommon with conventional TMZ dosing. A retrospective review (conducted at Sidney Kimmel Comprehensive Cancer Center at Johns Hopkins, Baltimore, MD) found grade 3–4 thrombocytopenia occurred in 19% of patients and grade 3–4 neutropenia or anemia occurred in at least 8% of patients. Of the 10 patients that experienced grade 3–4 thrombocytopenia, 9

patients (17% of total) discontinued treatment [59]. A pooled analysis from 4 randomized trials for newly diagnosed GBM showed only 291 of 624 (46.6%) patients continued with maintenance TMZ (150 mg/m^2 for 5 days every 28 days) [60]. Lastly, TMZ is known to cause healthy brain tissue damage. Although hard to study in humans, rats treated with TMZ (25 mg/kg) experienced a 34% decrease in new cells generated in the granule cell layer within the hippocampus [61]. While TMZ has numerous drawbacks, including treatment efficacy, hematologic toxicity, and healthy brain damage, there is a reliance on it for first-line treatment due to its ability to accumulate within the brain [62]. Other chemotherapeutics and treatment options are limited because of the BBB, which restricts drug penetration into the brain.

When the tumor recurs or when the patient stops responding to the initial treatment, different salvage therapies are used, although there is no standardized regimen. Due to the diffuse nature of the tumor, only 25% of patients are eligible for a second surgery [63]. If another surgery is performed, biodegradable chemotherapy wafers containing carmustine can be placed in the resection cavity [64]. Other options include the vascular endothelial growth factor receptor inhibitor cediranib, the anti-vascular endothelial growth factor monoclonal antibody, bevacizumab [65], re-irradiation [66], and other chemotherapeutics (e.g., irinotecan and Liposomal irinotecan) [67].

2.1.2 The Invasive Front

As evident by the local recurrence patterns, the infiltrating cancer cells that invade the healthy brain tissue are usually located within 1-2 cm from the original lesion and result in an ~80% local recurrence rate (**Figure 2.2**) [44, 45]. Less than 2%

of patients with GBM have metastasis beyond the brain, which tends to occur in late stage diseases and after surgery [68]. The infiltrative cells that invade the healthy brain are difficult to treat due to the inability to safely remove them all during surgical resection and the inability to effectively deliver chemotherapy to them because of the intact BBB [69]. Genomic analyses have revealed invasive glioma cells and recurrent tumors are distinctly different from the primary tumor, usually as a result of treatment. For example, the primary tumor core is known to contain glioma stem cells enriched with CD133+ that resemble proneural cells. In contrast, glioma cells on the invasive edge are enriched for CD109+ and resemble a mesenchymal subtype [70].

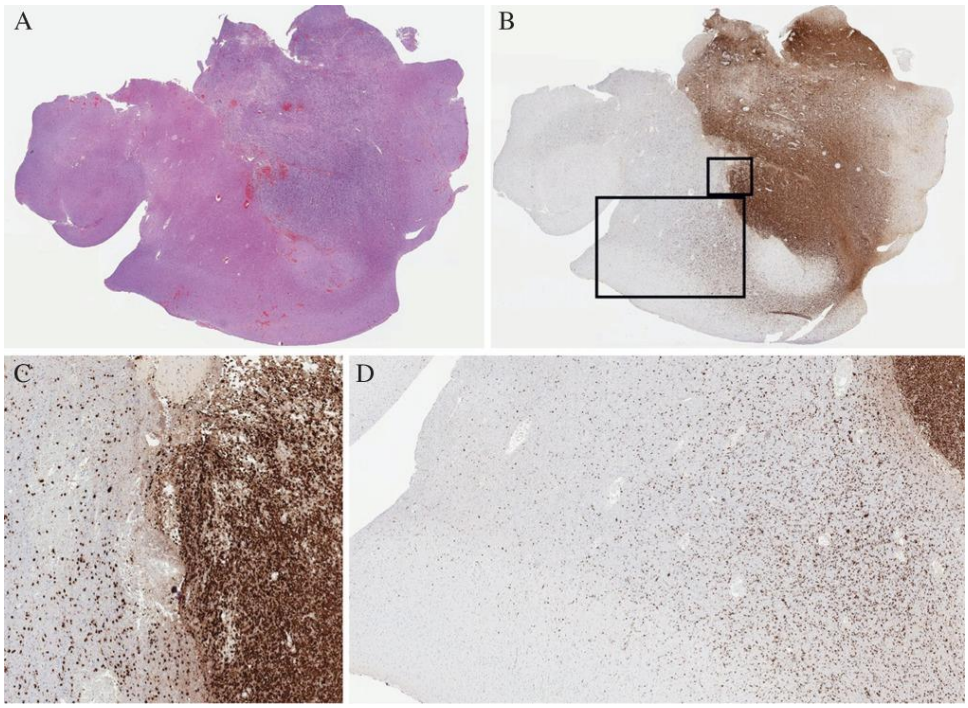

Figure 2.2 Glioblastoma and the Invasive Front. (**a**) H&E-stained cortical section of glioblastoma. (**b**) IDH1 R132H immunostaining highlights the neoplastic cells. (**c,d**) IDH1 R132H-positive neoplastic cells at the tumor edge and centimeters away into the healthy brain. *Reprinted from Olar and Aldape. Using the molecular classification of glioblastoma to inform personalized treatment. J. Pathol., 232: 165-177, 2013. Permission obtained from Elsevier and Copyright Clearance Center's RightsLink®.*

There are numerous molecular mechanisms and positive feedback loops underlying GBM motility. Some of the well-understood factors include tumor stiffness and hypoxia. Tumor stiffness, which is upregulated by the production of collagen, fibronectin, hyaluronic acid, and laminin, promotes glioma cell migration and is correlated with glioma progression [71]. Studies have shown that GBM cell lines spread extensively and migrate rapidly on highly rigid extracellular matrixes. Less rigid extracellular matrix comparable to typical brain tissue result in rounded and stationary cells [72]. The glioma's stiff extracellular matrix promotes invasion by upregulating promigratory factors. For example, the overexpression of hyaluronic acid in the tumor microenvironment promotes cell invasion through positive feedback regulation of nuclear factor-κB, a transcription factor that regulates cancer cell proliferation, differentiation, motility and survival [73]. The activation of nuclear factor-κB is linked to stem-like cell maintenance, epithelial-to-mesenchymal transition, promotion of angiogenesis, and resistance to radiotherapy [74]. Additionally, in response to a stiff extracellular matrix, glioma cells will upregulate matrix metalloproteinase proteins (MMP), secreted or membrane-anchored endoproteinases, to degrade and remodel their environment. By destroying their surrounding environment, glioma cells can invade and migrate. Commonly, MMP-9 is not detected in healthy brain samples, but active MMP-9 is found in 50% of tumors [75]. MMPs create positive feedback loops with other pro-migratory factors. MMP-2 and MMP-9 will active the dormant pro-migratory transforming growth factor-β, which stimulates the production of more MMP-2 [76]. Transforming growth factor-β is known to promote an epithelial-to-mesenchymal transition in cancerous cells. After receiving signals or sensing factors including,

transforming growth factor -β or hypoxia from other cancerous cells, glioma cells will begin to migrate or invade outwards from the primary tumor [71]. They will transition from an epithelial to mesenchymal state, detach from the primary tumor by recycling (i.e., endocytosing) their integrin and cadherin connections, remodel their microtubule network (i.e., form a leading edge), and upregulate new integrins that form links with the existing surrounding structures such as α9β1 and CD44 [77].

Low tumor oxygenation or hypoxia results from microvascular hyperplasia, an exacerbated form of angiogenesis. The secretion of proangiogenic factors, such as vascular endothelial growth factors and interleukin-8 (IL-8), results in the hyper-proliferation and recruitment of endothelial cells and, ultimately, the rapid growth of defective and permeable blood vessels. The collapse of these blood vessels yields hypoxic foci throughout the tumor. The diminished nutrients promote glioma migration and invasion [78]. Additionally, the overexpression of the proangiogenic factors, is correlated with poor prognosis in glioma patients [79].

2.1.3 Relevance to Dissertation

The focus of this dissertation is on the treatment of brain cancer. The glioma cells that invade the healthy brain are the main source of disease recurrence, which elude current treatment options [44, 45]. As such, understanding why current treatment options are not effective against the invasive cells and the mechanisms behind glioma invasion will help govern therapeutic discovery and implication. Surgical resection of all the invasive cells is not feasible and unsafe [80]. Surgical recession is stopped as soon as functional brain tissue is reached [80]. On the other hand, the intact BBB diminishes the efficacy of the follow-up chemotherapy regimen [7]. This

simultaneously drives the need to develop a treatment strategy that can directly kill the glioma cells during surgery and synergize with the chemotherapy regimen.

In this dissertation, the adjunctive treatment modality, PDT, and the new drug delivery system, pure-drug carrier-free nanoparticles of VP, have been the focus of study for treating GBM. Another technique to treat GBM relies on another photosensitizer, pro-drug ALA, to aid in the surgical removal of the primary tumor. However, this surgical technique does not focus on the invasive cells. The following sections will discuss this surgical technique in detail and examine the limitations we seek to overcome. While our focus here is on treating GBM, we believe the developed drug delivery system is relevant to other therapeutics and cancers. **Chapter 7** will focus on developing our nanoparticle and discussing its other biomedical applications.

2.2 The Neurovascular Unit

The brain is one of the most vascularized organs in the body. The neurovascular unit, composed of endothelial cells, neural cells (i.e., astrocytes, neurons), pericytes, microglia, and the basement membrane, regulates nutrient transport, maintains brain homeostasis and protects the central nervous system [81-83]. Nutrients are carried up to the brain through large cerebral arteries, which consist of smooth muscle cells and endothelial cells, with neurons and astrocytes nearby. The cerebral arteries branch into smaller pial arterioles, which consist of endothelial cells, smooth muscle cells, meningeal cells, and perivascular nerves that run along the surface of the brain. Pial arterioles then branch into penetrating arterioles, which penetrate through the fluid-filled Virchow-Robin space and into the brain. The intracerebral arterioles, which contain a single layer of smooth muscle cells, will then branch into brain capillaries,

known as the BBB (**Figure 2.3**) [84]. Besides maintaining a high degree of permeability, the neurovascular unit regulates blood flow, angiogenesis, neurogenesis, and neurotransmitter turnover [85]. For example, glutamate, an excitatory neurotransmitter, is released by neurons within the brain. However, large concentrations of glutamate can be damaging to nerve cells. Glutamate is normally taken up by astrocytes through the EAAT1 transporter. Glutamate is either metabolized to α-ketoglutarate by glutamate-dehydrogenase and used within the tricarboxylic acid cycle or converted into glutamine by glutamine synthetase and shuttled back over to neurons [84]. However, damage to cells within the neurovascular unit can disrupt this cycle. Instead of astrocyte taking up glutamate, they can secrete it, leading to neuron cell death [86]. When designing methods to open the BBB, it is critical to avoid severe damage to cells of the neurovascular unit.

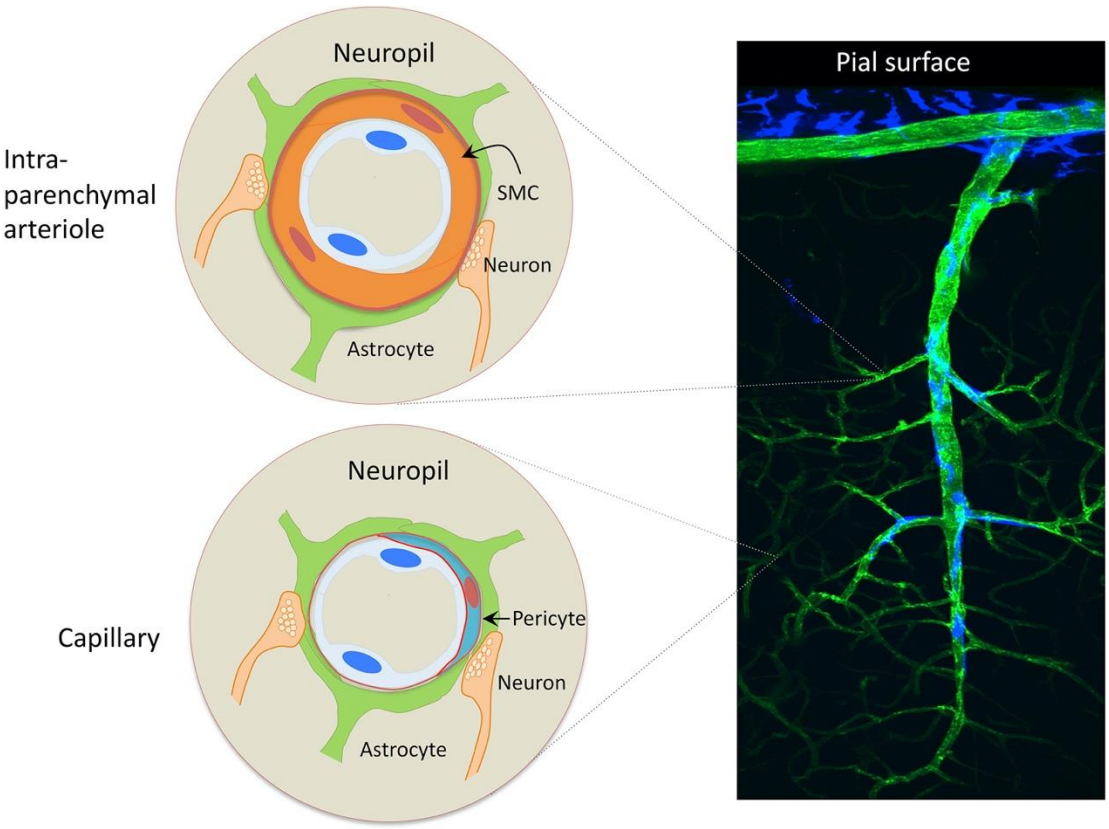

Figure 2.3 The Neurovascular Unit. (**Left**) Diagrams of the intraparenchymal arterioles and the capillaries within the brain. (**Right**) Lipophilic dye DiO was used to visualize the vasculature (green). CD206 immunocytochemistry was used to visualize the macrophages (blue) located in the perivascular and subarachnoid space. *Reprinted from Iadecola, The Neurovascular Unit Coming of Age: A Journey through Neurovascular Coupling in Health and Disease. Neuron 96(1): 17-42., 2017. Permission obtained from Elsevier and Copyright Clearance Center's RightsLink®.*

2.2.1 The Blood-brain Barrier

The BBB is a network of continuous non-fenestrated capillaries within the neurovascular unit. There are two main cell types that form the BBB: a single layer of microvascular endothelial cells that forms the vessel well and supporting mural cells that include pericytes and astrocytic foot processes [83]. The endothelial cells and pericytes secrete a vascular basement membrane (i.e., extracellular matrix) comprised of type IV collagen, laminin, and other glycoproteins, that aids in signaling processes.

The BBB forms a physical and chemical barrier between the circulatory and central nervous systems, tightly regulating the influx and efflux of biological substances for the brain parenchyma [7, 83]. Nutrients required for proper brain function enter the brain via transporter proteins, carrier-specific transcytosis, diffusion across the endothelial cells, and extremely restricted paracellular diffusion [87].

Compared to other endothelial cells throughout the body, the endothelial cells of the BBB are characterized by the presence of inter-endothelial tight junctions and the lack of caveolae at the luminal surface [88]. The cell-to-cell junctions that join the adjacent endothelial cells greatly limit the paracellular flux of solutes, forcing most molecules to undergo receptor-mediated endocytosis and transcytoses. For example, the BBB restricts and regulates the movement of ions and fluid, specifically K^+ and Ca^{2+}, through transporters, to ensure the brain interstitial fluid is optimal for neuronal function [89].

Pericytes sit on the abluminal surface of the endothelial tube and are identified by Platelet-derived growth factor receptor beta (PDGFR-β) and neuron-glia antigen 2 (NG2) expression [90]. Their proximity to the endothelial cells allows for ion, metabolite, and messenger exchange. Their phagocyting capabilities aid with the removal of toxic metabolites. Similar to smooth muscle cells, pericytes possess contractile characteristics. In response to depolarization or neurotransmitter action, their contractile proteins allow them to control the diameter of the capillary and regulate blood flow [88].

Astrocytes are the most abundant cell type in the CNS. Their endfeet encases the vascular tube, forming an interface between the vascular and the neuroglia in the

neurovascular unit. This neurovascular union allows astrocytes to relay signals to pericytes that regulate blood flow. Their main function is to help maintain the brain's ionic, amino acid, neurotransmitter, and water concentrations [91]. Numerous studies have shown the importance of astrocytes in BBB formulation as well as the ability of purified astrocytes to provide similar BBB features to other blood vessel types [92].

2.2.2 Endothelial Cell-Cell Junctions

Adherens, tight, and gap junction proteins govern endothelial cell-to-cell interactions. The over 40 proteins within the cell-cell junction are responsible for cell adhesion, barrier formation, and the exchange of nutrients between cells (**Figure 2.4**) [93]. Transmembrane proteins create junction complexes with identical proteins on adjacent cells at sites of cell-to-cell contact and are tethered to the actin cytoskeleton by various intracellular components (**Figure 2.4**) [94]. Proper formation of the junction complexes is crucial for vascular function as cell-cell interactions regulates angiogenesis, cell migration, and cell polarity [94]. Diminished junction integrity has been associated with numerous diseases including, cancer, stroke, ischemia, atherosclerosis, and many neurodegenerative diseases [95].

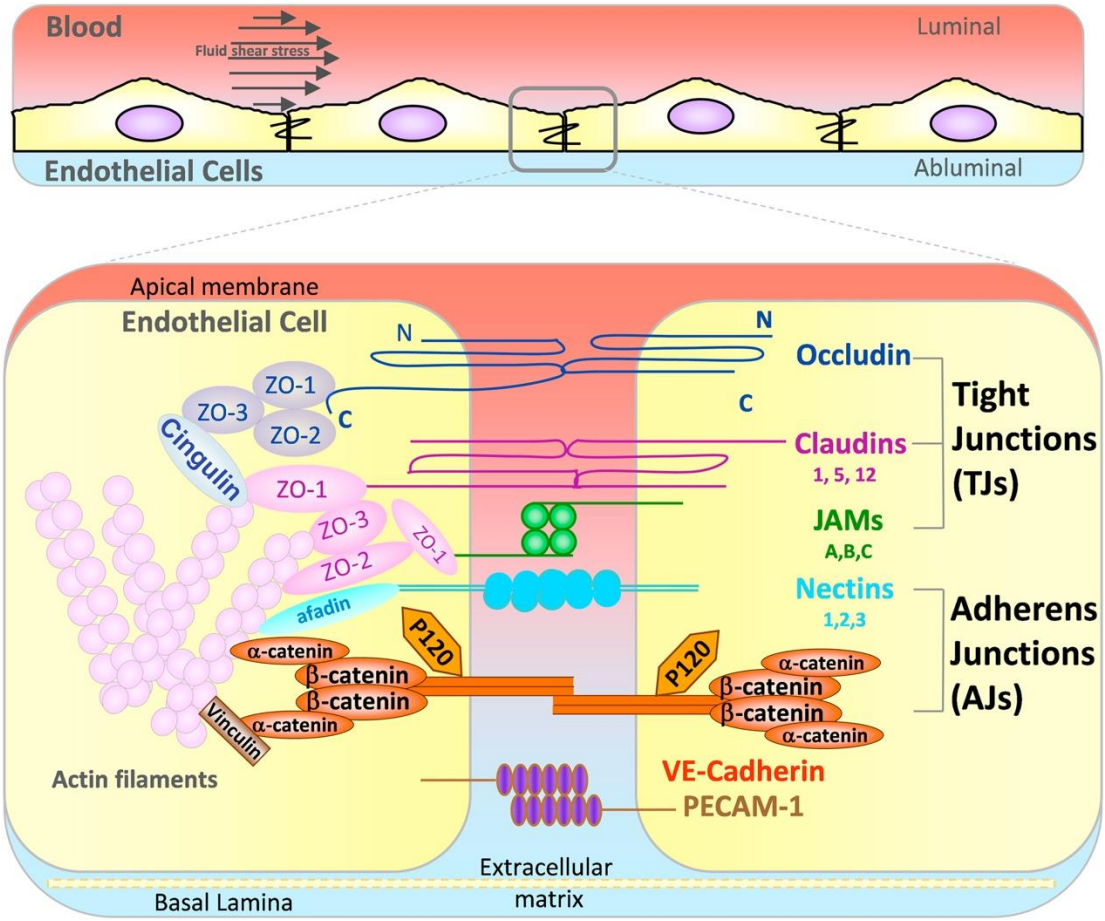

Figure 2.4 Endothelial Cell-Cell Junction. (**top panel**) Endothelial cells create a barrier between the circulatory and central nervous systems, which are exposed to constant fluid shear stress. (**bottom panel**) Transmembrane proteins that form the cell-cell junction. Tight and adheren junction proteins are responsible for cell adhesion and barrier formation. The transmembrane proteins are connected to the actin cytoskeleton via scaffolding proteins. *Reprinted from Cerutti and Ridley, Endothelial cell-cell adhesion and signaling. Experimental Cell Research 358(1): 31-38. 2017. Open access. Permission given by Elsevier (Creative Commons CC-BY license).*

Adherens junctions initiate and maintain cell-to-cell contact, a critical first step in tight junction formation. Adherens junctions are primarily formed by cadherin proteins, with vascular endothelial (VE)-cadherin being strictly expressed in endothelial cells. Cadherin adhesion relies on homophilic, Ca^{2+}-dependent interactions at the extracellular domains [96]. The intracellular domains, which contain binding

locations for transcription factors, are connected to the cytoskeleton via β- catenin or γ-catenin. The transcription factor p120 also binds to this domain, which prevents endocytosis of the cadherins via inhibited translocation to the nucleus [97]. Translocation of p120 to the nucleus initiates clathrin-dependent endocytosis and increases barrier permeability. Another pathway to modulate cadherin-mediated permeability is through increased cellular contraction. Phosphorylation of myosin light chain results in the activation of p21-activated kinase and increased contraction [97]. Lastly, ve-cadherin can diminish the angiogenetic effects of vascular endothelial growth factor by inhibiting the internalization and signaling of vascular endothelial growth factor receptor-2 [98].

Tight junction transmembrane complexes on the apical region of the intracellular cleft regulate and limit the paracellular flow of ions, solutes, lipids, and proteins. They prevent the diffusion of charged, large (>400 Da), and hydrophilic (> 8 hydrogen bonds) molecules between the apical and basal sides of the cell and into the brain. They help establish an apical-basal polarity within the cell barrier [7]. Tight junctions are composed mainly of occludin and claudin proteins which are linked to the cytoskeleton via intracellular zonula occluden proteins (e.g., ZO-1/-2/-3). The near-continuous formation and linkage of the claudin proteins between cells create a pore size of ~4.6 Å [99]. The different amino acid sequences within the first extracellular loop impose a charge selectivity on molecules that can diffuse past. [100]. Claudin-5, the most enriched tight junction protein at the BBB, is distinct to endothelial cells. The expression is regulated by VE-cadherin via VE-cadherin-mediated AKT activation and the exclusion of Forkhead box protein 01, a negative regulator of claudin-5 expression,

in the nucleus [101]. To further enhance the formation and integrity of the junction network, the nearby astrocytes and pericytes secret growth factors and morphogens (e.g., cyclic AMP, transforming growth factor-β, and bFGF), that regulate microvascular homeostasis [102, 103].

It is increasingly clear that the presentation of junctional proteins (i.e., pattern, geometrical organization, edge-presentation) and cell morphology plays a vital role in regulating the permeability of cerebral endothelium [104-108]. As cell-cell junctions mature in vitro, VE-cadherin and ZO-1 reorganize from a serrated perpendicular geometry to a continuous strand linear to the cell edge [107-109]. Previous studies have shown junction maturity is dependent on extracellular matrix stiffness, and immature junctions are sites of drug penetration [108].

2.2.3 Endothelial Cell Efflux Transporters

In addition to restricting the entry of molecules into the brain via a physical barrier, the BBB is lined with ATP-binding cassette (ABC) efflux transporters that redirect drugs from the brain endothelial cells back into the bloodstream [110]. ABC transporters, localized to the luminal surface of endothelial cells, transport a wide range of substances against their concentration gradient via ATP hydrolysis [110]. ABC transporters are two homologous transmembrane proteins that adopt an inward-open confirmation with an exposed substrate-binding cavity. After a given substrate attaches to the binding domain and ATP binds to the nucleotide-binding domain, the protein shifts into an inward-closed confirmation, and the drug is transported out of the cell [111]. There are multiple types of ABC transporters present at the BBB that have overlapping substrate recognition [112].

Drug efflux transporters comprise 10–15% of all proteins in the neurovascular unit [113]. Two of the most common ABC transporters at the BBB are ATP Binding Cassette Subfamily B Member 1 (ABCB1, also known as P-glycoprotein, P-gp) and ATP binding cassette subfamily G member 2 (ABCG2). Up-regulation of ABC transporters has traditionally been associated with multidrug cancer resistance of tumors. These transporters create a major hurdle when delivering drugs to brain cancers [88]. The development of ABCB1 and ABCG2 as therapeutic targets has been unsuccessful for many reasons including: (1) ABC transporters are found throughout the entire body and inhibition within normal tissue can result in additional side effects, (2) first generation inhibitors were not very potent, and patients were not screened for ABC expression before treatment, (3) pharmacokinetic interactions required chemotherapy dose reductions or resulted in the potential underdosing of patients, and (4) tumor cells and the BBB can contain multiple types of ABC transporters and the inhibition of one type can result in the over expression of others [114].

For drug delivery to brain tumors to be effective, it must overcome the physical barrier created by tight junction proteins and the metabolic barrier created by ABC efflux transporters. This challenge highlights the necessity to develop a treatment strategy that can simultaneously modulate both proteins within the BBB.

2.2.4 Drug Delivery to the Brain and Clinical Applications

As a result of the physical and metabolic barriers present within the BBB, drug delivery to the brain is incredibly challenging. Numerous preclinical drug delivery systems have been engineered to overcome the BBB. These systems rely on disruption of BBB (paracellular route), enhanced transcellular transport, cell-based delivery

(transcellular route), or by passing the BBB via direct delivery to brain tissues (e.g., intrathecal, intraventricular, intranasal, and convection-enhanced delivery). Nanoparticle carriers have also been engineered with surface modifications that can aid in overcoming the BBB [8]. Most of these methods remain in preclinical studies due to low efficacy.

Despite being the subject of studies for several decades, selective opening of the BBB junction network at the desired site without killing the brain endothelial cells remains challenging in the clinic. Several strategies have been developed to disrupt the tight junction network of the BBB, including the infusion of hyperosmolar solutions, biochemical disruption, focused ultrasound, and electromagnetic radiation [8]. Nevertheless, these methods are not yet universally available in the clinic due to a number of limitations, such as low efficiency, invasiveness, lack of selectivity, or adverse events [8-11]. For example, clinical BBB opening with hypertonic solutions (e.g., arabinose, mannitol) lacks regional specificity and can induce a pronounced fluid shift [115, 116]. Existing site-specific methods (e.g., focused ultrasound [8, 117, 118], thermal therapy [119, 120], and radiation [121, 122]) can enhance drug delivery across the BBB but are often associated with increased risk of edema, hemorrhage, inflammation, or neurotoxicity. As a result, there is a clear need for a method that can dissociate the endothelial tight junction while sparing the endothelial cells.

2.2.5 Relevance to Dissertation

The intact BBB near the tumor-invaded brain regions limits chemotherapy effectiveness. Compared to the leaky BBB within the primary tumor, the BBB within the tumor-invaded brain regions stops almost all drugs from reaching and eradicating

the remaining infiltrative cells [123]. One of the main focuses of this dissertation is to enhance drug delivery to the brain by repurposing a photochemistry-based cancer treatment modality and understanding the mechanisms behind BBB opening. **Chapter 4** will focus on understanding mechanistically how our selected treatment alters the cell-cell junctions in primary brain endothelial cells in vitro. We will further examine the drug delivery of a smaller molecule, dextran, and larger 100 nm liposomes across a monolayer of brain endothelial cells and determine how long the BBB remains 'open' after treatment. **Chapter 7** will focus on engineering a drug delivery system and using a photochemistry-based treatment modality to open the BBB in rats. **Chapter 8** will focus on developing a high throughput model for the screening of ABC inhibitors and present preliminary data on the photochemical modulation of efflux transporters.

2.3 Photodynamic Therapy

Light has been used in medicine for thousands of years. Ancient civilizations in Egypt, India, and China used light to treat skin diseases, including psoriasis and cancer [124]. In the 21st century, light and optics have significantly impacted modern medicine [125]. PDT is now a prominent tool being used in basic science and clinical practice to understand and manage disease [126-128]. PDT dates to the early 20th century in Germany when dyes and light were combined to treat skin cancer. Modern interest in PDT began in the 1960s with the discovery of the photosensitizer hematoporphyrin derivative [129]. Notably, Dr. Thomas Dougherty helped pioneer the field of photomedicine in the 1970s when he completed the first controlled clinical study in humans and was instrumental in the first FDA approval of a photosensitizer, Photofrin, for cancer treatment [130, 131].

2.3.1 Fundamental Principles

PDT is a photochemistry-based, non-thermal approach in which a non-cytotoxic agent (i.e., photosensitizer) is energized by harmless light of an appropriate wavelength to produce cytotoxic agents. While there are multiple photochemical processes that an energized photosensitizer can undergo, this section will focus on the most predominant process, a type II photochemical reaction [13]. After absorbing a photon with a certain amount of energy, the photosensitizer's electrons will move into a single excited state. From here, the excited electrons can relax back to ground state or undergo intersystem crossing (i.e., altering their spin direction) and move into a triplet excited state. Now when the electrons relax from this longer-lived triplet state, an energy transfer to molecular oxygen can take place, resulting in the production of reactive oxygen species (ROS, e.g., $^1O_2$, H_2O_2, $O_2^{\bullet-}$, $\bullet OH$) [129]. For each photon absorbed by the photosensitizer, a single ROS may be produced. The predominant form of ROS produced is singlet oxygen ($^1O_2$), an oxidizing agent, which will be quantified in **Chapters 3, 5, and 7**. The excited state photosensitizer can also produce a fluorescence emission, instead of ROS, which will be discussed in *section 2.3.3*. After administration, and like chemotherapy, non-targeted photosensitizers will spread throughout the body. However, unlike chemotherapy, PDT treatment can be spatiotemporally controlled [18]. Generally, photosensitizers at doses used for PDT treatment are considered inert and won't impact healthy tissues. After a set amount of time after photosensitizer administration and at the desired treatment site, light can be delivered at different powers and for different durations. When light delivery is stopped, the photochemical reaction is also immediately stopped. The generated

cytotoxic singlet oxygen is short-lived, with a half-life of 0.01–0.04 μs, and will stay confined to the treatment site [132, 133].

Numerous parameters impact the amount of singlet oxygen produced and PDT treatment outcomes. Depending on the amount produced, singlet oxygen can kill or modulate cells and tissues [23, 134], with threshold values required to induce tumor necrosis studied extensively by Dr. Theresa Busch [135]. Parameters, known as dosimetry (**Figure 2.5**) [132], that can impact PDT treatment include: 1. Photosensitizer type and tumor accumulation. Photosensitizing agents can have different backbones, such as porphyrins and chlorins. Not all photosensitizers will have the same singlet oxygen yield. Photosensitizers can be pro-drugs that are converted to an active form within a cell. Other photosensitizers require drug delivery vehicles which may alter their pharmacokinetics and biodistribution; 2. Photosensitizer activation wavelength and light dose parameters. Tissues have an extensive range of optical absorption and scattering coefficients, which can impact light penetration depth and photosensitizer activation. The laser power (W/cm^2) and the total amount of light, fluence (J/cm^2), a tissue receives, can impact photosensitizer photobleaching (i.e., the destruction of the ground state photosensitizer by ROS) and tissue oxygen concentrations; 3. Tumor oxygenation. A type II photochemical reaction requires ground state oxygen. Hypoxic tumors, where oxygen is limited, can diminish PDT efficacy [132].

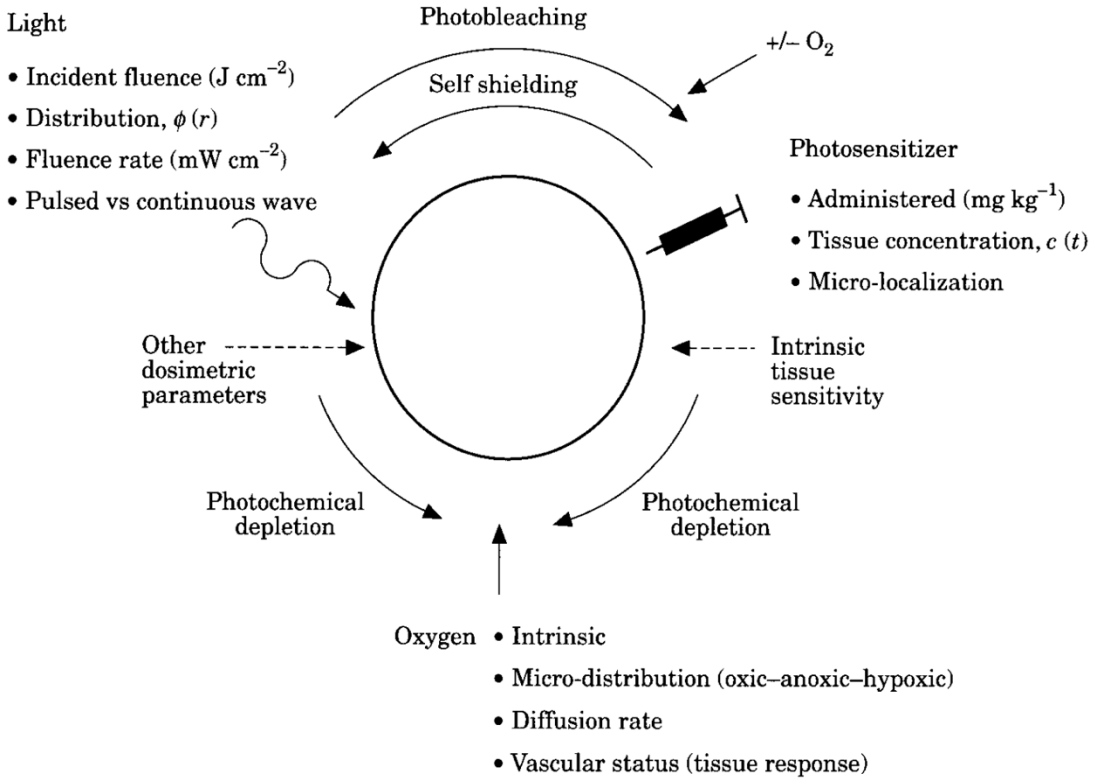

Figure 2.5 Photodynamic Therapy Dosimetry Factors. Outlined are the interdependent factors, including photosensitizers, light, and oxygen, and the corresponding mechanisms that impact PDT treatment outcomes. *Reprinted Wilson et al., Implicit and explicit dosimetry in photodynamic therapy: a New paradigm. Lasers Med Sci. 1997. Permission obtained from Springer Nature and Copyright Clearance Center's RightsLink®.*

Light-activated photosensitizers produce singlet oxygen, an oxidizing agent, that inflicts direct damage to subcellular organelles (e.g., mitochondria, endoplasmic reticulum, lysosome), which can lead to cell death [129]. The mitochondria are one of the common sites for intracellular photosensitizer accumulation, including for the photosensitizer VP, which will be discussed further in *Section 5.3.4* and throughout this work [136]. The production of singlet oxygen by light-activated photosensitizers can cause photodynamic disruption of the mitochondrial membrane (i.e., membrane depolarization), which triggers the release of cytochrome c, a potent initiator of

intrinsic apoptotic cell death [21]. After the release from the mitochondria, cytochrome c will interact with the apoptotic protease activating factor-1 in the cytosol, forming an apoptosome. Apoptosomes will go on to activate caspase-9 and eventually caspase-3, initiating a caspase cascade and cell death [137]. PDT has also been shown to photochemically degrade the anti-apoptotic protein Bcl-2 while leaving pro-apoptotic proteins Bad and Bax unaffected [138, 139]. This shifts the balance in target cells from an anti-apoptotic state to a more pro-apoptotic state [21]. These processes are known to bypass cell-death signaling pathways required for more traditional cancer treatments, such as chemotherapy. In addition, photosensitizers and PDT treatment does not result in the same side effects as chemotherapy [126, 134], allowing PDT treatment to be incorporated into the clinical workflow for many diseases.

PDT typically involves the high optical energy (80-300 J/cm^2) activation of photosensitizers [134, 140-143] and has historically been approved for the treatment of superficial diseases beneath the skin or in the lining of organs where a light source can reach [140]. With the advancement of fiber optic light conduits, there is now the clinical possibility for PDT to treat and permeabilize tumors that have grown deeply into the skin or other organs via intraoperative, endoscopic, or interstitial procedures [144]. *Sections 2.3.2, 2.3.3,* and *2.3.4* will now focus on different photosensitizers and PDT clinical applications.

2.3.2 Photosensitizers

Photosensitizers are non-toxic agents that can generate cytotoxic ROS upon optical irradiation with the appropriate wavelength of light. Tetrapyrrole structures such as porphyrins and chlorins are commonly studied and used in PDT treatments,

many of which are FDA approved. The aromatic structure of porphyrin, which contains four pyrrole rings and 18 π- (or delocalized) electrons, makes it an ideal molecule for PDT applications. In general, photosensitizers used in clinical applications should have a strong absorption peak (i.e., q-band) in the red to the near-infrared spectral range, possess a large triplet quantum yield, have minimum dark toxicity effects (i.e., inert prior to light activation), and have relatively fast clearance [129, 145]. The optical therapeutic window for light-based treatments is considered 650-950 nm, where light has its maximum depth of penetration in tissue. Oxygenated hemoglobin strongly absorbs light below 600 nm, and water strongly absorbs light above 950 nm [146]. In addition, wavelengths longer than 850 nm do not provide enough energy to excite oxygen to its singlet state [129, 145].

As mentioned previously, the first FDA-approved photosensitizer for PDT treatment was Photofrin in 1995. It remains one of the most widely used photosensitizers in the world [147]. However, Photofrin has a relatively low maximum absorption peak at 630 nm and an elimination half-life of 17 ± 4.3 days, leading to poor treatment outcomes and skin toxicity. Second-generation porphyrin-based photosensitizers have been developed to overcome these setbacks. Two photosensitizers discussed throughout this dissertation and in a direct comparison in *Sections 3.3.1* and *3.3.2* are ALA-induced PpIX and VP (also known as benzoporphyrin derivative). ALA is a prodrug converted into its active form PpIX through the heme synthesis pathway. In healthy cells, PpIX is converted into the final product, heme, but in cancer cells, a lack of NADH results in low levels of ferrochelatase which results in a buildup of PpIX [148]. In 2017, the US FDA approved 5-aminolevulinic acid (5-

ALA; Gleolan®) as an intraoperative imaging agent in patients with suspected high-grade gliomas [149]. This will be discussed in more detail in *Section 2.3.3*.

VP is a second-generation porphyrin-based photosensitizer. It has more ideal photochemical properties, including a 689 nm q-band for PDT treatment, a 24-hour elimination half-life, and an 86% singlet oxygen yield [150-153]. In 2001, the FDA approved the polydisperse liposomal formulation of VP, Visudyne®, for treating wet age-related macular degeneration. Free-form VP is not used clinically due to its inability to form sufficient hydrogen bonds with water. In an aqueous solution, free-form VP will experience uncontrollable aggregation, resulting in a significantly reduced fluorescence emission signal, $^1O_2$ production, and poor pharmacokinetics [21]. Visudyne® has been used worldwide to treat hundreds of thousands of patients, and evidence suggests treatment is safe, has minimal severe treatment side effects (e.g., only 1-4% of patients experience severe vision decrease), and can reduce the risk of visual loss in patients [154, 155]. For the treatment of age-related macular degeneration, Visudyne® is administered to patients intravenously, and about 15 minutes later it is activated by a 689 nm laser to target and destroy the overgrown blood vessels within the eye [156]. Compared to ALA-induced PpIX, which requires intracellular conversion, VP can be activated on-demand at much shorter drug-light intervals. Since its approval, Visudyne® has been evaluated in numerous clinical trials, including for the treatment of refractory brain tumors (NCT00002647), pancreatic ductal adenocarcinoma (NCT03033225), and vertebral metastases (NCT02464761). While Visudyne® has shown promise in treating different cancers, the liposome can induce toxicity to normal tissues, trigger immunogenic responses, and reroute the

therapeutic payload to organs associated with the mononuclear phagocyte system (MPS) [6]. The immunological and toxicological consideration for liposome design will be discussed in depth within **Chapter 6**. The impact of lipids and other biomolecules on the photochemical properties of VP will be discussed in **Chapter 5**. Alternative drug delivery systems for VP will be discussed in **Chapter 7**.

2.3.3 Fluorescence Guided Resection

Besides generating cytotoxic ROS during PDT treatment, the singlet excited-state photosensitizer can also emit a photon, which is helpful for fluorescence imaging and image-guided resection of tumors [157]. Surgical resection of tumors remains a first-line treatment modality for many cancer types, including GBM. The fluorescence signal produced by photosensitizers accumulated within a tumor can allow surgeons to better define tumor location and margins during the procedure. This enhanced surgical technique has increased the number of patients that can have a complete resection and improved safety by diminishing damage to normal tissue [158, 159]. Generally, fluorescence-guided resection (FGR) uses much lower laser powers and total fluence (> 5 mW/cm^2, 0-20 J/cm^2) and can also use blue light to excite the photosensitizers Soret band.

Numerous photosensitizers have been used FGR imaging probes for a wide range of cancers. Notably, indocyanine green is approved for laparoscopic surgery, methylene blue is used to visualize ureters during colorectal procedures and map sentinel lymph nodes during breast cancer surgeries, and the cetuximab-IRDye800CW was recently approved in Japan for use in head and neck cancers [158]. One particularly successful photosensitizer for the FGR of GBM is ALA-induced PpIX [149]. In 2017,

the FDA approved 5-ALA (Gleolan®) as an intraoperative imaging agent in patients with suspected high-grade gliomas [149]. Upon excitation with ultraviolet/blue light (375-440 nm), gliomas that contain the 5-ALA-induced protoporphyrin IX (PpIX) emit a violet-red fluorescence, which the naked eye can easily visualize (i.e., without filters) for resection [160]. Fluorescence-guided brain tumor surgery is routinely applied in some clinical centers, whereas the combination of FGR and PDT is under active preclinical and clinical studies. While this FDA-approved surgical technique has shown to increase the mean patient survival by 3 months compared to standard white light surgery [159], FGR and ALA-mediated PDT have not yet achieved long-term survival [161]. Fluorescence imaging of PpIX and VP will be discussed further in *Sections 3.3.2* and *5.3.4*.

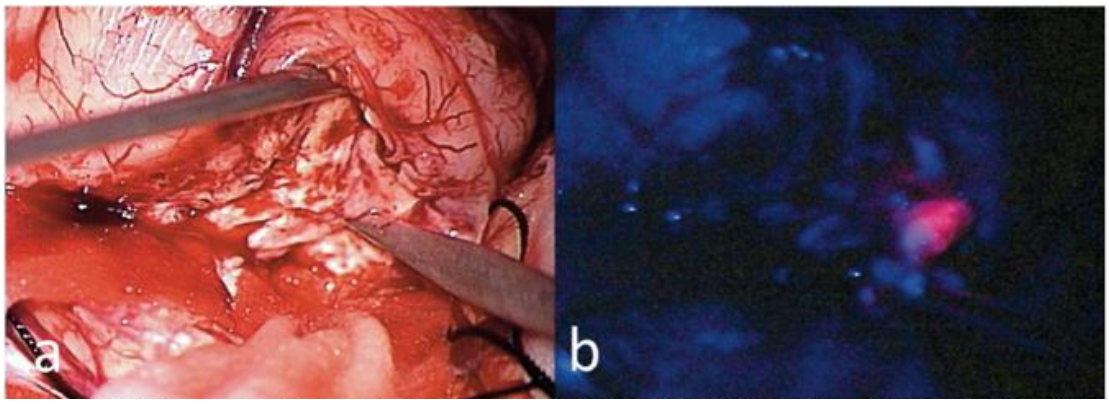

Figure 2.6 ALA mediated Fluorescence Guided Resection of GBM. (**a**) White light surgery shows a relatively homogenous tumor appearance. (**b**) ALA induced PpIX fluorescence under blue excitation light helps identify the cancerous lesion. *Reprinted Hadjipanayis, et al., What is the Surgical Benefit of Utilizing 5-ALA for Fluorescence-Guided Surgery of Malignant Gliomas? Neurosurgery. 2015 Nov; 77(5): 663–673. Permission obtained from Wolters Kluwer and Copyright Clearance Center's RightsLink®.*

2.3.4 Clinical Applications

PDT has shown promise in treating different ailments. FDA approvals include treatment of head and neck cancers [162], esophageal cancer [163], non-small cell lung

cancer [164], and advanced cutaneous T-cell lymphoma [165]. It is also approved in Mexico for prostate cancer [166] and Japan for unresectable locally advanced or recurrent head and neck cancer (NCT03769506). The remaining sections and chapters will focus on using ALA-induced PpIX and VP to treat GBM. As previously mentioned, ALA is a prodrug administered as an oral solution to patients. Alternatively, in aqueous solutions, free-form VP will experience uncontrollable aggregation, resulting in complete self-quenching, minimum singlet oxygen production, and poor pharmacokinetics [21]. Therefore, for effective patient delivery, VP must be solubilized or incorporated into a drug delivery vehicle. The current gold standard for delivering VP to patients is in its phospholipid-associated form, Visudyne®. Adding 5ml of water to the freeze-dried lipids and VP followed by vigorous shaking results in a self-assembled polydisperse liposome that has an average diameter of 524.8 ± 547.5 nm and a VP concentration of ~2.8mM [167]. Visudyne® is being tested in several clinical trials evaluating PDT for pancreatic ductal adenocarcinoma (NCT03033225) [168], recurrent and metastatic prostate cancer (NCT03067051, NCT02939274), breast neoplasms (NCT02872064), and pleural malignancies (NCT02702700). Surgery immediately followed by PDT has been studied in the clinic for brain tumors (NCT03048240, NCT03897491, NCT00003788) [143, 169]. In fact, a single adjunctive dose of PDT has been shown to add up to 18 months to the lifespan of patients with GBM [12].

2.3.5 Photodynamic Priming

Targeting the tumor microenvironment, including the vasculature, could provide additional opportunities to modulate tumor physiology and enhance the

delivery of therapeutic agents for improved treatment outcomes. Previous studies have demonstrated the ability of PDT to permeabilize tumor vasculature and the BBB for enhanced intratumoral drug delivery [14-20]. However, despite the promising preclinical results using PDT to permeabilize the BBB and treat brain tumors, the side effects, including edema, neurotoxicity, and even animal death, remain a major concern in the clinic [15, 170-172]. A study by Hirschberg and colleagues in 2007 showed that the human equivalent dose of the photosensitizer ALA (125 mg/kg) and a light dose of 26 J could open the BBB for up to 3 days, but also resulted in the death of 25% of tumor-bearing rats. To address this issue, our lab has introduced priming which operates at low doses of optical energy and photosensitizer (i.e., in vitro dose is <1 μM × J/cm^2) to modulate biomolecular targets without killing the organism. Leveraging subtherapeutic doses of PDT can also impact tumor immune response and overcome drug resistance by modulating efflux transporters.

Traditional PDT uses light doses of 80-300 J/cm^2 to induce cancer cell killing. Traditional PDT also uses large photosensitizer doses (e.g., 2.0 mg/kg VP in mice, the human equivalent dose [173]) and a longer drug-light interval to ensure the photosensitizer accumulates within both the vasculature and the tumor. Alternatively, PDP uses light doses in the range of 10-80 J/cm^2 to modulate the vasculature without damaging the surrounding tissues. PDP uses smaller photosensitizer doses (e.g., 0.25 mg/kg in mice, ¼ the human equivalent dose [19]) and a shorter drug-light interval, usually between 15-90 minutes, to ensure the photosensitizer is confined to the vasculature [174]. Encouraging results have been obtained with PDP for pancreatic and brain tumors. **Chapter 4** will explore how PDP can be used to disassociate the

endothelium of the BBB that has an exceptionally high degree of junctional tightness without damaging the surrounding healthy brain.

2.3.6 Relevance to Dissertation

As is evident from the numerous clinical trials (NCT03048240, NCT03897491, NCT00003788, NCT01966809, NCT00002647, NCT01682746), the photochemistry-based treatment modality, PDT, has shown promise in treating GBM. PDT has also shown promise in opening the tumor vasculature and enhancing intratumoral drug delivery. Our lab has recently shown that sublethal PDT improves vascular permeability and enhances ONIVYDE® (Liposomal irinotecan) extravasation into pancreatic tumor parenchyma by up to 11-fold without damaging the surrounding healthy pancreas [175]. This dissertation will expand our knowledge and focus on how PDT can be used to enhance drug delivery to the brain and treat brain tumors.

Throughout this dissertation, photosensitizers, PDT, and PDP will be examined for the treatment of GBM. **Chapter 3** will focus on light penetration depth in the rodent brain. A direct comparison between PpIX and VP will be performed. **Chapter 4** will focus on the meninism behind PDP-induced BBB opening to enhance drug delivery to residual GBM cells. **Chapter 5** will focus on improving VP photochemical properties via biomolecule-VP conjugates. Lastly, **Chapter 7** will focus on a pure-drug carrier-free nanoparticle of VP for GBM treatment.

Chapter 3. Photodynamic Effect Depth in the Rodent Brain [1]

3.1 Introduction

Light and optics have had significant influence on modern medicine [125]. PDT, a major output of this work, is now being used extensively in basic science and clinical practice to understand and manage disease [126-128]. FGR and PDT using different photosensitizers (e.g., VP, 5-ALA, Photofrin®, temoporfin, hematoporphyrin derivative) have been evaluated clinically for patients with brain cancer (e.g., NCT03048240, NCT03897491, NCT00003788, NCT01966809, NCT00002647, NCT01682746). The pro-drug photosensitizer, ALA (Gleolan®) was approved in 2017 as an intraoperative imaging agent in patients with high-grade gliomas [149]. In addition, a single adjunctive dose of PDT has been shown to add as much as 18 months to the lifespan of GBM patients [12]. In a small-scale study, the combination of FGS and PDT increased the mean survival of GBM patients from 24.6 to 52.8 months, compared to FGS alone [176]. However, long-term survival using FGS and/or PDT has not been achieved. It is well recognized that limited light penetration in brain tissues, and the poor selectivity and delivery of the photosensitizers impacts treatment outcomes.

Tissue optical properties influence light delivery and impact PDT outcomes [177]. Red light penetration depth is typically 0.1-0.3 cm in tissues [125]. This

1 This chapter was adapted from Inglut C.T., Gaitain B., et al. "Predictors and Limitations of the Penetration Depth of Photodynamic Effects in the Rodent Brain". *Photochem Photobiol.2020 Mar;96(2):301-309.* Permission obtained from John Wiley and Sons to use this material in this dissertation. B.G. was a co-author. He co-wrote several sections in this chapter, and helped perform and analyze the experiments for Figures 3.4.

penetration depth is defined as the depth at which the incident optical energy drops to 1/e (~37%) [125]. A number of *ex vivo* and *in silico* studies have already shown that the remaining 37% of photons can reach up to 2-5 cm deep in brain tissues [178-184]. A series of studies by Wilson, Perria, and Cheng have shown that 630 nm light activation of hematoporphyrin derivative induces tumor necrosis and cell killing at 0.8-1.5 cm deep within the brain [185-187]. On the other hand, Olzowy et al. demonstrated that 630 nm light activation (200 mW/cm^2) of 5-ALA-induced PpIX induces cerebral tissue damage only up to 0.4 cm deep [188]. Based on prior work showing that 690 nm light can penetrate approximately 40% further than 633 nm light in bladder tissue [189], here, we test if VP could be activated by 690 nm light at further depths in the brain, compared to using 635 nm light-activated PpIX.

Both VP and PpIX are hydrophobic molecules and tend to aggregate in biological environments, leading to low bioavailability, heterogeneous biodistributions, and reduced PDT efficacy. Nanoliposomes, composed of a hydrophobic lipid bilayer and an aqueous core, are the most studied and clinically used photosensitizer delivery vehicles [190]. In 2001, a polydisperse liposomal formulation of VP (Visudyne®, 0.2-1 μm in diameter) was approved by the FDA for treatment of patients with wet age-related macular degeneration [145, 191]. A clinical study using Visudyne®-PDT to treat patients with refractory brain tumors is also taking place (NCT00002647) [192]. While PpIX production in tumors is commonly derived from the oral or systemic administration of 5-ALA prodrug [149], there has been a resurgence of interest in PpIX delivery using different nanoformulations to, in part, bypass the heterogeneous and low conversion of 5-ALA to PpIX observed in some

tumors [193-195]. Based on these advances, here, we synthesized monodisperse Liposomal formulations of VP (Liposomal VP) and PpIX (Liposomal PpIX). Using these photosensitizing liposomes, we examined the limits of PDT as a function of tissue depth and light fluences in *ex vivo* rat brains, by monitoring the changes in photosensitizer photobleaching and singlet oxygen ($^1O_2$) production. This chapter will give us insights into which photosensitizer is more advantageous for the targeting of microscopic GBM infiltrates that can be up to 2cm away from the primary tumor.

3.2 Materials and Methods

3.2.1 Synthesis and Characterization of Liposomal VP and Liposomal PpIX

Liposomes containing VP or PpIX within its bilayer (Liposomal VP and PpIX) were synthesized via freeze-thaw extrusion as described previously [19, 175, 196-198]. Briefly, lipids, dipalmitoylphosphatidylcholine (DPPC), cholesterol, and distearoylphosphatidylethanolamine-methoxy polyethylene glycol (DSPE-PEG), and 1,2-dioleoyl-3-trimethylammonium-propane (DOTAP) (Avanti Polar Lipids), were co-dissolved with VP (50 nmoles, U.S. Pharmacopeial) at 0.15 mol% VP-to-lipid ratio or PpIX (60 nmoles) at 0.18 mol% PpIX-to-lipid ratio. Chloroform was removed via rotary evaporator overnight in order to create a thin film, which was rehydrated with 1 mL of deionized water. The lipid suspension was subjected to freeze-thaw cycles (4-45°C). The dispersions were extruded through polycarbonate membranes (0.1 μm pore size) at 42°C to form unilaminar vesicles. The final concentration of the dispersions was estimated by absorbance using the established molar extinction coefficient of VP in DMSO (~34,895 $M^{-1}cm^{-1}$ at 687 nm) or PpIX in chloroform (~171,000 $M^{-1}cm^{-1}$ at

407 nm) or DMSO (~170,000 $M^{-1}cm^{-1}$ at 407 nm). The fluorescence properties Liposomal VP (Excitation/Emission: 435/650-750 nm) and Liposomal PpIX (Excitation/Emission: 405/600-800 nm) was determined using a multi-mode microplate reader (Synergy Neo2, BioTek). Particle size and zeta potential were measured on the Nanobrook (Brookhaven). Photosensitizers were diluted to 5 μM in phosphate buffered saline (PBS) for all optical-based characterization. The production of singlet oxygen from photoactivated VP and PpIX was monitored indirectly using the probe, Singlet Oxygen Sensor Green (SOSG). Briefly, 0.5 μM Liposomal VP or Liposomal PpIX were mixed with 25 μM SOSG (Thermo Fisher Scientific) in PBS. Samples were irradiated with 635 nm light (100 mW/cm^2) for Liposomal PpIX or 690 nm light (100 mW/cm^2) for Liposomal VP, at different fluences of 0-80 J/cm^2 (ML6600 series laser module, Modulight). The fluorescence intensity of the cleaved SOSG probe (Excitation/Emission: 504/525 nm) was acquired using a microplate reader prior to and following irradiation.

3.2.2 Photobleaching of Photosensitizers in Ex Vivo Rat Brains

The activation of VP and PpIX was measured via photobleaching in Sprague Dawley rat brains (Innovative Research). Glass capillaries (300 μm in diameter; 1 cm in length) containing 5 μM of photosensitizer were placed in the brains at varying depths (0-2 cm). The brain tissues were exposed to 635 nm red light for Liposomal PpIX or 690 nm Near-infrared light for Liposomal VP using a diode laser (ML6600, Modulight). A range of fluences from 0-80 J/cm^2 (100 mW/cm^2) were examined. After PDT, capillaries were removed, and the fluorescence emission from Liposomal VP (or

Liposomal PpIX) was measured using a reflectance fluorescent microscope equipped with a 375 nm laser diode (L375P70MLD, Thorlabs).

3.3 Results and Discussion

3.3.1 Synthesis and Characterization of Liposomal VP and Liposomal PpIX

Liposomal VP and Liposomal PpIX (Liposomal PpIX) were reproducibly synthesized via the freeze-thaw extrusion method [19, 175, 196, 197]. A lipid composition of dipalmitoylphosphatidylcholine (DPPC), cholesterol, and distearoylphosphatidylethanolamine-methoxy polyethylene glycol (DSPE-PEG) at a 20:10:1 molar ratio was used based on the clinically approved PEGylated Liposomal formulations [199, 200]. Here, both Liposomal VP and Liposomal PpIX were grafted with 3 mol% of PEG and formed in the size range of ~135-150 nm with a narrow size distribution (polydispersity index, PdI < 0.1). Cationic 1,2-dioleoyl-3-trimethylammonium-propane (DOTAP, 8 mol%) was introduced to the lipid composition to provide a zeta-potential of +10-12 mV (**Table 3.1**). Photosensitizers (VP or PpIX) were adsorbed in the liposomal lipid-bilayer via hydrophobic and ionic interactions [201]. Our stability results suggest that 1-4 months of dark storage at 4°C and in PBS did not affect the overall size or monodispersity (PdI <0.1) of Liposomal VP (139.7±11.8 nm in diameter) and Liposomal PpIX (150.9±6.6 nm in diameter)

Table 3.1 Liposomal VP and PpIX. Overview of the characterization of Liposomal VP and Liposomal PpIX detailing their respective hydrodynamic diameter, polydispersity index, and zeta potential. Values are presented as mean±standard deviation. N ≥ 3, where N equals the amount of samples synthesized.

Parameters	L-VP	L-PpIX
Hydrodynamic diameter (nm)	135.7 ± 8.0	153.1 ± 4.9
Polydispersity index (PdI)	0.06 ± 0.02	0.04 ± 0.02
Zeta potential (mV)	10.1 ± 1.2	12.4 ± 1.8

While liposomes can maintain the stability and photoactivity of photosensitizers in biologically relevant media for effective PDT, hydrophobic photosensitizers in the lipid bilayer of liposomes are prone to quenching [201-203]. To test if the unquenched photosensitizers (VP or PpIX) are stabilized in the liposomes and could be photo-activated for PDT, we evaluated the stability, quenching factor, and singlet oxygen ($^1O_2$) production of each photosensitizer in both free and liposomal forms, with or without light activation. Changes in photosensitizer absorbance and fluorescence were monitoredand in PBS (**Figure 3.1a, b**). In Figure 1a, the absorbance (blue dotted line) and fluorescence (red dotted line) spectra for free VP in PBS were significantly lower than that of Liposomal VP (solid lines) in PBS, indicating the rapid aggregation of free VP molecules under physiological conditions without being encapsulated in a liposomal formulation. Similarly, 'recovery' of the absorbance (blue dotted line) and fluorescence (red dotted line) spectra of PpIX photosensitizers in PBS was made possible by the liposomal formulation (**Figure 3.1b**). These results suggest that the unquenched photosensitizers (VP or PpIX) are stabilized in the liposomes and could be activated by light for PDT, even without the release of photosensitizers from the liposomes.

Light activation of photosensitizers results predominately in a type II reaction which produces highly reactive $^1O_2$ [23]. The $^1O_2$ quantum yield of VP ($\Phi\Delta$= 0.86) is significantly higher than that of PpIX ($\Phi\Delta$= 0.56) [150-153]. Using the SOSG probe, we indirectly evaluate if 690 nm light activation of VP could produce $^1O_2$ more efficiently than 635 nm photo activated PpIX in PBS. Light activation of VP generated a markedly higher SOSG fluorescence intensity than that generated by PpIX, in an energy dependent manner (**Figure 3.2a**). The SOSG fluorescence signal began to plateau at 60-80 J/cm^2. It is speculated that an insufficient supply of ground state oxygen or available molecular probe lowered the SOSG signal at 80 J/cm^2. These results indicate Liposomal VP can produce more $^1O_2$ than Liposomal PpIX upon light activation under our experimental conditions.

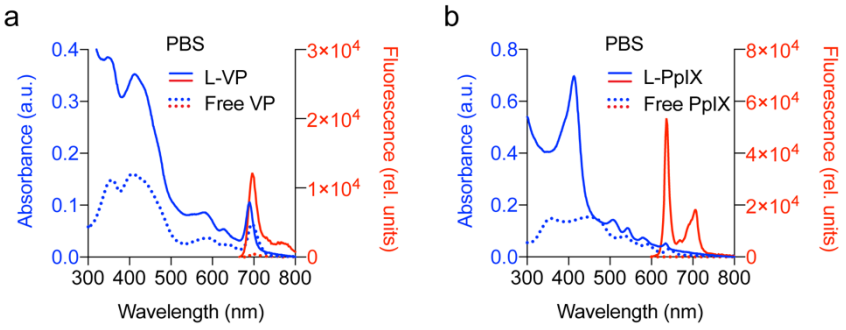

Figure 3.1 Absorbance and fluorescence spectra of VP and PpIX (**a**) Free-form VP fully has a strong absorbance peak at 435 nm (soret band) and 690 nm (Q band). Typically for PDT, VP is activated at 690. VP fluoruence emission *has a* peak in the near-infrared range (λ_{max} at ~700 nm). Free VP is hydrophobic and readily aggregates in PBS, as demonstrated by the decrease in magnitude of the absorbance spectrum, resulting in fluorescence quenching of VP with minimal photoactivity (< 2%). Encapsualting VP in a Liposomal formulation restores its fluorescence and photoactivity (35.8±0.2%) in PBS. (**b**) Free-form PpIX fully shows a strong absorbance peak at 405 nm (soret band), with multiple Q bands in the green to red range. Typically, PpIX is activated by 635 nm light or 375-440 nm light for PDT or FGS, respectively. The fluorescence signal emitted by PpIX is in the red/ near-infrared range between 635 and 700 nm. Likewise, free-form PpIX aggregates in PBS, leading to a quenched state that is no longer activatable at 635 nm. Similarly, the encapsulation of PpIX within a Liposomal formulation restores its fluorescence and photoactivity up to 82.8±0.1%. N ≥ 6, where N equals the number of wells conducted over 3 trials.

3.3.2 Evaluation of the Tissue-depth Dependent Photodynamic Effects of VP and PpIX

Photobleaching is a process in which a photosensitizer (or fluorophore) permanently loses the ability to fluoresce and/or undergo type I/II reactions due to photochemical damage and covalent modification of the photosensitizer. Measuring the loss of fluorescence as the photosensitizer is photobleached is perhaps the most well studied and easily accessible tools for PDT monitoring and dosimetry in preclinical (**Figure 3.2b**) and clinical settings [204-207]. For example, Tyrrell et al. showed patients lesions with significantly higher levels of PpIX photobleaching post PDT had complete clearance at 3 months [208]. Here, we examined the penetration depth of the photodynamic effects in rat brains by monitoring the loss of fluorescence, as the photosensitizer is photobleached, after surface light illumination. Briefly, capillaries filled with 5 μM of Liposomal VP or Liposomal PpIX, were inserted into the *ex vivo* rat brains at varying heights followed by surface illumination using appropriate wavelengths (i.e. 690 nm for Liposomal VP; 635 nm for Liposomal PpIX) (**Figure 3.3**). After light activation, the total fluorescent signal was compared to a negative

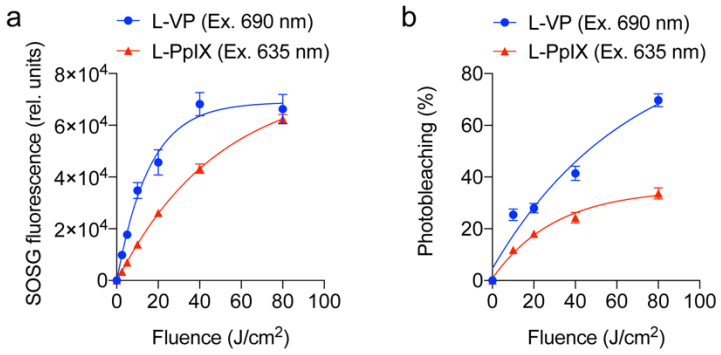

Figure 3.2 Singlet Oxygen Production and Photobleaching of Liposomal VP and Liposomal PpIX. (**a**) SOSG fluorescence emission and (**b**) photobleaching percentage of Liposomal VP and Liposomal PpIX with respect to increasing fluences of light at 690 nm and 635 nm, respectively. N ≥ 6, where N equals the number of wells assessed over 3 trials.

control to determine the degree of photobleaching. A non-linear decrease in the percentage of Liposomal VP (or Liposomal PpIX) photobleaching was observed with increased tissue depth and reduced fluence (**Figure 3.4a,b**). Up to 10% photobleaching of Liposomal VP was observed at 1.4-2 cm (**Figure 3.4a,c**), while negligible (0-2%) photobleaching of Liposomal PpIX was observed at 1 cm deep in brain tissue (**Figure 3.4b,c**). This result appears to be similar to previous findings [209, 210]. Dereski and colleagues demonstrated that Photofrin®, upon 632 nm light activation, induces a necrotic zone ~0.35 cm deep within male Fisher rat brains [209]. A clinical study showed talaporfin, which is activated at a longer wavelength of 664 nm, could induce PDT damage (based on demyelination) up to 0.8 cm in a patient with recurrent glioma [210]. It has also been shown that illumination geometry impacts the depth of brain tissue damage induced by PDT. Specifically, using hematoporphyrin derivative-based PDT, Perria et al. found that the depth of necrosis with surface illumination was 1.5 cm deep, compared with the 0.8 cm radius of cell killing found by Cheng et al. using an implanted optical fiber [185-187]. Further studies comparing surface illumination with illumination using implanted optical fibers are warranted.

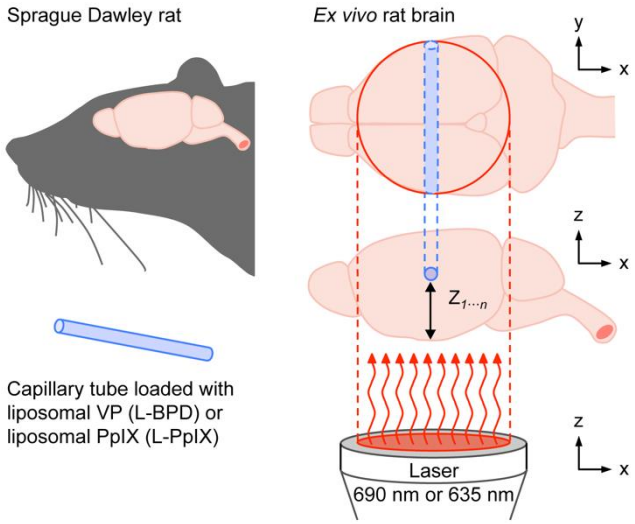

Figure 3.3 Experimental setup for examining the limit of the photodynamic effect. Glass capillaries containing Liposomal VP or Liposomal PpIX (5 μM) were inserted at various depths (Z) in rat brains and exposed to 690 nm or 635 nm light (surface illumination)

The degree of photobleaching across the different energies (40 and 80 J/cm^2) converge as depth increases (**Figure 3.4a,b**) since the loss of light intensity is non-linear. Light penetration can be modeled using the simple 1-dimensional (1-D) equation $\phi(z) = Eke^{-\mu z}$ [211], where $\phi(z)$ is the fluence rate (W/cm^2) dependent on depth (cm), z. E is the irradiance delivered on the surface of the tissue (W/cm^2), k is backscattered light that augments irradiance on the surface of the tissue, and μ is the attenuation coefficient (cm^{-1}). The amount of energy lost is modeled as an exponential decay (e^{-z}). Therefore, it is expected that the depth of photodynamic effects would be proportional to $\phi(z)$, and the depth versus degree of photobleaching should also have an exponential decay. However, due to the specular reflectance when the light hits the brain, and the boundary condition of the air-brain barrier, the trend shows a plateau followed by an exponential decay (**Figure 3.4a,b**). Yet, based on the model set up, the light initially penetrating the brain at very shallow depths should have a fluence rate slightly greater than the initial irradiance, and photobleaching should be greater [212-

214]. Light scattering in tissue is anisotropic (i.e., has a g factor of 0.9 on a -1 to 1 scale), meaning most light will forward scattering and a small amount of light is scattered back [215]. There is also a possibility of some backscattered light that hits the air-brain barrier to be reflected back into the brain again. This additional light scattering will increase the fluence rate as depth increases. However, based to the depth intervals taken, this phenomenon cannot be seen (**Figure 4a,b**).

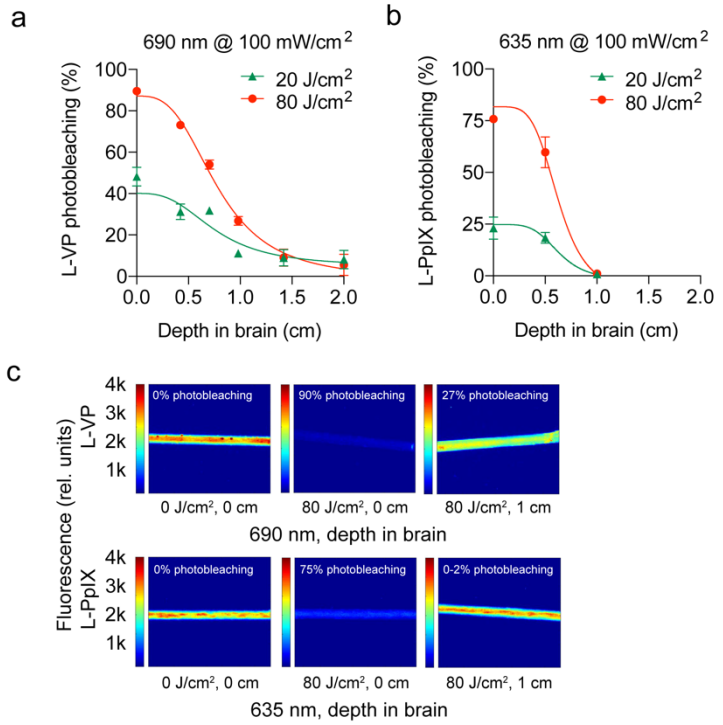

Figure 3.4 Depth of Photosensitizer Activation within Brain Tissue Determined via Degree of Photobleaching. Photobleaching of (**a**) Liposomal VP and (**b**) Liposomal PpIX were evaluated at different depths and fluences. (**c**) At 80 J/cm^2, 27% Liposomal VP photobleaching was observed 1 cm deep in tissue, in contrast to only 0-2% photobleaching of Liposomal PpIX. N ≥ 3.

The fact that PpIX demonstrated a shallower penetration depth than VP is not all that surprising. The main reason comes down to the activation wavelength. VP was activated using a 690 nm wavelength and PpIX was activated with a 630 nm

wavelength. Although this is only a 60 nm shift, there is an appreciable drop in absorption by up to 40-50% [216-218]. This led to the 690 nm light penetrating double the depth of 630 nm light [219]. The depth of treatment is described with the equation $z_{rx} = \delta \ln(\frac{Etk}{H_{th}})$ [213]. Z_{rx} is the depth penetration of the photodynamic effect, δ is optical penetration depth (cm), t is the exposure time (s), and H_{th} is the minimum amount of energy needed to make the photodynamic effect on the tissue (W*s/cm^2). Looking at this equation, increasing the E or t increases the depth of the effect by ln(Et), while increasing the wavelength would increase the optical penetration depth, which as a result would increase the penetration depth of the photodynamic effect in a proportional manner.

While Liposomal VP has greater potential for deeper activation and larger production of $^1O_2$ in tissue, ALA-induced PpIX is a valuable tool for the FGS of gliomas. A digital comparison of the two capillary tubes (**Figure 3.5**) filled with Liposomal VP (top) and Liposomal PpIX (bottom) reveal PpIX can be seen easier compared to VP. The capillaries were placed at similar heights, 0.04-0.05 cm below

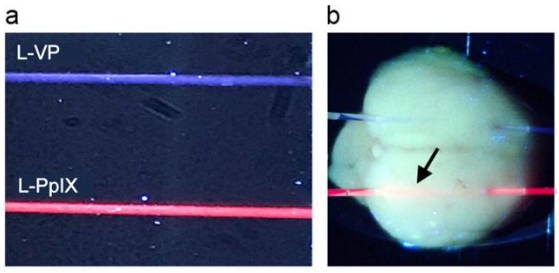

Figure 3.5 Visualization of the Fluorescent Emission of Liposomal VP and Liposomal PpIX when Excited at 375 nm. (**a**) Capillaries filled with the photosensitizers (Liposomal VP or PpIX, 5 μM) were excited with 375 nm and captured with a phone camera (OnePlus 5). PpIX's fluorescent signal can be easily visualized by the naked eye. (**b**) Capillaries were inserted into the brain and were excited to examine if the fluorescent signal could be visualized through brain tissue. The emission signal from PpIX could be seen when the capillary was inserted ~0.04-0.05 cm deep in tissue (black arrow).

the surface of the brain and excited with 375 nm light, a similar wavelength of light used for FGS. The higher fluorescence quantum yield of PpIX (ΦF= 0.155) and its fluorescence peak at 630 nm make it easier for the naked eye to visualize. VP fluoresces at 700 nm and has a lower fluorescence quantum yield (ΦF= 0.051) [150-153]. Even if the same number of photons were being emitted, the emitted 630 nm light is seen with 10 times greater sensitivity by the human eye than the 690-710 nm light [220].

In summary, the results show that the liposomal formulations improve the stability and photoactivity of VPand PpIX in PBS. Near-infrared light (690 nm) activation of Liposomal VP induces $^1O_2$ production, which causes photobleaching of VP up to 2 cm deep in brain tissues. In contrast, no photobleaching was observed beyond 1 cm deep in brain tissues upon red light (635 nm) activation of Liposomal PpIX. The enhanced penetration depth of Liposomal VP-mediated PDT effects in the brain tissue paired with the use of PpIX for tumor visualization opens the door to developing and optimizing the combination of FGS and PDT for recurrent brain tumors, which typically occur within 1-2 centimeters of the original tumor [44, 45, 221]. Characterization and optimization of Liposomal PpIX based FGS and Liposomal VP-mediated PDT in *ex vivo* brain tissues will pave the way towards investigating these new concepts in animals and eventually in patients.

Chapter 4. Understanding the Effects of Photodynamic Priming on Endothelial Cell–Cell Junctions for Enhancing Drug Delivery[2]

4.1 Introduction

As described in *Section 2.2*, the unique capillaries within the brain, known as the BBB, limit the diffusion of large or small compounds from the bloodstream into the brain. This specialized neurovascular unit, composed of endothelial cells, neural cells (e.g., astrocytes, pericytes, neurons) and basement membrane, regulates brain homeostasis and protects the central nervous system [81-83]. The cell-to-cell junctions that join the brain endothelial cells are composed of a wide variety of components, such as vascular endothelial-cadherin (VE-cadherin) adherens junction protein, zonula occludens (ZO) scaffold proteins, and claudin-5 tight junction protein. The tight junction transmembrane complexes located on the apical region of endothelial cells prevent the transport of hydrophilic, highly charged, and/or large (>400 Da) molecules [7]. In addition, astrocytes and pericytes secret growth factors and morphogens (e.g., cyclic AMP) to further enhance the formation and integrity of the junction network [102, 103]. The endothelial cell-cell junction at the BBB is one of the key factors that limit drug transport to the brain [87, 95]. Despite being the subject of studies for several decades, selective opening of the BBB junction network at the desired site without killing the brain endothelial cells remains a challenging task in the clinic.

2 This chapter was adapted from Inglut C.T., Gray K.M., et al., "Photodynamic Priming Modulates Endothelial Cell–Cell Junction Phenotype for Light-activated Remote Control of Drug Delivery". IEEE J Sel Top Quantum Electron. Jul-Aug 2021;27(4):7200311. Permission obtained from IEEE to use this material in this dissertation. K.M.G helped perform and analyze the experiments for Figures 4.2, 4.3, and 4.4.

A number of strategies have been developed to disrupt the tight junction network of the BBB, including the infusion of hyperosmolar solutions, biochemical disruption, focused ultrasound, and electromagnetic radiation [8]. Nevertheless, these methods are not yet universally available in the clinic due to a number of limitations, such as low efficiency, invasiveness, lack of selectivity, or adverse events [8-11]. For example, clinical BBB opening with hypertonic solutions (e.g., arabinose, mannitol) lacks regional specificity and can induce a pronounced fluid shift [115, 116]. Existing site-specific methods (e.g., focused ultrasound [8, 117, 118], thermal therapy [119, 120], and radiation [121, 122]) can enhance drug delivery across the BBB but are often associated with increased risk of edema, hemorrhage, inflammation, or neurotoxicity. As a result, there is a clear need for a method that can dissociate the endothelial tight junction while sparing the endothelial cells.

PDT is a photochemistry-based treatment modality that involves the light activation of non-toxic photosensitizers or fluorescent dyes. High optical energy (e.g., 80-300 J/cm^2) activation of photosensitizers is used to generate reactive oxygen species that can damage the vasculature and kills cells [175]. In fact, surgery immediately followed by PDT has already been studied in the clinic for brain tumors (NCT03048240, NCT03897491, NCT00003788) [143, 169]. A single adjunctive dose of PDT has been shown to add up to 18 months to the lifespan of patients with GBM [12]. Despite the promising preclinical and clinical results using PDT to permeabilize the BBB and treat brain tumors, the side effects of PDT, including edema and neurotoxicity, remain a major concern in the clinic [15, 170-172].To address this issue, we have introduced PDP which operates at low doses of optical energy and

photosensitizer (i.e., < 1 μM × J/cm^2) to modulate biomolecular targets without killing the organism [175]. We have shown that PDP improves vascular permeability and enhances ONIVYDE® (Liposomal irinotecan) extravasation into pancreatic tumor parenchyma by up to 11-fold without damaging surrounding healthy pancreas [175]. A combination of PDP and ONIVYDE® inhibited tumor growth, reduced metastasis, and doubled the median progression-free survival in pancreatic cancer mouse models [19, 175, 222]. While encouraging results have been obtained with PDP for pancreatic cancer treatment, there is work to be done to ensure that PDP can be used to disassociate the endothelium of the BBB that has a particularly high degree of junctional tightness.

It is increasingly clear that the presentation of junctional protein (i.e., pattern, geometrical organization, edge-presentation) and cell morphology plays an important role in regulating the permeability of cerebral endothelium [104-108]. Despite that information, the impact of sub-cytotoxic photochemistry on the presentation of junctional protein remains relatively understudied, presumably due, in part, to the lack of reliable quantitative analysis routines. Here, for the first time, we utilized a novel Junction Analyzer Program (JAnaP) [105, 223] to quantify junction phenotype in response to PDP at various light energy densities using human brain microvascular endothelial cells (HBMECs). Images of immuno-stained ZO-1 and VE-cadherin were analyzed using the JAnaP to calculate the percent of the cell perimeter presenting continuous, punctate, or perpendicular junctions before and after PDP. Furthermore, a transwell permeability assay was used to demonstrate that BBB permeability to fluorescein isothiocyanate–dextran (FITC-dextran) or rhodamine-loaded liposomes (rhodamine-liposome) can be precisely controlled via light activation. This chapter will

give insights into how PDP modulates cell-cell junctions and how it can be used to enhance drug delivery past the endothelial cell barrier.

4.2 Methods

4.2.1 Cell Culture

Primary HBMECs were purchased from Cell Systems (ACBRI 376) and cultured as previously described [108]. Briefly, cells were cultured in flasks coated with 0.1% gelatin and grown in RPMI-1640 medium supplemented with 20% FBS, 1% Pen/Strep, 2 mM L-glutamine (Thermo Fisher Scientific, Waltham, MA), 30 μg/mL endothelial cell growth supplement (Millipore Sigma, Burlington, MA), and 100 μg/mL heparin (Millipore Sigma) at 37 °C, with 5% CO_2. Cells were used for experiments within 7-10 passages. Cells arrived mycoplasma-free and were tested and found to be mycoplasma-free approximately 6 months later using the MycoAlert PLUS Mycoplasma Detection Kit (Lonza, LT07-701).

4.2.2 Substrate Coating and Experimental Conditions

On day 1 of experiments, glass bottom 24-well plates (662892, Greiner Bio-One, Kremsmünster, Austria) or transwell inserts (24 well format, 1.0 μm pore size, Falcon, Abilene, TX) were respectively coated with 175 μL or 35 μL of 100 μg/mL fibronectin (F2006, Sigma Aldrich, St. Louis, MO) for 30 minutes at 37 °C. After coating, the excess fibronectin was removed, and the surfaces were rinsed with 37 °C PBS. Cells were seeded at a density of 5×10^4 cells/cm^2 and then cultured for 5-9 days. On days 2-10, cells were treated with medium containing cAMP supplements: 250 μM of 8-CPT-cAMP (Abcam, ab120424) and 17.5 μM of RO-20-1724 (0415, Tocris

Bioscience, Bristol, United Kingdom). Once supplemented medium was introduced to the cells, all of the following medium changes contained the supplements.

4.2.3 Cell Viability and Metabolic Activity Assays, and Immunostaining

Briefly, on day 1 of experiments, HBMECs were plated at 5×10^4 cells/cm^2 within fibronectin-coated glass-bottom plates. The following day, the cAMP supplemented medium was introduced to the system and cells were grown for 48 hours to confluency. On day 4, cells were incubated with 0.25 μM benzoporphyrin derivative (VP, U.S. Pharmacopeia, Rockville, MD) in the supplemented medium for 24 hours. On day 5, prior to PDP, cells were washed twice with PBS and the fresh supplemented medium was added to each well. For PDP, cells were irradiated with 690 nm red light (0-5 J/cm^2, 6 mW/cm^2, bottom illumination). Light activation was performed using the ML6600 series laser system (690±5 nm; 1.5 W max output power; SMA fiber output with SMA905 connector, Modulight, Tampere, Finland). Cell metabolic activity and cell viability were determined via 3-(4,5-dimethylthiazol-2-yl)-2,5-diphenyltetrazolium bromide (MTT) assay and LIVE/DEAD® staining, respectively, at 24 hours or 72 hours after PDP. Surviving cells for PDP treated samples were normalized to a no treatment control. Cell confluency is defined as the number of cells stained with Calcein AM per frame, normalized to the no treatment control. Cell morphology was assessed 90 minutes after PDP (see *Junction analysis)*.

4.2.4 Immunostaining of Junction Proteins

At 90 minutes after PDP, HBMECs were rinsed with 37 °C PBS and fixed with 1% formaldehyde in PBS (Thermo Fisher Scientific) for 20 minutes. Prior to

permeabilizing the cell membrane for 5 minutes with 0.25% TritonX-100 (Sigma-Aldrich) in PBS, cells were washed three times for 5 minutes each, with room temperature PBS. After permeabilization, the PBS wash steps were repeated and the samples were blocked for 1 hour at room temperature with 2% goat serum (Abcam, Cambridge, United Kingdom) in PBS. Cells were incubated with primary antibodies against ZO-1 (rabbit polyclonal, Thermo Fisher Scientific, 61-7300, 1:500) and VE-cadherin (mouse monoclonal, Santa Cruz, sc-9989, 1:50) in 2% goat serum overnight at 4°C. The following day, cells were washed and blocked in 2% goat serum for 1 hour. Cells were incubated with secondary antibodies goat anti-rabbit Alexa Fluor 488 (Abcam, ab150077, 1:100) or goat anti-mouse Alexa Fluor 568 (Thermo Fisher Scientific, A-11004, 1:100), and Hoechst (Thermo Fisher Scientific, H3570, 1:2500 or 4 μg/mL), in PBS for 1 hour at room temperature. Cells were washed prior to imaging. Note that all steps were performed under gentle rocking.

4.2.5 Microscopy

For the LIVE/DEAD® assay, samples were imaged using the Lionheart (BioTek) at 20X. For cell-cell junction experiments (fixed-cell), samples were imaged using a 60X oil objective on an inverted microscope (IX83 Olympus microscope, Olympus cellSens Software). Images were captured using the red, green, and blue filters. Images shown within the manuscript were enhanced via ImageJ for better visualization of the cell-cell junction.

4.2.6 Junction Analysis

Cell morphology and cell-cell junction organization were quantified using the JAnaP, available for download at https://github.com/StrokaLab/JAnaP. Briefly, the cell perimeter was traced via "waypointing" for ZO-1 images (green fluorescent channel, A488) which were then projected onto the images of VE-cadherin (red fluorescent channel, A568), as previously described in [223]. To isolate ZO-1 and VE-cadherin, threshold values of 15 and 5 were applied, respectively. Further guidance on how to identify threshold values can be found in the supplement of [105] and in the JAnaP User-Guide available using the link above. Next, the cell morphological parameters, including area, solidity, and circularity, were calculated. Specifically, solidity equals the area of the cell divided by the area of the convex (**Figure 4.1a**). Circularity equals 4π times the cell area divided by the cell perimeter squared (**Figure 4.1b**). Junction morphology was quantified by calculating the percent of the cell edge presenting continuous or perpendicular junction [223]. The specific phenotypes were classified based on the length of the junction that overlapped the cell edge (> 15 pixels for continuous junction) and the relative aspect ratio with respect to the cell edge (> 1.2 pixels for perpendicular junction, otherwise punctate). These values served as constant parameters when using the JAnaP.

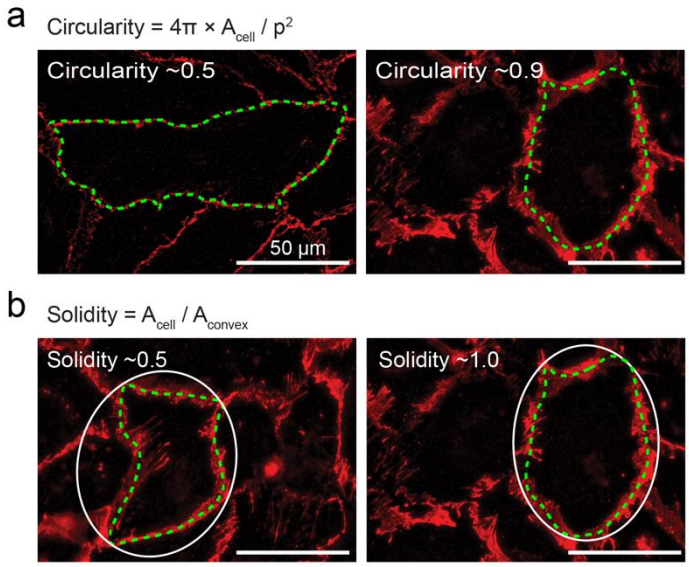

Figure 4.1 Cell shape factors. Equations and schematics represent how (**a**) circularity and (**b**) solidity are calculated. Cells are stained for VE- cadherin (red). Green dashes represent waypoints that trace the cell perimeter (p), showing the area of a cell (A_{cell}). White circles represent the area of the cell convex (A_{convex}).

4.2.7 Western Blot Analysis

VE-cadherin expression was analyzed using a standard Western blot analysis protocol (Bio-Rad). Briefly, HBMECs were seeded at a density of 5×10^4 cells/cm^2 within FBN-coated 35 mm petri dishes and grown to confluency. On day 2, cAMP supplemented medium was added to the cells. On day 4, cells were incubated with 0.25 µM VP in the supplemented medium for 24 hours. On day 5, prior to PDP, cells were washed twice with PBS and the fresh supplemented medium was added to wells. For PDP, cells were irradiated with 690 nm red light (0 J/cm^2 or 1.2 J/cm^2, 6 mW/cm^2). Prior to collection, cells were washed thrice with cold PBS. Lysates were collected 90- and 24-hours post PDP by scrapping the cells off the petri dish within cold PBS. After centrifugation, cells were lysed with cold radioimmunoprecipitation assay (RIPA) buffer containing 1x protease and phosphatase inhibitor cocktail (Thermo Fisher

Scientific). The total protein from cell lysates was quantified using a Bichoninic acid protein assay (Thermo Fisher Scientific). Cell lysates (20 μg) were separated on precast 4-12% Bis-Tris protein gels (NuPAGE) and electrotransferred onto PVDF membrane (Thermo Fisher Scientific). Membranes were blocked either with 5% milk/TBST or 5% bovine serum albumin/TBST solution, for VE-cadherin and GAPDH, respectively. Proteins were sequentially detected using an anti-VE-cadherin antibody (1:1000, Santa Cruz sc-9989) according to the manufacturer's guidelines. GAPDH (1:500, Cell Signaling #2118) was used as the loading control. Visualization of protein bands was achieved using chemiluminescence (SuperSignal, Thermo Fisher Scientific). The membranes were imaged with the FluorChem E System (ProteinSimple, San Jose, CA). Quantitative analysis of protein expression was done using ImageJ software.

4.2.8 Liposome Synthesis and Characterization

Liposomes, fluorescently labeled with rhodamine, were synthesized via freeze-thaw extrusion as described previously [19, 175]. Briefly, dipalmitoylphosphatidylcholine (DPPC), cholesterol, distearoylphosphatidylethanolamine-methoxy polyethylene glycol (DSPE-PEG) and 1,2-dioleoyl-sn-glycero-3-phospho-(1'-rac-glycerol) (DOPG) (Avanti Polar Lipids, Alabaster, AL, USA) were codissolved with 1,2-dipalmitoyl-sn-glycero-3-phosphoethanolamine-N-(lissamine rhodamine B sulfonyl) (Also known as 16:0 Liss Rhod PE) in chloroform. A thin film was created via rotary evaporator overnight. The film was rehydrated with 1 mL of deionized water. The lipid suspension was subjected to freeze-thaw cycles (4–45°C). The dispersions were extruded through polycarbonate

membranes (0.1 μm pore size) at 42°C to form unilaminar vesicles. The final concentration of the rhodamine was checked using a fluorescence standard curve measured using a BioTek Synergy Neo2 plate reader (Excitation/Emission: 560/596 nm). The Omni (Brookhaven, Holtsville, NY, USA) measured particle size of monodispersed rhodamine-liposomes to be ~100 nm in diameter (**Table 4.1**).

4.2.9 Transwell Permeability Assay

For permeability studies, HBMECs (5×10^4 cells/cm^2) were seeded on transwell inserts that had been pre-coated with fibronectin. On the next day, cAMP supplemented medium was added, and cells were allowed to grow to confluency. On day 2 or 4, VP (0.25 μM)-containing medium was added to the upper chamber for 24 hours of incubation. Following this, cells were washed twice with PBS, fresh medium was added, and light was delivered to initiate PDP (690 nm, 0.6 J/cm^2 or 1.2 J/cm^2, 6 mW/cm^2, bottom illumination). Immediately following PDP, 400 μL of FITC-Dextran (1 mg/mL, 70 kDa, Sigma-Aldrich) or rhodamine-loaded liposomes (5 μM) was added to the upper (apical) chamber and allowed to diffuse across the membrane into the lower (basolateral) chamber. At different time points, the medium in the lower chamber was collected and the fluorescence signal was measured using a BioTek Synergy Neo2 plate reader (Excitation/Emission: 492/518 nm for FITC, or 560/596 nm for rhodamine). When evaluating the permeability of FITC-Dextran, on each of the following time points, the upper chamber was replenished with 400 μL of fresh FITC-dextran solution (1 mg/mL) and the lower chamber was also replenished with fresh medium (800 μL), in order to continue daily permeability evaluation. When evaluating the permeability of rhodamine-loaded liposomes, 30 minutes prior to collection, the

upper chamber was replenished with 400 µL of fresh rhodamine-loaded liposomes (5 µM) and the lower chamber was replenished with fresh medium (800 µL). The apparent permeability coefficients (Papp, cm/min) of FITC-dextran solution (1 mg/mL) or rhodamine-loaded liposomes (5 µM) were from the following equation:

$$P_{app} = V_r \times (dC / dt) / (C_0 \times A)$$

V_r is the volume of the basolateral chamber (cm^3). dQ/dt is the slope of the cumulative concentration of the FITC-dextran (or rhodamine-liposome) in the basolateral chamber over time (µmol/L/min). C_0 is the initial concentration of FITC-dextran (or rhodamine-liposome) in the apical chamber (µmol/L). A is the membrane surface area of the inserts (cm^2).

4.2.10 Statistical Analysis

Data analysis was performed using PRISM GraphPad 8 [224]. Both the Anderson-Darling test and D'Agostino & Pearson test were used to determine the normality of the data sets. When examining cell and junction morphology, the Kruskal-Wallis test followed by Dunn's multiple comparison test were used to evaluate statistically significant difference. An alpha value of 0.01 was used as the cut-off value to determine significance, where ** $p < 0.01$, *** $p < 0.001$, and **** $p < 0.0001$. Three separate trials were conducted for all experiments. No batch effects were found. For transwell permeability experiments, a two-way ANOVA with multiple comparisons (mixed effects analysis) was used to assess statistically significant difference among groups. An alpha value of 0.05 was used as the cut-off value to determine significance, where * $p < 0.05$, ** $p < 0.01$, *** $p < 0.001$, and **** $p < 0.0001$. These analysis strategies were adopted from previously published works [108].

4.3 Results & Discussion

4.3.1 Sub-cytotoxic PDP in HBMECs

For safe and effective drug delivery to the brain, it is of paramount importance to disrupt the BBB locally and transiently without causing endothelial cell death or vascular shutdown. Typically, PDT involves the high optical energy (e.g. 80–300 J/cm^2) activation of PS in order to produce sufficient $^1O_2$ that can collapse the vasculature and induce cell apoptosis or necrosis [134, 140-143, 225]. Recently, we have shown that PDP, with slightly lower optical energy (75 J/cm^2) and VP PS, can improve vasculature permeability to nanomedicine in pancreatic tumors without causing normal tissue damage [19, 175, 222]. Other groups have shown the ability to permeabilize the BBB within mice using lower optical energies (10-40 J/cm^2) and the prodrug ALA, however, vascular damage and edema often occur [15-17]. In this study, we used LIVE/DEAD® assay and MTT (metabolic-based) assay to determine the threshold of PDP in HBMECs in vitro. To recapitulate the in vivo basement membrane and enhance the brain endothelial phenotype, HBMECs were plated on fibronectin and treated with 8-(4-chlorophenylthio) adenosine-3',5'-cyclic monophosphate sodium salt (CPT-cAMP) and RO-20-1724. The basal lamina fibronectin protein was selected over 7 other extracellular matrix components based on our prior work that showed fibronectin-coating results in the greatest HBMEC cell-cell junction expression [108, 226]. cAMP and RO-20-1724 were introduced to enhance the junction phenotype, inhibit Rho/ROCK signaling in endothelial cells, and limit the formation of stress fibers by blocking myosin light chain phosphorylation [105, 108, 227].

Here, free-form VP was incubated with HBMECs at a concentration of 0.25 μM for 24 hours prior to 690 nm light activation (0–5 J/cm^2, 6 mW/cm^2). At 24 hours post-PDP, the viability of HBMECs was assessed by LIVE/DEAD® assay. In a separate study, 72 hours post-PDP, mitochondrial activity was determined via MTT assay. **Figure 4.2** shows that PDP at light doses of ≤ 2.5 J/cm^2 had minimal effects on the viability and metabolic activity of HBMECs. At 5 J/cm^2, PDP significantly decreased the mitochondrial activity by 35.7±6.4% (**Figure 4.2a**), induced 17.7±6% cell death (**Figure 4.2b**), and reduced the confluency of HBMECs by 63.6% (**Figure 4.2c, Figure 4.3**). It is well established that VP localizes to the mitochondria and induces depolarization of mitochondrial membrane potential efficiently upon light illumination in cells [138, 139]. Therefore, it is not surprising that PDP-treated HBMECs experience a larger loss in mitochondrial activity (by MTT assay) than cell membrane integrity (by LIVE/DEAD®). Based on these results, optical energies of 0.06, 0.3, 0.6, and 1.2 J/cm^2 (at a fixed irradiance of 6 mW/cm^2) were selected for the following experiments, while VP concentration is fixed at 0.25 μM.

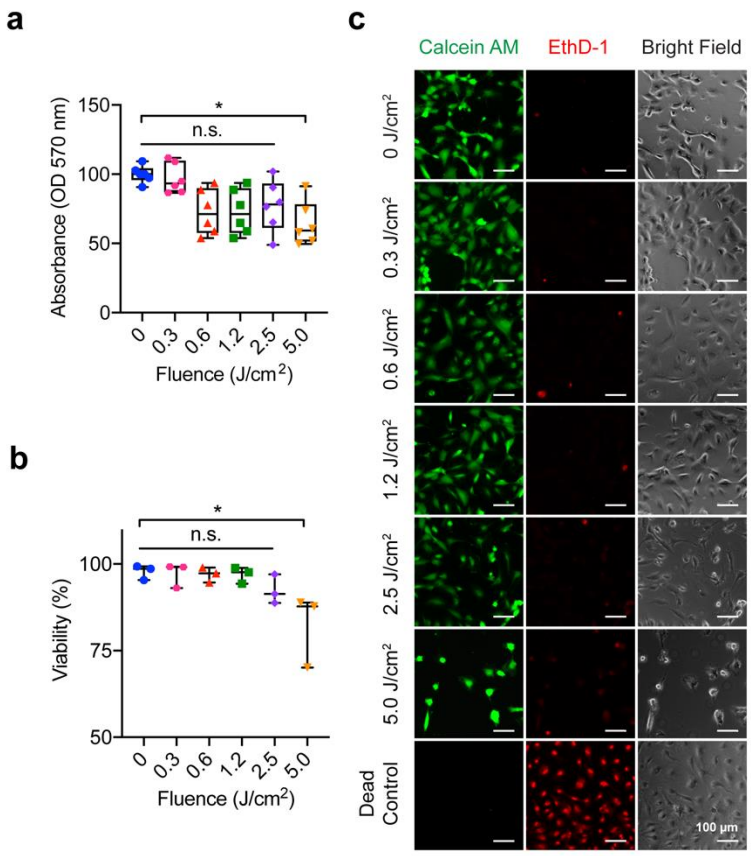

Figure 4.2 PDP is Sub-cytotoxic to HBMECs. HBMECs were incubation with VP (0.25 µM) for 24 hours followed by light activation (690 nm, 0–5 J/cm^2, 6 mW/cm^2). The metabolic activity and viability of HBMECs were examined via (a) MTT assay (b) Live/Dead® imaging at 72 hours and 24 hours post-PDP, respectively. (c) Representative images from the Live/Dead® assay (green channel: Calcein AM, red channel: ethidium homodimer-1, EthD-1) show a confluent monolayer up to a PDP dose of 1.2 J/cm^2 (scale bars = 100 µm). Cell viability and metabolic activity were only significantly reduced by the 5.0 J/cm^2 PDP dose. For Live/Dead® analysis, a One-Way ANOVA with multiple comparisons was used to calculate significant differences, where n.s. indicates not significant ($p > 0.05$), * $p < 0.05$. N=3, where N equals the number of trials performed. For MTT analysis, the Kruskal-Wallis test with a Dunn's multiple comparison test was used to calculate significant differences, where n.s. indicates not significant ($p > 0.05$), * $p < 0.05$. N=6, where N equals the number of wells assessed over 3 trials. Box plots show the mean and the likely range of variation. Error bars show the maximum and minimum values.

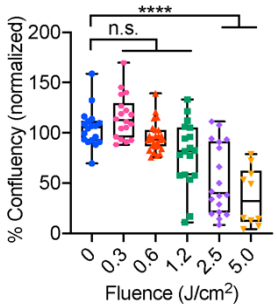

Figure 4.3 Low dose PDP does not Impact Cell Confluency. HBMECs were incubated with VP (0.25 μM) for 24 hours followed by light activation (690 nm, 0–5 J/cm^2, 6 mW/cm^2). The confluence of HBMECs was determined from Live/Dead® imaging at 24- post-PDP. The number of cells stained with Calcein AM (green channel) per frame was normalized to the control group. A One-Way ANOVA with multiple comparisons was used to calculate significant differences, where n.s. indicates not significant ($p > 0.05$), * $p < 0.05$, ** $p < 0.01$, *** $p < 0.001$, and **** $p < 0.0001$. $N > 10$, where N equals the number of images captured over 3 trials. Box plots show the mean and the likely range of variation. Error bars show the maximum and minimum values.

4.3.2 PDP Slightly Alters Cell Morphology and F-actin Organization

To better understand how PDP impacts the brain endothelium, we first examined the impact of PDP on HBMEC morphology (i.e., area, solidity, and circularity) and F-actin organization using the well-established JAnaP. We observed that PDP (0.06–1.2 J/cm^2) moderately increases the circularity and solidity of HBMECs by 3–13%, suggesting cells were under stress (**Figure 4.4a,b**). However, this increase is modest compared to dying cells (cells treated with 5 J/cm^2) that had on average a 23.5% increase in circularity (data not shown). PDP did not impact the HBMECs area (**Figure 4.4c**) nor perimeter (**Figure 4.5**). At the higher light doses of 0.6 and 1.2 J/cm^2, PDP-induced F-actin reorganization from cortical bands near the cell edge to stress fibers throughout the HBMECs (**Figure 4.4d**). It appeared VE-cadherin also showed a change in morphology, which motivated us to investigate further. Our new findings agree with previous observations by Ota et al. and others, which showed that the reactive oxygen species produced by PDT can induce morphological changes

and actin stress fiber formation in human umbilical vein endothelial cells [104, 228, 229]. Further, these reports showed that actin stress fiber reorganization from cortical bands to stress fibers in human umbilical vein endothelial cells was also accompanied by the mislocalization of VE-cadherin [104]. In addition, stress fiber formation and induced permeability could be mitigated with the use of inhibitors. Forskolin/rolipram or 8CPT-2′O-Me-cAMP inhibit further reaction of phosphorylated RhoA, which reduced stress fiber formation and maintained the baseline permeability.

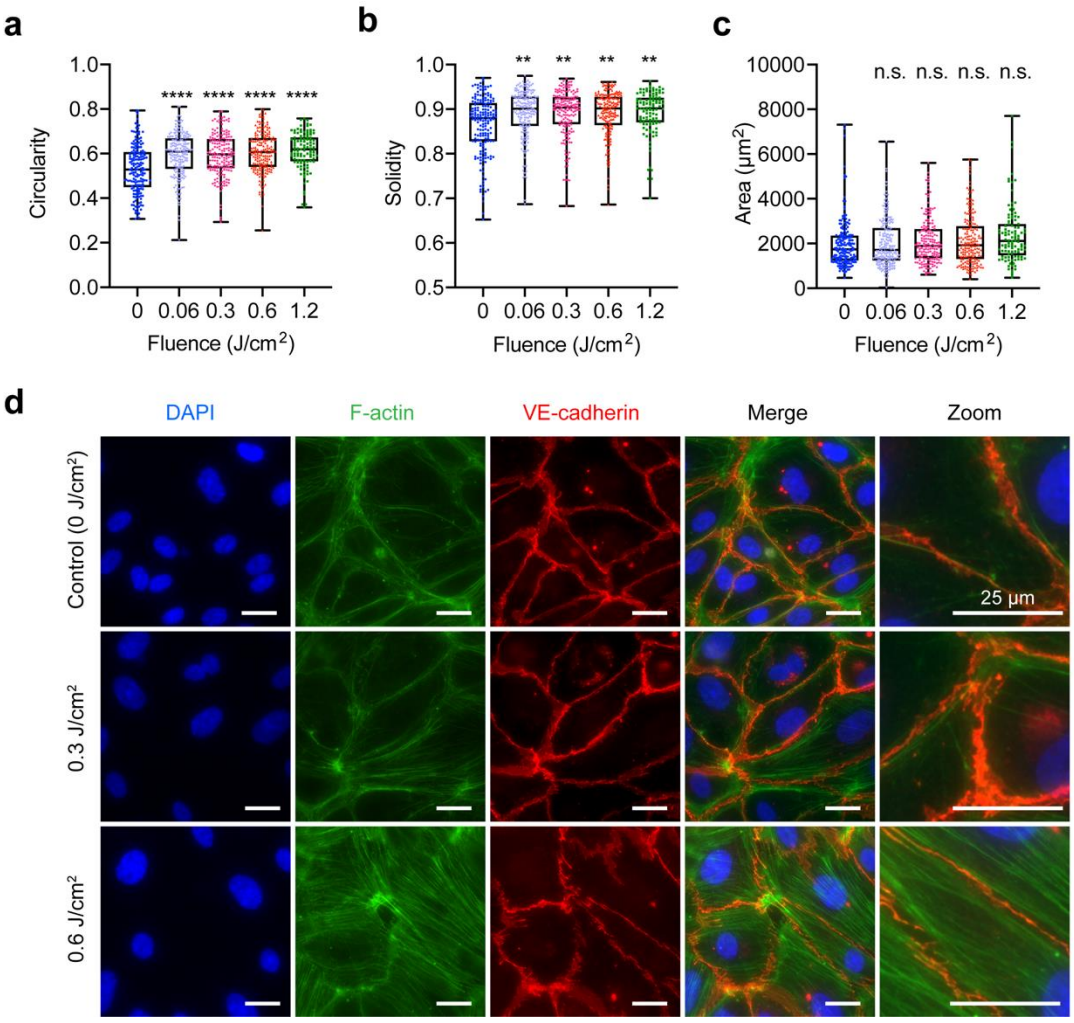

Figure 4.4 PDP Alters Cell Morphology and the Organization of F-actin. HBMECs were grown to confluency and primed with 690nm red light (0–1.2 J/cm^2, 6 mW/cm^2). At 90 minutes post priming, cells were fixed and stained for F-actin and VE-cadherin. (a-c) Cell shape factors. All PDP light doses modestly increase HBMEC (**a**) circularity and (**b**) solidity. (**c**) PDP had no impact on HBMEC area. (**d**) Representative fluorescence images of F-actin (green) organization. VE-cadherin (red) staining is used to show the cell edge. PDP light doses ≥ 0.6 J/cm^2 resulted in the rearrangement of F-actin from cortical bands near the cell boundary to stress fibers throughout the cell. All scale bars are 25 μm. The Kruskal-Wallis test with a Dunn's multiple comparison test was used to calculate significant differences, where n.s. indicates not significant ($p > 0.05$), ** $p < 0.01$, *** $p < 0.001$, and **** $p < 0.0001$. The significance between the experiment group and the control is presented. $N > 105$, where N is the number of cells, from 3 different trials. Box plots show the mean and the likely range of variation. Error bars show the maximum and minimum values.

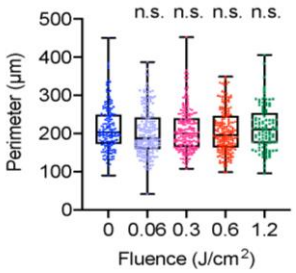

Figure 4.5 PDP does not Alter Cell Perimeter. 90-minutes post priming (0-1.2 J/cm^2, 6 mW/cm^2), cells were fixed and stained for VE-cadherin and ZO-1. The cell perimeter was traced via 'way pointing' within the JAnaP. The Kruskal-Wallis test with a Dunn's multiple comparison test was used to calculate significant differences, where n.s. indicates not significant ($p > 0.05$). The significance between the experiment group and the control is presented. $N > 105$, where N is the number of cells, from 3 different trials. Box plots show the mean and the likely range of variation. Error bars show the maximum and minimum values.

4.3.3 PDP Alters the Endothelial Cell-cell Junction Morphology

Among the 40 different transmembrane and scaffold proteins that form an endothelial cell-cell junction in the brain, VE-cadherin and ZO-1 are two of the important and foundational proteins that regulate BBB permeability. VE-cadherin is the primary transmembrane structural adhesive protein present in adherens junctions of HBMECs, prior to the formation of tight junctions, thus deeming it the junctional backbone [230-232]. ZO-1 is a scaffolding protein that regulates the recruitment and assembly of tight junction proteins (e.g., occludins and claudins) at the cytoplasmic surface of intercellular junctions [233]. It is also well established that rearrangement of VE-cadherin and ZO-1 regulates vascular permeability [234-238]. As cell-cell junctions mature, VE-cadherin and ZO-1 reorganize from a serrated perpendicular geometry to a continuous strand linear to the cell edge [107-109].

We next investigated whether PDP could reverse the maturity of endothelial cell-cell junction through the rearrangement of VE-cadherin and ZO-1. Similar to the previous experiments, HBMECs were seeded in FBN-coated wells and treated with

cAMP to start with mature cell-cell junctions [108]. Specifically, we examined the percentage of junction coverage per cell, as well as the pattern of junctions present at the cell edge (i.e., continuous mature junctions, perpendicular immature junctions, or punctate immature junctions) (**Figure 4.6a**). Representative fluorescence images (**Figure 4.6b**) show that PDP can reduce junctional coverage at the edge of the cell and significantly alter junction morphology. The changes in the HBMEC junction phenotype in response to PDP at various light energy densities (fluences) were further quantified using JAnaP as described by us previously (**Figure 4.7**). JAnaP analysis revealed that PDP modestly reduced the coverage of VE-cadherin (72.4±0.8%) and ZO-1 (64.6±0.7%) at the cell edge by 10-20% in a light dose-dependent manner (**Figure 4.7a,b**). This decrease in junctional coverage induced by PDP was accompanied by changes in junction morphology. We found that PDP not only decreases the mature VE-cadherin continuous junctions by ~17% (from 56.58±1.13% to 46.71±1.33%) (**Figure 4.7c**) but also increases the immature VE-cadherin perpendicular junctions by ~46% (from 7.91±0.26% to 11.61±0.38%) in a light dose-dependent manner (**Figure 4.7e**). Similar trends were observed with ZO-1, where PDP decreases the mature ZO-1 continuous junctions by ~27% (**Figure 4.7d**) and increases the immature ZO-1 perpendicular junctions by ~38% at 1.2 J/cm^2 (**Figure 4.7**). Further analysis revealed that PDP (0.3-1.2 J/cm^2) increases the protrusion length (e.g. tip-to-tip distance [223]) of ZO-1 perpendicular junction, but not VE-cadherin perpendicular junction (**Figure 4.8**). The changes in perpendicular junction protrusion could be a result of F-actin stress fibers pulling on the connected tight junction proteins (ZO-1), but not adherens junction proteins (VE-cadherin). It has been reported by others that

PDT could cause the internalization of VE-cadherin and intercellular gaps, resulting in the disappearance and discontinuous junctions at the cell edge [104]. Interestingly, PDP did not significantly alter the amount of punctate, or dotted, junctions for VE-cadherin and ZO-1 ($p > 0.05$) (**Figure 4.7g,h**). The number of punctate junctions was most likely unchanged after PDP, as cells were able to remain in constant contact with each other.

Previous reports have shown that endothelial monolayer confluency impacts VE-cadherin expression and pattern [239-241]. Zhang et al. also showed that PDT downregulates the expression of VE-cadherin at the BBB in mice [17]. If PDP induced large gaps in the cell monolayer, as a result of cell death, it is speculated that downregulation of VE-cadherin would occur via clathrin-coated endosomal internalization [242]. Here, western blot analysis shows that PDP did not significantly alter the expression of VE-cadherin in HBMECs (**Figure 4.9**). The above results demonstrate that PDP not only induces cellular stresses as evident by increased stress fiber formation, roundness, and solidity, but also promotes morphological changes to junction proteins. Most importantly, PDP can shift a stable endothelial monolayer into an immature state while maintaining HBMEC viability.

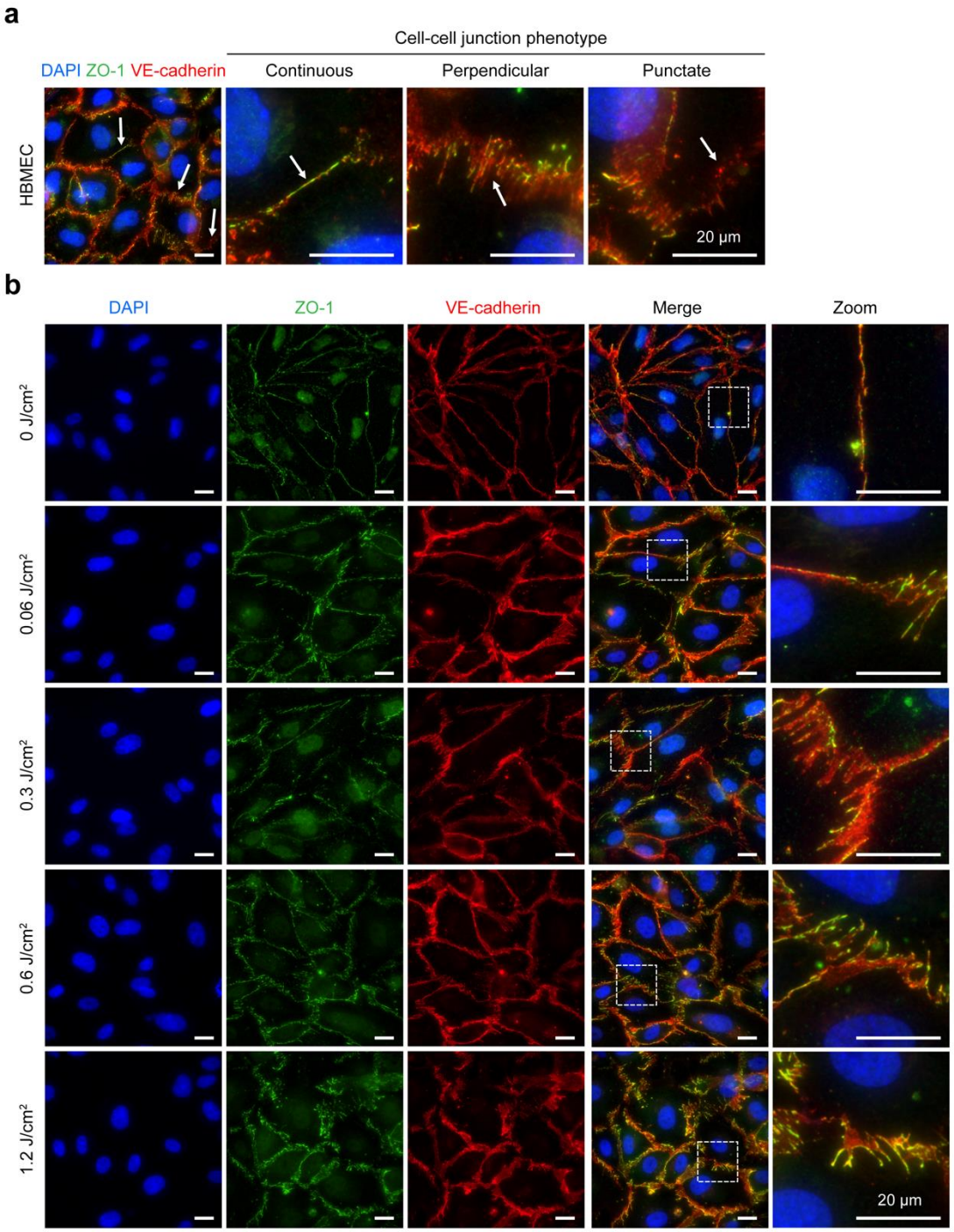

Figure 4.6 PDP Modulates Endothelial Cell-cell Junction Phenotype. At 90 minutes post-priming, cells were fixed, stained, and imaged. (a) Representative fluorescence image of PDP modulated HBMEC with stained nuclei (blue), ZO-1 (green), and VE-cadherin (red). White arrows show regions of different cell-cell junction phenotypes: continuous linear junctions, perpendicular junctions, and dotted punctate junctions. (b) Representative fluorescence images of non-treated cells (0 J/cm^2) and photodynamic primed cells (0.06–1.2 J/cm^2). PDP generates immature HBMEC monolayers by decreasing linear continuous junctions and increasing perpendicular junctions, in a light dose-dependent manner. All scale bars are 20 μm.

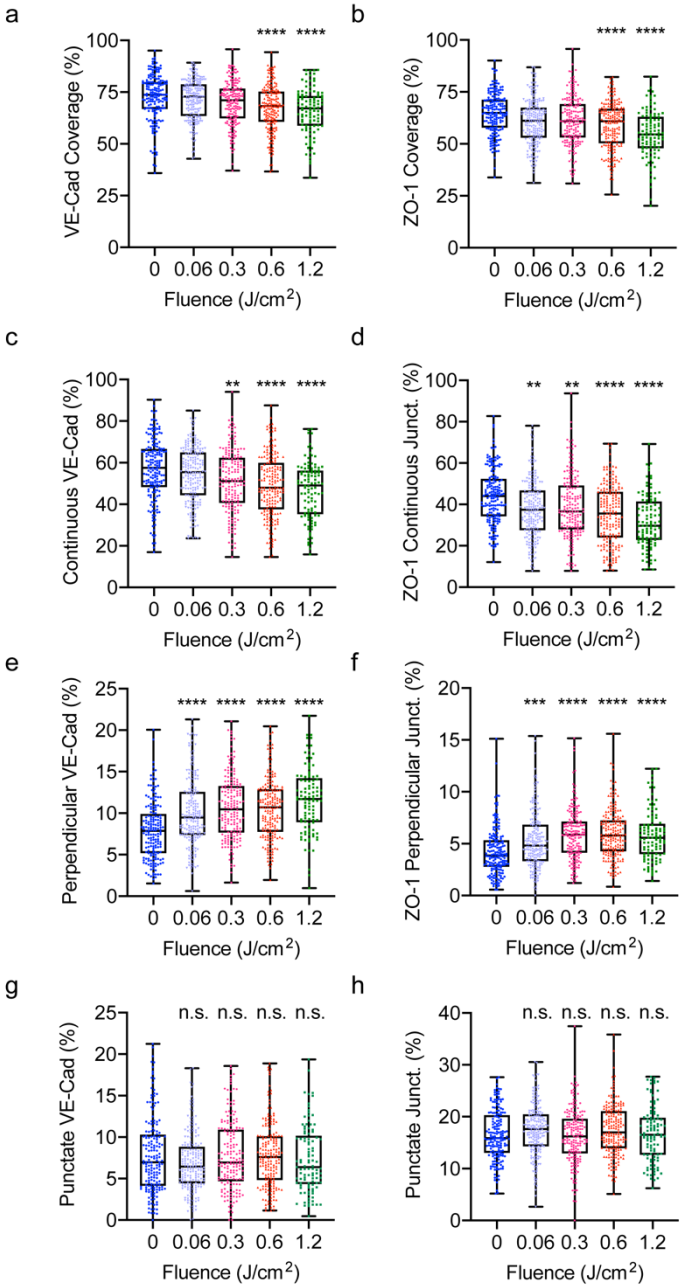

Figure 4.7 Quantitative Analysis of Junction Phenotype. At 90 minutes post-priming (0–1.2 J/cm^2, 6 mW/cm^2), cells were fixed, stained, and analyzed with the JAnaP. (a, b) The percent of the cell edge that is covered by a junction, for VE-cadherin and ZO-1, respectively. Edge presentation of continuous (c, d), perpendicular (e, f), and punctate (g, h) junctions for VE-cadherin and ZO-1, respectively. PDP resulted in a light dose-dependent decrease in mature junctions and an increase in unstable junctions. The Kruskal-Wallis test with a Dunn's multiple comparison test was used to calculate significant differences, where n.s. indicates not significant ($p > 0.05$), ** $p < 0.01$, *** $p < 0.001$, and **** $p < 0.0001$. The significance between the experiment group and the control is presented. $N > 105$, where N is the number of cells assessed over 3 trials. Box plots show the mean and the likely range of variation. Error bars show the maximum and minimum values.

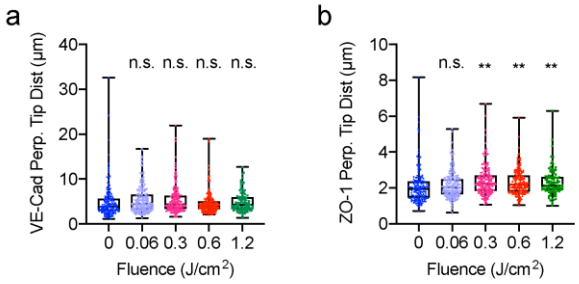

Figure 4.9 PDP Impact on Protrusion Length. PDP did not alter the (**a**) protrusion length (i.e., tip-to-tip distance) of VE-cadherin perpendicular junctions, (**b**) but modulated the protrusion length of ZO-1 perpendicular junctions. At 90 minutes post-priming (0-1.2 J/cm^2, 6 mW/cm^2), cells were fixed and stained. The JAnaP calculated the protrusion length of the perpendicular junctions after cells were way pointed. The Kruskal-Wallis test with a Dunn's multiple comparison test was used to calculate significant differences, where n.s. indicates not significant ($p > 0.05$). The significance between the experiment group and the control is presented. $N > 105$, where N is the number of cells, from 3 different trials. Box plots show the mean and the likely range of variation. Error bars show the maximum and minimum values.

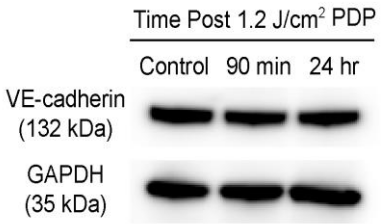

Figure 4.8 PDP does not Alter Total Junction Protein Expression. HBMECs were grown to confluency, incubated with VP (0.25 μM) for 24 hours, and primed (690 nm, 1.2 J/cm^2, 6 mW/cm^2). Representative immunoblotting of VE-cadherin confirms protein expression was unchanged at 90 minutes and 24 hours post-priming. GAPDH was used as the loading control. N=4, where N is the number of gels ran over 2 lysates.

4.3.4 PDP Induces HBMEC Permeability to FITC-dextran

We have previously demonstrated that the number of discontinuous VE-cadherin and ZO-1 junctions correlates positively with HBMEC permeability [108]. Similarly, Li et al. showed that a change in the pattern of ZO-1 (from "linear" junction to a "discontinuous, segmented and dotted" phenotype) is associated with increased

permeability in HBMECs [227]. Knowing that PDP can modulate the morphology of cell-cell junctions (**Figures 4.6** and **4.7**), we next examined the ability of PDP to improve HBMEC permeability to FITC-dextran or rhodamine-liposomes using a transwell model. At different time points after PDP, the amount of FITC-dextran (or rhodamine-liposome) that diffuses from the apical chamber into the basolateral chamber was quantified using a plate reader and the apparent permeability coefficient (P_{app}, cm/min) was calculated.

Without PDP (0 J/cm^2), a baseline diffusion of FITC-dextran into the basolateral chamber was observed (**Figure 4.10a**). The average P_{app} of FITC-dextran is ~7.5×10^{-5} cm/min, similar to that observed by others (**Figure 4.10b**) [243, 244]. By day 7, the P_{app} of FITC-dextran in the untreated HBMECs control group began to increase. This observation is consistent with other's reports showing that prolonged activation of cAMP may cause a delay in the repression of Ras-related protein (R-Ras), resulting in the disruption of VE-cadherin and endothelial cell barriers [245]. PDP at 0.6 J/cm^2 and 1.2 J/cm^2 significantly improved the diffusion of FITC-dextran across the HBMEC monolayer by ~2.6-fold and 4-fold, respectively, in a dose-dependent manner (**Figure 4.10a**). The P_{app} of FITC-dextran was found to be the highest at 2-3 days post-PDP. On day 2, transwells primed with 1.2 J/cm^2 had approximately 40.86% of their starting FITC-dextran diffuse into the basolateral chamber. By days 6 and 9, the P_{app} of FITC-dextran in the PDP groups (0.6 and 1.2 J/cm^2) were found to be similar to that of the control group (0 J/cm^2). The transwell models that received the higher optical energy (1.2 J/cm^2) took an additional 3 days to recover presumably due to increased cell contractility and number of immature junctions. Although this was an in

vitro model, our findings are consistent with previous findings showing that PDP-assisted endothelial opening persists at least up to 3 days in vivo [175]. These results also suggest that PDP dose can be customized to control the degree and duration of endothelium permeabilization.

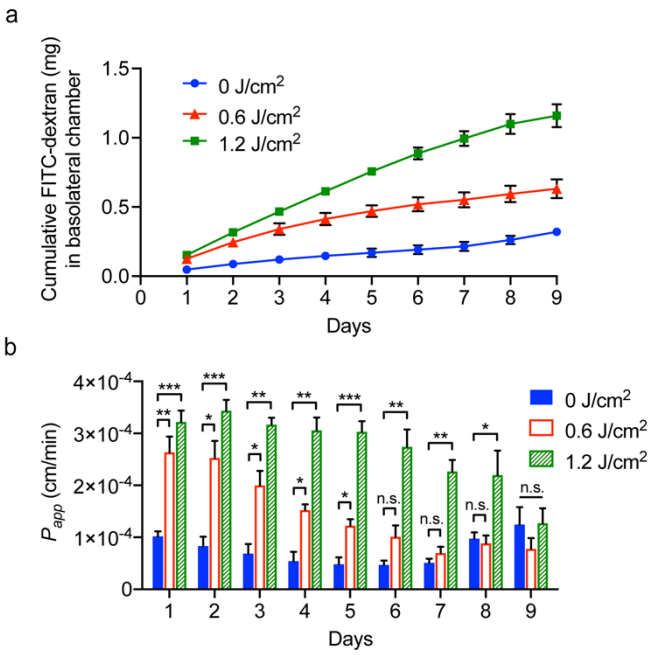

Figure 4.10 PDP Improves HBMEC Monolayer Permeability to FITC-dextran. (**a**) Cumulative FITC-dextran that traversed the HBMEC transwell model. Over 9 consecutive days, PDP (0.6-1.2 J/cm^2, 6 mW/cm^2) resulted in 2.6–4-fold more FITC-dextran crossing into the bottom transwell chamber. (**b**) Apparent permeability coefficient, P_{app}. PDP temporarily and reversibly induced a relatively high degree of permeability in HBMECs. By day 6 and 9, the integrity of the monolayers recovered. A two-way ANOVA with multiple comparisons was used to determine significance, where *P < 0.05, **P < 0.01, ***P < 0.001, n.s.: nonsignificant.

We have previously shown that PDP can improve the permeability of 'leaky' tumor vasculature to liposomes by 11-fold in vivo [175]. We next tested if PDP also improved rhodamine-liposomes, ~100 nm in diameter (**Table 4.1**), penetration across the HBMEC monolayer cultures that have a particularly high degree of junctional tightness. The permeability of rhodamine-liposomes was monitored up – to ~48 hours

(**Figure 4.11**), as the clinically relevant liposomes typically have a circulation half-life of 24–48 hours [246, 247]. Without PDP (0 J/cm^2), the average P_{app} of rhodamine-liposomes is ~1.1×10^{-7} cm/min. PDP at 0.6 J/cm^2 significantly improved the P_{app} of rhodamine-liposomes by 14.6-, 9.8-, and 5.0-fold at 1, 25 and 49 hours, respectively, compared to the control (0 J/cm^2). This improvement in the P_{app} of rhodamine-liposomes was even more pronounced when using PDP and 1.2 J/cm^2 (38.5-, 18.1-, and 11.5-fold at 1, 25 and 49 hours, respectively). We observed that only less than 0.09% of the rhodamine-liposomes diffused into the basolateral chamber. This tightness properties displayed in our model was found similar to others in vitro model [248]. At 1.2 J/cm^2, PDP facilitated the leakage of up to 3.43% of the liposomes into the basolateral chamber over a 30-minute incubation period. This significant (30-fold) improvement in drug penetration across the endothelial barrier suggests that PDP is a promising modality for enhancing drug devilry across the BBB in vivo, where less than 0.14%ID/g of the injected liposomes can cross the rat BBB [249-253]. While ALA-mediated PDT and focused ultrasound [104, 254, 255] can also improve the drug delivery across the endothelial monolayer by 2-5.3 fold, these modalities are often cytotoxic and can potentially lead to undesired normal tissue destruction. In addition, liposomes can be designed to penetrate the BBB. For example, Dai et al. showed only 0.58% of liposomes decorated with CDX peptide could cross a monolayer of rat primary brain capillary endothelial cells over a 3-hour period [248].

This is the first study to demonstrate that PDP can significantly improve endothelial permeability to both macromolecules and nanoparticles in a transwell model. The uniqueness of PDP lies in its spatiotemporal selectivity, which offers the

opportunity to confine endothelial permeabilization to the site where the light is directed. This spatiotemporal control of PDP may further reduce normal brain tissue damages and warrants further investigation in animals. While it is true that light penetration depth (i.e., the depth at which the incident optical energy drops to 37%, 1/e) is typically 1-4 mm in the brain, we have recently shown that diffused red light (i.e., the remaining 37% optical energy) can reach up to 1.5-2 cm deep in rat brains to activate VP for PDP [22]. This suggests that intraoperative PDP is sufficient to manage brain diseases that are 1-2 cm in depth (e.g., the unresectable, invasive margin of most brain cancers). For deeper brain tissues, light can be delivered to the entire target using stereotactically placed fibers in the clinic (similar to laser probes currently used for interstitial thermotherapy) [80, 256-259]. In this study, the clinically relevant, longer wavelength PS, VP, (690 nm, deeper light penetration) was selected for PDP. This is an alternative to ALA (Gliolan®)-induced protoporphyrin IX (PpIX, 635 nm), which is currently approved for fluorescence-guided surgery of brain tumors [149, 260] and is generally reserved for treating topical lesions [140, 261]. In fact, we have shown that 690 nm light activation of VP induces PDP effects at further depths in rat brain (1.5-2 cm), compared to 635 nm light activation of PpIX (≤ 1 cm) [22]. Therefore, an immediate future direction would be to compare the efficacy of PDP for BBB opening using both FDA-approved VP and Gliolan® in vivo.

Table 4.1 Physical Parameters of Rhodamine-liposomes.

Parameters	L-Rhod
Hydrodynamic diameter (nm)	104.08 ± 3.39
Polydispersity index (PdI)	0.06 ± 0.02

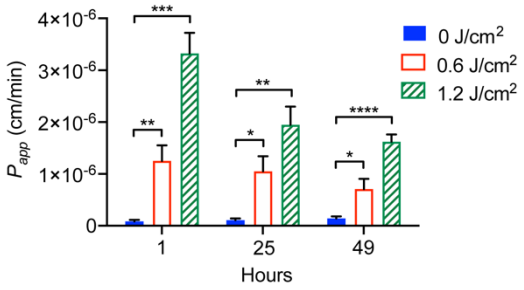

Figure 4.11 PDP Improves HBMEC Monolayer Permeability to Rhodamine-liposomes. Priming (0.6-1.2 J/cm^2, 6 mW/cm^2) the transwells resulted in the apparent permeability coefficient, P_{app}, of the HBMECs to increase by as much as 38.5-fold, allowing rhodamine-nanoliposomes to diffuse into the basolateral chamber. A two-way ANOVA with multiple comparisons was used to determine significance, where n.s. indicates not significant ($p > 0.05$), * $p < 0.05$, ** $p < 0.01$, *** $p < 0.001$, and **** $p < 0.0001$. The significance between the experiment group and the control is presented. $N \geq 5$, where N is the number of inserts measured over 3 trials. Error bars show SEM.

4.4 Conclusion

In summary, the complexities of the brain necessitate the innovation of a drug delivery strategy capable of overcoming the neurovascular unit while leaving normal brain cells undamaged. An emerging paradigm in brain drug delivery suggests that stimuli-responsive strategies can more accurately control BBB permeability at the right time, right place, and for the appropriate duration. Both PDT and focused ultrasound hold great clinical promise for overcoming the BBB. However, their cytotoxic nature and associated adverse events limit the clinical application and efficacy of drug delivery. To address these challenges, we applied a sub-lethal, photodynamic modality to reverse the mature brain endothelial cell–cell junction. The photodynamic priming approach is inspired by recent advances in tumor vascular permeabilization, which improves drug delivery to pancreatic tumors. Here, for the first time, we showed that PDP could significantly alter the

endothelial cell–cell junction phenotype (i.e., continuous, punctate, or perpendicular), and improve nanoparticle penetration across the tight endothelium by up to 30-fold. In **Chapter 7**, we will apply PDP to open the BBB within healthy rats. Future work will involve further characterization of multi-cycle PDP in cells and in animal models and will address the benefit of using a longer wavelength photosensitizer. In a small pilot study, we examined the colocalization of CD34 and claudin 5 after PDT treatment in healthy rat brain (PDT parameters discussed in Chapter 7). Compared to the unaffected left-brain hemisphere which had a colocalization of 96.2%, PDT decreased colocalization to 78.4%. The impact of PDP on other components of the neurovascular unit (e.g., pericytes, neurons), as well as the PS-light interval, will also be the subject of future studies. Building on our successes using PDP for pancreatic cancer treatment, this study opens up new avenues for developing brain targeting drug delivery systems.

Chapter 5. The Development of Verteporfin Biomolecules for Anti-glioma Photodynamic Therapy[3]

5.1 Introduction

As mentioned in *Sections 2.3.2* and *3.1*, free-form VP cannot be used clinically for treatment. VP is hydrophobic and in aqueous solutions it will form large uncontrollable agglomerations that will negatively impact pharmacokinetics and $^1O_2$ production. VP requires a carrier system for clinical delivery.

Light-activatable biohybrid conjugates offer great promise for anti-cancer PDT due to their ability to improve pharmacokinetics, minimize clearance of photosensitizing agents, and enhance tumor-specific cytotoxic effects [262]. PDT is a light-based treatment modality that is mechanistically distinct from conventional chemotherapy, radiation, and thermal ablation [126, 263]. Cytotoxicity related to PDT is governed by the localization of the photosensitizer, spatial confinement of near-infrared light activation, and the production of ROS (e.g., $^1O_2$, H_2O_2, $O_2^{\bullet-}$, •OH) that confer toxicity to cellular and subcellular targets [126, 263]. The direct damage to subcellular organelles (*e.g.*, mitochondria, endoplasmic reticulum, lysosome) allows a more channeled activation of programmed cell death pathways (*e.g.*, apoptosis, necroptosis, autophagy), and therefore bypasses many other cell-death signaling pathways required for chemotherapy and radiation to be effective [126, 263]. As a

3 This chapter was adapted from Inglut C.T.[#], Baglo Y.[#], Liang B.J., et al., "Systematic Evaluation of Light-Activatable Biohybrids for Anti-Glioma Photodynamic Therapy". J Clin Med. 2019 Sep; 8(9): 1269. No special permission is required to reuse this article published by MDPI under the terms and conditions of the Creative Commons Attribution (CC BY) license (http://creativecommons.org/licenses/by/4.0/). Y.B. was a co-first author ([#] denotes equal contribution) on this article. She helped perform and analyze the experiments for Figures 5.4, 5.5a-c, 5.6, 5.8a, 5.9a, and 5.10c. B.J.L. aided in synthesis and characterization (Figure 5.1-5.3).

result, PDT has been shown to reverse chemoresistance, synergize with chemotherapeutics and biological agents, and overcome compensatory survival pathways used by numerous cancers to evade standard treatments [19, 175, 197, 264-266].

In the past few decades, considerable attention has been given to improving the biocompatibility of organic photosensitizing agents, including porphyrins, chlorins, and synthetic dyes [127, 128]. It is increasingly evident that photosensitizing biomolecules (PSBMs), based on chemical conjugation or association of photosensitizers with biomolecules, strongly influence the performance of a given photosensitizer in biological environments [262]. To harness the full potential of PSBMs for cancer treatment, it is of paramount importance to achieve a general and comprehensive understanding of how different types of biomolecules alter the uptake, subcellular localization, and the cytotoxicity of photosensitizers. However, the numerous studies examining different PSBMs are not readily comparable as they typically cover a vast array of photosensitizers and treatment conditions [262]. This study systematically examines the impact of a panel of biomolecules on the behavior of VP, a FDA-approved photosensitizer now being routinely tested for cancer treatment and imaging [145, 191].

Amongst the PSBMs that are currently available in the clinic, phospholipid-, polymer-, and antibody-based formulations are popular ways to improve the water solubility, pharmacokinetics, and biodistribution of photosensitizers; however, little is known about how these re-formulation strategies alter cellular uptake, subcellular localization, and the end effects in PDT regimes against GBM. In 2000, phospholipid-

associated VP (i.e., Visudyne®) was approved by the FDA for PDT of wet age-related macular degeneration [145, 191]. Accordingly, Visudyne® is now being tested in several clinical trials evaluating PDT for pancreatic ductal adenocarcinoma (NCT03033225) [168], recurrent and metastatic prostate cancer (NCT03067051, NCT02939274), breast neoplasms (NCT02872064), and pleural malignancies (NCT02702700). In an early clinical study, Bown *et al.* tested the use of intravenous polyethylene glycol (PEG)-solubilized meso-tetrahydroxyphenyl chlorin for enhanced PDT against locally advanced, unresectable pancreatic cancer [267]. In this study, light was delivered to the tumor percutaneously under computerized tomographic guidance, which achieved a 100% response rate and a median overall survival of 9.5 months. Later on, Moore *et al.* employed Cremophor®-emulsified palladium-bacteriopheophorbide (TOOKAD®) for successful vascular-targeted PDT against prostate cancer [268]. Regarding antibody-based PSBMs, Schmidt *et al.* were the first to conduct a clinical study using antibody-directed phthalocyanine conjugates for targeted PDT in patients with advanced ovarian carcinoma [269]. More recently, a PSBM-based system using a cetuximab-IR700 conjugate (RM-1929) was designed for photoimmunotherapy of head and neck cancer and showed encouraging results in a clinical trial (NCT02422979) [270]. While the primary motivation of re-formulated photosensitizers with PSBMs is to improve the photo- and physio-chemical properties of the agents *in vivo*, it is apparent that the complex interactions between cellular uptake, subcellular localization, and molecular targets are more likely to govern the observed phototoxicity of a given PSBM.

In this study, we prepared and characterized a series of PSBMs by conjugating VP to (i) 1-stearoyl-2-hydroxy-sn-glycero-3-phosphocholine (16:0 Lyso PC) phospholipid, (ii) PEG-distearoylphosphoethanolamine-polyethylene glycol (DSPE-PEG) phospholipid-polymer conjugate, or (iii) anti-epidermal growth factor receptor monoclonal antibody cetuximab. The study of lipid-conjugated tetraphenylporphyrin photosensitizers was first reported by Komatsu *et al.* in 2002 to form spherical unilamellar vesicles with a diameter of 100 nanometers (nm) [271]. This work was later followed by studies from Zheng, Lovell, and others using different linking strategies, photosensitizers, and lipids to synthesize porphysome nanovesicles for effective light-based therapy of tumors [196, 203, 272]. Studies from Soukous and Hamblin showed that the surface charge and PEGylation of Chlorin e6 conjugates alter tissue-localizing prosperities and play an important role related to the efficacy of PDT for ovarian cancer [273, 274]. Hasan and others pioneered covalent conjugation of VP to Cetuximab for targeted photoimmunotherapy and fluorescence imaging [275-277]. The highly self-quenched VP conjugated to Cetuximab can be internalized by cancer cells through clathrin-mediated endocytosis and de-quenched *via* lysosomal proteolysis of the antibody [276, 278]. Here, using 16:0 Lyso PC-VP, DSPE-PEG-VP, Cetuximab-VP, and free-form VP, we present a full physical, photochemical, cellular uptake, and subcellular localization investigation under controlled experimental conditions. This chapter will explore how these properties relate to PSBM cytotoxicity in human GBM cells.

5.2 Methods

5.2.1 PSBM Preparation and Purification

Three types of PSBMs were synthesized by covalently linking VP to (i) 16:0 Lyso PC (MW. 532.68; Avanti-Polar Lipids), (ii) DSPE-PEG (MW. 2790.48; Avanti-Polar Lipids), and (iii) Cetuximab (MW. ~146k; Bristol-Myers Squibb). The 16:0 Lyso PC-VP conjugate was prepared by crosslinking the carboxylic acid group of VP to the hydroxyl functional group of 16:0 Lyso PC *via* the esterification reaction as described by others [167] and us previously [196]. Briefly, 16:0 Lyso PC, VP, 1-ethyl-3-(3-dimethylaminopropyl) carbodiimide, 4-(dimethylamino) pyridine, and N,N-diisopropylethylamine were mixed in dichloromethane at a fixed molar ratio of 1:5:50:25:60 (113 mg total) for 24 hours at room temperature. Dichloromethane was removed *via* rotary evaporation, and the residue was suspended in 5 mL of methanol prior to Sephadex® LH-20 gel chromatography column purification. Following which, methanol was removed *via* rotary evaporation and the purified 16:0 Lyso PC-VP was stored at -20°C. The DSPE-PEG-VP conjugates were prepared using carbodiimide crosslinker chemistry as described by others previously [279]. Briefly, 1-ethyl-3-(3-dimethylaminopropyl) carbodiimide, VP, and DSPE-PEG were mixed chloroform at a molar ratio of 50:10:1 (20 mg total) for 24 hours at room temperature. Chloroform was removed *via* rotary evaporation, and the resulting thin film was hydrated with 1.5 mL of methanol for purification with a Sephadex® LH-20 gel chromatography column. The purified DSPE-PEG-VP conjugates were dried *via* rotary evaporation and then stored at -20 °C storage. Conjugation of VP to Cetuximab was achieved using carbodiimide crosslinker chemistry as described by others and us previously [275, 278].

Briefly, PEGylation of Cetuximab was carried out by adding mPEG-NHS in DMSO (200 μL; 40,000 MW; 4 mg/mL) dropwise to Cetuximab (2 mL; 2 mg/mL) and allowed to stir overnight at 400 rpm at room temperature. PEGylated Cetuximab was reacted with the N-hydroxysuccinimidyl ester of VP (VP-NHS) at 1:9 molar ratios for 20 hours. The resulting Cetuximab-VP conjugates were purified using a Zebra spin desalting column (7kDa MWCO; Thermo) pre-equilibrated with 30% DMSO in PBS, and then washed in a 20 mL centrifugal filter tube (30kDa MWCO; Amicon) three times with 5% DMSO in PBS prior to storage at 4ºC. The purified 16:0 Lyso PC-VP and DSPE-PEG-VP conjugates were analyzed using matrix-assisted laser desorption ionization-time of flight mass spectrometry (MALDI-TOF MS; Bruker). The VP concentration of PSBM was estimated by absorbance in DMSO using the established molar extinction coefficient of VP in DMSO (~34,895 M^{-1} cm^{-1} at 687 nm) [19]. The Cetuximab-VP purity was confirmed by gel fluorescence imaging analysis of free VP following sodium dodecyl sulfate-polyacrylamide gel electrophoresis (SDS-PAGE). The protein content of Cetuximab-VP was evaluated by bichoninic acid protein assay (Thermo). VP conjugation efficacy was determined by dividing the amount of antibody-conjugated VP in the purified Cetuximab-VP by the total amount of VP added initially.

5.2.2 Photophysical and Photochemical Characterizations

The fluorescence-based optical characterization (Excitation/Emission: 422/650-750 nm) of PSBMs in PBS or DMSO was determined using a multi-mode microplate reader (BioTek). Fluorescence photoactivity is defined as the maximal fluoresce intensity of PSBM in PBS divided by the maximal fluoresce intensity of PSBM in DMSO. The singlet oxygen yield of PSBM was studied in 96-well plates as described previously [19, 278]. Briefly, VP and SOSG

were fixed at 5 μM, and light (690 nm, 10 J/cm^2, 10 mW/cm^2) was delivered vertically. The microplate reader acquired the fluorescence signals of SOSG (Excitation/Emission: 504/525 nm).

5.2.3 Cell Culture

Human GBM cell lines U251 and U87 were obtained from American Type Culture Collection (ATCC) and cultured in Eagle's Minimum Essential Medium cell culture medium (Cellgro), supplemented with 10% (v/v) FBS (Gibco), 100 U/mL penicillin and 100 μg/mL streptomycin (Lonza), according to the manufacturer's instructions. The GBM39 patient-derived xenograft was originally obtained from patients at the Mayo Clinic by Dr. Jann Sarkaria. Molecular genetic alterations and patient tumor information for GBM39 has been previously determined and described [280]. GBM39 was derived from the primary GBM tumor of a 51-year-old male prior to radiation, chemotherapy (TMZ), craniotomy, and Carmustine (BCNU) wafers (Gliadel). GBM39 cells were cultured in DMEM/F12 medium using StemPro NSC SFM Kit (ThermoFisher A1050901) including neural supplement, bFGF, and EGF, supplemented with 100 U/mL penicillin and 100 μg/mL streptomycin (Lonza), and 5mM GltaMAX (GIBCO). GBM39 cells were cultured to 70% confluency in a Poly-L-lysine (Sigma) and laminin (GIBCO) coated culture flask before seeding. All cell lines were maintained in 5% CO_2 at 37°C. Cultures were tested mycoplasma free after resuscitation.

5.2.4 Photodynamic Therapy of Glioblastoma Cells Using PSBMs

For PDT studies, U251 and U87 cells were plated in 35-mm Petri dishes at a cell density of 7.5×10^4 and 2.5×10^5 cells *per* dish, respectively, to allow overnight culture. Attached cells with 80-90% confluency were incubated in serum-free medium containing free VP or PSBMs at desired concentrations for 24 hours, at which time cells were irradiated with 690 nm red light (20 J/cm^2, 150 mW/cm^2, bottom illumination) in the fresh complete culture medium. Light activation was performed using the ML6600 series laser system (690±5 nm; 1.5 W max output power; SMA fiber output with SMA905 connector, Modulight). Cell viability was determined by MTT assay at 24 hours after 690 nm light irradiation. Cell survival fractions for PDT treated samples were normalized to the no treatment controls. The no treatment controls were incubated in serum-free medium with no exposure to free VP or PSBM's and were not subject to irradiation. Alternatively, cells were collected 4 hours post-treatment and incubated with Annexin V FITC and propidium iodide (Abcam, ab14085) for flow cytometry analysis (BD FACSCelesta). Mitochondrial membrane potential ($\Delta\Psi m$) was examined *via* tetramethylrhodamine ethyl ester (TMRE) assay (Abcam). Briefly, U251 cells were cultured overnight in 96-well black wall plates at a density of 3,000 cells/well, and then incubated with PSBM for 24 hours (0.15 μM of free VP, 0.25 μM of 16:0 Lyso PC-VP, 0.5 μM of DSPE-PEG-VP, and 0.5 μM of Cetuximab-VP). After incubation, cells were washed twice with PBS and exposed to 690 nm light (0 or 1 J/cm^2, 10 mW/cm^2). After PDT, cells were incubated with TMRE (250 nM)-containing medium for 25 minutes, washed twice with 0.2% bovine serum albumin within PBS, and subjected to fluorescence readings (Excitation/Emission: 549/575 nm) using a

microplate reader (BioTek). Controls include no light irradiation and 150 μM of carbonilcyanide p-triflouromethoxyphenylhydrazone (FCCP). Lysosome damage was examined *via* LysoTracker Red incorporation. Briefly, cells were incubated with 0.15 μM free VP, 0.25 μM 16:0 Lyso PC-VP, 0.5 μM DSPE-PEG-VP, or 0.5 μM Cetuximab-VP for 24 hours and irradiated with 690 nm red light (20 J/cm^2, 150 mW/cm^2, bottom illumination). At 30 minutes after light treatment, cells were incubated with 100 nM LysoTracker Red in serum free medium for 15 minutes at 37°C and washed twice with PBS. At least 20,000 events were collected by the flow cytometer (BD FACSCelesta) using the BD Horizon PE-CF594 filter (Excitation/Emission: 561/610) and analyzed with FlowJo software.

5.2.5 PSBM Uptake and Localization Studies in Glioblastoma Cells

To evaluate PSBM uptake, U251 (or U87) cells were plated in 35-mm Petri dishes at 2×10^5 and 2.5×10^5 cells *per* dish, respectively. Attached cells with 80-90% confluency were incubated in culture medium containing free VP or PSBMs (0-1 μM, 1 mL) for 24 hours. Cells were washed twice with PBS, harvested with trypsin, and lysed in Solvable solution (0.5 mL) at 4°C. VP fluorescence intensity (Excitation/Emission: 435/690±20 nm) was measured using a microplate reader (BioTek) converted to moles of VP based on appropriate standard curves. Protein concentration was determined using the Pierce bichoninic acid protein assay. To verify PSBM uptake using fluorescence microscopy imaging (Lionheart, BioTek), cells were plated at the same density within a 24-well glass bottom plate, and incubated with 0.25 μM free VP or PSBM for 24 hours. Before imaging, cells were washed twice with PBS, and nuclei were stained with Hoechst nucleic acid stain. Live cell imaging was

performed to confirm aldehydes did not impact analysis. Images were captured in quadruplet at specified locations for each well. Fluorescent intensity of VP was quantified and normalized. Confocal fluorescence imaging studies were performed to determine the subcellular localization of PSBMs in GBM cells. Briefly, cells were cultured overnight in 35-mm glass bottom dishes at 75,000 cells *per* dish and incubated with free VP or PSBMs for 24 hours before confocal imaging. After PBS washing, cells were stained with 1 mL 100 nM MitoTracker Green (M7514; Invitrogen) or 100 nM LysoTracker Red probes (DND-99; Invitrogen) for 30 min at 37 °C. Hoechst was utilized to stain the nuclei of the cells prior to confocal fluorescence imaging (Olympus FluoView-1000 confocal microscope) using a 10X or 40X objectives. Excitation of Hoechst/VP, MitoTracker, and LysoTracker were carried out using 405 nm, 488 nm and 559 nm lasers, respectively, with appropriate filters (Hoechst: 430-470 nm; VP: 650-750 nm; MitoTracker: 500-540 nm; LysoTracker: 570-620 nm). Profile plots were created using ImageJ software showing co-localization of PSBM and mitochondria or lysosomes [281].

5.2.6 Immunoblotting

U251 cells (7.5×10^5 cell *per* 35-mm dish) were treated with PSBM for 24 hours (0.15 μM of free VP, 0.25 μM of 16:0 Lyso PC-VP, 0.5 μM of DSPE-PEG-VP, and 0.5 μM of Cetuximab-VP) followed by irradiated at 690 nm (1 J/cm^2, 10 mW/cm^2, bottom illumination) in the fresh culture medium. At 6 and 24 hours post-PDT, cell lysates were collected in RIPA lysis buffer supplemented with 1% phosphatase and protease inhibitor cocktail. Protein lysates (20 μg) of each sample were separated on a NuPAGE 4–12% precast Bis-Tris gel (Mini-tank system, ThermoFisher) and

transferred onto a polyvinylidene difluoride membrane. Subsequent to blocking with 5% bovine serum albumin in TBST, the blot was incubated with primary antibody against LC3I/II (Cell Signaling, #4108) overnight at 4 °C followed by incubation with its secondary antibody for 2 hours at room temperature based on the supplier's advice. Visualization of protein bands was developed by chemiluminescence (SuperSignal, ThermoFisher) with exposure to Gel Imager (ProteinSimple). β-actin serviced as loading control.

5.2.7 Statistical Analyses

Results are mean ± standard error of the mean (SEM). Statistical tests were carried out using GraphPad Prism. All experiments were carried out at least in triplicate. Specific tests and number of repeats are indicated in the figure captions. Reported P values are two-tailed. One-way ANOVA statistical tests and appropriate post hoc tests were carried out to avoid type one error.

5.3 Results and Discussion

5.3.1 Synthesis and Characterization of PSBMs

16:0 Lyso PC-VP PSBMs were synthesized by an esterification reaction between the carboxyl groups of VP photosensitizers and the alcohol groups of 16:0 Lyso PC lipids. The hydrophobic VP placed along the alkyl side chain of 16:0 Lyso PC maintains an overall amphipathic structure of the 16:0 Lyso PC-VP (**Figure 5.1a**). To prepare DSPE-PEG-VP, VP was coupled to the polar PEG-modified head group of DSPE-PEG *via* amide coupling, ultimately changing the amphipathic structure by capping the hydrophilic PEG head with a hydrophobic VP molecule (**Figure 5.1b**).

MALDI-TOF mass spectrometer analysis of the purified 16:0 Lyso PC-VP conjugates showed a single primary product with a mass of 1196.4, compared to multiple products for the crude reaction mixture (**Figure 5.2a**). The observed peak mass for the purified DSPE-PEG-VP PSBMs was 3602.1 (**Figure 5.2b**), which is similar to others finding [279]. The final yields of 16:0 Lyso PC-VP and DSPE-PEG-VP were approximately 20.1±3.8% and 13.0±3.7%, respectively. It is well established that 16:0 Lyso PC-VP and DSPE-PEG-VP can self-assemble in aqueous medium into a variety of nano- to micron-scale vesicles when using the extrusion method [196, 203, 279]. The structure of the vesicles formed is dictated by the concentration of PSBMs as well as the self-assembling environment [196, 203, 279]. Here, our goal is to examine the cellular interaction of the monomeric PSBMs instead of their nano/micro-formulations. Under our experimental conditions, no nano- or micro-vesicles of 16:0 Lyso PC-VP or DSPE-PEG-VP were detected when using dynamic light scattering technique.

To prepare Cetuximab-VP conjugates (**Figure 5.1c**), 7 VP photosensitizers were attached to the lysine groups of each anti-EGFR antibody Cetuximab at a conjugation efficiency of 66.1±3.6%. PEGylation of Cetuximab before VP conjugation was necessary to prevent the aggregation of Cetuximab-VP conjugates [278]. We have previously confirmed that conjugation of 6-7 VP molecules *per* Cetuximab does not impair the selective binding and internalization of Cetuximab in EGFR positive cancer cells [278]. Sodium dodecyl sulfate-polyacrylamide gel electrophoresis was used to identify and monitor the purity of Cetuximab-VP, which is less than 1% free VP. Similar to 16:0 Lyso PC-VP and DSPE-PEG-VP, Cetuximab-VP can be in

incorporated into nanoconstructs by linking them to the outer layer of nanoparticles to achieve targeting functionality [128, 278, 282].

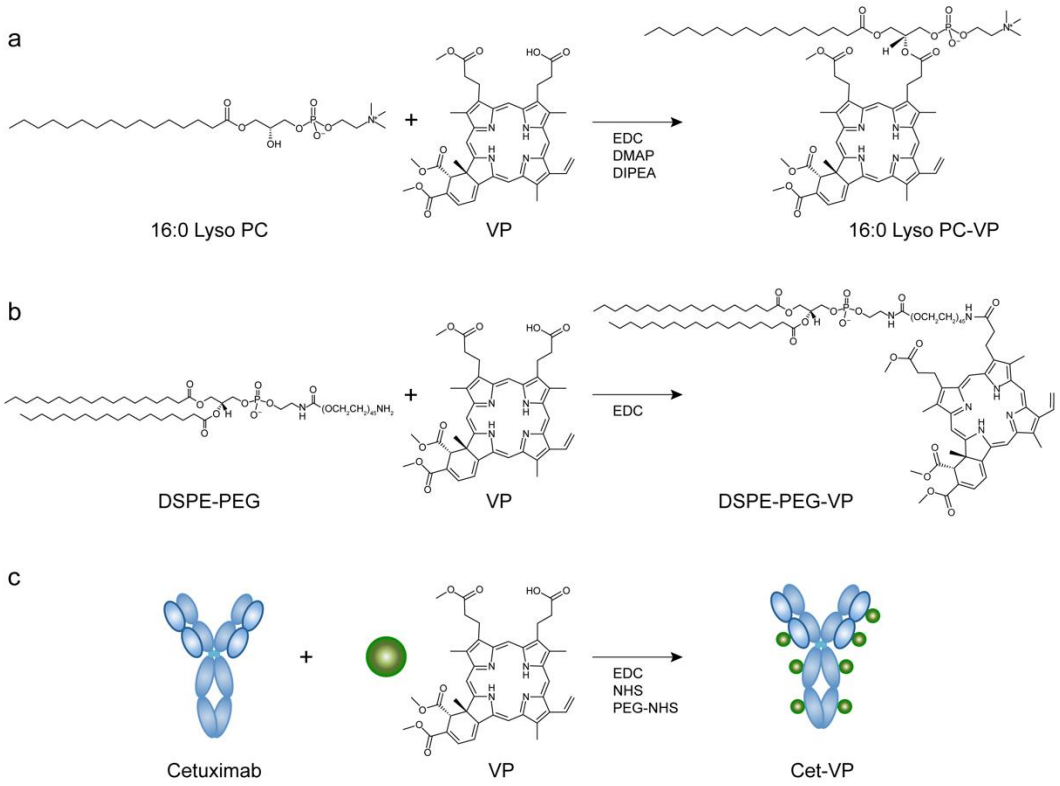

Figure 6.1 Synthesis Reaction and Chemical Structure of PSBMs. (a) 1-stearoyl-2-hydroxy-sn-glycero-3-phosphocholine (16:0 Lyso PC) was conjugated to VP *via* esterification reaction, resulting 1:1 ratio of 16:0 Lyso PC to VP. Carbodiimide crosslinker chemistry was employed to conjugate VP onto **(b)** PEG-distearoylphosphoethanolamine-polyethylene glycol (DSPE-PEG) and **(c)** monoclonal antibody cetuximab (Cet). Final conjugates contain 1:1 and 1:7 ratio of DSPE-PEG-to-VP and Cetuximab-to- VP, respectively. Green circles are to represent VP photosensitizers.

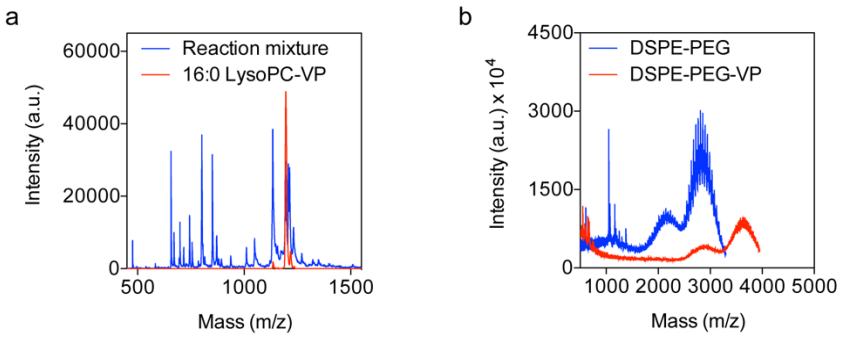

Figure 6.2 MALDI-TOF mass spectrometer analysis of 16:0 Lyso PC-VP and DSPE-PEG-VP. (**a**) Purified 16:0 Lyso PC-VP showed a single primary product with mass of 1196.4 (red line) compared the multiple products for the crude reaction mixture (blue line) (yield: 20.1±3.8%). (**b**) Purified DSPE-PEG-VP demonstrated a shift peak mass at 3602.1 (red line) compared to the crude reaction mixture (blue line) (yield: 13.0±3.7%, N≥3)

5.3.2 Photoactivity of PSBMs

Conjugation of VP to biomolecules is an expedient strategy to improve the photoactivity of VP under biologically relevant conditions. In clinical PDT practice, systemic VP photosensitizers are commonly activated by 690 nm light because near-infrared light penetrates deeper into the tissues than light of shorter wavelength [168]. Here, we showed that conjugation of VP to 16:0 Lyso PC, DSPE-PEG, or Cetuximab does not alter the Q band (690 nm) or the Soret peak (435 nm) of VP (**Figure 5.3a**). Red shift of the Q band was not anticipated, as the lipid conjugation reaction does not reduce the number of double bonds in the pyrrole rings of VP [283]. We further evaluated the fluorescence emission spectra (650-750 nm) of free VP and PSBMs (i.e., 16:0 Lyso PC-VP, DSPE-PEG-VP, or Cetuximab-VP) in PBS and in dimethyl sulfoxide (DMSO), using an excitation wavelength of 435 nm. The aggregation of free VP in PBS led to a nearly complete (>95%) fluorescence quenching as compared to fully solubilized VP in DMSO (**Figure 5.3b**). DSPE-PEG-VP restored the fluorescence emission signal of VP molecules in PBS and was the most effective at retaining up to

15% photoactivity of the VP (**Figure 5.3c**). In contrast, 16:0 Lyso PC-VP demonstrates less retention of photoactivity compared to that of DSPE-PEG-VP. This is likely caused by the improved stability due to the presence of PEG in DSPE. Cetuximab-VP shows the least retention of photoactivity at ~5%. This can be explained by our previous report and others that Cetuximab-VP conjugates at 1:7 ratio display up to 7-fold VP static quenching [275, 276]. More importantly, these highly self-quenched VP molecules on Cetuximab can be de-quenched by cancer cells upon lysosomal proteolysis of the Cetuximab antibody. This unique 'tumor-activation' function of Cetuximab-VP can be used to improve the selective delivery of VP for a safer photoimmunotherapy as shown by others and us [276, 278].

Type II photosensitization is the dominant process in VP-based PDT and produces highly reactive singlet oxygen ($^1O_2$), which confers toxicity to nearby targets by oxidizing proteins and lipids [23]. In this study, $^1O_2$ generation from light-activated PSBMs or free VP is monitored indirectly by using the fluorescence probe SOSG. We have previously confirmed that the VP fluorescence is negligible at the wavelength used to monitor the SOSG fluorescence [19]. Upon 690 nm light activation, the SOSG fluorescence intensity generated by DSPE-PEG-VP was at least 4 folds higher than that generated by free VP, Cetuximab-VP, and 16:0 Lyso PC-VP (**Figure 5.3d**). This correlates with our finding of DSPE-PEG-VP exhibiting the highest retention of photoactivity (**Figure 5.3c**). The SOSG fluorescence intensity generated from Cetuximab-VP was not significantly higher than that produced by free VP and 16:0 Lyso PC-VP upon light activation ($P > 0.05$, **Figure 5.3d**). This is likely due to the fluorescence quenching shown in **Figure 5.3c**. This data suggests that DSPE-PEG-VP,

with relatively stronger fluorescence emission spectra, improves the $^1O_2$ production under physiologically relevant conditions during light activation, compared to free VP, Cetuximab-VP, and 16:0 Lyso PC-VP; which may lead to a higher phototoxicity response for PDT.

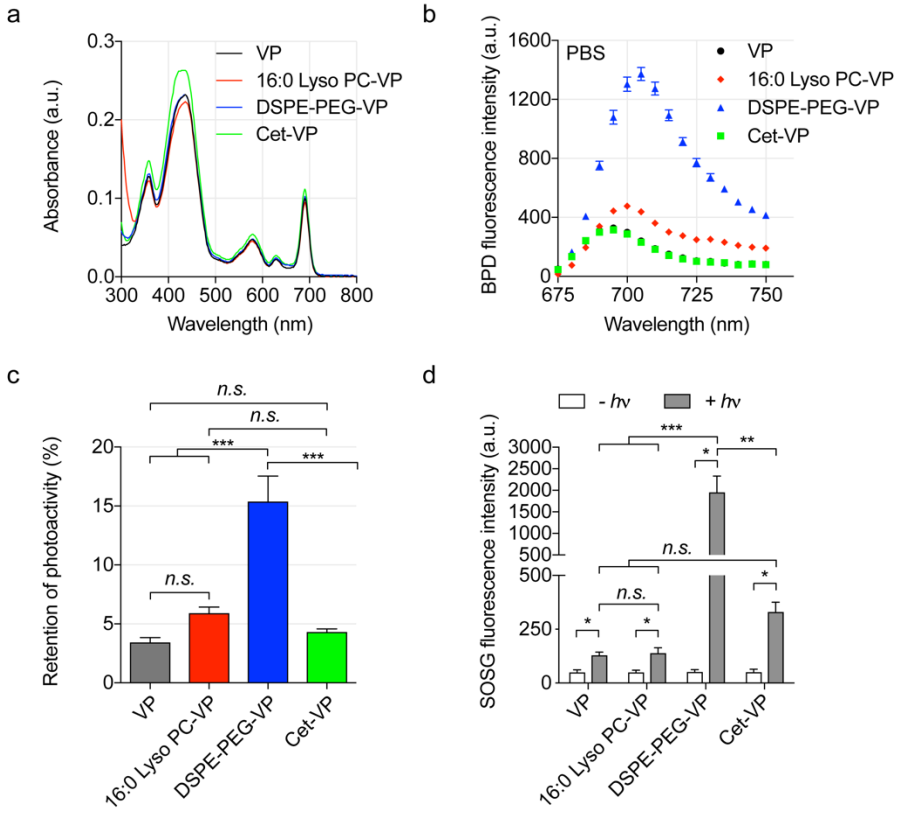

Figure 6.3 Photophysical and Photochemical Characterization of PSBMs. (a) Representative absorbance spectra of free VP, 16:0 Lyso PC-VP, DSPE-PEG-VP, and Cetuximab-VP in DMSO. Conjugation of VP on biomolecules did not alter the Q-band (690 nm). **(b)** Biomolecular conjugation of VP on DSPE-PEG and 16:0 Lyso PC regained fluorescence intensity of VP under physiological relevant condition. Fluorescence quenching was observed in Cetuximab-VP as in free VP. **(c)** Photoactivity is defined as the maximal fluoresce intensity (FI) of PSBM in PBS divided by the maximal fluoresce intensity (FI) of PSBM in DMSO. (n = 6, ***P < 0.001, *n.s.*: nonsignificant). **(d)** SOSG reports $^1O_2$ production from photo-activated (690 nm, 10 J/cm^2; 10 mW/cm^2) PSBMs and free VP in PBS at a fixed VP concentration of 5 μM. (n = 3, *P < 0.05, **P < 0.01, ***P < 0.001). N=6, where N equals the number of wells assessed over 3 trials.

5.3.3 Photodestruction of Glioblastoma Cells Using PSBMs

In the above studies, we have shown that PSBMs could improve the photoactivity of VP. We next investigated if this improvement in photoactivity translates to an enhancement in phototoxicity *in vitro* using two EGFR-positive GBM cell lines (U251, U87) (**Figure 5.4**). Here, 16:0 Lyso PC-VP, DSPE-PEG-VP, Cetuximab-VP, and free VP were incubated with GBM cells at different concentrations (0-3 μM) for 24 hours prior to 690 nm light activation (20 J/cm^2, 150 mW/cm^2, **Figure 5.4a**). 16:0 Lyso PC-VP, DSPE-PEG-VP, and free VP all showed negligible dark toxicity in U251 or U87 cells (**Figure 5.4b-d)**. It is not surprising that Cetuximab-VP (above 0.5 μM) showed a modest 25% dark toxicity in U251 cells (**Figure 5.4b**), as it has been verified that conjugation of 7 VP molecules onto Cetuximab does not take away the targeting functionality of Cetuximab [276, 278]. At 24 hours following PDT, the viability of cancer cells was assessed by MTT assay. Free VP was found to be the most potent PDT agent with an IC_{50} of 0.44 μM×J/cm^2 in U251 cells (**Figure 5.4a**), despite having the least retention of photoactivity and the lowest singlet oxygen yield under physiological conditions (**Figure 5.3c,d**). A significant decrease in phototoxicity was observed with 16:0 Lyso PC-VP (IC_{50}: 1.68 μM×J/cm^2), Cetuximab-VP (IC_{50}: 8 μM×J/cm^2), and DSPE-PEG-VP (IC_{50}: >60 μM×J/cm^2) (**Figure 5.4a,c**). This remarkable variation in the photo-cytotoxicity of PSBMs was also observed in the U87 cell line (**Figure 5.4d**). At a fixed PDT dose of 5 μM×J/cm^2, free VP reduced the viability of U87 cells by over 95%, and the loss of cell viability was dramatically reduced to approximately 40%, 13%, and 2% when using 16:0 Lyso PC-VP, Cetuximab-VP, and DSPE-PEG-VP, respectively (**Figure 5.4d**). This difference in

PDT efficacy does not correlate with the photoactivity and singlet oxygen yields of PSBMs in physiologically relevant buffers. We showed that DSPE-PEG-VP is the most photoactive formulation in a cell-free system, but it has the poorest *in vitro* PDT

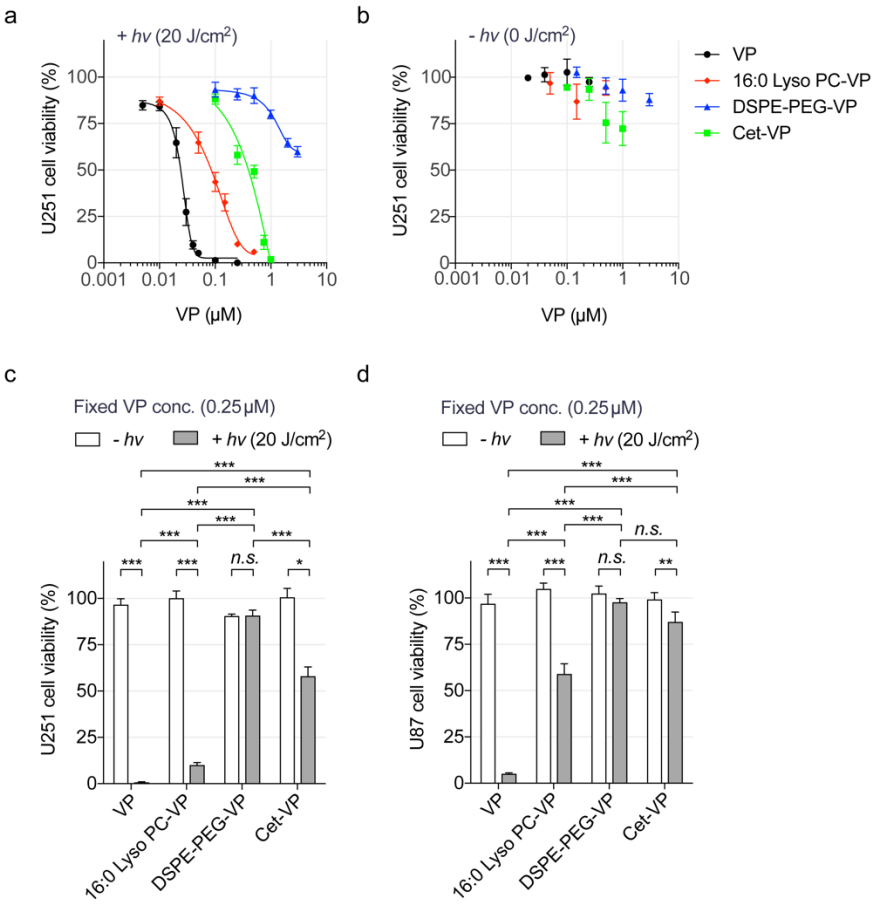

Figure 6.4 Near-infrared Light Activation of PSBMs Leads to Phototoxicity of Glioblastoma cells. (**a**) U251 glioblastoma cells were incubated with PSBMs at different VP concentrations (0-3 μM) for 24 hours prior to light illumination (0 or 20 J/cm^2, 150 mW/cm^2). Cell viability was evaluated via MTT assay at 24 hours after light activation. Light activated PSBMs (+hv) resulted in a significant loss of U251 viability compared to (**b**) PSBM treatments without light activation (–hv). (**c**) U251 and (**d**) U87 glioblastoma cells were incubated with i) free VP, ii) 16:0 Lyso PC-VP, iii) DSPE-PEG-VP, or iv) Cetuximab-VP at 37 °C for 24 hours prior to light irradiation at a fixed PDT dose of 5.0 μM × J/cm^2 (i.e., 0.25 μM VP and 20 J/cm^2). (n > 3, *P < 0.05, **P < 0.01, ***P < 0.001). N≥3, where N equals the number of wells assessed over 3 trials.

efficacy against GBM cells. These results motivated us to evaluate the cellular uptake and location of PSBMs.

5.3.4 PSBM Uptake

We compared the uptake of free VP and PSBMs in U87 and U251 cells at different drug incubation concentrations (0-1 μM). After 24 hours of incubation in U87 cells, free VP showed the highest percentage of cellular uptake at 0.36±0.08% *per* μg of protein, compared to 16:0 Lyso PC-VP uptake at 0.13±0.02% *per* μg of protein. Both DSPE-PEG-VP and Cetuximab-VP had the lowest uptake percentage in U87 cells at 0.06±0.01% *per* μg of protein and 0.07±0.0134% *per* μg of protein, respectively (**Figure 5.5a**). Similarly, the reduced cellular uptake of PSBMs was observed in U251 cells (**Figure 5.5b**). Comparative analyses showed comparable PSBM uptake between the U87 and U251 cells at the concentrations used (**Figure 5.6**). It is likely that the stealth function of PEG, or the overall change in amphipathic structure, inhibited the cellular uptake of DSPE-PEG-VP [29, 284]. Additionally, we have also reported that the limited intracellular uptake of Cetuximab-VP is due to the low photosensitizers-to-antibody ratio of Cetuximab-VP required for maintaining the antibody's targeting ability, as well as the limited amount of EGFR molecules presented on the cancer cell surface [278]. The cellular uptake of VP (or PSBM) was further correlated with PDT-mediated viability reduction to determine the PDT efficiency (i.e., percent of cell viability reduction *per* fmole of intracellular VP). Interestingly, the PDT efficiency of 16:0 Lyso PC-VP (~2.2%) was found to be significantly higher than that of free VP (~1.1%), DSPE-PEG-VP (0.1-0.3%), and Cetuximab-VP (0.6-0.9%) in both U87 and

U251 cell lines (**Table 5.1**). These results suggest that the cytotoxic mechanisms of PSBM-PDT are likely to be different from that of VP-PDT.

Light activation of photosensitizers not only result in cytotoxicity but can also generate fluorescence signal from the relaxation of excited singlet-state photosensitizers back to the ground state. Recently, Gliolan® (ALA) has been approved for use to visualize malignant tissue during glioma surgery [285]. This use of ALA-induced fluorescent protoporphyrin IX (PpIX) to accurately define brain tumor margins is critical to achieving optimal surgical outcomes [286]. We next tested if PSBMs at 0.25 μM can be used for fluorescence imaging of U251 cancer cells (**Figure 5.5c**). After 24 hours incubation at 37°C and followed by washing to remove loosely attached or non-attached agents, live cells treated with free VP showed the highest VP fluorescence signal, compared to cells treated with 16:0 Lyso PC-VP, DSPE-PEG-VP, or Cetuximab-VP (**Figure 5.5c**). Quantification of the fluorescence images showed that free VP exhibited ~2-10 fold higher fluorescence signal in U251 cells, compared to using 16:0 Lyso PC-VP, DSPE-PEG-VP, or Cetuximab-VP (**Figure 5.7**). While it is clear that free VP uptake is greater than that of the PSBMs, extraction data reveals that uptake is not significantly different for 16:0 Lyso PC-VP, DSPE-PEG-VP, and Cetuximab-VP at the fixed incubation concentration of 0.25 μM. However, fluorescent imaging quantification shows 16:0 Lyso PC-VP is slightly higher than DSPE-PEG-VP and Cetuximab-VP. It is well established that fluorescent probes can respond to changes in their microenvironments (*e.g.*, pH) [287, 288], which possibly explains this observation. While fluorescent imaging is warranted, the more accurate method is extraction due to VP being solubilized under the same conditions. It is obvious that our

ability to effectively image cancer cells correlates with the amount of the photosensitizing agents associated with the cells. However, these data do not suggest that 16:0 Lyso PC-VP, Cetuximab-VP, and DSPE-PEG-VP are poor imaging agents, as signal-to-background ratio of tumor to the surrounding normal tissue is a more important parameter to be carefully investigated *in vivo*.

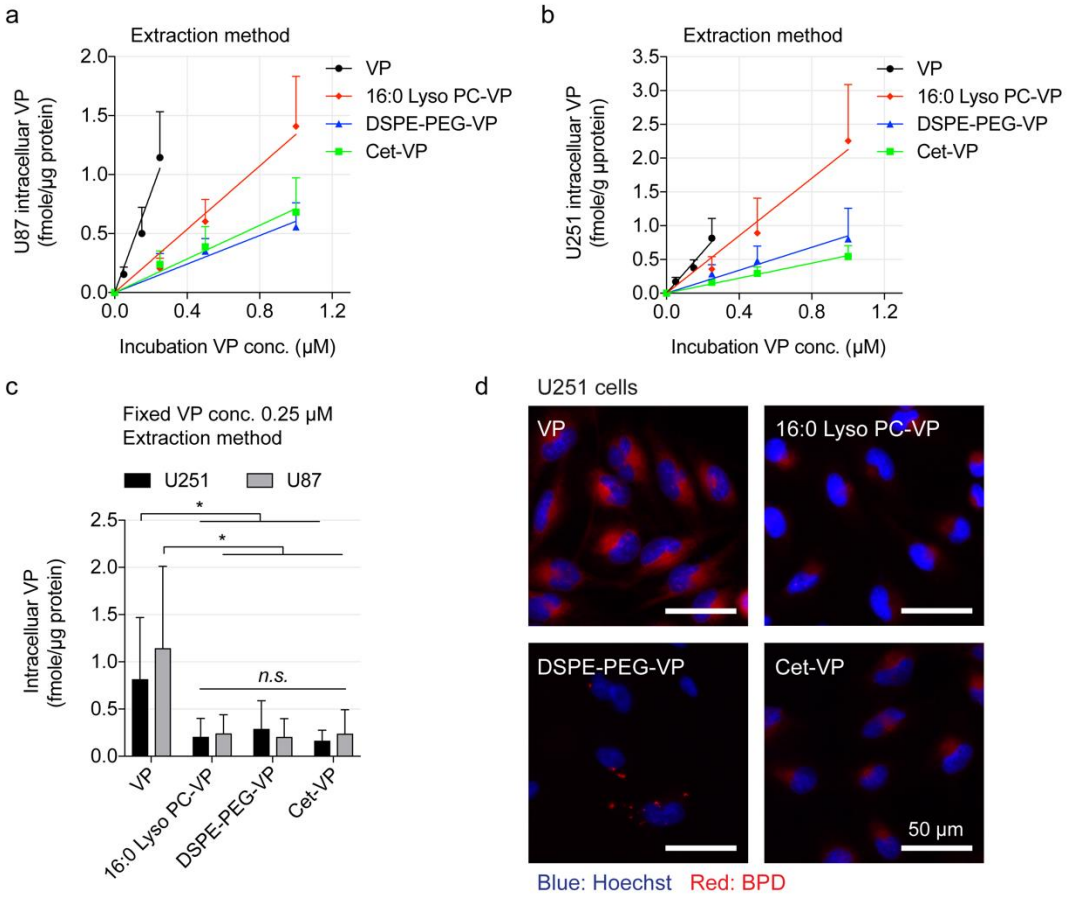

Figure 6.5 Cellular Uptake of PSBMs and Free VP. Quantification of (**a**) U87 and (**b**) U251 intracellular VP concentrations at 24 hours post-incubation with free VP, 16:0 Lyso PC-VP, DESP-PEG-VP, and Cetuximab-VP (0-1 µM) using extraction method. (**c**) Comparison of uptake of PSBM and free VP at 0.25 µM in both U87 and U251 cell lines. (n = 5, *P < 0.05). (**d**) Representative fluorescence imaging of VP photosensitizer (red) in U251 cells incubated with 0.25 µM free VP or PSBMs for 24 hours. Nuclear staining (blue, Hoechst); Scale bar = 50 µm. N≥3, where N equals the number of wells assessed over 3 trials.

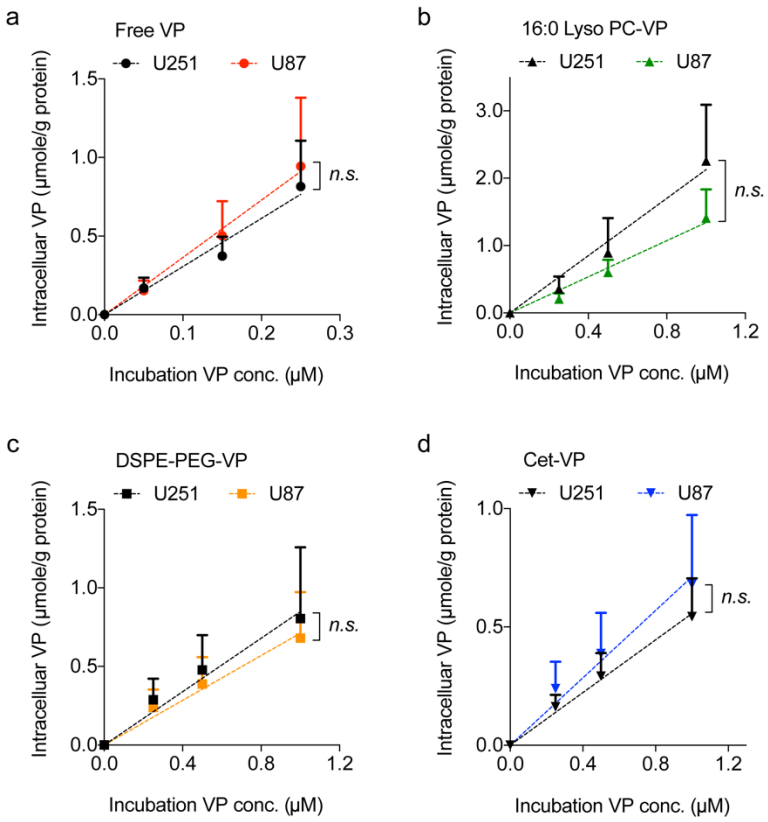

Figure 6.6 Comparison of PSBMs and Free VP Uptake in GBM Cell Lines. Quantification of (**a**) Free VP, (**b**) 16:0 Lyso PC-VP, (**c**) DSPE-PEG-VP, and (**d**) Cetuximab-VP intracellular VP concentrations at 24 hours post-incubation, in U251 and U87 cells, using extraction method. (*n* = 5, *n.s.*: nonsignificant).

Table 6.1 PDT Efficiency of Free VP and PSBMs in Glioblastoma Cells.

Groups*	U251 (PDT efficiency**)	U87 (PDT efficiency**)
Free VP	1.12±0.00%	1.07±0.00%
16:0 Lyso PC-VP	2.30±0.03%	2.14±0.29%
DSPE-PEG-BPD	0.29±0.09%	0.09±0.08%
Cet-VP	0.94±0.28%	0.57±0.24%

*Drug incubation concentration: 0.25 μM VP equivalent. **PDT efficiency: percent of viability reduction per fmole of intracellular VP. PDT drug-light interval: 24 hours. PDT light dose: 690 nm, 20 J/cm^2, 150 mW/cm^2.

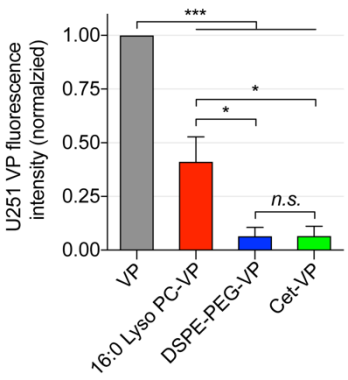

Figure 6.7 Quantification of VP Fluorescence Signal. U251 Cells were incubated with Free VP, 16:0 Lyso PC-VP, DESP-PEG-VP, and Cetuximab-VP (0.25 μM) for 24 hours. Quantification of fluorescence signal as determined by ImageJ software. (n = 4, *P < 0.05, ***P < 0.001, *n.s.*: nonsignificant).

5.3.5 Altered Subcellular Localization of PSBM

One of the preferred sites of localization for VP photosensitizer is mitochondria [138, 139]. Activation of VP by light causes photodynamic disruption of the mitochondrial membrane, which triggers the release of cytochrome c, a potent initiator of apoptotic cell death. PDT has also been shown to photochemically degrade the anti-apoptotic protein Bcl-2, while leaving pro-apoptotic proteins Bad and Bax unaffected [138, 139]. This shifts the balance in target cells from an anti-apoptotic state to a more pro-apoptotic state. To determine whether PSBMs are localized to the mitochondria, we incubated U251 cells with PSBMs for 24 hours and treated cells with MitoTracker prior to examination using a confocal fluorescence microscope (**Figure 5.8a**). U251 cells that had been incubated with free VP and Cetuximab-VP exhibited a strong and diffuse fluorescence signal throughout the cells. Converging the VP image and MitoTracker image gave a *pseudo-colored* yellow fluorescent pattern (**Figure 5.8a**), and the profile plot analyses confirmed the localization of free VP and Cetuximab-VP

at mitochondria (**Figure 5.8b**). In contrast, 16:0 Lyso PC-VP clustered in the peri-nuclear region with a reduced degree of mitochondria localization in U251 cells (**Figure 5.8**). The DSPE-PEG-VP fluorescence signal in U251 cells was minimal and heterogeneously distributed across different cells (**Figure 5.8**). It was further confirmed that peri-nuclear staining of 16:0 Lyso PC-VP related more to lysosomal incorporation (**Figure 5.9**) compared to mitochondria similar to that observed by others [203].

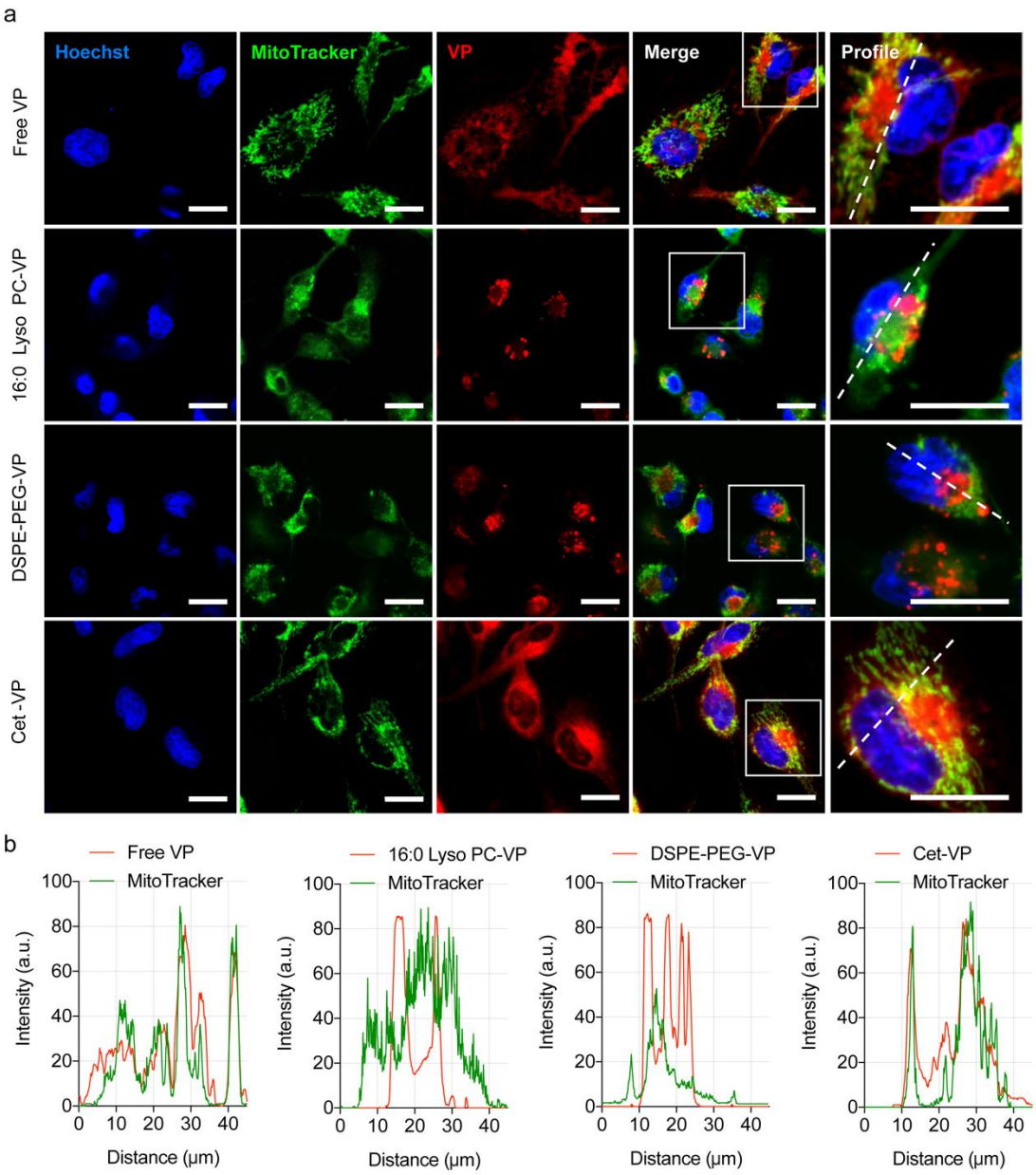

Figure 6.8 Mitochondrial Localization of Free VP and PSBMs in U251 Cells. (**a**) Representative confocal fluorescence images of U251 cells obtained after 24 hours of incubation with free VP, 16:0 Lyso PC-VP, DSPE-PEG-VP, and Cetuximab-VP. VP signal pseudo-colored in red. Mitochondria were stained with 100 nM MitoTracker (M7514; pseudo-colored in green); merging of images where yellow indicates co-localization of VP (red) and mitochondria (green). Nuclear staining (Hoechst; pseudo-colored in blue). Scale bar = 20 μm. (**b**) Profile plots were created using ImageJ software showing co-localization of mitochondria and free VP (or PSBM). N ≥ 3.

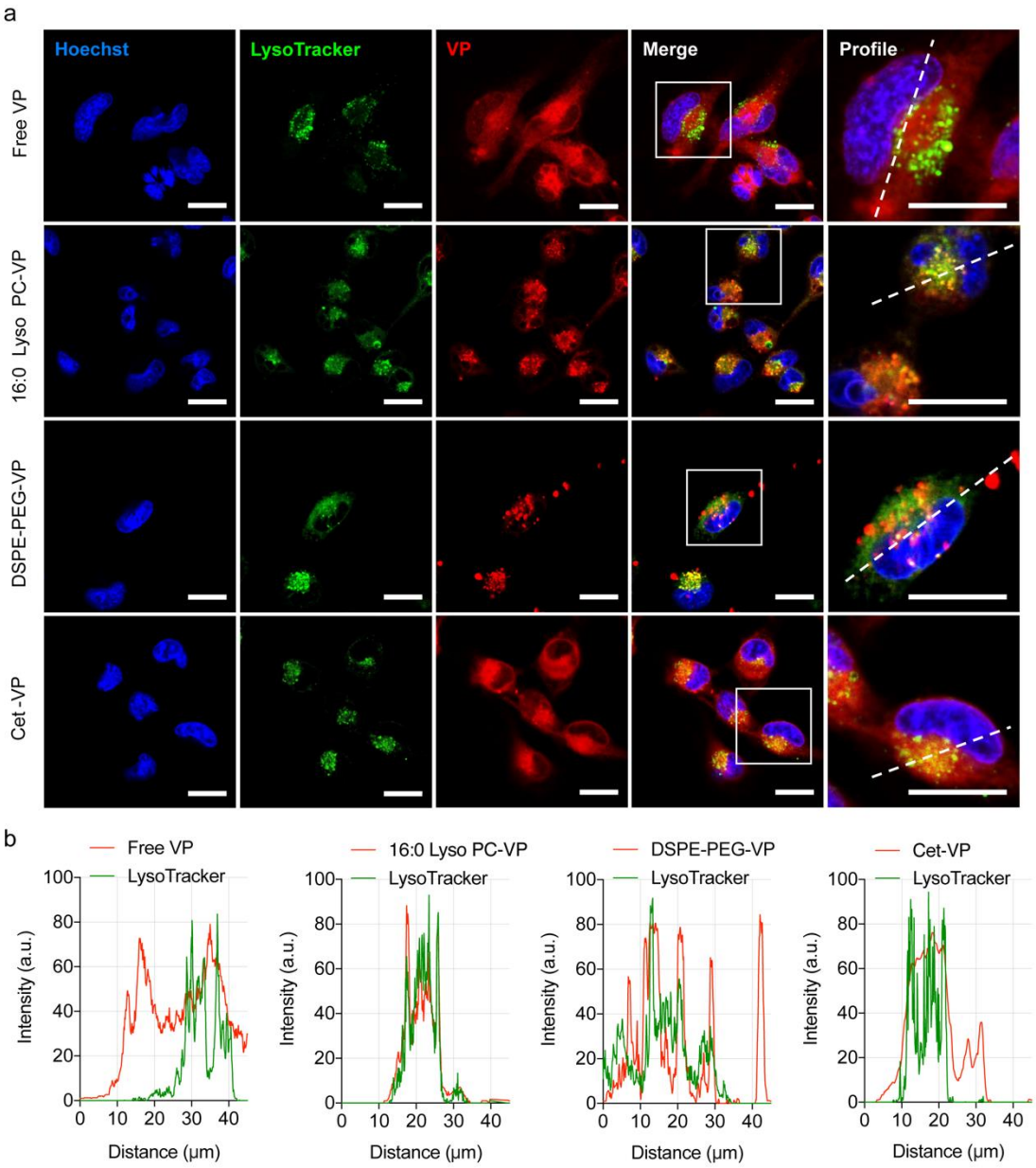

Figure 6.9 Lysosomal Localization of Free VP and PSBMs in U251 Cells. (**a**) Representative confocal fluorescence images of U251 cells obtained after 24 hours of incubation with free VP, 16:0 Lyso PC-VP, DSPE-PEG-VP, and Cetuximab-VP. VP signal pseudo-colored in red. Lysosomes were stained with 100 nM of LysoTracker probes (DND-99; pseudo-colored in green); merging of images where yellow indicates co-localization of VP (red) and lysosomes (green). Nuclear staining (Hoechst; pseudo-colored in blue). Scale bar = 20 μm. (**b**) Profile plots were created using ImageJ software showing co-localization of lysosome and free VP (or PSBM). $N \geq 3$.

We next investigate the ability of PSBM-based PDT to trigger apoptotic cell death,

damage lysosomes, regulate autophagosome formation, and depolarize mitochondrial membrane potential (ΔΨm). To account for the variations in PSBM uptake, U251 cells were incubated with different concentrations of free VP (0.15 μM), 16:0 Lyso PC-VP (0.25 μM), DSPE-PEG-VP (0.50 μM), or Cetuximab-VP (0.50 μM) to achieve an equivalent intracellular VP concentration (~0.35 μmoles *per* gram of protein) prior to light irradiation. In order to compare the degree of which the PSBMs can induce apoptosis, flow cytometric detection of apoptosis with Annexin V and propidium iodide was performed. Light fluence was fixed at 20 J/cm^2, which has been shown to reduce cell viability to nearly 0% at 24 hours after treatment (**Figure 5.4**; MTT assay). For flow cytometry-based apoptosis detection, cells were examined at 4 hours after light exposure to evaluate acute cellular injury (**Figure 5.10a**). Free VP, 16:0 Lyso PC-VP, and Cetuximab-VP all induced similar levels of apoptotic (~20%) and dead cells (~11%) (**Figure 5.10a**), while DSPE-PEG-VP had little impact on cell viability (~96%) although having the same intracellular concentration. Due to lysosomal localization, PDT using 16:0 Lyso PC-VP induced a high degree of lysosomal membrane permeabilization in U251 cells, decreasing the mean fluorescent intensity of LysoTracker to 40% compared to that of the no treatment control (**Figure 5.10b**). PDT treatment with free VP, DSPE-PEG-VP, and Cetuximab-VP modestly reduced the mean fluorescent intensity of LysoTracker (**Figure 5.10b**), suggesting minimal lysosomal damage. A number of studies have already shown that PDT-mediated lysosomal damage could induce autophagy [289-292]. Here, we evaluated autophagosome formation at 6 and 24 hours after PDT using free VP or PSBMs. Immunoblotting results indicated that PDT using free VP and PSBMs all induced an

increase of LC3-II in comparison to the no treatment control at 24 hours post-treatment (**Figure 5.10c**). Increase in LC3-II indicates the accumulation of autophagosomes, which can be seen even at 6 hours after irradiation for free VP, 16:0 Lyso PC-VP, and Cetuximab-VP. However, this does not guarantee autophagic degradation [293]. Owing to mitochondrial localization (**Figure 5.8**), PDT using free VP or Cetuximab-VP induced a high level of ΔΨm depolarization in U251 cells (**Figure 5.10d**). No ΔΨm depolarization was observed using 16:0 Lyso PC-VP and DSPE-PEG-VP for PDT of U251 cells (**Figure 5.10d**). A potent mitochondrial oxidative phosphorylation uncoupler, FCCP, was used as a positive control for ΔΨm depolarization [294]. Considering the time of incubation used (i.e., 24 hours) in our study and above findings, 16:0 Lyso PC-VP co-localization with MitoTracker (**Figure 5.9b**) could potentially be associated with auto-lysosomes containing mitochondria as suggested in Martins' study [295]. The observed Cetuximab-VP and free VP co-localization with LysoTracker could also be associated with auto-lysosomes containing mitochondria (**Figure 5.9b**). Further investigations into the cell/patient line-dependent phototoxicity and autophagy-associated cell death of PSBMs are warranted.

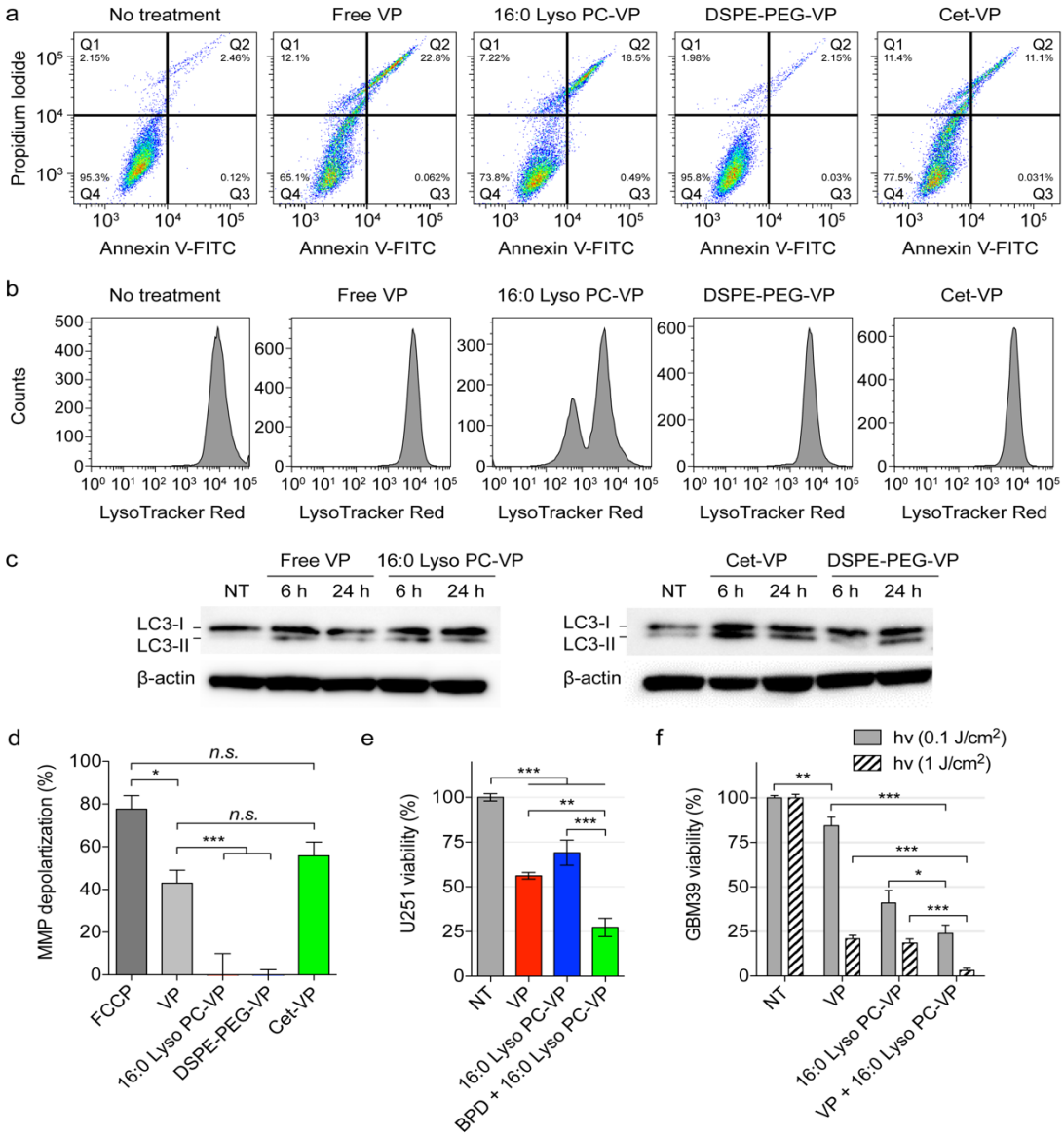

Figure 6.10 Acute Cellular Injury, Lysosomal Membrane Permeabilization, Autophagosome Formation, Mitochondrial Membrane Depolarization, and Combination Treatment using PSBMs and Free VP. Cells were incubated with PSBMs at their respective uptake concentrations (*i.e.*, 0.15 μM of free VP, 0.25 μM of 16:0 Lyso PC-VP, 0.5 μM of DSPE-PEG-VP, and 0.5 μM of Cetuximab-VP) for 24 hours prior to PDT. (**a**) Flow cytometric detection of apoptosis with Annexin V FITC and propidium iodide was performed at 4 hours after light irradiation (20 J/cm^2, 150 mW/cm^2) to detect living (Q4), early apoptotic (Q3), late apoptotic (Q2), and dead cells (Q1). (**b**) Lysosomal membrane permeabilization was assessed 30 minutes after PDT. (**c**) Immunoblotting of LC3-II was assessed 6 and 24 hours after PDT. (**d**) Mitochondrial membrane depolarization was assessed immediately after PDT. (**e-f**) Cell viability was determined *via* MTT assay at 24 hours post-PDT (690 nm, 0.1 J/cm^2 for U251; 0.1 and 1 J/cm^2 for GBM39, 10 mW/cm^2, bottom illumination). (n > 3, *P < 0.05, **P < 0.01, ***P < 0.001.

Studies by Martins *et al.,* Coincotta *et al.,* and Kessel showed that PDT directed against both lysosomes and mitochondria could enhance the overall efficacy of photo-killing of malignant human cells, murine hepatoma cells and sarcoma [295-299]. Some of the earlier studies utilized different types of photosensitizers for lysosomal targeting (*e.g.*, NPe6, EtNBs) and mitochondrial targeting (*e.g.*, VP), and thus require different wavelengths of light for PDT activation (i.e., NPe6, λ_{max} at 630nm; EtNBs, λ_{max} at 652 nm; VP λ_{max} at 690 nm). While PDT with photosensitizers accumulating in mitochondria leads to loss of $\Delta\Psi m$ and the release of pro-apoptotic mediators (*e.g.*, cytochrome c), light activation of photosensitizers that localizes in lysosomes could induce cell death *via* the release of proteolytic lysosomal enzymes [300]. Rizvi et al. have shown that 690 nm light action of Visudyne® and lipid-anchored Liposomal VP enhances PDT outcomes *via* multi-organelle targeting [299]. Similarly, here, we showed that single wavelength (i.e., 690 nm) light activation of both free VP and 16:0 Lyso PC-VP, which target mitochondria and lysosomes, respectively, could achieve a significant reduction in viability at 72.6±5.1%, compared to the modest viability reduction achieved by VP-PDT (43.8±1.8%) or 16:0 Lyso PC-VP-PDT (30.9±6.9%) (**Figure 5.10e**). Similarly, PDT using a mixture of VP and 16:0 Lyso PC-VP significantly reduced the viability of GBM39 cells by ~80%, compared to that using free VP (15.7±11.9% viability reduction) or 16:0 Lyso PC-VP (58.9±6.9% viability reduction) alone (**Figure 5.10f**). In contrast to that observed in U87 and U251 cell lines, 16:0 Lyso PC-VP was found to be more phototoxic compared to free VP in GBM39 cells at a fluence of 0.1 J/cm^2 (**Figure 5.10f**). Thus, further mechanistic investigations into the cell/patient line-dependent phototoxicity of PSBMs are needed. We speculate

that GBM39 cells showed resistance to free VP effect could be due to the activation of pro-survival mitophagy to maintain cell homeostasis. Thus, by compromising lysosomal function, as done using 16:0 Lyso PC-VP, GBM39 cells become more sensitive to photodamage triggered by VP-PDT. Martins and others have already showed this concept [295]. At a higher fluence of 1.0 J/cm^2, both 16:0 Lyso PC-VP and free VP led to GBM39 killing of approximately 80%, while the combination killed virtually 100% of the GBM39 cells. While the combinations of free VP and 16:0 Lyso PC-VP led to a greater decrease in cell viability compared to monotherapy, a synergistic effect (Two-way ANOVA, interaction *P* value < 0.0001, GraphPad Prism) was only seen within the GBM39 cells at 1.0 J/cm^2. A follow up full dose–response matrix study is required to identify and quantify synergistic, additive, and antagonistic dose regions. Additional animal research is also warranted to examine the benefits of combining 16:0 Lyso PC-VP and free VP to enhance the overall PDT efficacy.

5.4 Conclusion

In this study, we synthesized a panel of VP-based PSBMs with different molecular weights and physiochemical properties. We systematically analyzed how different classes of biomolecules (i.e., lipid-, PEG-, and antibody-based) influence the physical, photochemical, and biological properties of the VP photosensitizers. The simple and reproducible formulation strategies did not alter the Q-band of VP for PDT using 690 nm light activation. The instability of free VP in physiologically relevant media led to a complete fluorescence quenching. Conjugation of VP to 16:0 Lyso PC or DSPE-PEG slightly improved VP's fluorescence emission by up to 20%. Static quenching of VP molecules on cetuximab was expected, and could be de-quenched upon lysosomal

proteolysis of Cetuximab-VP for PDT, confirming previously findings [276, 278]. For all PSBMs and free VP, a strong correlation between the degree of photoactivity and singlet oxygen yield was observed in a cell-free system. However, no correlation was found between the evaluated physicochemical properties and the photodynamic therapeutic index of PSBMs in two GBM cell lines (U87, U251).

The uptake kinetics and subcellular localization of PSBMs were found to be the more critical factors for effective PDT and fluorescence imaging. Despite lower singlet oxygen production, the 16:0 Lyso PC-VP exhibited enhanced delivery of VP into GBM cells, compared to DSPE-PEG and Cetuximab-VP, and could be visualized by fluorescence imaging. While the clathrin-mediated endocytosis pathway and lysosomal proteolysis mechanism of Cetuximab-VP in cancer cells have been well-established by us and others, here, we present the new evidence that proteolyzed Cetuximab-VP co-localizes to mitochondria to efficiently induce mitochondrial membrane ($\Delta\Psi m$) depolarization upon light activation in GBM cells. Light activation of 16:0 Lyso PC-VP or DSPE-PEG-VP did not induce $\Delta\Psi m$ depolarization. This can be explained by the localization of 16:0 Lyso PC-VP in lysosomes, as well as the heterogeneous and negligible uptake of DSPE-PEG-VP in GBM cells. Our findings suggest that engineering PSBM for effective PDT is enabled by close examination of cellular trafficking and subcellular localization in order to predict their effectiveness. Importantly, it is apparent that no single parameter is predictive. Compared to PSBMs, free VP was found to be a more potent PDT agent *in vitro* due to its higher cellular uptake and mitochondrial incorporation, which leads to a pronounced mitochondrial oxidative stress with apoptosis activation.

It is well accepted that subcellular localization of the photosensitizer plays a significant role in the type of cell death mechanism that predominates. Employing different types of photosensitizers or functionalizing photosensitizers with targeting moieties to target one or multiple subcellular organelles (*e.g.*, mitochondria, lysosome, endoplasmic reticulum, golgi, plasma membrane) have also been reported [296, 297]. Here, we verified that 16:0 Lyso PC redirects VP to lysosomes. More importantly, we demonstrated that single wavelength light activation of both free VP and 16:0 Lyso PC-VP targeting multiple subcellular organelles is a superior approach compared to using free VP or 16:0 Lyso PC-VP alone. Above insights of the molecular and cytotoxic mechanisms of PSBMs are critical to inform the design, prediction and evaluation of more sophisticated photo-nanomedicine for glioma PDT and imaging.

In summary, our results reveal the variable trafficking and cytotoxicity of clinically relevant PSBMs for PDT, providing important insights into methods of PSBM evaluation as well as strategies to select PSBMs based on cellular uptake, subcellular localization, and cytotoxic mechanisms. While biologically informed combinations of PSBMs and free-form photosensitizers may lead to enhanced therapeutic effects, the cellular uptake of PSBMs need to be enhanced to fully exploit the dual targeting of organelles. **Chapter 6** will discuss the positive and the negative impacts of lipids (i.e., liposomes, lipid nanoparticle) on drug delivery, and highlight the numerous parameters that need to be considered for liposome design.

Chapter 6. Immunological and Toxicological Considerations for Liposome Use[4]

6.1 Introduction

Liposomes are vesicular structures composed of one or more concentric lipid bilayers surrounding an aqueous cavity [301-303]. The bilayers are predominantly composed of phospholipids, where the polar head groups interface with the outer and inner aqueous phases and the hydrophilic tails are sequestered within the bilayer [303]. Since their discovery by Alec Bangham in the 1960s [304, 305], liposomes have been studied extensively as drug delivery vehicles due to their capacity to load both hydrophilic and hydrophobic agents, as well as their high biocompatibility and tunable size, charge, and surface properties [301-303]. Liposomal encapsulated drugs first reached the clinic in 1995 with the FDA-approval of Doxil® (Liposomal doxorubicin) for the treatment of AIDS-related Kaposi's sarcoma, and Doxil® was later approved to treat ovarian cancer, and multiple myeloma [306]. Since the FDA approval of Doxil®, numerous liposomal formulations have been employed in the clinic for a wide array of applications, including cancer therapeutics, fungal disease treatment, analgesics, PDT, and viral vaccine delivery [190, 246]. However, despite the increasing prominence of liposomal drugs in the clinic, there is still limited knowledge regarding their toxicological effects on healthy cells and tissues, as well as the immunological responses they can elicit.

4 This chapter was adapted (modified) from Inglut C.T., et al., "Immunological and Toxicological Considerations for the Design of Liposomes". Nanomaterials 2020, 10(2), 190. No special permission is required to reuse this article published by MDPI under the terms and conditions of the Creative Commons Attribution (CC BY) license (http://creativecommons.org/licenses/by/4.0/).

Phospholipids, the primary building blocks of liposomes, are amphipathic molecules, meaning they have a hydrophilic region (e.g., polar phosphate head) and a hydrophobic section (e.g., non-polar fatty acid tail). When hydrated in an aqueous solution under artificial conditions, phospholipids spontaneously organize into liposomes due to their thermodynamic phase properties and self-assembling characteristics [307]. The physio-biochemical characteristics of liposomes can be modified by altering the types and ratios of phospholipids, as well as incorporating cholesterol into the bilayer and decorating the liposomal surface with PEG. These modifications can have drastic effects on healthy cells and tissues, as well as activate or suppress the immune system. These complex interactions, therefore, have immense implications for the clinical use of liposomal formulations and will be discussed in depth later in this review. Extensive research has been done to develop a variety of techniques to achieve optimized liposome formation and drug loading. Incorporating therapeutic agents into liposomes can be achieved either during liposome formation (e.g., passive loading) or after liposome formation (e.g., active loading). Passive loading can be further divided into three categories: mechanical dispersion methods, solvent dispersion methods, and detergent removal methods [301, 308, 309]. Alternatively, active loading can be accomplished by establishing a pH gradient, causing the unionized drugs that penetrate the lipid bilayer to become ionized due to the low pH within the liposome, resulting in entrapment [310, 311]. FDA approval has been granted for both passively loaded liposomal agents (e.g., Visudyne® and AmBisome®) and actively loaded liposomal agents (e.g., Doxil®, Myocet®, and Onivyde®) [312]. Most of the clinically used liposome-based products are

administered by intravenous (IV) injection, though some are also given by intramuscular injection (e.g., Inflexal® V and Epaxal®), by epidural injection (e.g., DepoDur™), or by intrathecal injection (e.g., Depocyt®) [246].

Liposomes are particularly useful for delivering hydrophobic agents, which otherwise have poor solubility in aqueous solutions and limited bioavailability [24, 25]. VP (also known as benzoporphyrin derivative), for example, is a hydrophobic photosensitizer that is used for PDT, a light-based therapeutic modality. While VP self-aggregates in aqueous solutions, Liposomal VP (marketed as Visudyne®) has improved solubility for intravenous administration and is FDA-approved to treat wet age-related macular degeneration [145, 191]. To date, Visudyne® is being evaluated in multiple clinical trials for PDT of cancer due in part to its favorable pharmacokinetic profiles (i.e., rapid clearance), leading to low phototoxic skin reactions [313]. In addition to improving drug solubility, liposomes have a variety of other advantages as drug delivery vehicles, such as high biocompatibility, modifiable physicochemical and biophysical properties, and protection of large drug payloads from degradation, inactivation, and dilution in circulation [302, 314]. Liposomes are also being engineered to deliver drugs to parts of the body that are exceptionally difficult to access (e.g., central nervous system) [315]. Intravenously-injected liposomal drug formulations provide the additional benefit of preferentially accumulating in tumor tissues due to the enhanced permeability and retention effect, thereby incorporating an inherent mechanism for passive tumor targeting [27, 28].

Another key advantage is that liposomal encapsulation of drugs increases the therapeutic index by decreasing the accumulation of drugs in organs and other healthy

tissues [26-28]. For example, anthracyclines, a group of potent chemotherapeutics, can induce severe cardiotoxicities, including cardiomyopathy and congestive heart failure. This limits the range of doses that can be safely administered. Using liposomes to deliver doxorubicin, one of the most widely used and most cardiotoxic anthracyclines, avoids drug accumulation in myocardial tissues, improving the overall response rates and attenuating the risk of cardiotoxicity [316, 317]. For instance, liposomal encapsulation of doxorubicin increased the median lethal dose (LD_{50}) by approximately 2-fold in mice (32 vs. 17 mg/kg) and 1.5-fold in beagle dogs (2.25 vs. 1.5 mg/kg) compared to free-form doxorubicin [318]. Similarly, liposomal encapsulation of irinotecan (i.e., Onivyde®), another chemotherapeutic agent used in multiple solid organ cancers, enables improved pharmacokinetics, increased maximum tolerable dose, and protection of irinotecan from hydrolysis-mediated inactivation in circulation [319]. Though liposomes have demonstrated the ability to reduce the accumulation of drugs in some organs and healthy tissues, they tend to reroute them to other sites. One meta-analysis concluded that on average, less than 1 % of nanoparticles end up delivered to solid tumors [320]. This underscores a key problem for liposomal agents, which largely accumulate in organs associated with the mononuclear phagocyte system (MPS), where they can impair liver function by attenuating phagocytic capacity and depleting macrophages [321].

While liposomes are used to reduce systemic toxicity from the encapsulated agents, the liposome itself can impart toxicity to normal tissues and elicit an immune response (**Figure 6.1**). Cationic liposomes, which are largely studied for gene delivery, are known to elicit toxicity in macrophages, macrophage-like cells, and monocyte-like

cells, as well as decrease the secretion of important immuno-modulators [322-324]. Liposomes can also trigger immunogenic responses, though the nature and degree of these responses can vary depending on several properties, including surface charge, size, and pegylation [325-327]. Therefore, despite the many advantages of using liposomes for drug delivery, there are also important drawbacks that must be considered, as they present real challenges for clinical translation. This mini-review will explore these limitations in-depth, with an emphasis on toxicities and unfavorable interactions with the immune system, to shed light on some of the lesser-known areas where liposomes have room for improvement as drug delivery vehicles.

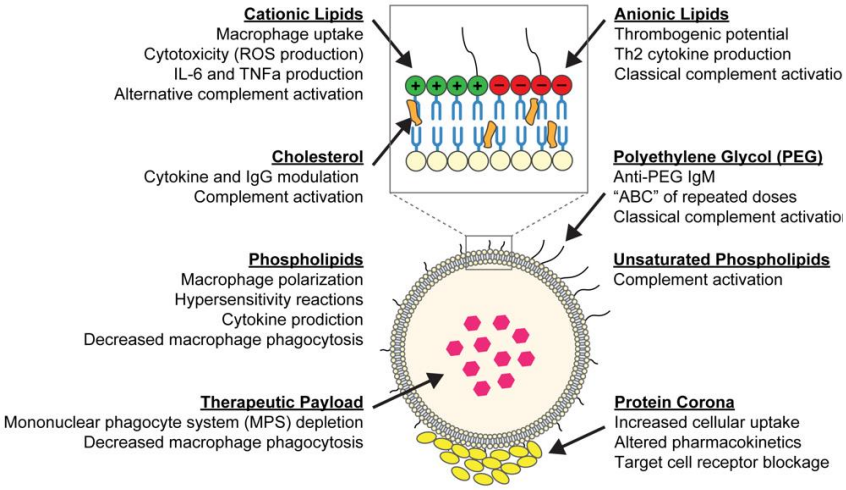

Figure 7.1 Schematic of a Liposome and its Common Building Blocks. The Liposomal bilayer is composed of phospholipids (cationic or anionic) and cholesterol, and the surface can be decorated with polyethylene glycol (PEG). Hydrophilic drugs can be entrapped within the aqueous core, while hydrophobic drugs can be loaded into the lipid bilayer. Once injected into the bloodstream, a protein corona, comprised largely of apolipoproteins, immunoglobulins, and complement proteins, is formed on the liposome surface. The protein corona, which is impacted by the Liposomal surface chemistry, governs liposome-cell interactions. The immunological and toxicological effects caused by each liposome component, imparted on cells throughout the body, are summarized throughout the diagram.

6.2 Toxicological Evaluation of Liposomes and Their Building Blocks

Liposomes are typically composed of numerous building blocks, including phospholipids, cholesterol, and PEG, each impacting their functionality. Phospholipids, the main component of liposomes, are diverse molecules with a variety of isomers. The most commonly used phospholipids for liposome formation include lecithins from egg and soy, as well as sphingomyelins [328]. Common variations to the phospholipid hydrophobic acyl (fatty acid) tail include the degree of saturation (i.e. saturated vs unsaturated) and length, which can impact the oxidizing properties and drug release profiles of liposomes [329]. For example, Luo et al. showed that PDT-mediated oxidation of unsaturated lipids (i.e., 1,2-dioleoyl-sn-glycero-3-phosphocholine, or DOPC, 18:1 PC) in the liposomal bilayer could facilitate the controlled release of doxorubicin. Increasing the concentration of DOPC in liposomes from 0% to 10% enhanced the release rate of doxorubicin from liposomes by up to 10-fold upon light-activation of photosensitizers [330]. Different phospholipid head groups, with some of the most prevalent being phosphatidylcholine (PC), phosphatidylserine (PS) and phosphatidylethanolamine (PE), can alter the surface charge and the polymorphic phase (i.e., the type of assembly) in an aqueous medium [331]. Although PC is a neutral molecule, it has a positively charged choline group attached to a negatively charged phosphate group, making it a zwitterionic molecule. Alternatively, PS contains a negatively charged phosphate group attached to the serine group, giving it an overall negative charge, mainly due to the low (2.2-3.6) pKa of the carboxyl group within the serine [332]. More recently, there is an increased research interest in formulations of lipid-drug (or photosensitizer) conjugates to improve the

pharmacokinetics and therapeutic index of liposomal therapeutics [196, 333, 334]. Similarly, the incorporation of PEG, a polymeric steric stabilizer, is widely used to increase the blood circulation time of liposomal formulations [29, 284]. The addition of PEG into Liposomal doxorubicin extended the terminal half-life from 16.4 hours to 77 hours in patients with metastatic breast cancer [335, 336]. Once liposomes enter the bloodstream, plasma proteins interact with and adsorb onto the liposome surface. It has been previously shown that the liposomal surface chemistry (e.g., charge and pegylation) impacts the blood protein adsorption (known as the “protein corona"), which influences how liposomes interact with healthy and diseased cells [337-339]. Protein adsorption occurs due to an advantageous increase in entropy, resulting in a decrease in Gibbs free energy (ΔGabs) [340]. A comprehensive study by Hadjidemetriou et al. examined the in vitro and in vivo protein corona formation on three different types of liposomes, including pegylated liposomes, non-pegylated liposomes, and monoclonal antibody-conjugated liposomes [341]. In this study, pegylated liposomes had the lowest protein adsorption at ~100,00 μg protein/μM lipid, while non-pegylated liposomes had double the amount of protein adsorption. However, all liposomes had relatively consistent protein corona compositions, with the most abundant bound proteins being apolipoproteins, immunoglobulins, and complement proteins.

While the topic of nanoparticle-protein adsorption is an active field of study [340-343], several studies have evaluated the toxicity and side effects of liposomes. Papahadjopoulos et al. first reported the cytotoxicity of liposomes in healthy mouse fibroblast L929 cells in 1973. They discovered that incorporation of 3% or 10% of

lysophosphatidylcholine (lysolecithin, lysoPC) into liposomes increases cellular uptake (i.e., polykaryocytosis) by ~7%. The number of viable L929 cells after liposomal incubation was significantly lowered from 97% to less than 37% [344]. Similarly, Pagano et al. showed that extensive accumulation of egg yolk lecithin vesicles in Chinese hamster lung fibroblast V79 cells results in considerable cell death [345]. One of the first studies evaluating liposomal toxicity in vivo was carried out by Adams and colleagues in 1977 [346]. In this study, five different types of liposomes with varying net surface charges were synthesized and injected into the mouse brain. Results showed that liposomes containing 9 mol% of dicetyl phosphate (net negative charge) were the most toxic, causing epileptic seizures and rapid death in animals. Injection of dicetyl phosphate alone resulted in the death of all mice within one hour. Brain sections stained with haematoxylin and eosin (H&E) revealed tissue necrosis, nerve damage, and loss of Nissl substance. Similarly, liposomes containing 9 mol% of stearylamine (net positive charge) caused widespread brain damage and respiratory failure. Alternatively, liposomes containing 9 mol% of phosphatidic acid (net negative charge) were well tolerated with only small hemorrhages and necrosis limited to the injection site. The least toxic liposomes were those composed of 45 mol% of lecithin or dipalmitoyl lecithin (neutral charge), which resulted in minimal toxic reactions and morphological changes, even after 3 repeated doses. While liposomes are typically considered pharmacologically inactive with minimal toxicity [301, 314], their toxicity is tightly related to the type of model, exposure time, dose, and/or surface properties. For example, Shi et al. showed the LD_{50} using F98 glioma cells was 6.07 μM for empty DPPC-based cationic liposomes while DSPC-based anionic liposomes had an LC_{50} >

509 μM. Within an intracranial F98 glioma rat model, carboplatin loaded cationic pegylated liposomes resulted in a median survival time of 29 days, while anionic pegylated liposomes had a median survival of 49.5 days [347]. Similarly, Fan et al. showed that cationic liposomes incubated with bone marrow derived dendritic cells had an LC_{50} around 0.2 mg/ml, while ovalbumin-loaded anionic liposomes had an LC_{50} > 4 mg/ml [348]. In *Section 6.2*, we examine some of the different mechanisms through which liposomes induce cellular toxicity.

As liposomes rose in popularity, many research groups began to modify the phospholipid structure and test different surface chemistries [349, 350]. Studies in the early 1990s by Parnham et al. [351] and Lappalainen et al. [352] examined and suggested different assays for the screening of liposomal toxicity. Some of these in vitro viability and morphology assays include MTT, 3H thymidine uptake, and lactate dehydrogenase. It was shown that 40 μM of liposomes containing dimethyldioctadecyl ammonium bromide (18:0) and dioleoylphosphatidylethanolamine (DOPE, 18:1 PE) reduce the viability of human cervical squamous cell carcinoma cells by 50% [352]. Liposomes containing N-(2,3-Dioleoyloxy-1-propyl)trimethylammonium methyl sulfate (DOTAP, 18:1 TAP) at a concentration of 10 μM or 40 μM only had minor effects on the cancer cells [352]. There is also evidence demonstrating anionic lipids have a higher thrombogenic potential [353]. Anionic liposomes have been shown to induce platelet aggregation in guinea pigs [354], as well as blood cell aggregation in mice, which became temporally trapped in lung capillaries [355]. To ensure that intravenous injection of liposomes does not induce pro-aggregatory effects or pharmacodynamic changes (e.g. necrosis, edema, loss of tissue) at the site of entry,

appropriate platelet aggregation assays and local tolerance studies should be performed. The mechanical damage during injection should be accounted for as well, and distinguished from any toxicological effects [351]. In April 2018, the FDA published updated guideline for liposome products in industry [356]. Although explicit details are not specified, critical parameters ranging from physicochemical characterization (e.g., pegylation, net charge, leakage rate during shelf storage) to pharmacokinetic profiles are established. Radiolabeled mass-balance excretion and metabolism studies are required, as they reveal quantitative connections to toxicity, and provide information on the in vivo activity of new chemical entities including pharmacology and pharmacokinetics [357].

6.2.1 Toxicity of Cationic Liposomes

Cationic liposomes have been studied extensively to enhance the stability and delivery of negatively charged nucleic acid therapeutics [358-363], and their toxicities and side effects have also been carefully examined [322-324, 364-371]. For example, Filion and Phillips studied the toxicity and immunomodulation of seven different DOPE (18:1 PE)-based cationic liposomes that range from +15.0 to +42.9 mV [322]. In this comprehensive study, liposomes containing DOTAP, dimethyldioctadecyl ammonium bromide, 1,2-dimyristoyl-3-trimethylammonium-propane (DMTAP, 14:0 TAP), 1,2-dipalmitoyl-3-trimethylammonium-propane (DPTAP, 16:0 TAP), or 1,2-stearoyl-3-trimethylammonium-propane (DSTAP, 18:0 TAP) were highly toxic to macrophages and monocyte-like U937 cells, but not to resting or activated T lymphocytes. It was speculated that these cationic liposomes were non-toxic to T cells due, in part, to minimal uptake. Additionally, the cytotoxicity of cationic liposomes

increased at higher zeta potentials. Dimethyldioctadecyl ammonium bromide -containing liposomes (+40.0 ± 9.0 mV) were the most toxic to macrophages, with a 50% effective dose (ED_{50}) <10 nmol/ml, while DSTAP-containing liposomes (+15.0 ± 6.3 mV) were the least toxic, with an ED_{50} >1000 nmol/ml. Loading plasmid DNA into liposomes significantly reduced the zeta potential, but did not decrease their cytotoxicity [322]. The cytotoxicity of the liposomes was significantly lowered by incorporating 10 mol% of 1,2-dipalmitoyl-sn-glycero-3-phosphoethanolamine (DPPE, 16:0 PE)-PEG2000 or replacing DOPE with 1,2-dipalmitoyl-sn-glycero-3-phosphocholine (DPPC, 16:0 PC). These modifications reduced the binding and endocytosis of liposomes by ~96% by macrophages and hindered their ability to destabilize the endosomal membrane [322]. In addition to inducing cytotoxicity in macrophages, the cationic liposomes also mitigated the secretion of nitric oxide and tumor necrosis factor-α, which are important signaling molecules for triggering non-specific defense against pathogens and enhancing T and B lymphocyte responsiveness [322].

Similarly, Takano et al. and Aramaki et al. showed that the intracellular uptake of cationic liposomes (~42 mV) in mouse macrophage-like cell line RAW264.7 correlates with the degree of apoptosis and the generation of ROS [323, 324]. However, the incorporation of 7.5% and 10% DPPE-PEG into liposomes reduced their uptake by ~30-45-fold and increased cell viability by ~20-38%. Inclusion of DPPE-PEG also led to a decrease in ROS production [323], which diminished the toxic effects of liposomes [324]. Soenen et al. showed that adverse effects from cationic liposomes can be reduced by using ROS scavengers or a calcium channel blocker in 3T3 fibroblasts [372]. Based

on these studies and many others [322, 365-367, 369-371, 373], cytotoxicity could be readily detected in a wide range of cells upon increasing the zeta potential values of liposomes beyond ~30 mV, in a charge dependent manner. In general, cationic liposomes are uptaken by phagocytic cells to a greater extent and induce the formulation of ROS, which damages organelles (e.g., mitochondria), and promotes higher intracellular Na+ levels, compared to neutral and negatively charged liposomes [323, 324, 371-375].

Using animal models, Kedmi et al. showed that intravenous injection of cationic liposomes (+54.3 ± 6.1 mV) containing DOTAP-induced hepatotoxicity and pro-inflammatory responses [365]. The cationic liposomes significantly reduced the body weight of C57BL/6 mice by up to 5.5% and increased liver enzymes in serum by 3-6-fold compared to neutral and negatively charged (−59.2 ± 4.9 mV) liposomes. Cationic liposomes also increased the amount of Th1 and Th17 cytokines by 10-24 fold at 2 hours post-injection [365]. In rats, Knudsen and colleagues demonstrated that the administration of DOTAP/CHOL liposomes (+53 ± 2 mV) led to an upregulation of oxidative stress response gene and the DNA repair enzyme in the liver, as well as increased DNA strand breaks in the lungs [366]. While cationic liposomes are promising vehicles for gene delivery, understanding their toxicities to immune cells and regulation of inflammatory responses are critical for improving therapeutic benefits and avoiding immune toxicity.

6.2.2 Interactions with the Mononuclear Phagocyte System

While liposomes improve the pharmacokinetic profiles of therapeutics, they also redirect the therapeutic payloads to the MPS (previously known as the

reticuloendothelial system, RES), [376-378]. The MPS is a collection of phagocytic cells (e.g., progenitor, monocytes and macrophages) located within the bone marrow, lymph nodes, spleen, and liver. The MPS is responsible for the removal of antigens from the body, and is the main site of liposome accumulation [379, 380]. Several rodent studies have shown that Doxil® accumulates within the liver and spleen (e.g., the two major organs of the MPS [376]) to a greater extent than other organs shortly after intravenous injections [381-385]. In cynomolgus monkeys, Kimelberg et al. found that liposomal encapsulation of [^{3}H]MTX caused a 160-fold increase in [3H]MTX uptake by the spleen compared to the free-form [^{3}H]MTX [378]. It has been observed by many researchers that the redirection of liposomal chemotherapy to the MPS induces toxicity and depletion of immune cells, especially the Kupffer cells in the liver [321, 386-391]. To study the impact of liposomes on the phagocytic function of MPS cells in mice, Allen et al. tested several compositions of egg PC-CHOL liposomes [386]. Injection (IV) of larger, multilamellar liposomes (synthesized using 200-450 nm filters) significantly decreased the phagocytic index of the liver by approximately 50% in mice, compared to using small unilamellar liposomes. The phagocytic index did not recover until 3 weeks post-injection, and further doses of liposomal injections lead to accumulated in the spleen. Multiple injections caused a significant decrease in the phagocytic index of the spleen and a 2.5-fold increase in the spleen weight. The function and weight of the spleen did not recover until 8 days after the last liposome injection.

Several groups have also studied the impact of drug-containing liposomes on liver macrophages. Daemen et al. showed that intravenous injection of non-pegylated, short-

circulating Liposomal doxorubicin in rats reduced the number and phagocytic capacity of liver macrophages by up to 85-90%, compared to placebo liposomes [321]. The phagocytic capacity of liver macrophages was impaired for 8 days, and full recovery took 2 weeks. A follow-up study examined the effects of long-circulating Liposomal doxorubicin containing ~4.8 mol% PE-PEG on the phagocytic activity of macrophages [391]. The pegylated liposomes reduced the phagocytic capacity and number of liver macrophages by 63% at 72 hours after injection. Compared to non-pegylated liposomes, pegylated liposomes delayed the cytotoxic effects on liver macrophages by 24 hours and modestly reduced the depletion of macrophage by 7%. While pegylation of liposomes reduces the blood protein adsorption and increases blood circulation time, the ultimate impact of pegylated and non-pegylated liposomes on macrophages and liver function was similar.

Research groups have also shown that within the tumor microenvironment, liposomes can polarize tumor-associated macrophages (TAMs) [392-394]. The reprogramming of classically activated (M1) TAMs, which have a role in eradicating tumor cells in their early stages, to alternatively activated M2-like TAMs have been shown to promote tumor growth and metastasis, as shown in **Figure 6.2** [395, 396]. In an orthotopic ovarian carcinoma (ID8- vascular endothelial growth factor -GFP) mouse model, La-Beck et al. showed that empty liposomes increased tumor volume by over 3-fold and doubled the number of metastatic sites, compared to the vehicle control [392]. Similarly, Sabnani et al. and Rajan et al. found that compared to the vehicle control (e.g., 5% dextrose solution, saline), empty pegylated liposomes accelerated the growth of subcutaneous TC-1 tumors in mice [394, 397]. The accelerated tumor growth

was attributed to diminished macrophage function and number of tumor-specific T cells [397], as well as a 66% decrease in M1-TAMs and a 100% increase in M2-TAMs [394]. Based on these results, strategies to overcome immunosuppression and tumor progression triggered by liposomes may potentially improve the efficacy of some liposomal anticancer drugs. New insights into the underlying molecular mechanisms may yield the key to designing new liposome-based immunotherapies.

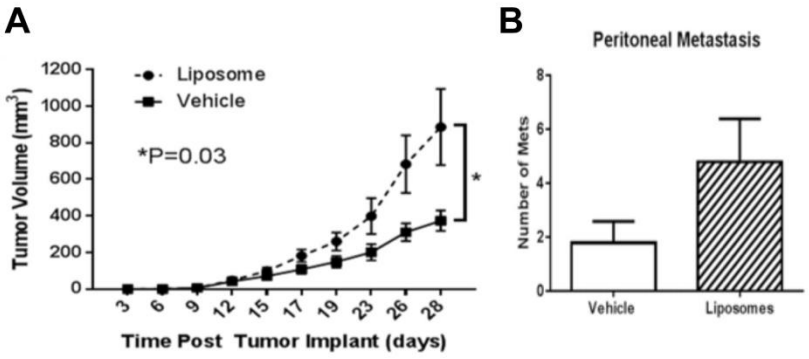

Figure 7.2 Intravenously Injected Liposomes Impact Cancer Progression. Liposomal polarization of classically activated M1 tumor associated macrophages (TAMs) to M2-like TAMs can result in carrier-induced immunosuppression and accelerated tumor development. Compared to vehicle control, empty (placebo) liposomes (**a**) accelerated tumor growth in a TC-1 subcutaneous mouse model and (**b**) increased the number of metastatic sites in an orthotopically implanted ID8-VEGF-GFP ovarian carcinoma mouse model on day 36. *Reprinted from Inglut C.T., et al. and La-Beck et al., Harnessing Liposome Interactions With the Immune System for the Next Breakthrough in Cancer Drug Delivery. Front. Pharmacol., 12 March 2019. (No permission required, under the Creative Commons Attribution License, to use, distribution or reproduction in other forums.)*

6.2.3 Effect of Cholesterol Content on the Toxicity of Liposomes

Cholesterol is commonly used to alter the mechanical properties and functionality of liposomes [398-400]. Cholesterol improves the stability and drug entrapment efficacy of liposomes by enabling more dense assembly of phospholipids [398-403]. Smaby et al. demonstrated that cholesterol condenses the lipids (e.g. from 63 to 44 Å2/molecule; 16:0-18:1 PC liposomes), thereby increasing the compressibility of

liposomes from 123 to 401 mN/m [404]. The concentration of cholesterol can also impact the surface charge and permeability of liposomes [401]. Incorporation of 50 mol% cholesterol into 1,2-distearoyl-sn-glycero-3-phosphocholine (DSPC, 18:0 PC) liposomes reduced the zeta potential from 2 to -5.5 mV [405]. The presence of cholesterol also reduced the permeability coefficients of phospholipid vesicles to small molecules and ions [406]. A previous study showed that cholesterol prevents the aggregation and fusion of liposomes, leading to enhanced penetration into the skin [403]. In additional to structural stability and drug efflux related studies, several groups have examined the toxicity and immunogenicity of cholesterol. Adams et al. showed that injection of 5-10 mg of cholesterol into the mouse brain resulted in mild signs of edema and loss of internal neuronal structures [346]. Others have shown that free-form cholesterol induces macrophage apoptosis via the stiffening of the endoplasmic reticulum [407] and promotes the production of tumor necrosis factor-α and interleukin 6 (IL-6) [408]. Roerdink et al. showed that incorporation of 50 mol% of cholesterol into DSPC-based liposomes decreased their liver accumulation (from 70% to less than 40%) and extended the blood circulation half-life by 3-fold in rats [409]. It has also been shown that cholesterol-containing liposomes decrease macrophage uptake and immunoglobulin G response in mice [410]. Similarly, incorporation of high levels (43 mol%) of cholesterol in ovalbumin-liposomes significantly reduced immunoglobulin G response by 10-fold in mice [411]. In a Li 210 leukemia mouse model, Ganapathi et al. showed that cytarabine-loaded liposomes containing 50 mol% of cholesterol increased animal survival by up to ~20%, compared to using cytarabine-loaded liposomes containing 10 mol% of cholesterol or free-form cytarabine [412]. However,

it is unclear if this enhanced cancer killing is due to increased cellular uptake of liposomes or an increase in the sustained release of cytarabine from cholesterol-containing liposomes. While the incorporation of cholesterol into liposomes mitigates macrophage uptake and antibody production, other studies have shown that cholesterol could activate the immune system by promoting interactions with C3, a protein associated with the complement system [413-415]. This is discussed extensively in *Section 6.3.2.*

6.3 Activation of the Immune System

Biomaterials introduced into the body can initiate immune responses in the host tissue. As shown in previous work, host defense mechanisms and inflammatory responses to biomaterials are known to be activated by the complement response [416]. The products from complement response activation may assist neutrophil aggregation and migration towards inflammatory sites [416]. Earlier research suggests that PEG-based hydrogels cause increased inflammatory responses compared to a silicone-based hydrogels. This change was visualized through increased IL-1β expression in the host tissues after implantation of a PEG-based hydrogel [417]. It is also thought that complement activation can induce a foreign body reaction [416]. During this process, host inflammatory cells and foreign body giant cells are activated to destroy the implanted material. Previous studies have demonstrated that thick macrophage capsules accumulate on PEG-based hydrogels as a result of the FBR when compared to other hydrogels lacking PEG [417].

Liposomes, like other nanoparticles used in drug delivery, interact with proteins in the body to trigger innate immune system responses [418-420]. Once liposomes have been administered to the patient, circulating proteins can adsorb to the surface of the liposome, thereby creating a protein corona unique to the characteristics of the liposome. The protein corona can then induce the activation or suppression of various immune responses [421]. Particularly, liposomes interact with complement proteins to activate the complement cascade and increase the body's response to antigens [418, 421, 422]. The incorporation of PEG into liposomes has been shown to promote immunogenic responses via complement activation and the anti-PEG antibody production [37]. For these reasons, liposomes are being used as vaccine adjuvants to potentiate the immunological response to antigens. Antigen-liposomal complexes can increase and maintain exposure of the antigen in the lymph nodes, allowing for enhanced uptake by immature phagocytic antigen-presenting cells (e.g. macrophages and dendritic cells) [423-425]. A notable antigen-liposome adjuvant system, AS01, has been studied in multiple different disease clinical trials [426], and was FDA approved as a shingles vaccine (Shingrix) in 2017.

The liposomal surface charge and the size can impact the type and efficiency of the immune response. A study by Badiee et al. investigated the effects of the surface charge of recombinant rgp63-loaded liposomes on the immune response of mice with leishmania after subcutaneous injections. Neutral liposomes were found to promote a Th1 (e.g., interferon γ, IL-12) immune response more efficiently than positively charged liposomes. The largest IL-4, immunoglobulin Ga, and immunoglobulin G1 response were induced by positively charged liposomes. A Th2 (e.g. IL-5, IL-6, IL-10)

response, but not a Th1 immune response, was caused by liposomes with a negative surface charge [427]. In regards to liposome size, a follow-up study by Badiee et al. showed that 100 nm liposomes induce a Th2 response, while liposomes larger than 400 nm induce a Th1 response [428]. This was due, in part, to their altered pharmaceutics and intracellular trafficking. Similarly, Henriksen-Lacey et al. showed that intramuscularly injected ~200 nm CAF01 cationic liposomes induced the greatest IL-10 response in mice [429], while medium (500 nm) liposomes induced the largest interferon-γ and IL-1β response. The 200 nm and 1.5 μm liposomes were drained more rapidly by the lymph node, while the 500 nm liposomes were well retained at the site of injection [429].

6.3.1 Pro-Inflammatory Cytokine Production

Liposomal interactions with blood cells lead to cytokine production and the activation of the immune system [360, 365, 430, 431]. The activation of the complement cascade also promotes the secretion of cytokines from immune cells [432, 433]. This concept is well demonstrated in the first liposomal gene silencing clinical trial (NCT00882180). Liposomes were loaded with siRNAs that were chemically modified to minimize immunostimulation and administered intravenously. However, there was still a dose-dependent induction of proinflammatory cytokines. Cytokines, including IL-6, IP-10, granulocyte colony-stimulating factor, and tumor necrosis factor-α, peaked 6 hours post-injection. One of the largest liposome doses, 1.25 mg/kg, resulted in the most IL-6 present in the patients' blood (~9000 pg/mL). There was also a ~3-10 fold increase in Bb complement protein for patients who received a dose larger than 0.2 mg/kg [360]. Yamamoto et al. demonstrated that cytokine induction by HEPC-

based liposomes is comparable to that of a potent activator of monocyte and macrophages, lipopolysaccharides. Also, incubation of liposomes with human peripheral blood induced monocyte-derived cytokines (IL-6, IL-10, IL-1β, interferon-y and tumor necrosis factor-α) but not lymphocyte-derived cytokines (IL-2, IL-4 and IL-5). In the same study, it was shown that the size of liposomes directly affects the degree of cytokine release, in vitro, in a size-dependent manner. Liposomes with an 800 nm diameter induced the production of 6000 pg/mL of IL-1β, while 50 nm liposomes produced virtually none [430].

For gene delivery using liposome-DNA complexes, previous reports have shown that nonspecific cytokine production from toll-like receptor-9 positive immune cells occurs due to unmethylated CpG dinucleotides (CpG motifs) abundantly present in pDNA [434, 435]. Liposome-DNA complexes also induced the production of type I interferons, irrespective of the frequency of CpG motifs in DNA and the expression of toll-like receptor-9 [436]. However, a study conducted by Yasuda et al. showed that immune activation by liposome-DNA complexes is highly dependent on the type of cationic liposome. In murine macrophage-like cell line, RAW264.7, non-CpG containing Lipofectamine2000 liposomes (+35.1 mV) induced the largest cytokine production (500-900 pg/ml), while DOTMA/DOPE and DOTMA/CHOL liposomes (+32.7 mV) produced less than one-fifth of that amount [437]. Furthermore, Lipofectamine2000 liposomes containing non-CpG motif DNA induced interferon-β and IL-6 production by macrophages cultured from toll-like receptor-9 deficient mice [437]. These liposome-induced inflammatory responses are critical to consider for

clinical applications, as increased levels of cytokines can cause side effects (e.g., grade 1–2 chills/rigors, flu-like symptoms) [360, 438].

6.3.2 Recognition of Liposomes via Complement Activation

The complement system is a part of the innate immune system responsible for the recognition of foreign objects in the body [432]. It is composed of over 30 plasma proteins that interact with each other to opsonize (e.g., C3b) and clear liposomes, as well as induce a series of inflammatory responses by liberating anaphylatoxins (e.g., C3a, C4a, C5a) (**Figure 6.3**) [422, 432]. Early reports indicated that liposomes activate the alternative pathway via C3 binding and conversion, which is independent of antibody recognition. Cunningham et al. showed that C3 conversion occurs when cationic liposomes are incubated in serum from C1r-deficient and C2-deficient patients [414]. Liposomes without cationic lipids or with less than 20 mol% of cholesterol were unable to convert C3 in C2-deficient serum [414]. However, later reports show complement activation is dependent on the surface chemistry and composition of liposomes [439-441]. A study by Chonn and colleagues showed that liposomes containing 20 mol% of anionic lipids activated the classical pathway in a Ca(2+) dependent manner. Calcium is required in the classical pathway, as it is used for C1qr2s2 complex formation. Cationic liposomes activated the alternative pathway by reducing the C3-C9 levels in Ca(2+) depleted serum. In addition, liposomes containing unsaturated lipids or 45 mol% of cholesterol promoted complement protein interactions. In contrast, neutral liposomes, even at a high lipid concentration of 50 mM, did not activate the complement pathways [415]. Bradley et al. showed anionic liposomes can also activate the classical pathway in an antibody-independent manner via direct binding of C1q to the liposomal surface [441]. Liposome size, pegylation, and cholesterol content can also contribute to the degree and nature of complement activation. For example, studies have suggested that larger liposomes, over 200 nm in diameter, were associated with an increase in complement protein opsonization and alternative pathway

activation [442, 443]. Liposomes containing PEG typically induce IgM antibody production, followed by (classical) complement activation [37]. A study by Alving et al. showed a cholesterol dependent activation, with liposomes containing 73 mol% cholesterol promoting the greatest classical pathway activation [444]. While examining the hypersensitivity reactions (HSRs) induced by different components of Doxil®, Szebeni et al. demonstrated that negatively charged PEG-PE is a potent C protein activator, and the degree of complement activation correlates with HSRs [445]. When PEG-PE-based liposomes were incubated with human serum, there was a 2.5-4-fold increase in soluble complement S5b-9 (C5b-9), compared to HSPC-based liposomes which had no impact on complement activation [445]. Activation of C5b-9 following exposure to pegylated liposomes has been associated with development of HSR [446], which is discussed in the following section.

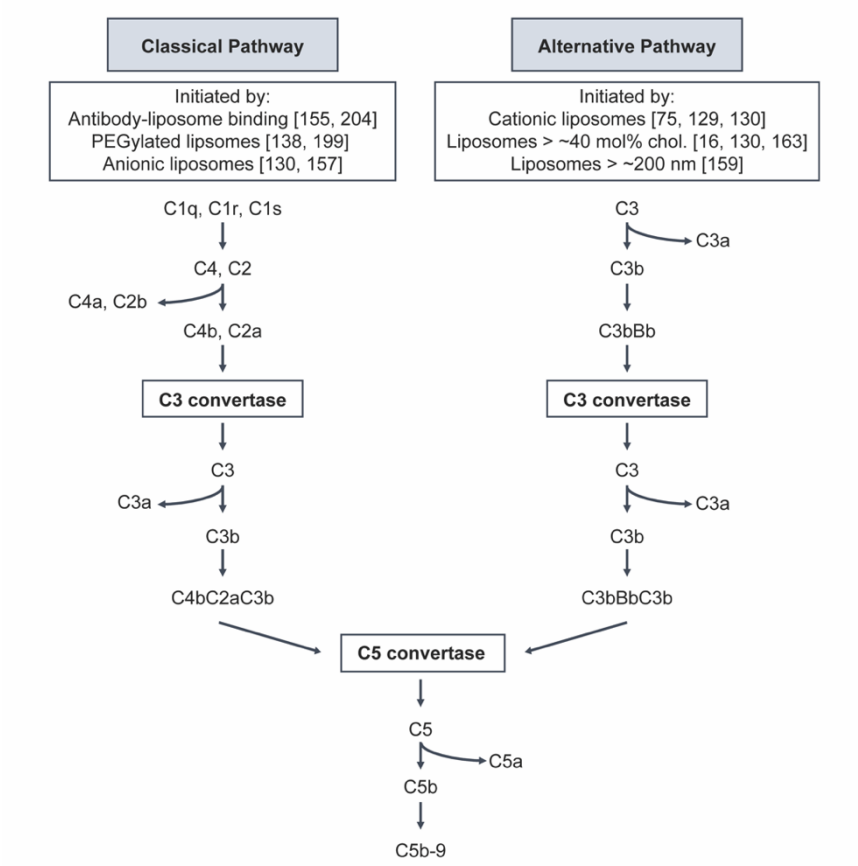

Figure 7.3 Schematic Overview of the Complement System Highlighting Two of the Main Activation Pathways (Classical vs. Alternative). Previous studies have shown that classical pathway activation is initiated by antibody-liposome binding, pegylated liposomes, and anionic liposomes. The alternative pathway can be initiated by cationic liposomes, liposomes containing more than 40 mol% cholesterol (Chol), and liposomes larger than 200 nm in diameter. During the complement cascade, C3b opsonin covalently binds to the surface of the liposome, marking it for removal by the MPS. The released anaphylatoxins (C3a, C4a, and C5a) prompt the activation of leukocytes.

6.3.3 Hypersensitivity Reactions

Liposomes have also been shown to induce HSR [447-454]. HSR are non-IgE-mediated pseudo-allergic immune responses, which usually develop immediately after intravenous infusion when the body is exposed to an antigen or liposomes [446]. While 6.8% of the 705 patients who received Doxil for refractory AIDS-related Kaposi's sarcoma experienced HSR with symptoms ranging from dyspnea and tachypnea to

hypotension and hypertension, the underlying causes remain unclear [454, 455], with some researchers attributing similar reactions to complement activation. [456, 457]. Later reports have shown HSR are correlated with PEG-induced complement activation, however high levels of C activation may be necessary, suggesting the involvement of other pathogenic factors [445, 446, 458]. This subset of HSR, known as C activation-related pseudoallergy, can be reduced by slowing the rate of infusion, diluting the Doxil dose, or premedicating with a corticosteroid [459]. In a 4-patient study, grade 3 HSR induced by Doxil occurred almost immediately after the start of infusion in all patients and treatment was stopped. Premedication with ranitidine and hydroxyzine prior to the resumption of Doxil infusion eliminated HSR in 3 of the 4 patients [450]. Similarly, data analysis performed by Chanan-Khan et al. showed, on average, 8% of people who received Doxil experienced HSR [446]. Additionally, 3% of refractory ovarian cancer patients who were pretreated with corticosteroids and antihistamines to minimize adverse reactions still experienced HSR. Chanan-Khan et al. further showed HSR occurrence can be as high as 45% for patients receiving Doxil. Within this Phase 1 clinical study, 92% of the patients who experienced HSR had significantly elevated Plasma SC5b-9 levels [446]. HSR have been suggested to be caused by the liposomal vehicle of Doxil rather than the encapsulated drug, as these reactions are not known to occur with standard doxorubicin [445, 446]. It should also be noted that other chemotherapies, such as Taxol (paclitaxel), which relies on a formulation vehicle, and carboplatin, are known to cause HSR [460, 461].

Using pig models, Szebeni et al. showed that pulmonary hypertension reactions are dependent on composition, size, and administration method of liposomes [449].

Large, neutral, multilamellar liposomes composed of 1,2-dimyristoyl-sn-glycero-3-phosphocholine (DMPC, 14:0 PC) and DSPC induced pulmonary hypertension, while smaller liposomes (< 200 nm) caused no hemodynamic changes [449]. An additional study by Szebeni et al. showed that highly negatively changed liposomes containing L-α-phosphatidylglycerol initiated CARPA to the greatest extent in pigs, suggesting that surface charge may also play a role [462]. Fülöp et al. showed a 300-600% increase in pulmonary arterial blood pressure after the infusion of pegylated Liposomal prednisolone sodium phosphate in pigs [448]. The risk of these side effects was reduced by using a slow infusion protocol (0.04 ml/kg/h) with a 3-step dose escalation [448]. It is now recommended that Doxil be administered at 1 mg/min to help minimize these adverse reactions [463]. Within a 2018 Nature Nanotechnology Perspective, authors suggested that the next steps for minimizing HSR and CARPA are identifying induced biomarkers and understanding the underlying mechanisms via in vitro assays [464].

6.3.4 Anti-PEG Response

Liposomal interactions with immune cells can cause antibody production against liposome components, such as PEG [37, 326, 465-469]. The rapid production of antibodies (e.g. immunoglobulin G, M, E) from B lymphocytes, in a T cell-independent manner, is another mechanism in the recognition and removal of liposomes from the body [470]. Antibody binding impacts the blood circulation time and treatment efficacy of liposomes and initiates classical complement activation. IgM antibodies are the first produced, by the spleen, in response to an antigen or liposomes, as seen in **Figure 6.4** [467, 471, 472]. One of the first studies to notice an increase in antibody production

was by Bucke and colleagues in 1998 when studying the biodistribution of liposomes with different surface modifications [473]. Additionally, Cheng et al. were one of the first to show that anti-PEG IgM monoclonal antibodies were generated by the spleen of mice in response to PEG-immunoconjugates [474]. Based on blood concentration levels and binding, IgM antibodies were more efficient in clearing the PEG-immunoconjugates from the blood than immunoglobulin G [474].

Since then, several groups have studied antibody production in preclinical animal models, which helped to explain the accelerated blood clearance seen after repeated dosing of liposomes. Ishida et al. showed that pegylated liposomes incubated with serum derived from rats pre-injected with liposomes had an increased liposome-protein binding index by approximately 2-fold compared to serum obtained from rats that were not pre-injected with liposomes [326]. Also, there was a 17-fold increase in IgM binding to pegylated liposomes compared to the non-pegylated liposomes. A follow-up study by Ishida and colleagues revealed a T cell-independent response to pegylated-liposomes in both Wistar rats and BALB/c nu/nu mice [465]. A relatively low anti-PEG immunoglobulin G response was seen 3-5 days after injection of pegylated liposomes and a potent IgM response occurred 3-10 days post injections in Wistar rats. In the absence of T-cells, a ~9-fold increase in IgM was observed 10 days post-injection in BALB/c nu/nu mice [465]. Additionally, using a pig model, Kozma et al. showed that anti-PEG IgM concentration in blood peaks at 7-9 days after low dose intravenous injection of pegylated liposomes [458]. The anti-PEG IgM levels remained elevated above normal, by approximately 10-fold, for 6 weeks. Using ex vivo spleen cells derived from pigs pre-injected with pegylated liposomes, they showed an increase in

IgM+ B-cells bound to Doxil® from 1.88% to 5.50% [458]. The association between the underlying mechanism of PEG immunogenicity and the "accelerated blood clearance" of subsequent liposome injections will be discussed in the next section. In contrast to the immunogenic effects, it is critical to point out that PEG may have additional immunosuppressive effects by decreasing inflammation and fibrosis, as seen in organ preservation [475], which warrants further investigation.

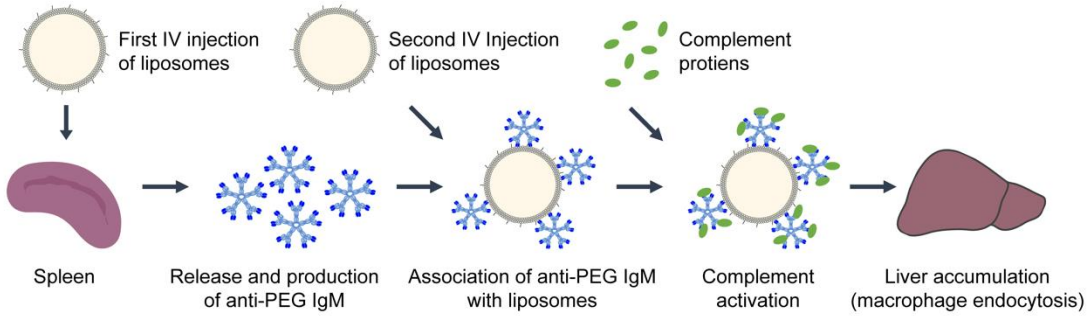

Figure 7.4 Schematic Overview of the Events that Alter the Pharmacokinetics of Repeated Intravenous Doses of Pegylated Liposomes. The first dose of pegylated liposomes stimulates the production of anti-PEG IgM antibodies by B cells within the spleen. This leads to the accelerated blood clearance of subsequent doses, during which circulating anti-PEG IgMs bind to the liposomes, initiating classical complement activation and decreasing blood circulation half-life.

6.3.5 Accelerated Blood Clearance

As previously mentioned, the addition of PEG to liposomes can increase their blood circulation half-life and prolong the uptake by the MPS [29]. It is also well accepted that after repeated injections of pegylated liposomes, they lose their "stealth" ability and are more quickly cleared from the blood [30-43]. This phenomenon, known as "accelerated blood clearance" (ABC), is caused by the abundant secretion of anti-PEG immunoglobulin M, G, and E, followed by the opsonization of C protein fragments (complement activation), and finally uptake by macrophages, depicted in **Figure 6.4** [30-42]. Dams et al. first observed a dramatic change in the circulatory half-

life of intravenously injected 99mTc-labeled pegylated-liposomes in rats and monkeys, but not mice [30]. In a male rhesus monkey, the blood circulation half-life of the second dose of pegylated-liposomes dropped from 87.5 hours to 14.2 hours. Although further liposome injections after the second dose had similar kinetics as the first, the ABC of the second dose occurred if it was administered 1-4 weeks after the first. Rats transfused with blood or serum from rats that were previously injected with liposomes also experienced ABC. The percent of the injected dose of liposomes in blood transfused rats at 4 hours dropped from 52% to less than 23% in the blood, suggesting the ABC is caused by a soluble serum factor [30].

Studying the ABC of liposomal chemotherapy in rodents may not be ideal, as Laverman et al. confirmed that Doxil® injections in rats lead to hepatosplenic macrophage depletion, and therefore a second injection of Doxil® did not experience ABC [31]. However, if the first dose was empty pegylated liposomes, an injection of Doxil® within one week was cleared rapidly from circulation in rats [31]. Similarly, in Beagle dogs, Suzuki et al. showed that repeated doses of Doxil® at 20 mg/m^2 did not have altered pharmaceutics, but repeated doses less than 2 mg/m^2 were more rapidly cleared from the blood and elicited an IgM response [40]. The half-life of the second injection at 2 mg/m^2 was reduced from 24.1 hours to 1.5 hours. Larger doses of Doxil® could have caused damage to B cells within the spleen, attenuating antibody production, or the uptake capacity of Kupffer cells may have been saturated/suppressed by the first large dose [40]. It is critical to point that the clinical relevance of ABC phenomenon induced by repeated injection of pegylated liposomes remains debatable, since Gabizon et al. observed a significant decrease in clearance ($P < 0.0001$) from the

1st through the 3rd cycle of pegylated Liposomal doxorubicin in humans [476]. The wide use of PEG in healthcare, hygiene, and beauty products suggests that most patients will likely have pre-existing anti-PEG antibodies [477], which could potentially impact the degree of ABC in patients. Other parameters that have been shown to impact the ABC of liposomes are lipid dose, with increasing amounts of the prior dose altering the pharmacokinetics of the subsequent injections in a sigmoid manner [34], liposome composition, with unsaturated lipids causing a more pronounced ABC [33], and time- and frequency- of injections [30, 32, 33, 478].

6.4 Conclusion

For two and a half decades, liposomal drug formulations have been administered in the clinic for the treatment of a variety of ailments, ranging from cancer to fungal disease. They boast an array of advantageous features, including biocompatibility, tunable properties, and capacity for loading hydrophilic and hydrophobic agents, making them convenient drug delivery vehicles. However, despite their clinical relevance and therapeutic potential, there is still a scarcity of knowledge regarding the downsides associated with the administration of liposomes. This mini-review presents a summary of existing knowledge regarding such limitations, divided into two main sections: 1.) Toxicological Evaluation of liposomes and their Building Blocks, and 2) Activation of the Immune System. One of the main toxicological concerns is that cationic liposomes, which are primarily used for nucleic acid delivery, can be toxic to macrophages and reduce their secretion of important immunomodulators. Additionally, following intravenous injection, liposomes end up sequestered in the organs of the MPS, such as the spleen and liver. This induces toxicity in these organs, causing the

depletion of cells that are critical for proper immune system function. As for activation of the immune system, liposomes can induce an inflammatory response that is characterized by the release of pro-inflammatory, monocyte-derived cytokines. Similarly, liposomes have been shown to activate the complement pathway, though the degree of activation is dependent on several factors such as size, charge, and mol% of cholesterol. Another important mechanism of immune activation is the anti-PEG response, which occurs when pegylated liposomal formulations activate the production of PEG antibodies by B lymphocytes. This leads to recognition and clearance by the immune system. In fact, repeated administrations of pegylated liposomes have been shown to cause accelerated blood clearance, robbing liposomes of their stealth capabilities. This underscores the idea that the dosing of liposomal agents must be carefully optimized to avoid premature clearance and maximize the therapeutic benefits of each injection. Depending on injection speed, liposomes can also induce hypersensitivity reactions, including cardiopulmonary distress. Mode of delivery and speed of administration are therefore key considerations for clinical applications of liposomal formulations. Overall, liposome-mediated toxicity to healthy tissues, coupled with the activation of the immune system, raises important concerns regarding their use. While liposomes are an attractive tool to reduce the dose-limiting side effects of therapeutics in patients, the liposomes themselves can impart new toxicities that are still not fully understood. There is still much work to be done to understand the mechanisms through which liposomes interact with the immune system before the full potential of liposome-based systems for gene and drug delivery can be achieved.

Chapter 7. Carrier-free, Amorphous Verteporfin Nanoparticles for Enhanced Photodynamic Cancer Therapy and Brain Drug Delivery

7.1 Introduction

As mentioned in *Section 2.3.2*, verteporfin (VP, also known as benzoporphyrin derivative) is a photosensitizer with excellent singlet oxygen yield for PDT [152] and minimal systemic toxicities due to rapid clearance primarily via liver-mediated mechanisms [313]. PDT involves the intravenous administration of VP followed by non-thermal 690 nm laser activation of VP to generate highly cytotoxic, short-lived ROS. While VP has proven advantageous in a wide range of disease contexts, the molecule is relatively hydrophobic [479] and, to date, has required carrier systems for clinical delivery [264, 480, 481]. In 2000, FDA approved a liposomal formulation of VP (Visudyne®) for PDT of age-related macular degeneration [482, 483]. Significant clinical efforts have since demonstrated the utility of Liposomal VP for PDT of chorioretinal conditions [484] and cancers [485, 486].

Liposomes have improved the solubility of photosensitizers [487], but cell-level delivery can still be augmented. For example, studies have shown that free-form VP accumulated within cancer cells by 1-2 orders of magnitude higher than Liposomal VP formulations [196, 488, 489]. Furthermore, lipophilic photosensitizers are generally encapsulated in the lipid bilayer of liposome with limited loading capacity and increased risk of photosensitizer self-quenching—a bottleneck for an effective PDT in the clinic. Lovell and colleagues demonstrated that up to 80,000 porphyrin-lipid conjugates could be packed into the lipid bilayer of each liposome [203]. The high packing density results in highly self-quenched porphyrins that convert absorbed light

into heat energy rather than releasing fluorescence signal and singlet oxygen generation. The reported maximum loading capacity of porphyrin in liposomes is 15 molar % with up to 11-fold self-quenching. Considering the clinical value of liposomes, but understanding their limitations for photosensitizer delivery, we sought to develop a carrier-free nanoformulation with efficient photosensitizer delivery and release for enhanced PDT.

Carrier-free nanodrugs offer the opportunity to deliver higher levels of hydrophobic photosensitizers. They allow for a theoretical drug loading capacity of 100% and eliminate the reliance on lipids, polymers, and/or co-solvents for drug delivery. Several synthesis schemes, such as media milling and solvent-antisolvent precipitation methods, are available for producing carrier-free nanodrugs with crystalline or amorphous structures. Nanodrugs with a crystalline character (referred to as nanocrystals) have high saturation solubility, and high stability post injection due to the minimized Gibbs free energy [490]. Nanocrystals have been leveraged for extended-release of antiretroviral therapies [491-493], anticancer drugs [494, 495], and other medications [496]. However, in the context of PDT, the potential for prolonged photosensitizer bioavailability from nanocrystal could potentially be unfavorable in terms of skin phototoxicity. In contrast, amorphous nanodrugs generally possess a higher saturation solubility and, consequently, an increased dissolution velocity (creation of high C_{max}, reduction of t_{max}) compared to equally sized nanocrystals [497]. However, prerequisites for utilization of carrier-free, amorphous photosensitizer products for PDT are that the stability can be maintained throughout the shelf-life of the product and photosensitizers can be light-activated for ROS generation.

Here, we report the first carrier-free, amorphous photosensitizer nanodrug using VP (termed NanoVP). The size of the NanoVP can be precisely controlled either by adjusting the solvent-to-antisolvent ratio or changing the initial drug concentration. NanoVP exhibits excellent stability over 1-year storage, enhances VP accumulation in cells, and fully de-quenches in biological systems for superior photochemical singlet oxygen generation compared to the standard Liposomal VP formulation. In comparison with other photosensitizer formulations that are commonly used in the clinic, we demonstrate that NanoVP is a superior PDT agent for the treatment of brain tumors, as well as the safe and selective opening of the BBB without damaging normal brain tissues.

7.2 Methods

7.2.1 NanoVP Synthesis and Characterization

NanoVP was prepared using the solvent antisolvent precipitation method. Free-form VP powders (US Pharmacopeia) were dissolved in dimethyl sulfoxide (DMSO, solvent) to achieved different initial concentrations (1-40 mM) and then injected dropwise into deionized water (antisolvent), under stirring, at room temperature. Different solvent-antisolvent ratios (1:50-1:10) were tested for formulating NanoVP. Free-form VP molecules not loaded into the NanoVP were removed by dialysis (Spectrum Labs, MWCO 300 kDa) against PBS at 4°C for 24 hours. The hydrodynamic diameter, polydispersity, and zeta potential were measured using particle sizer and zeta potential analyzer (NanoBrook Omni, Brookhaven Instruments). VP concentration was determined based on UV-Vis absorbance in DMSO (Synergy Neo2, BioTek

Instruments) using established molar extinction coefficient (VP: $\varepsilon = 80{,}500\ M^{-1}cm^{-1}$ at 435 nm, $\varepsilon = 34{,}895\ M^{-1}cm^{-1}$ at 687 nm). Entrapment efficacy is the percentage of VP that is successfully entrapped into the NanoVP. Loading capacity is the amount of VP loaded per unit weight of the NanoVP. NanoSight tracking analysis (NanoSight LM10, Malvern Instruments) was used to determine the number of particles per mL. Liposomes are considered 'gold standard' nanocarreirs for VP delivery. Liposomes containing VP within phospholipid bilayers were synthesized via freeze-thaw extrusion technique [19] and used as a control group.

7.2.2 Transmission Electron Microscopy

The size, morphology, and microstructure of NanoVP were studied using a transmission electron microscope (TEM; JEOL JEM-2100 LaB6, 200 kV). For conventional TEM, NanoVP (10 μL) was pipetted onto a Lacey carbon grid (Ted Pella) and air dried overnight before examination. To exclude the possibility of artifacts due to sample dehydration, ionic liquid (3 μL, Hilem IL-1000, Hitachi) was used as a pretreatment reagent for TEM examination of wet specimens. Images were taken at high magnifications (10,000-100,000x). Due to small particle sizes and to enhance diffraction intensity, selected area electron diffraction was used to collect electron diffraction patterns.

7.2.3 NanoVP Stability, Photoactivity, and Photosensitizer Release Profile

The stability of NanoVP particles in PBS at 4°C was determined by monitoring their hydrodynamic size and polydispersity index using a particle sizer analyzer for up to one year. NanoVP singlet oxygen ($^1O_2$) generation, self-quenching, and drug release

were studied in 96-well plates as described previously [21]. NanoVP and SOSG at 5 μM were mixed and irradiated with 690 nm light (10 J/cm^2, 10 mW/cm^2; ML6600, Modulight). A multi-mode microplate reader (Synergy Neo2, BioTek) acquired fluorescence signals of VP (Excitation/Emission: 435/650-750 nm) or SOSG (Excitation/Emission: 504/525 nm) before and after light irradiation. Self-quenching (F_{DSMO}/F_0) is defined as the fluorescence after disruption of the NanoVP using DMSO (F_{DSMO}) divided by the fluorescence of the NanoVP in PBS (F_0). Photosensitizer release from NanoVP (de-quenching) was studied by monitoring the gain in VP fluorescence signal in PBS/DMSO buffer (0-100% v/v) at room temperature or in Eagle's Minimum Essential Medium (Cellgro) with 0-10% v/v fetal bovine serum (FBS, Gibco) at 37°C.

7.2.4 NanoVP Electrostatic Stabilization

The electrostatic stability of NanoVP was probed using the neutral polymer, poloxamer 407 (Pluronic ® F-127; Sigma), and the cationic polymer, polyethylenimine. Polymers were dissolved in water according to manufacturer's instructions and were added to the antisolvent (ultra-pure deionized water) prior to drop wise synthesis or after NanoVP particles were formed, at a 1:5 polymer: VP ratio (w:w). In both instances, the addition of positively charged polyethylenimine resulted in uncontrollable agglomeration, while NanoVP particles coated with poloxamer 407 appeared to remain stable. Dynamic light scattering and laser Doppler electrophoresis measurements showed that NanoVP coated with poloxamer 407 has a hydrodynamic diameter of 112.7±5.9 nm (PdI: 0.10±0.01) and a zeta potential of -32.6±1.8 mV. ynamic light scattering and laser Doppler electrophoresis measurements cannot be accurately performed on large agglomerations.

7.2.5 Cancer Cell Cultures

Human GBM U87 and mouse 3T3 fibroblast cells were obtained from ATCC and cultured per vendor's instructions. The human breast cancer MCF-7 parental cell line, the P-gp-overexpressing MCF-7 TX400 subline, and the ABCG2-overexpressing MCF-7 MX100 subline were cultured in Eagle's Minimum Essential Medium supplemented with 10% FBS, 100 U/mL penicillin, 100 µg/mL streptomycin, and 0.01 mg/ml insulin (Sigma) as previously described [196]. Cells were maintained in 5% CO_2 at 37°C and tested to be free of mycoplasma (MycoAlert, Lonza).

7.2.6 Evaluation of Photosensitizer Uptake and PDT Responses In Vitro

Cells were cultured overnight in 35-mm Petri dish or 96-well black wall plates (1-3.3×10^4 cells/cm^2) and then incubated with photosensitizers (i.e., NanoVP, free-form VP, or Liposomal VP; 0.25 µM) for 24 hours. Subsequently, cells were washed twice with PBS and incubated with photosensitizer-free complete medium. Photosensitizer uptake in cells was determined using extraction methods followed by VP fluorescence measurements (Excitation/Emission: 435/700±10 nm, Synergy Neo2, BioTek) or visualized using fluorescence imaging (Lionheart, BioTek) as described previously [21]. PDT was performed by exposing the cells to 690 nm light (0-10 J/cm^2, 10-50 W/cm^2, bottom illumination; ML6600, Modulight). The generation of intracellular ROS was studied using 2',7'–dichlorofluorescin diacetate probe (DCFDA, Thermo Fisher) and the mitochondrial membrane potential was examined via TMRE assay (Abcam). Expressions of total and cleaved caspase 3 were examined by immunoblotting. At 24 hours after PDT, cell viability was determined using MTT [3-(4,5-dimethylthiazol-2-yl)-2,5-diphenyltetrazolium bromide] assay or neutral red assay (abcam) following the vendor's protocol. For dark toxicity evaluation, cells were incubated with media containing photosensitizers (0-40 µM) for 72 hours followed by MTT assay. The

photosensitizer efflux by ABC transporters was studies in MCF-7 and its multi-drug resistant sublines (MCF-7 TX400 and MCF-7 MX100) by adapting our protocol.

7.2.7 Intracellular ROS Production using DCFDA

Intracellular ROS production was examined via 2',7'–dichlorofluorescin diacetate (DCFDA; Thermo Fisher) assay. U87 cells were plated in 96-well black wall plates (Krystal) at a density of 2.2×10^4 cells/cm^2. On the next day, cells were incubated with complete culture medium containing 0.25 μM of NanoVP, free VP, or Liposomal VP for 24 hours. On day 3, prior to PDT, cells were washed twice with PBS and incubated with 10 μM DCFDA for 30 minutes. Cells were irradiated with 690-nm red light (0-10 J/cm^2, 50 mW/cm^2; ML6600, Modulight). For the positive control, cells were incubated with 0.1 mL of 100 μM H_2O_2 for 15 minutes. The fluorescence signal of the cleaved DCF probe (Excitation/Emission: 485/535±15 nm) was measured using a microplate reader (Synergy Neo2, BioTek).

7.2.8 Mitochondrial Membrane Potential using TMRE

Mitochondrial membrane potential (ΔΨm) was examined via TMRE (Abcam) assay. U87 cells were plated in 96-well black wall plates at a density of 2.2×10^4 cells/cm^2. After a 24-hour incubation with 0.25 μM of NanoVP, free VP, or Liposomal VP, cells were washed twice with PBS and exposed to 690-nm light (0-10 J/cm^2, 50 mW/cm^2). After PDT, cells were incubated with 250 nM TMRE for 25 minutes and washed twice with 0.2% bovine serum albumin within PBS. Samples were subjected to fluorescence readings (Excitation/Emission: 549/575±10 nm) using a microplate reader or fluorescence and phase contrast imaging (Lionheart, BioTek). Controls

include no light irradiation and incubation with 100 μM of FCCP, a mitochondrial uncoupler, for 25 minutes. PDT and FCCP treated samples were normalized to a no treatment control.

7.2.9 Caspase-3 Western Blots

Expression of total and cleaved caspase-3 were examined using immunoblotting techniques. U87 cells were plated in 35-mm Petri dish (Falcon) at a density of 2.2×10^4 cells/cm^2. Cells were incubated with 0.25 μM of NanoVP, free VP, or Liposomal VP for 24 hours. Cells were washed twice with PBS and irradiated with 690-nm light (10 J/cm^2, 50 mW/cm^2) in fresh culture medium. At 1 hour after PDT, cell lysates were collected in RIPA buffer supplemented with 1% protease inhibitor. Protein lysates (22 μg) were separated on a 4-12% precast Bis-Tris gel (NuPAGE) and transferred onto a nitrocellulose membrane. After blocking with Odyssey blocking buffer (Li-COR) for 1 hour, blots were incubated with primary antibody against beta-actin (#3700, cell signaling), caspase 3 (#9662, Cell Signaling,), or cleaved caspase 3 (#9661, Cell Signaling) overnight at 4 °C. Blots were washed with 1X Tris-Buffered Saline, 0.1% Tween® 20 Detergent buffer followed by incubation with IRDye 680RD goat anti-mouse secondary antibody (926-68070, Li-COR) or IRDye 800CW goat anti-rabbit secondary antibody (926-32211, Li-COR) for 1 hour at room temperature based on the supplier's advice. Visualization of protein bands was developed using the LiCor ODYSSEY CLx (Li-COR). β-actin serviced as a loading control. Band intensity was determined using LiCOR ODYSSEY CLx software. PDT treated samples were normalized to a no treatment control.

7.2.10 Drug Efflux Assay

To study ABC transporter-mediated photosensitizer efflux, MCF-7, MCF-7 TX400, or MCF-7 MX100 were plated in 35 mm petri dishes (Falcon) at a density of

3.3 x10^4 cells/cm^2. The next day, cells were incubated with 1 mM of NanoVP, free VP, or Liposomal VP for 4 hours at 37 ºC with or without ABC drug transporter inhibitors (ABCG2 inhibitor: 10 mM fumetrimorgin C; P-gp inhibitor: 2.5 mM tariquidar). Subsequently, cells were washed twice with PBS, trypsinized, and lysed in RIPA buffer at 4 ºC. VP fluorescence (Excitation/Emission: 435/650-750 nm) was measured using a multi-mode microplate reader and intracellular VP concentration was determined with appropriate VP standard curves. Intracellular VP was normalized to total cell protein. The total protein amount was determined using Pierce bichoninic acid protein assay (Thermo Fisher).

7.2.11 In Vivo PDT and Photosensitizer Biodistribution

Animal protocols were approved by University of Maryland, College Park Institutional Animal Care and Use Committee. Xenograft mouse model of GBM were established by subcutaneously injecting U87 cells (1×10^6 cells in PBS/Matrigel®) into the flank of J:NU mouse (4-5 weeks old, #007850, Jackson Laboratory). Tumor volumes were longitudinally monitored using calipers and calculated using the standard estimation formula, $V=½\times length\times width^2$, where length equals the maximum tumor diameter in millimeters and width equals the diameter that is perpendicular to the length. Treatments were initiated 2 weeks post-implantation when tumors reached ~100 mm^3. At 2 hours post-intravenous injection of photosensitizers (i.e., NanoVP or Liposomal VP; 0.25 mg/kg) or PBS, a vertical 690 nm laser beam (100 J/cm^2, 100 mW/cm^2; ML6600, Modulight) was focused on the tumor to activate PDT. A cloth was used to protect animal skin from light exposure. Change in tumor volume was monitored for up to 2 months. The specific growth rate of tumors was estimated using

the equation (1/V)(dV/dt), where *V* is tumor volume and *t* is time. To examine photosensitizer biodistribution, tumor and normal tissues were collected at 2- and 24-hours post-injection of photosensitizers. Fluorescence images of VP in organs, tumors, and standards containing known VP concentrations were acquired using a reflectance fluorescent microscope equipped with a 375 nm laser diode (6 mW, L375P70MLD, Thorlabs), a 692 nm filter (FF01-692/40-25 Semrock), and a 12-bit CCD camera (EM-CCD, PCO, Kelheim, Lower Bavaria, Germany). Fluorescence images were processed by using a standard curve to convert the intensities into concentration using MATLAB.

7.2.12 Photodynamic Opening of the Blood-brain Barrier in Rodents

Animal protocols were approved by University of Maryland, School of Medicine Institutional Animal Care and Use Committee. Sprague-Dawley rats (4-5 weeks old, Envigo) received intravenous injection of NanoVP (0.25 or 0.5 mg/kg) or 5-aminolevulinic acid (5-ALA, 20 or 125 mg/kg) at 30 min or 4 hours before PDT. PDT parameters, including photosensitizer concentration, drug-light interval, irradiance and radiant exposure, were selected based our experience or other's clinical work. At 30 minutes post-photosensitizer injection, rats were anesthetized with isoflurane, secured within a stereotaxic frame, and craniotomy was performed to expose the right cerebral hemisphere. PDT was performed by light activation of the exposed brain (NanoVP: 690 nm, 80 or 100 J/cm^2; 5-ALA: 635-nm, 60 or 80 J/cm^2; 40 or 85 mW/cm^2; ML6600, Modulight). At 90 minutes post-PDT, rats received intravenous injection of Evans blue dye (2%, 4 mL/kg) to determine the BBB integrity using imaging and extraction methods. In a small group of PDT animals that did not receive Evans blue injection, brain tissues were collected, sectioned, and processed for

(i) histological (H&E) analysis and (ii) Luxol Fast Blue staining of myelin/myelinated axons and Nissl bodies. H&E and immunohistochemistry slides were imaged using the whole slide Aperio AT2 scanner system (Leica Biosystems). All image analysis was accomplished using Aperio and Halo imaging analysis software (v3.3.2541.300; Indica Labs), and image annotations were performed by a pathologist (B.K). Fields were excluded if they contained large areas of artifact such as folds or tears.

7.2.13 Rat Craniotomy

Rats were anesthetized with isoflurane and secured within a stereotaxic frame. During the 30-minute drug-light interval, a craniotomy was performed. The top of the rat head was shaved, and the skin was removed. The periosteum was retracted to the edges of the skull. Using a micro drill (OmniDrill35, WPI), a circle about 4 mm in diameter was sketched into the right parietal bone. Drilling was stopped periodically, and PBS was applied to prevent heating. The drilled bone was removed and any bleeding that occurred from surgery was stopped prior to light irradiation. After a 30-minute circulation period with Evans blue, rats were sacrificed via isoflurane overdose and decapitation, and brains were harvested. Digital images were immediately captured, and the brains were frozen at -80°C.

7.2.14 Evans Blue Quantification

Evans blue was quantified as previously described [498]. Briefly, the brain hemispheres were thawed on ice, minced, and incubated with formamide for 30 minutes at 55°C followed by 4 days at room temperature. Samples were centrifuged to pellet the tissue and the optical density of Evans blue within the supernatant at 610 nm

was measured on a multi-mode microplate reader. Standard curves were used to determine the amount of Evans Blue in each brain hemisphere.

7.2.15 Brain Histology

The effects of PDT on healthy brain tissues were examined 2 hours after light irradiation. Brains were harvested and frozen within optimum cutting temperature compound (Tissue-Tek) at -80°C. Cryocut sections (5 μm) from frozen rat brains were collected at the level of rostral and caudal to the treatment area and fixed in a mixture of glutaraldehyde and formaldehyde. H&E staining was performed using the Sakura® Tissue-Tek® Prisma™ automated stainer. The slides were hydrated and stained with commercial hematoxylin, clarifier, bluing reagent and eosin-Y. A regressive staining method was used. This method intentionally overstains tissues and then uses a differentiation step (clarifier/bluing reagents) to remove excess stain. The slides were cover slipped using the Sakura® Tissue-Tek™Glass® automatic cover slipper and dried prior to review. For Luxol Fast Blue staining, sections were hydrated and stained overnight at room temperature. Sections were immersed in 95% alcohol to remove excess stain. Slides were then washed in distilled water and quickly immersed in 0.05% lithium carbonate. Tissue sections were then placed in 70% ethanol until a sharp contrast between the corpus callosum and cortex developed. Sections were washed in distilled water, stain with cresyl violet acetate, differentiate in several changes of 95% alcohol, dehydrated with ethanol, cleared in xylene, and mounted. Slides were scanned at 20X using an Aperio AT2 scanner (Leica Biosystems) into whole slide digital images.

7.2.16 Statistical Analyses

Results are presented in mean ± SEM. Statistical tests were carried out using GraphPad Prism (GraphPad Software). Specific tests and number of repeats are indicated in the figure captions. Reported P values are two-tailed. One-way ANOVA statistical tests and appropriate post hoc tests were carried out to avoid type-I error.

7.3 Results

7.3.1 Formulation and Characterization of NanoVP

VP is barely soluble in water and prone to forming J-type aggregates in physiologically relevant buffers (**Figure 7.1a**). To date, intravenous delivery of VP in the clinic relies on the use of liposome, which serves as a solubilizer. Here, we successfully prepared a well-dispersed, carrier-free nanodrug of VP (NanoVP) using the solvent-antisolvent precipitation technique (**Figure 7.1b**). After dissolving VP in 100% DMSO at 7 mM, one part of sample was added dropwise to fifty parts of stirring water at room temperature and followed by dialysis against PBS at 4°C. Because DMSO and water are miscible, the introduction of VP DMSO solution in water creates local supersaturation of VP, which is thermodynamically unfavorable and could lead to the production of amorphous solids (precipitation) or crystals (crystallization). TEM micrographs revealed that NanoVP particles are spherical-like, amorphous, monodispersed, and ~100 nm in diameter (**Figure 7.1c-e**, **Figure 7.2**). The lack of electron diffraction further verified the amorphous structure of NanoVP (**Figure 7.1f**). TEM study using ionic liquid-treated samples showed that sample dehydration, destined for conventional TEM, has a negligible influence on the structure and size of NanoVP (**Figure 7.3**). Other attempts at synthesis, including adding VP (in 100%

DMSO) dropwise into PBS, resulted in uncontrollable agglomeration (**Figure 7.4**), potentially because the salts in PBS either served as nucleation sites or changed the charge of the dispersion [490].

Dynamic light scattering and laser Doppler electrophoresis measurements showed that NanoVP has a hydrodynamic diameter of 105.7±6.7 nm (PdI: 0.13±0.1) and a zeta potential of -32.9±0.3 mV (**Figure 7.1g**). Dialysis for purification and buffer exchange had minimal impact on NanoVP size (110.2±7.5 nm), PdI (0.13±0.2), and zeta potential (-29.6±6.7 mV) (**Figure 7.1g**). NanoVP has an entrapment efficacy of 91.6±7.5%, reflecting minimal loss during sample preparation and dialysis. The loading capacity of NanoVP is 100% at 706,000±38,000 VP molecules per nanoparticle, which is approximately 1455-fold greater than Liposomal VP (485±75 VP molecules per nanoparticle, **Figure 7.5**). The size of the NanoVP is tunable between 65 nm and 150 nm by increasing the photosensitizer concentration in solvent (1-40 mM, **Figure 7.1h**) or the DMSO:Water ratio (2-25%, **Figure 7.1i**). However, a starting VP concentration beyond 15 mM or a DMSO:Water ratio higher than 6% resulted in multi-peak size distribution (**Figure 7.6a,b)**. NanoVP, synthesized using 1-7 mM VP and 2% DMSO:Water ratio, was found stable for over one year in water (pre-dialysis) and at least five months in PBS (post-dialysis) (**Figure 7.7**). Further studies indicated NanoVP stability is maintained via electrostatic repulsion forces between the particles (**Figure 7.8**).

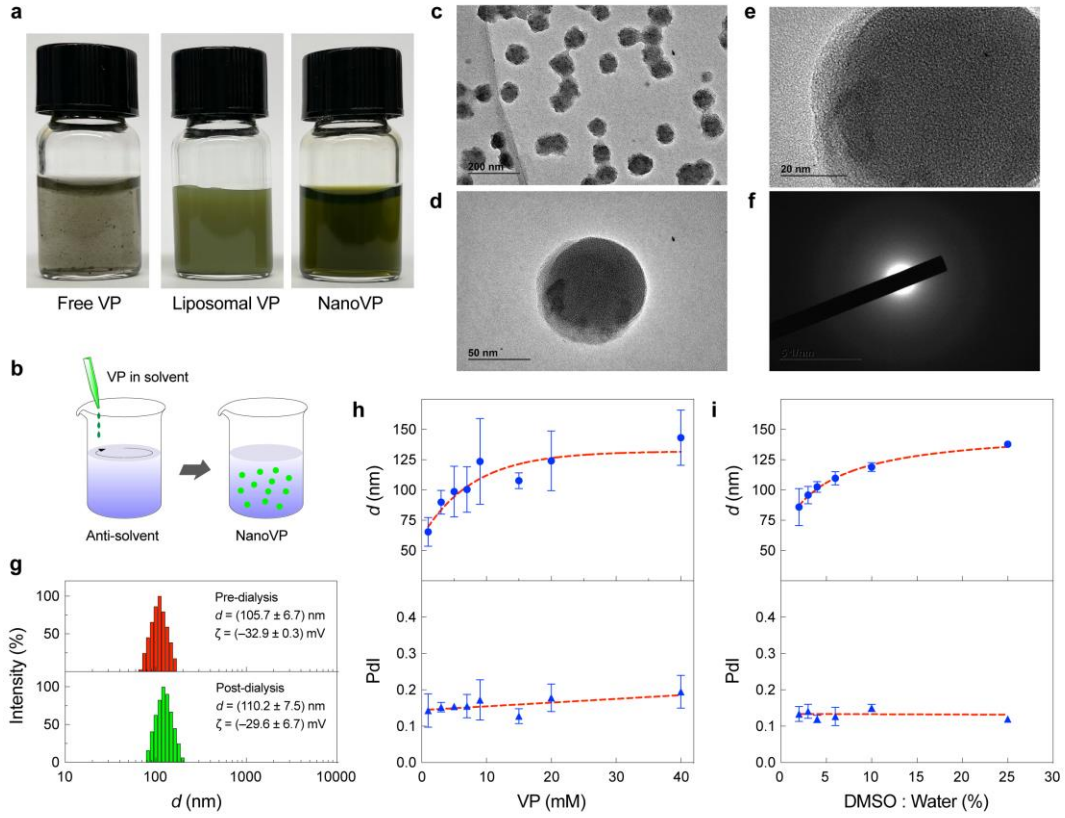

Figure 8.1 Physical Assessment of the Amorphous Nanodrug of Verteporfin (NanoVP). (**a**) Representative digital image of free-form VP, Liposomal VP, and NanoVP in PBS. (**b**) Schematic depiction of the solvent-antisolvent precipitation method for preparation of NanoVP. Panel (**c**) depicts representative transmission electron microscopy (TEM) micrographs (Scale bar = 200 nm) and (**d, e**) close-up views of monodispersed NanoVP. Panel (**f**) shows a representative image of selected area electron diffraction of the amorphous NanoVP. (**g**) Representative intensity plots, the average hydrodynamic diameter, and the average zeta potential of NanoVP diameter pre and post dialysis. The hydrodynamic diameter and polydispersity index (PdI) of NanoVP (**h**) as a function of initial VP concentration in DMSO or (**i**) as a function of DMSO:water ratio. $N \geq 3$, where N equals the number of samples. Error bars show the SEM.

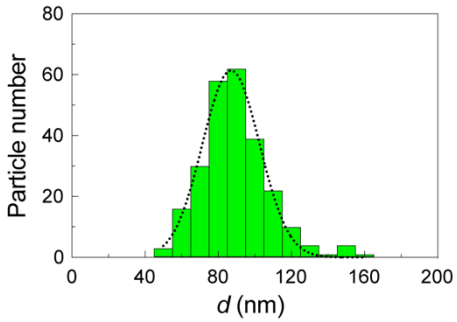

Figure 8.2 Size Quantification of NanoVP TEM Micrograph Images. Black line shows the gaussian distribution curve of the data set. Bin size = 10 nm. n = 250 particles.

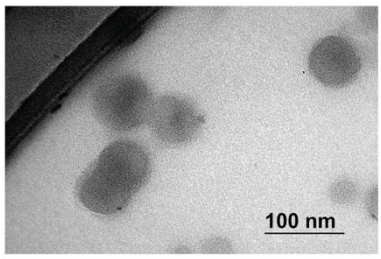

Figure 8.3 Representative Ionic Liquid TEM Micrograph. A second electron imaging technique was used to verify the 'drying effect' did not impact NanoVP structure or morphology. Scale bar = 100 nm.

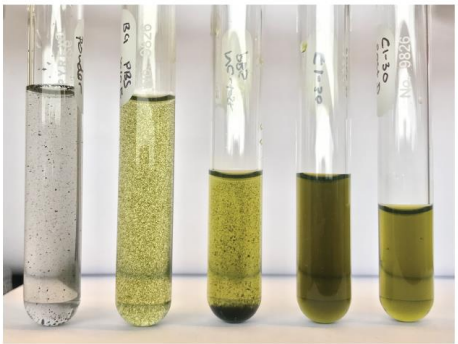

Figure 8.4 Alternative NanoVP Synthesis Methods. Representative digital images of (**a**) VP lyophilized powder was added to PBS and did not dissolve. Fully dissolved VP in DMSO was added into PBS (**b**) dropwise and (**c**) non-dropwise. Adding VP solution directly into PBS results in uncontrolled VP aggregation. (**d**) NanoVP synthesis following established preparticipation method in water. (**e**) NanoVP post dialysis in PBS.

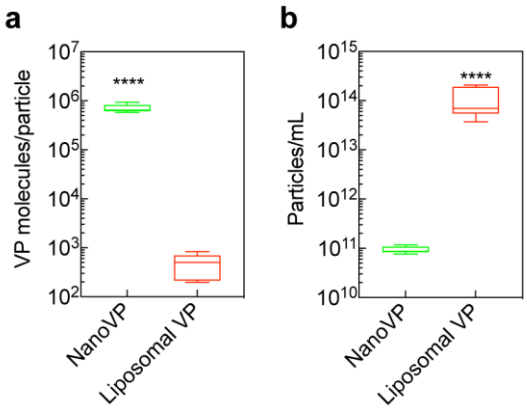

Figure 8.5 Loading Capacity of NanoVP and Liposomal VP. (**a**) The amount of VP molecules per nanoparticle was determined using the following formula: $VP_{particle}$ = $Concentration_{solution}$ * N_A / particles per ml solution. (**b**) Particles per ml solution. Two tail t-test was used to calculate significant differences, where **** $p < 0.0001$. $N \geq 3$. Box plots show the mean and the likely range of variation. Error bars show the maximum and minimum values.

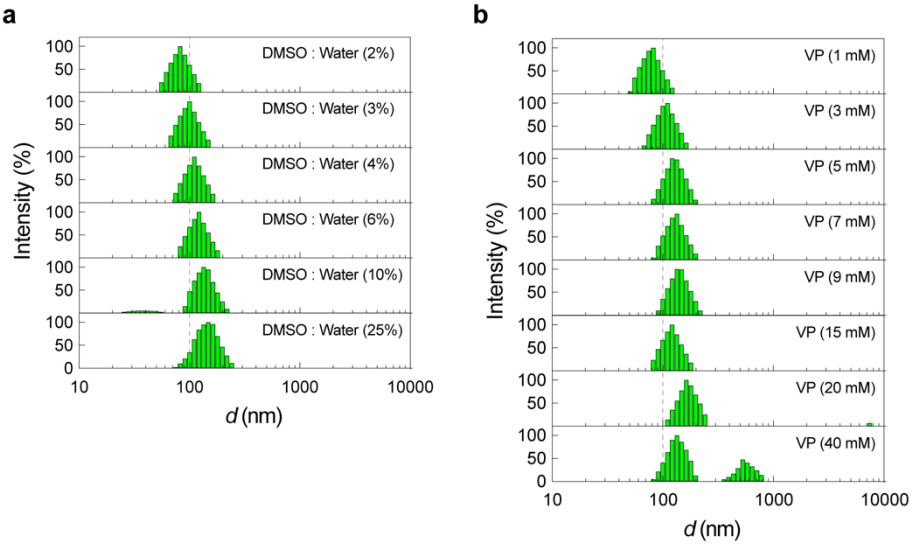

Figure 8.6 NanoVP Diameter. Representative intensity plots of NanoVP as a function of (**a**) DMSO: Water ratio and (**b**) initial VP concentration.

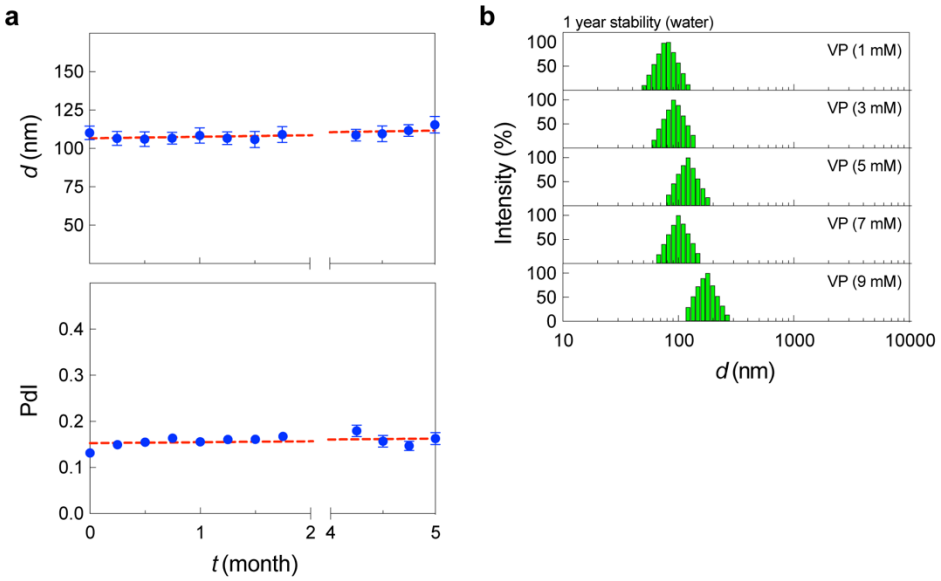

Figure 8.7 NanoVP Shelf Life. (**a**) NanoVP diameter and PdI in PBS and (**b**) representative intensity plots in water. N≥3, where N equals the number of samples.

Figure 8.8 Probing NanoVP Electrostatic Stabilization. Representative digitals images of NanoVP coated polymers. NanoVP was synthesized with (**left**) neutral polymer poloxamer 407 or (**right**) cationic polymer polyethylenimine. Poloxamer 407 had no impact on NanoVP stability, size, nor PdI. Polyethylenimine caused NanoVP to form large aggregates. N≥3, where N equals the number of samples.

7.3.2 Photo-activable NanoVP

VP is a modified porphyrin derivative that displays a chlorin-type spectrum in organic solvents. In DMSO, the absorption spectrum of VP is characterized by a distinct Q band in the near-infrared region at 687 nm and a strong Soret band at 435 nm (**Figure 7.9a**). The absorption spectra of NanoVP, free-form VP, and Liposomal VP were identical in DMSO, where VP is mainly in its monomeric form. At an

excitation wavelength of 435 nm, the fluorescence emission spectra of NanoVP in DMSO can be recorded around 700 nm (**Figure 7.9a**). When NanoVP is well-dispersed in PBS, a broadening of the Soret band and a red-shifted Q band were observed (**Figure 7.9b**). This suggests that monodispersed NanoVP consists of self-assembled J-aggregates. On the contrary, liposomes maintain some monomeric form of VP in PBS, showing a minimal decrease in the Soret band and without a red-shift displacement of the Q band as expected (**Figure 7.9b**). Driven by the spatial confinement of high-number VP in a 100 nm diameter particle, NanoVP generates extensive fluorescence self-quenching up to 328-fold in PBS in a concentration-dependent manner (**Figure 7.9c**). The degree of self-quenching in free-form VP or Liposomal VP were only up to 78-fold or 2-fold, respectively. VP quenching can decrease the photochemical production of singlet oxygen ($^1O_2$) (a Type II reaction). Upon light activation (690 nm, 10 J/cm^2, 10 mW/cm^2), highly quenched NanoVP and free-form VP in PBS did not produce any significant amount of $^1O_2$, as indicated by the minimal SOSG fluorescence signal (**Figure 7.9d**). On the contrary, light activation of Liposomal VP generates an up to 34-fold higher SOSG signal, compared to NanoVP. Similar to that observed in clinical PDT practice, we also confirmed that light activation of NanoVP, free-form VP, or Liposomal VP results in limited photothermal effects (ΔT=2-3°C; **Figure 7.10**).

The highly quenched NanoVP can be dequenched in the presence of serum proteins and in cancer cells for photosensitized $^1O_2$ production. **Figure 7.9e** shows that increasing the serum protein level from 0.15 to 10 % v/v decreases NanoVP quenching from 92-fold to 3.2-fold. Disaggregation of NanoVP in serum-containing media and U87 cells was further studied by longitudinal monitoring the VP fluorescence signal

(**Figure 7.11**). After adding NanoVP to 10% v/v serum-containing media, a rapid increase in VP fluorescence within 30 minutes is followed by the plateau of the signal, whereupon the signal remains constant at 38% of that fully dissolved in DMSO (**Figure 7.11a**). Similar trends were observed after adding NanoVP to U87 cells in serum-containing media (**Figure 7.11b**) or PBS (**Figure 7.11c**), where fluorescence recovery was the highest in NanoVP samples, compared to free-form VP and Liposomal VP. To check the recovery of photochemical activity of NanoVP in U87 cancer cells, DCFDA was used as a fluorescent probe for the detection of ROS generation (**Figure 7.9f**). Upon light activation (690 nm, 10 J/cm^2, 50 mW/cm^2), disaggregated NanoVP produced significantly higher intracellular ROS (~2-fold, $P < 0.001$), compared to that of Liposomal VP and the positive control (100 μM H_2O_2).

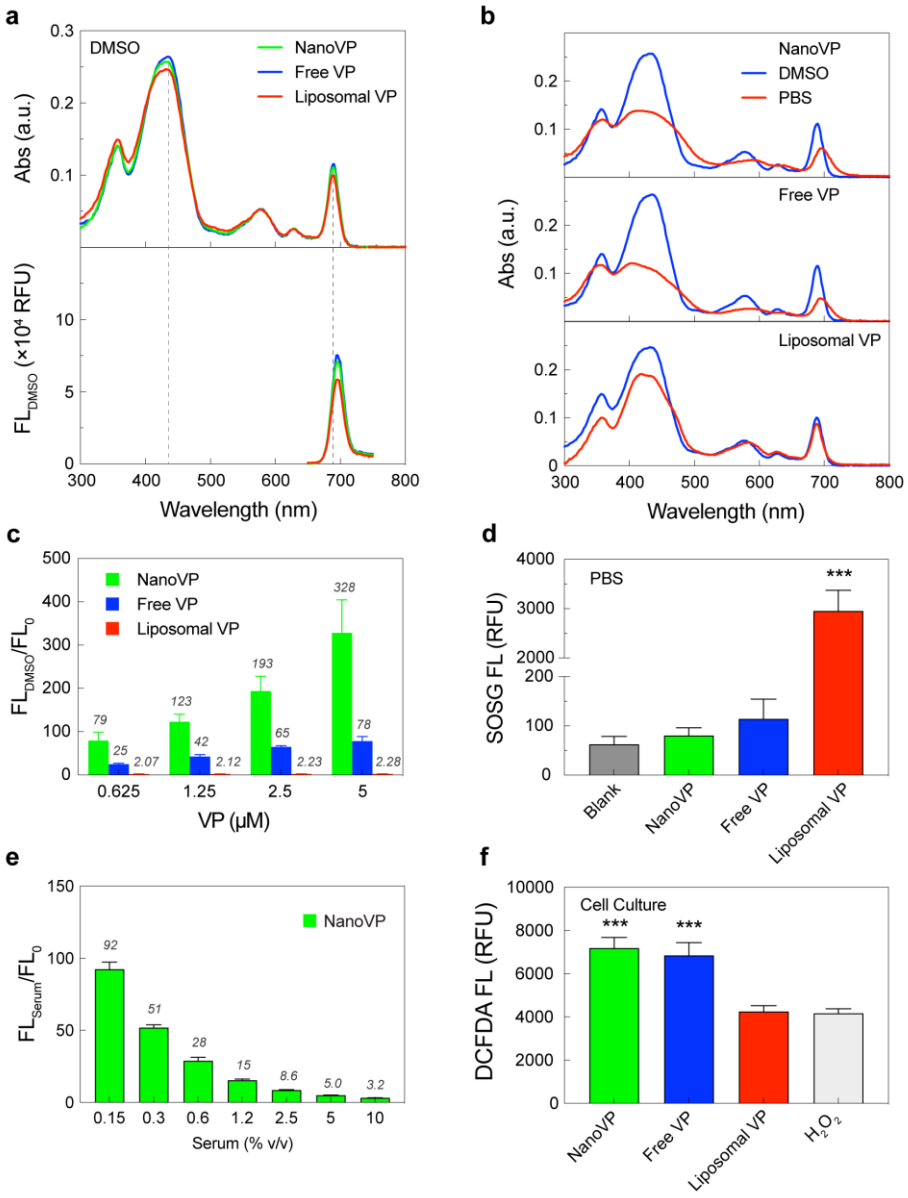

Figure 8.9 Photochemical Characterization of NanoVP, Free-form VP, and Liposomal VP. (**a**) Representative absorbance and fluorescence (FL) spectra of 5 μM NanoVP, free-form VP, and Liposomal VP in DMSO. VP was excited at excitation 435 ± 10 nm. (**b**) Representative absorbance spectra of NanoVP, free-form VP, and Liposomal VP in PBS (red) and DMSO (blue). (**c**) Fluorescence quenching, the maximum fluorescence intensity of 0.625-5 μM NanoVP, free-form VP, and Liposomal VP in DMSO (FL_{DMSO}) divided by the maximum intensity within PBS (FL_0). (**d**) Singlet oxygen production from NanoVP, free-form VP, and Liposomal VP-mediated PDT (10 J/cm^2, 10 mW/cm^2). (**e**) Fluorescence quenching of NanoVP as a function of serum concentration in PBS. (**f**) The intracellular ROS production from NanoVP, free-form VP, and Liposomal VP-mediated PDT (10 J/cm^2, 50 mW/cm^2). One-way ANOVA with multiple comparison test was used to calculate significant differences, where *p<0.05, ** p < 0.01, *** p < 0.001. N ≥ 3, where N equals the number of wells conducted over 3 trials. Error bars show SEM.

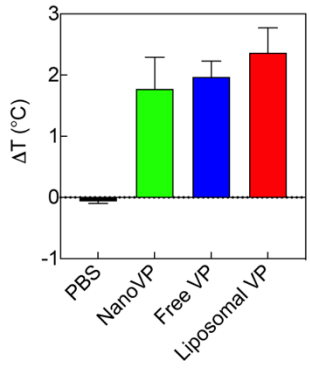

Figure 8.10 High Power Light Activation of VP Results in Limited Photothermal Effects. NanoVP, free-form VP, or Liposomal VP (40 μM) in PBS were light activated (50 J/cm^2, 0.5 W/cm^2) and solution temperature was measuring. Error bars show SEM. N≥6, where N equals the number of wells conducted over 3 trials.

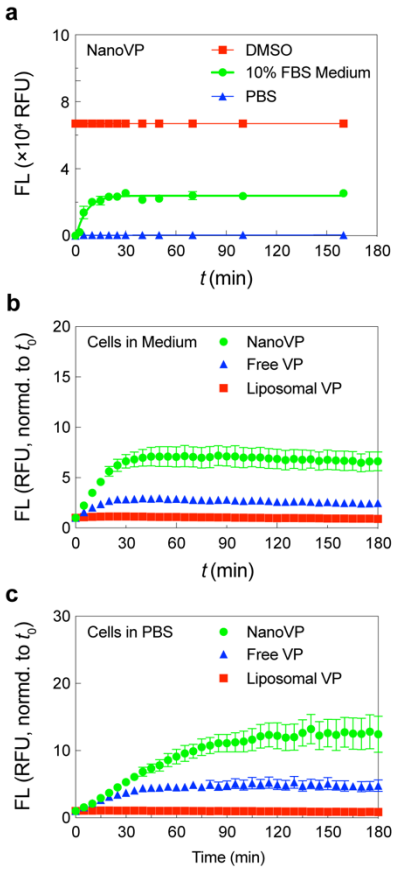

Figure 8.11 NanoVP Fluorescence Recovers in Physiologically Relevant Mediums. (**a**) The time-dependent fluorescence signal (Excitation/Emission: 435/700) of 5 μM in PBS, DMSO, and complete cell culture medium supplemented with 10% FBS at 37°C. (**b**) The time-dependent normalized fluorescence signal of NanoVP, free-form VP, and Liposomal VP when incubated with a monolayer of U87 cells within cell culture medium or (**c**) PBS over a 3-hour period at 37°C. N≥6, where N equals the number of wells conducted over 3 trials.

7.3.3 In vitro NanoVP Uptake and PDT Efficacy

The therapeutic efficacy of PDT depends on the concentration of photosensitizer in cancer cells. U87 cells treated with NanoVP resulted in ~2-fold higher intracellular concentration of VP (129.8±29.1 ng per mg of protein) compared to using Liposomal VP (66.2±8.1 ng per mg of protein) (**Figure 7.12a**). The uptake of NanoVP in U87 cells was similar to free-form VP. MTT assay revealed that NanoVP has a stronger anti-cancer PDT effect than Liposomal VP (**Figure 7.12b**). NanoVP and free-form VP exhibited the lowest half-maximal inhibition concentration (IC_{50}) of 0.20 $\mu M \times J/cm^2$ in U87 cells, while Liposomal VP displayed a 4-fold higher IC_{50} of 0.81 $\mu M \times J/cm^2$. The cellular uptake and PDT efficacy were further examined in non-cancerous 3T3 mouse fibroblast cells (**Figure 7.13**). The intracellular uptake of NanoVP in 3T3 cells was 49.9% greater than Liposomal VP. This resulted in a 2-fold IC_{50} increase from ~0.4 $\mu M \times J/cm^2$ for NanoVP to 0.8 $\mu M \times J/cm^2$ for Liposomal VP. NanoVP-PDT in U87 cells has a 50% lower IC_{50} compared to 3T3 cells, while the IC_{50} of Liposomal VP-PDT remained similar in both U87 cancer 3T3 cells. These results indicate that the intracellular uptake and anti-cancer PDT efficacy of NanoVP is significantly higher than that of Liposomal VP.

We and others have previously shown that VP preferentially accumulates in mitochondria and light activation of VP depolarizes the mitochondrial membrane potential ($\Delta\Psi m$) to trigger apoptosis [21, 499, 500]. Here, we reported that light activation (690 nm, 10 J/cm^2, 50 mW/cm^2) of NanoVP results in the largest degree of $\Delta\Psi m$ depolarization, as indicated by TMRE assay (**Figure 7.12c,d**). Quantification and normalization of the TMRE signal reveals NanoVP-PDT depolarizes $\Delta\Psi m$ by nearly

60%, while Liposomal VP-mediated PDT results in a modest depolarization of ΔΨm by ~35%. The potent mitochondrial oxidative phosphorylation uncoupler, FCCP, was used as a positive control. PDT-induced mitochondria damage can usually trigger the intrinsic apoptosis pathway leading to caspase-3 activation [501] within a few hours after light activation [502-504]. Immunoblotting results indicate that PDT using NanoVP or free-form VP induced a ~2.4-fold increase in cleaved caspase-3 formation one hour post light activation (**Figure 7.12e,f**). In addition, NanoVP and free-form VP-mediated PDT significantly reduced total (pro) caspase-3 expression (i.e., non-activated caspase-3) by ~50%, resulting in a cleaved-to-total caspase 3 ratio of ~4.4. Liposomal VP-PDT resulted in the lowest ratio of ~2.2. Neutral red uptake assay revealed that light-activation (690 nm, 1 J/cm^2, 50 mW/cm^2) of NanoVP, free-form VP, or Liposomal VP does not affect lysosomal integrity in U87 cancer cells. (**Figure 7.14**).

We have previously shown that free-form VP can be effluxed by ABC drug transporters, ABCG2 and P-gp, in cancer cells and thereby reducing PDT efficacy [196]. Using a human breast cancer cell line MCF-7, and their sub-lines (ABCG2 MCF-7 MX100 and or P-gp-overexpressing MCF-7 TX400) [196, 505], we discovered that NanoVP is a substrate of ABCG2 and P-gp (**Figure 7.15)**. Our studies further demonstrated the use of fumitremorgin C (ABCG2 inhibitor) and tariquidar (P-gp inhibitor), can improve the accumulation of NanoVP in MCF-7 MX100 and MCF-7 TX400 cells, respectively.

In general, PDT requires very low doses of photosensitizers (nM-μM) to be effective. Recent clinical and preclinical studies have reported that high doses of VP (mM) can induce potent 'dark' toxicity (without light activation) in cancer cells,

including GBM (NCT04590664) [506-508]. In complete darkness, NanoVP exhibited an IC_{50} of 12-14 μM in U87 cells and 3T3 cells, similar to that of free-form VP (**Figure 3g, Figure 7.16)**. NanoVP treatment at, or above, 20 μM significantly reduced cell viability by 75%, while Liposomal VP exhibited no significant cytotoxicity presumably due to the poor intracellular VP uptake **(Figure 7.12h,i)**.

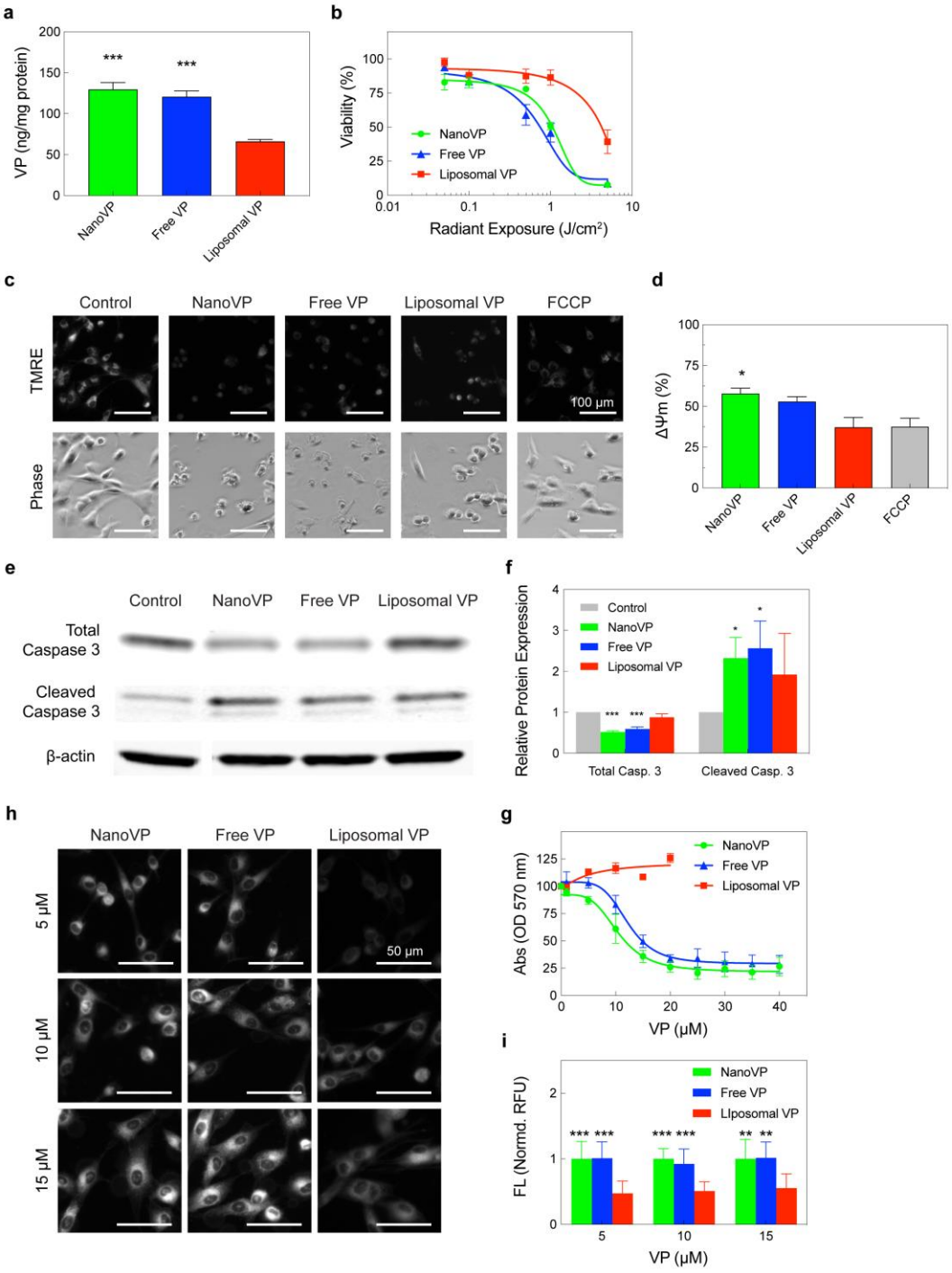

Figure 8.12 In Vitro PDT Efficacy of NanoVP within U87 Cells. (**a**) The intracellular VP concentration determined via extraction method at 24 hours post incubation with 0.25 µM NanoVP, free-form VP, or Liposomal VP. (**b**) Cell viability measured via MTT assay 24 hours after NanoVP, free-form VP, or Liposomal VP-mediated PDT (0-5 J/cm^2, 10 mW/cm^2). (**c**) Representative fluorescence images of the TMRE probe and phase constant images of U87 cells at 30 minutes after PDT. (**d**) Mitochondrial membrane depolarization quantified via TMRE probe 1-hour after NanoVP, free-form VP, or Liposomal VP-mediated PDT (10 J/cm^2,

50 mW/cm^2). Depolarization is calculated using the following formula: $\Delta\Psi m = 1-(T_f/T_c)$, where T_a is the TMRE fluoresce signal from FCCP or a treatment group, and T_c is the TMRE fluoresce signal from the control group. (**e**) Representative immunoblotting showing changes in total and cleaved caspase 3 expression in U87 cells at 1 hour post PDT. (**f**) Quantification of total and cleaved caspase 3 expression in U87 cells at 1 hour post PDT (10 J/cm^2, 50 mW/cm^2). A two-tail (total) and one-tail (cleaved) t-test was used to calculate significant differences. (**g**) Cell viability measured via MTT assay 72 hours after incubation with non-PDT activated (0 J/cm2, 0 mW/cm^2) NanoVP, free-form VP, or Liposomal VP. (**h**) Representative fluorescence images of NanoVP, free-form VP, or Liposomal VP within U87 cells. Scale bar = 50 μm. (**i**) Quantitative analyses of NanoVP, free-form VP, or Liposomal VP fluorescence signal in U87 cells. Fluorescence signals were normalized to the largest signal for each concentration. One-way ANOVA with multiple comparison test was used to calculate significant differences, where * $p < 0.05$, ** $p < 0.01$, and *** $p < 0.001$. N≥6, where N equals the number of wells conducted over 3 trials. Error bars show SEM.

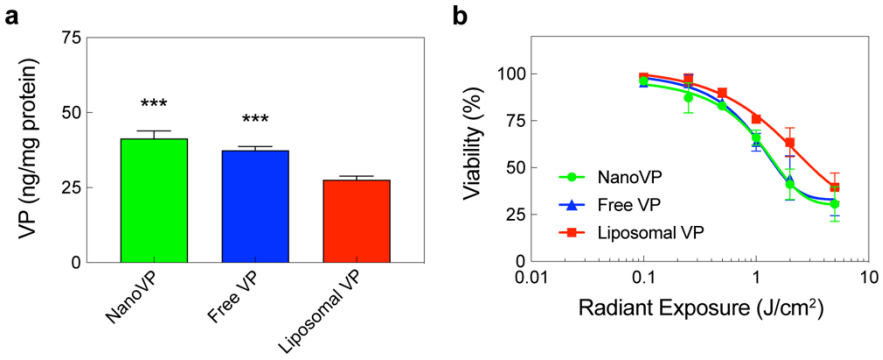

Figure 8.13 PDT Efficacy within 3T3 Fibroblast Cells. (**a**) The intracellular VP concentration determined via extraction methods at 24 hours post incubation with 0.25 μM of NanoVP, free-form VP, or Liposomal VP. (**b**) Cell viability measured via MTT assay 24 hours after NanoVP, free-form VP, or Liposomal VP-mediated PDT (0-5 J/cm^2, 10 mW/cm^2). One-way ANOVA with multiple comparison test was used to calculate significant differences, where *** $p < 0.001$. Error bars show SEM. N≥6, where N equals the number of wells conducted over 3 trials.

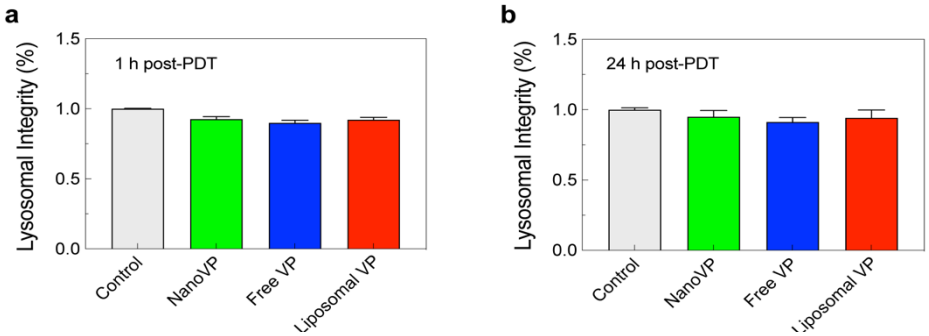

Figure 8.14 VP-mediated PDT does not Induce Lysosomal Damage. Lysosomal damage assessed via neutral red uptake assay (**a**) 1 and (**b**) 24 hours post PDT (1 J/cm^2, 50 mW/cm^2) of 0.25 µM NanoVP, free-form VP, or Liposomal VP. One-way ANOVA with multiple comparison test was used to calculate significant differences, where * $p < 0.05$, N≥3, where N equals the number of wells conducted over 3 trials. Error bars show SEM.

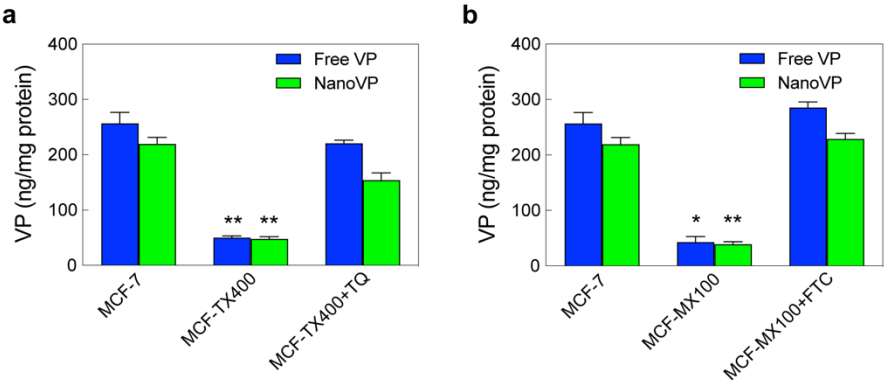

Figure 8.15 NanoVP is a Substrate for ABC Transporters ABCG2 and P-gp. Intracellular VP concentration determined via extraction methods at 4 hours post incubation with 1 µM NanoVP or free VP. Breast cancer cells overexpressing (**a**) P-gp (MCF-7 TX400) or (**b**) ABCG2 (MCF-7 MX100), and parental MCF-7 cells were incubated with and without inhibitors (10 µM fumitremorgin C for ABCG2 or 2.5 mM tariquidar for P-gp). Two-way ANOVA with multiple comparison test was used to calculate significant differences, where * $p < 0.05$, ** $p < 0.01$, N≥3, where N equals the number of wells conducted over 3 trials. Error bars show SEM.

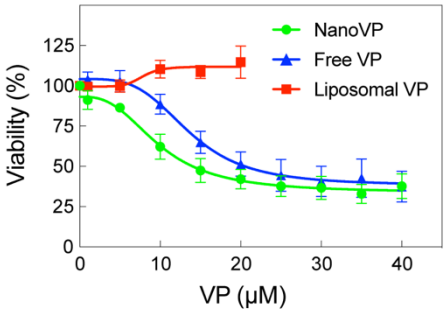

Figure 8.16 NanoVP Dark Toxicity in 3T3 Cells. Cell viability measured via MTT assay 72 hours after incubation with non-PDT activated (0 J/cm2, 0 mW/cm^2) NanoVP, free-form VP, or Liposomal VP. N≥6, where N equals the number of wells conducted over 3 trials.

7.3.4 NanoVP Enhances Anti-Glioblastoma PDT

To assess the efficacy of NanoVP-PDT in controlling GBM tumors in vivo, PDT was performed fourteen days following subcutaneous implantation of U87 cells in mice, when tumors reached approximately 100 mm^3 in volume (**Figure 7.17**). Liposome VP-PDT served as the clinical gold standard. For PDT, light (690 nm) irradiation was performed two hours after a single intravenous injection of NanoVP or Liposomal VP at 0.5 mg/kg. At 2-11 days after treatment, NanoVP-PDT reduced tumor volume by up to 35%, whereas continued tumor growth was observed in 'no-treatment' control and 'Liposome VP-PDT' over this same period (**Figure 7.17a**). At 21 days post-treatment, the mean tumor volume reduction in mice treated with 'NanoVP-PDT' and 'Liposome VP-PDT' was 70% and 44%, respectively, compared to 'no-treatment' control animals. These results suggest that NanoVP is a superior anti-tumor PDT agent compared to Liposomal VP. Further analysis revealed that animals treated with 'NanoVP-PDT' experienced a significant tumor growth inhibition at a specific growth rate of around -4.3 %/day between days 0-11 after treatment (**Figure 7.17b**). With only a single cycle of treatment, tumor regrowth can be observed 11 days after 'NanoVP-PDT' with a specific growth rate of approximately 5.3 %/day, similar to that of 'no-treatment' and 'Liposome VP-PDT'. In 'NanoVP-PDT' and 'Liposome VP-PDT' treated animals, the change in mouse weight was consistent with 'no-treatment' mice, indicating that PDT does not appreciably add to the systemic toxicity (**Figure 7.18).** It is noteworthy that with a single cycle of treatment, only modest survival benefits were observed after 'NanoVP-PDT' (median survival: 33 days) and 'Liposome VP-PDT' (median survival: 31 days), compared to 'no-treatment' control (median survival: 25)

(**Figure 7.17c**). These results point out challenges in achieving meaningful improvements in treatment response for GBM and highlight the need for combination strategies developed to provide durable tumoricidal control. In addition to changes in tumor volume, noticeable visual differences on tumor surfaces were observed (**Figure 7.17d**). At six days post-treatment, 'NanoVP-PDT' resulted in a significantly larger dark, possibly necrotic, area that covered the majority of the tumor (30.5 mm^2), while 'Liposomal VP-PDT' led to a smaller (13.6 mm^2) and more localized necrotic patch (**Figure 7.17d,e**). Finally, fluorescence imaging of VP in mouse tissues revealed that NanoVP and Liposomal VP have a similar biodistribution profile at 2 and 24 hours post intravenous injection (**Figure 7.17f, Figure 7.19)**.

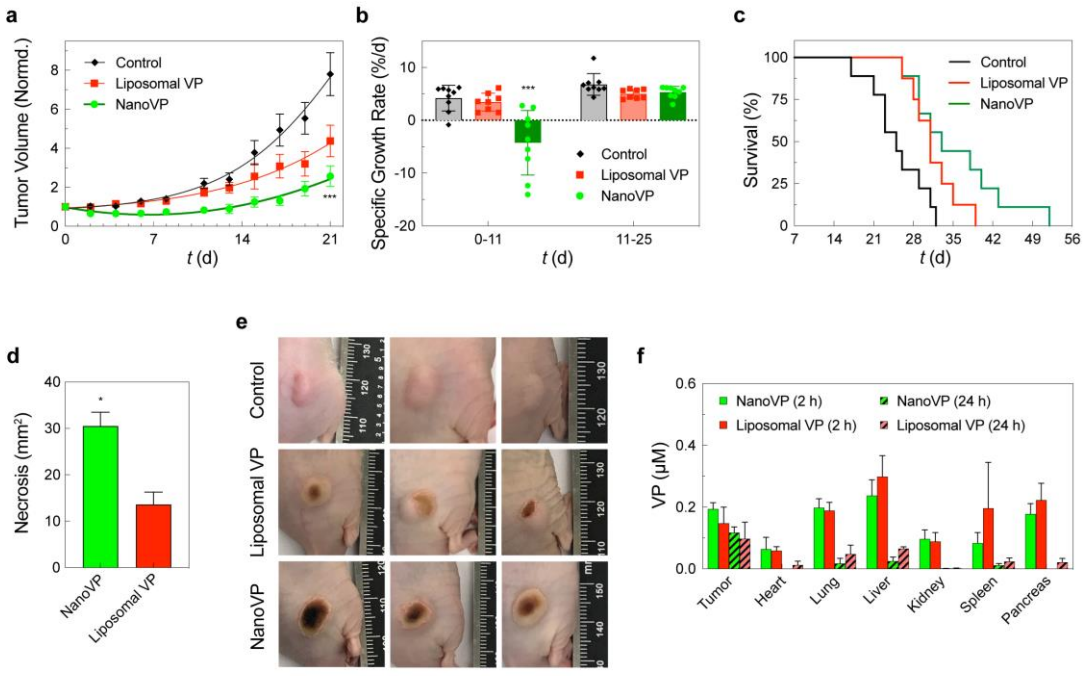

Figure 8.17 The Phototoxicity and Biodistribution of NanoVP and Liposomal VP in an U87 Glioblastoma Xenograft Mouse Model. PDT treatment (100 J/cm^2, 100 mW/cm^2) was initiated ~14 days after subcutaneous U87 cancer cell implantation when tumor volumes reached approximately 100 mm^3. Mice were randomized into groups that received (i) no-treatment, (ii) Liposomal VP 0.5 mg/kg, (iii) NanoVP 0.5 mg/kg. (**a**) Tumor volume was longitudinally monitored and calculated using the standard estimation formula, $V=½\times length\times width^2$, where length equals the maximum tumor diameter in millimeters and

width equals the diameter that is perpendicular to the length. Tumor volumes were normalized to the initial volume at the time of treatment. (**b**) The specific growth rate of tumors 0-11 days and 11-25 days post PDT were determined using the following formula: specific growth rate = (1/V)(dV/dt), where V is tumor volume and t is time. (**c**) Kaplan-Meier plot of tumor diameter greater than 1.5 cm (n = 7–8 animals per group). (**d**) Quantification of the surface area above the tumor that was impacted by PDT treatment. (**e**) Representative digital images of tumors 6 days post PDT treatment. (**f**) Quantitative analyses of VP fluorescence intensity within the tumor and organs, 2 and 24 hours after VP injection. One-way ANOVA with multiple comparison test was used to calculate significant differences, where * $p < 0.05$, ** $p < 0.01$, and *** $p < 0.001$. $N \geq 7$, where N equals the number of animals conducted over 2 trials. Error bars show SEM.

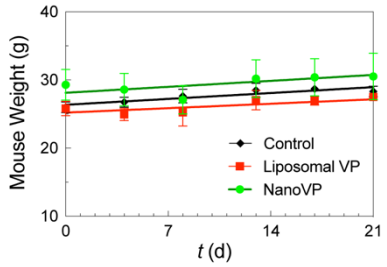

Figure 8.18 Mouse Weight post PDT Treatment. PDT had no impact on weight. N≥5.

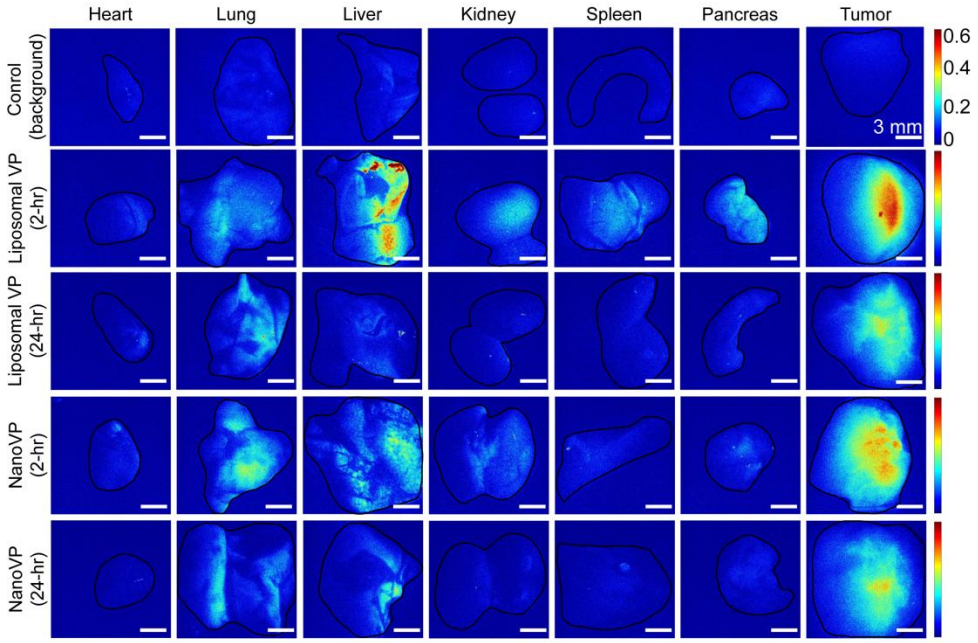

Figure 8.19 VP Biodistribution in Mice Organs and U87 Tumors. Representative fluorescence images of NanoVP and Liposomal VP in mice organs and U87 tumors at both 2- and 24-hrs post i.v. injection. Scale bar = 3 mm.

7.3.5 NanoVP-PDT Modulation of the Blood-brain Barrier in Rats

The BBB remains a critical obstacle to the effective treatment of GBM and other central nervous system diseases. Low-dose PDT priming, an enabling technology for minimally invasive tumor treatments, allows transient opening of the BBB through modulating endothelial cell-cell junction phenotype. Here, we evaluate the utility and safety of low-dose NanoVP-PDT priming for spatially targeted BBB opening in healthy rats with intact BBB (**Figure 7.20a**). The 5-ALA (Gliolan®), an FDA-approved photosensitizer prodrug routinely used for PDT opening of the BBB, served as benchmark group is our study. We identified a 5.5-fold increase of total Evan Blue accumulation in NanoVP-PDT-treated brain compared to 5-ALA-PDT treated brain tissues ($P < 0.05$) (**Figure 7.20b,c**). The spatiotemporal selectivity of PDT confines Evan Blue delivery to the right-brain hemisphere where the light is directed, thereby reducing normal tissue damage. The use of the longer activation wavelength photosensitizer, NanoVP (690 nm), for deeper tissue penetration is also an advantage over using the 5-ALA-induced protoporphyrin IX (PpIX, 635 nm) (**Figure 7.20d**). We showed that 690 nm light activation of NanoVP improves Evan Blue delivery at further depths in rat brains (visible up to 4-5 mm), compared to 635 nm light activation of 5-ALA-induced PpIX (visible up to 1 mm). Histological changes of brain tissue after PDT were studied microscopically on sections stained with H&E or Luxol Fast blue. Compared to the left-brain hemisphere that did not receive treatment due to the intact skull, the right-brain hemisphere did not have any signs of low-dose PDT priming-induced damage. H&E staining revealed no detectable lesions at the site of treatment (right hemisphere) and, Luxol fast blue staining was symmetrical with no evidence of

demyelination (**Figure 7.20e**). Alternatively, rats that received traditional high dose PDT had signs of brain damage within the neuropil parenchyma (brain cortex) (**Figure 7.21)**. This result agrees with previous studies that show dose escalation results in increased signs of edema and brain damage [17].

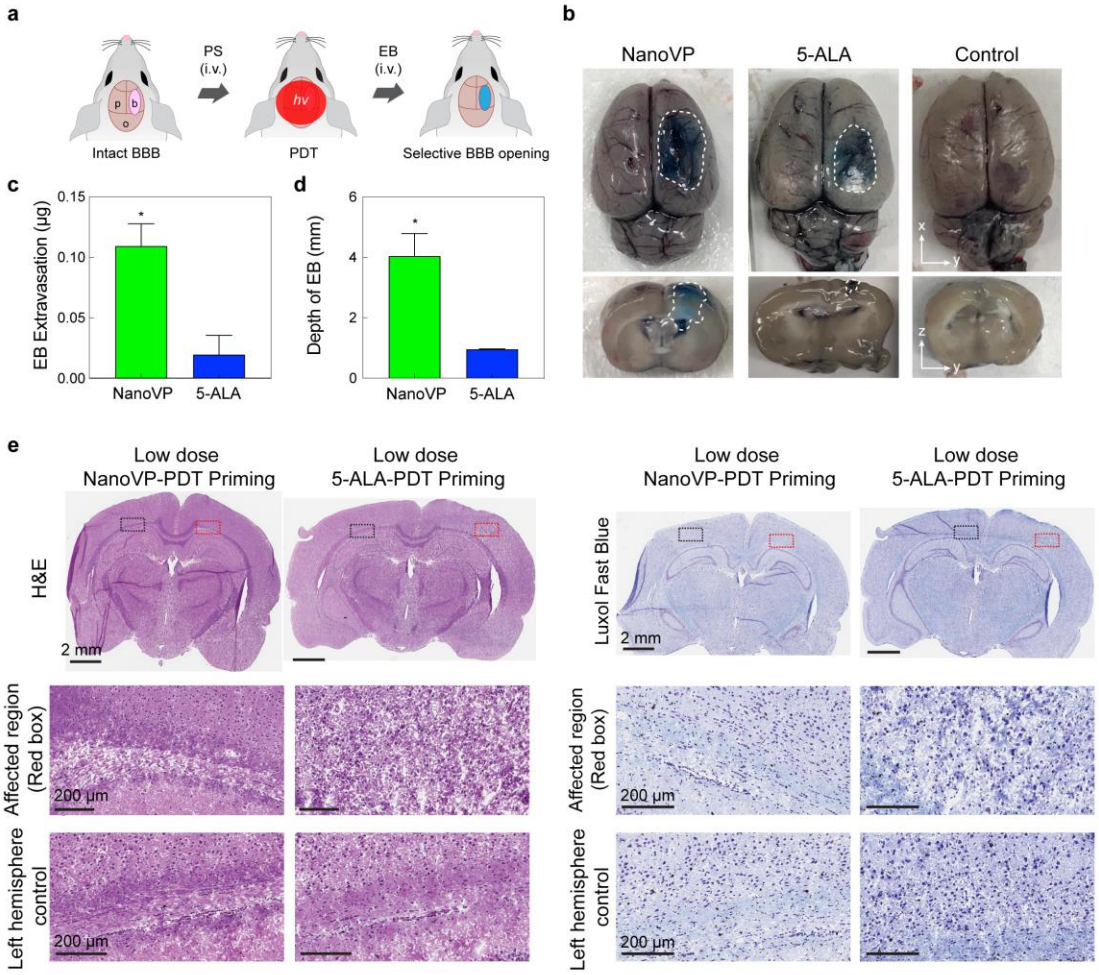

Figure 8.20 PDT-induced Blood-brain Barrier Opening within the Rat Brain. (**a**) Schematic depiction of experimental design. NanoVP (0.25 mg/kg) or 5-aminolevulinic acid (5-ALA, 20 mg/kg) were intravenously administered 30 minutes PDT (NanoVP: 690 nm, 80 J/cm^2; 5-ALA: 635 nm, 80 J/cm^2; 85 mW/cm^2) was performed on the exposed right brain hemisphere. After 90 minutes, Evans blue was intravenously administered to the rats and circulated for 30 minutes prior to brain harvesting. (**b**) Representative top and cross-sectional images of Evans blue within the brain after PDT-induced BBB opening (**c**) Quantification of Evans blue extracted from the right brain hemispheres (n ≥ 3 rats per group, background subtracted). (**d**) Quantification of maximum depth that extravasated Evans blue can be visualized within the brain. (**e**) Representative histopathology of rat brain tissue after traditional and low-dose PDT treatment. Photomicrographs of brain sections stained with H&E and Luxol

fast blue. Two tail t-test was used to calculate significant differences, where n.s. indicates not significant ($p > 0.05$), * $p < 0.05$. Error bars show SEM. $N \geq 3$.

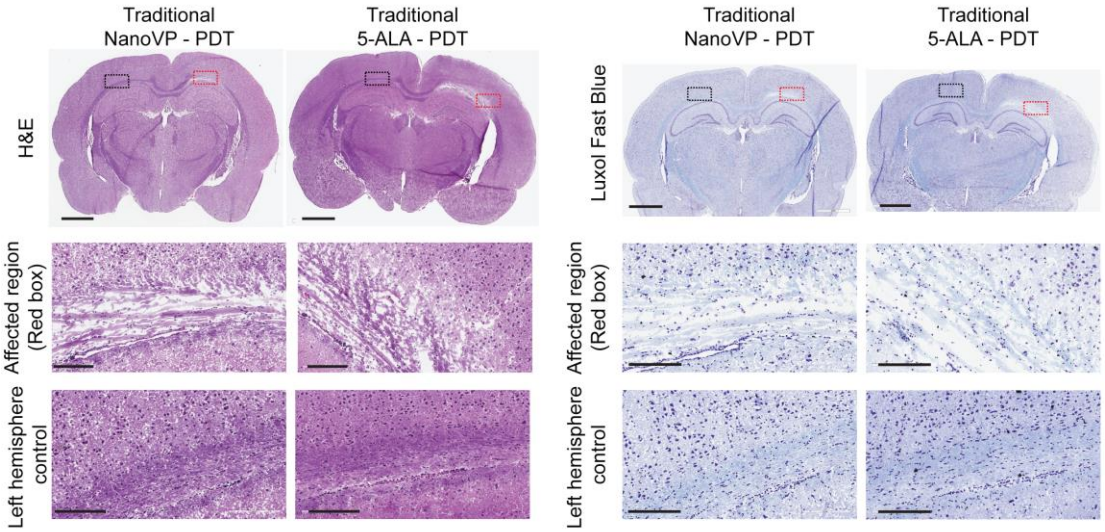

Figure 8.21 Traditional PDT Damages Healthy Brain Tissue. Representative photomicrographs of brain sections stained with H&E and Luxol fast blue. Photosensitizers (0.5 mg/kg VP or 125 mg/kg 5-ALA) were photoactivated (VP: 100 J/cm^2, 40 mW/cm^2; 5-ALA: 60 J/cm^2, 40 mW/cm^2) 30-minutes (for VP) or 4-hours (for 5-ALA) after intravenous injection. Brains were harvested 90 minutes post PDT. N≥3.

7.4 Discussion

PDT using Liposomal VP has already helped hundreds of thousands of patients globally with wet age-related macular degeneration [145]. Since its FDA approval in 2001, Liposomal VP has been tested clinically to treat a wide range of cancers, including primary breast, retinoblastoma, and refractory brain tumors. Liposomal VP-PDT is currently being evaluated for unresectable solid pancreatic tumors or advanced pancreatic cancer (NCT03033225), and the chemotherapeutic effects of Liposomal VP are being evaluated in patients with recurrent high-grade EGFR-mutated glioblastoma (NCT04590664). Free-form VP is not used clinically because the large VP agglomerations created in aqueous buffers will negatively impact its pharmacokinetics and singlet oxygen yield. Pure-drug nanoparticle delivery systems offer tools to

improve the pharmacokinetic profile of hydrophobic drugs and minimize the reliance on solubilizing agents [509]. In this study, we report a new pure-drug nanoparticle of VP (NanoVP) that significantly improves photosensitizer delivery to cancer cells. Our in vivo findings and results show the safety, feasibility, and potential utility of NanoVP for PDT of gliomas, as well as BBB opening to enhance drug delivery with no evidence of microscopic normal tissue injury.

Solvent antisolvent precipitation is a simple and reproducible formulation strategy to synthesize stable nanoparticles of VP. The size of NanoVP is tunable between 65 nm and 150 nm by increasing the photosensitizer concentration in solvent or the DMSO:Water ratio. Similarly, others demonstrated a larger initial concentration and higher solvent:antisolvent ratio could increase the size of nanodrug paclitaxel [510]. Synthesis optimization revealed that monodispersed NanoVP can be produced using an initial VP concentration of less than 15 mM and a DMSO:Water ratio below 6%. A future direction includes examining the impact of solvent type (e.g., ethanol or methanol) on NanoVP formation, size, and stability. The amorphous structure of the prepared NanoVP, showed by X-ray diffraction data, represents another major advantage in the quest to immediately convert quenched NanoVP into its un-quenched molecular form in presence of the serum components or cells, which recovers fluorescence signal and PDT capability.

Previous studies have also shown that pure-drug nanoparticles can improve cellular pharmacokinetics while liposomes hinder therapeutic uptake [489, 511, 512]. As a direct result of improved cellular accumulation, NanoVP was found to be a more potent PDT and chemotherapeutic agent than the traditional Liposomal VP. This result

is similar to previous studies that have shown free-form drugs, including doxorubicin [513], and paclitaxel [511], are uptaken more effectively in a variety of cancer cells compared to their liposomal counterparts. Free-form VP is lipophilic and can passively diffuse through the cell membrane [514, 515]. It is speculated that NanoVP had a similar accumulation rate as free-form VP, as NanoVP is readily dissociated into its molecular form in presence of the serum components or cells. When VP is encapsulated within a liposome, the mode of cellular entry is generally altered from passive diffusion to endocytosis [516], hindering the overall drug accumulation rate. We further present evidence that NanoVP-PDT, similar to free-form VP-PDT, effectively produces intracellular ROS, induces mitochondrial membrane potential ($\Delta\Psi m$) depolarization, and initiates intrinsic apoptosis upon light activation. Typically, PDT requires very low doses of photosensitizers (in the nanomolar to micromolar range) to be effective. Recent clinical and preclinical studies have reported high concentrations of VP (in the millimolar range) can induce 'dark' cytotoxicity in cancer cells, including GBM (NCT04590664) [506-508]. A 10-100-fold higher dose of VP, compared to the PDT dose, has been shown to downregulate Bcl-2, disrupt the YAP/TAZ-TEAD complex interaction, and induce cancer cell death without light activation [506, 507]. We demonstrated that the enhanced cellular uptake of NanoVP resulted in superior non-PDT killing effects. Alternatively, Liposomal VP alone did not inhibit cancer growth at the same millimolar incubation concentrations.

While this report offers many findings and formulation advances related to VP-PDT, there are some notable limitations. In subcutaneous glioma mouse models, NanoVP-PDT effectively reduced initial tumor growth, outperforming Liposomal VP-

PDT. Although VP-PDT has been used successfully in the clinic to treat different cancers, a single cycle of PDT, like most cancer regimens, is insufficient to achieve a long-term survival. In our study, NanoVP increased the median survival of mice bearing subcutaneous tumors by over a week. This result is similar to our previous study, where we demonstrated a single dose of VP-PDT (0.25 mg/kg) could reduce OVCAR-5 tumor volume by up to 55% but did not increase overall survival [278]. Similar to chemotherapy, radiation and immunotherapy, NanoVP-PDT would require multiple treatment cycles to effectively eradicate the entire cancerous cell population and warrants further investigation. Nonetheless, a single cycle of NanoVP-PDT remains an attractive adjuvant therapy that can be combined with surgery. In a prior clinical study, Liposomal VP-PDT decreasing tumor volume could convert patients with previously unresectable pancreatic tumors to become candidates for surgery [168]. In addition surgery, PDT has been successfully combined with chemotherapy, radiation or immunotherapy, due to different mechanisms of action and their non-overlapping side effects [19]. Biodistribution analysis revealed NanoVP tended to have a higher tumor accumulation, while Liposomal VP accumulation more within the liver, pancreas, and spleen. Taken together, these results suggest that NanoVP could be an adequate replacement for our pegylated Liposomal VP formulation. A further examination of the pharmacokinetics and PDT parameters (e.g., light fluence, drug-light interval) will be important next steps in determining if NanoVP is a good replacement for the clinically used non-pegylated liposome formulation.

Drug delivery to brain tumors remains especially difficult due to the BBB, a specialized network of capillaries in the brain. The high degree of tightness and

integrity imposed by the BBB limits the effective delivery of more than 98% of small-molecule therapeutics to the brain [7]. While many treatment modalities have shown promise in opening (i.e., permeabilizing) the BBB and enhancing brain drug delivery, they often result in edema and neurotoxicity, limiting their clinical use [8-11, 117]. Numerous groups have shown the potential of light-activated 5-ALA (Gliolan®)-induced protoporphyrin IX (PpIX) to open the BBB in rodents [16, 517]. Hirschberg and colleagues showed larger doses of 5-ALA-PDT could open the BBB for up to 72 hours [14, 15], but treatment resulted in early signs of necrosis up to 5 mm away from the primary brain tumor. In addition, non-tumor-bearing animals that received 125 mg/kg 5-ALA and 54 J experienced a 50% mortality within 5 days of treatment. Here, we studied the effects of NanoVP-PDT at subtherapeutic doses to achieve photodynamic priming [175, 518]. This approach is particularly relevant for brain tumors, where surrounding healthy tissue damage and intratumoral drug accumulation are a major concern. In this study, we demonstrated that NanoVP-PDT mediates BBB opening to increase in EB accumulation in the brain by 5.5-fold compared to using 5-ALA-PDT. More importantly, we show for the first time that low-dose PDT using NanoVP did not result in healthy brain tissue damage.

Finally, we believe that intraoperative NanoVP-PDT has a high translational potential. Surgery followed by PDT of GBM has been studied in the clinic (e.g., NCT03048240, NCT03897491, NCT00003788) [143, 169]. Despite promising results, the side effects of PDT remain a major concern [14, 16, 519-521]. We believe the most advantageous, safe initial application of low dose PDT is following tumor resection while patients are in the operating room. In this context, patients will receive PDT

intraoperatively via fiber optic light conduits placed within the resection cavity [143, 169]. Our ultimate goal is to open the BBB and sterilize unresectable, brain-invading tumor cells in real-time, under controlled conditions, during open surgery. Light penetration depth (defined as the depth at which the incident optical energy drops to 37%, 1/e) is typically 1-4 mm in most tissues [125]. Others and we have shown that diffused light (i.e., the remaining 37% optical energy) could reach up to 1.5-2 cm in tissues [185-187]. Wilson, Perria, and Cheng have demonstrated that light (635 nm) activation of porphyrin induces tumor killing up to 1.5 cm deep in the brain [185-187]. In rat brain tissues, we have shown that diffused light (690 nm) can reach up to 1.5-2 cm deep in rat brains to activate VP for effective PDT [22]. This suggests that VP-PDT is sufficient to manage post-surgical residual GBM cells (typically within 1-2 cm from the border of the original lesion) that are responsible for ~80% recurrence. Moreover, the self-limiting depth of effect avoids non-specific priming of the underlying tissue. Rarely, the GBM recurrence occurs distant beyond 2 cm of the resection cavity [522]. For distant recurrence ("ghost" cells) or inoperable GBM, light can be delivered to the entire tumor using stereotactically placed fibers in the clinic [80, 256]. Our next step is to investigate NanoVP-PDT after primary tumor resection to open the BBB and enhance the subsequent delivery of chemotherapy or immunotherapy to invasive, microscopic cancer cells embedded within healthy brain tissues.

7.5 Conclusions

The BBB remains a critical obstacle to the effective treatment of central nervous system diseases, such as GBM—the most common and deadliest form of primary brain cancer in adults. In this study, we report a novel, amorphous, pure-drug nanoparticle of

verteporfin for PDT of GBM and controlled BBB opening in rats. The findings revealed the capability of this new verteporfin nanoformulation to provide a safer and more effective option for cancer PDT and brain drug delivery applications. Our findings demonstrate the capability of this nanoformulation to control the opening of BBB with spatiotemporal precision and no sign of normal tissue injury, providing opportunities for improved delivery of chemotherapies, immunotherapies, nanomedicines to brain tumors.

Chapter 8. Development of a High-Throughput Screening Strategy for Discovery of Human and Zebrafish ABC Transporter Substrates

8.1 Introduction

The human brain, one of the most vascularized organs in the body, is protected from circulating toxins (and potential therapeutics) that might gain entry by specialized capillaries known as the BBB [83]. The BBB is part of a larger and more complex neurovascular unit, composed of endothelial cells, neural cells (i.e., astrocytes, neurons), pericytes, microglia, and the basement membrane. It regulates nutrient transport, maintains brain homeostasis, and protects the central nervous system [81]. The BBB is composed of a physical and active barrier between the circulatory system and the brain parenchyma. Tight junction transmembrane complexes located on the apical region of the intracellular cleft prevent the diffusion of charged, large (>400 Da), and hydrophilic (> 8 hydrogen bonds) molecules between the apical and basal sides of the cell [7, 82]. The endothelial cells are also lined with ABC transporters that redirect toxins and therapeutics back into the bloodstream [110]. ABC transporters, localized to the luminal surface of endothelial cells, transport a wide range of substances against their concentration gradient via ATP hydrolysis [110]. Two of the highly expressed ABC transporters at the human BBB are Pg-p (also known as ABCB1) and ABCG2. The BBB is a major hurdle when delivering therapeutics to the brain [88]. Decades of research has shown the difficulties in treating brain malignancies as many therapeutics cannot successfully enter the brain because they are transported by one or both ABC transporters [523].

Mouse models have consistently demonstrated the major role ABC transporters play in keeping chemotherapeutic agents out of the brain. One of the first murine studies demonstrated deletion of the *Abcb1a* gene resulted in a 20-fold increase in brain vincristine levels compared to wild-type mice [524]. Upon identification of ABCG2 as a major component of the BBB, studies examined the effects of deleting *Abcb1a* and *Abcb1b* (the two murine homologs of human *ABCB1*), *Abcg2* (the murine homolog of human *ABCG2*), or both [525, 526]. Interestingly, these studies suggested cooperativity between the two transporters in keeping substrates out of the brain. In the case of vemurafenib, for example, deletion of *Abcb1a/b* and *Abcg2* resulted in a nearly 20-fold increase in the brain concentration of vemurafenib 24 hours after a 5 mg/kg dose compared to wild-type mice, while deletion of *Abcb1a/b* or *Abcg2* alone resulted in virtually no increase [527]. Despite the growing evidence that these transporters remain a significant impediment to the treatment of brain metastases, no therapies have been approved to increase penetration of chemotherapy drugs into the brain. While mouse models have provided many insights into the roles of ABC transporters at the BBB, mice are expensive to maintain and are not amenable to high-throughput screening. Thus, the development of models that would lead to novel therapies to treat brain metastases would be of importance in the treatment of cancer.

The zebrafish (Danio rerio, Dr) has emerged as a cheaper and more efficient model compared to rodents for studying the role of transporters at the BBB [528, 529]. Similar to humans, zebrafish have a functioning BBB comprised of endothelial cells that form claudin-5 and zona occludens-1 tight junction complexes that limit drug transcytosis [530, 531]. However, zebrafish possess no direct homolog of human

ABCB1; they instead have 2 genes that are closely related: zebrafish *Abcb4* and *Abcb5*[532]. In the case of human *ABCG2*, there are 4 homologs: zebrafish *Abcg2a*, *Abcg2b, Abcg2c* and *Abcg2d* [533]. Our lab has previously characterized the different zebrafish homologs of human ABCB1 and ABCG2, and demonstrated that Abcb4 [534] and Abcg2a have a substrate and inhibitor profile similar those of human proteins, respectively. More importantly, we discovered both Abcb4 and Abcg2a are present at the zebrafish BBB [534]. We have since been developing transgenic zebrafish models of the BBB where firefly luciferase or NanoLuc luciferase expression will be under the control of the glial fibrillary acidic protein promoter, leading to expression in the astrocytes behind the BBB. When the zebrafish BBB is disrupted either by inhibiting ABC transporters at the zebrafish BBB or otherwise increasing permeability, the luciferase substrates will cross the BBB and react with the luciferases, yielding a bioluminescent signal. Prior to a working zebrafish model, we must first determine if luciferase substrates are also ABC transporter substrates. The firefly luciferase substrate luciferin and the NanoLuc substrate coelenterazine are transported by ABCG2 or both ABCB1 [535] and Abcg2 [536], respectively. It is not known if luciferin, coelenterazine, or other coelenterazine analogs are substrates for the zebrafish transporters. In addition, we foresee the firefly luciferase zebrafish model having a much lower sensitivity compared to the NanoLuc luciferase model, as the NanoLuc luciferase reaction is known to be 150-fold brighter [537]. Here, we transfect human *ABCB1* and *ABCG2*, and the zebrafish homologs *Abcg4* and *Abcg2a*, as well as NanoLuc luciferase into HEK-293 cells to allow for complete characterization of the many NanoLuc substrates. The development of this zebrafish and cell-based model

could lead to the discovery of compounds that increase permeability of the BBB via novel mechanisms.

8.2 Methods

8.2.1 Cell Transfection

HEK293 cells (ATCC, Manassas, VA) were transfected with empty pcDNA3.1 vector or with vector containing full length *abcb4* or *abcg2a* (Genscript, Piscataway, NJ) flanked by a FLAG tag. The MDR-19 and R5 cell lines were generated from HEK293 cells transfected with full-length human *ABCB1* or *ABCG2* and has been previously described [538]. Transfected cells were grown in MEM medium (Mediatech, Manassas, VA) and were maintained in 2 mg/ml G418 (Mediatech) and 40 μg/ml hygromycin B. Clones expressing similar levels of ABCB1, ABCG2, Abcb4 or Abcg2a protein were selected based on FLAG and NanoLuc expression as detected by immunoblot.

8.2.2 Immunoblotting

Expression of ABC transporters and NanoLuc luciferase were examined using immunoblotting techniques. Transfected HEK293 cells were plated in 100-mm Petri dish (Falcon) at a density of 31,250 cells/cm^2 for 24 hours. Whole cell lysates (20 μg) were collected in RIPA buffer supplemented with 1% protease inhibitor and heated for 20 minutes at 37°C. Protein lysates were separated on a 4-12% precast Bis-Tris gel (NuPAGE) and transferred onto a nitrocellulose membrane. After blocking with Odyssey blocking buffer (Li-COR) for 1 hour at room temperature, blots were probed with primary antibody against FLAG (Millipore-Sigma, Milwaukee), ABCB1 (C219,

Signet Laboratories, Dedham, MA, 1:250), ABCG2, or β-actin overnight at 4 °C. The blot was then incubated with IRDye 680RD goat anti-mouse secondary antibody (926-68070, Li-COR) or IRDye 800CW goat anti-rabbit secondary antibody (926-32211, Li-COR) for 1 hour at room temperature based on the supplier's advice. Visualization of protein bands was developed using the LiCor ODYSSEY CLx (Li-COR). β-actin serviced as a loading control.

8.2.3 Cytotoxicity Assays

Transfected HEK293 cells were plated in 96 well plates (vendor) at a density of 15,625 cells/cm^2 and were allowed to adhere overnight. Cytotoxic drugs (doxorubicin for ABCB1& Abcb4; THZ1 for ABCG2 & Abcg2a) with or without ABC inhibitors (3 μM elacridar for ABCB1 & Abcb4; 5μM Ko143 for ABCG2 & Abcg2a) were subsequently added in triplicate, and plates were incubated for 72 hours at 37 °C. HEK293 cells not expressing a transporter (Empty vector cells, EV) was used as a control. Cell viability was measured via CellTiter-Glo (Promega, Madison, WI) assay. Luminescence was measured on a microplate reader (Tecan Infinite M200 Pro, Tecan Group) and GI_{50} (50% growth inhibitory) concentration values were calculated as the concentration at which 50% luminescence was observed compared to untreated cells.

8.2.4 High-throughput Substrate Screening

Transfected HEK293 cells were plated in 96 well plates at a density of 31,250 cells/cm^2. The next day, ABC inhibitors (3 μM elacridar for ABCB1 & Abcb4; 5 μM Ko143 for ABCG2 & Abcg2a) or complete media were added in quintuplicate and incubated with cells for 30 minutes at 37 °C. Furimazine, coelenterazine, or

coelenterazine analogs, were subsequently added to the cells at a working solution of 470nM for 1 minute at room temperature. Medium containing ABC transporters and NanoLuc substrates was immediately removed and replaced with fresh cell culture medium. After a 1-minute stabilization period, luminescence was measured on a microplate reader, every minute, for a total of 5 measurements. Brightness of the NanoLuc substrates was measured in EV cells in a similar manor but without the removal of the substrates.

8.3 Results

8.3.1 Establishment and Characterization of HEK293 Cells Stably Expressing an ABC Transporter and NanoLuc Luciferase

To characterize NanoLuc substrate specificity with human ABCB1 and ABCG2, and zebrafish homologs, Abcb4 and Abcg2a, we transfected HEK293 cells with either empty vector plasmid, or vector encoding full-length *ABCB1, abcb4, ABCG2*, or *abcg2a*. Zebrafish transporter proteins both had a 5' FLAG tag. Clones were selected based on reactivity with an anti-FLAG, anti-ABCB1, anti-Abcg2, and anti-NanoLuc antibodies, as shown in **Figure 8.1**. As expected, the FLAG-tagged proteins ran slightly higher than the predicted molecular weight of zebrafish Abcb4 (141 kDa) and Abcg2a (72 kDa). Additionally, all transfected cells expressed low levels of human ABCB1, as HEK293 cells have a small baseline expression.

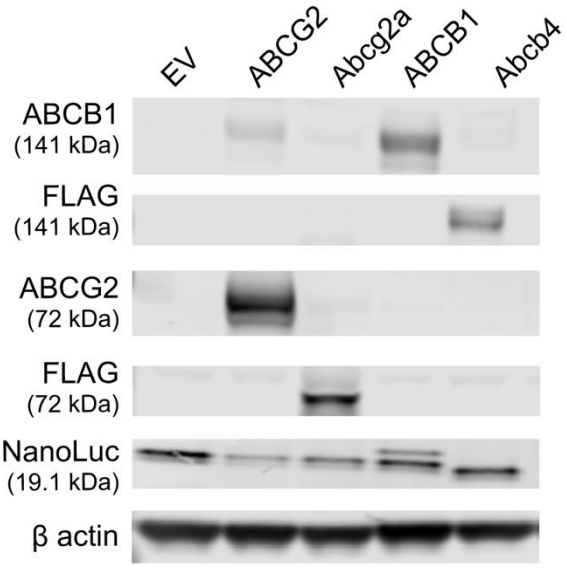

Figure 9.1 Immunoblot of HEK293 Transfected Cell Lines. HEK 293 cells overexpress human Abcg2 and ABCB1, zebrafish Abcg2a and Abcb4, and NanoLuc luciferase.

8.3.2 Chemotherapy cytotoxicity Assessment within Double Transfected Cells

To ensure the doubly transfected cell lines maintain their ABC transporter-mediated efflux capabilities, cytotoxicity assays with known substrates of ABCB1, ABCG2, Abcb4, and Abcg2a were performed. Overexpression of human ABCB1 or zebrafish Abcb4 conferred resistance to doxorubicin (**Figure 8.2b,c**). Incubation with the elacridar inhibitor sensitized both cell lines to the chemotherapy, decreasing the GI_{50} by 47.9- and 23.0- folds, respectively. Similarly, the overexpression of human ABCG2 and zebrafish Abcg2a conferred resistance to THZ1, and the Ko143 inhibitor decreased the GI_{50} by 30.0- and 13.7- fold, respectively. As the zebrafish homolog proteins are not identical to the human transporters, it's not unsurprising that the inhibitors were not as effective in reducing the GI_{50} (summarized in **Table 1**) for the zebrafish transfected cell lines. Alternatively, EV cells not expressing an ABC

transporter were sensitive to both chemotherapeutics (**Figure 8.2a,d**). EV cells incubated with doxorubicin and with or without the elacridar inhibitor, had a GI50 of approximately 0.0285 µM. Similarly, EV cells incubated with THZ1, with or without the Ko143 inhibitor, had a GI50 of approximately 0.0255 µM.

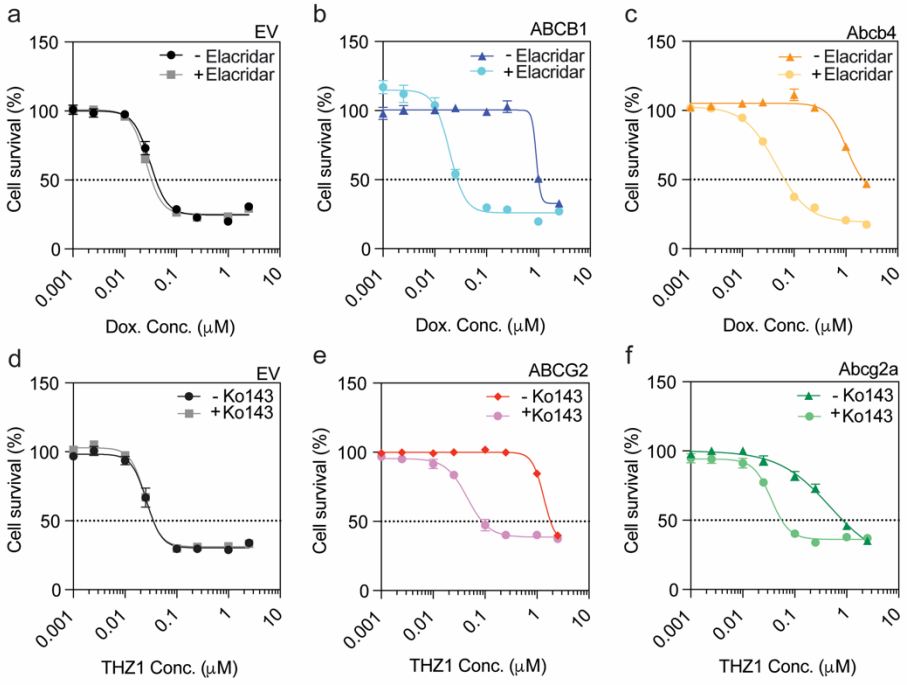

Figure 9.2 Cytotoxicity Screening within Transfected HEK 293 cells. Double transfected cell lines maintain ABC transporter function. Transfected HEK293 cells were incubated with (**a-c**) doxorubicin with or without the elacridar inhibitor, or (**d-f**) THZ1 with or without the Ko143 inhibitor, for 3 days. N ≥ 6, where N equals the number of wells assessed over 3 trials.

Table 9.1 GI_{50} Summary of Transfected HEK293 cells. GI_{50} values for (**a**) doxorubicin and (**b**) THZ1.

a

GI_{50} Dox (µM)	- Elacridar	+Elacridar	fold change
EV	0.031	0.026	1.19
ABCB1	0.91	0.019	47.89
Abcb4	1.036	0.045	23.02

b

GI_{50} THZ1 (µM)	- KO143	+KO143	fold change
EV	0.026	0.025	1.04
ABCG2	1.352	0.045	30.04
Abcg2a	0.48	0.035	13.71

8.3.3 High Throughput Screening of NanoLuc Substrates

The zebrafish larva brain at 5 days post fertilization is only ~1.5 mm in length and ~500 μm in thickness [539]. Foreseeing sensitivity problems within the future in vivo assay, we first determine which NanoLuc substrates will produce the brightness luminescence signal. A panel of coelenterazine analogs were evaluated within EV cells. Furimazine, the substrate specifically developed to react with NanoLuc luciferase produce the brightness luminescence signal which was 35.9-fold larger than native coelenterazine (**Figure 8.3**). In fact, 4 other coelenterazine analogs produced a greater signal than native coelenterazine. The substrates that produced the smallest signal, coelenterazine-cp and coelenterazine-n, had a luminescence value that was 99.4% and 97.3% smaller than furimazine.

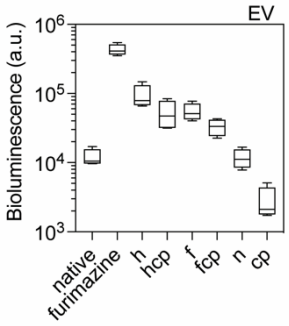

Figure 9.3 Bioluminescence Signal of Native Coelenterazine and its Analogs. HEK 29 cells that were transfected with NanoLuc luciferase but not an ABC transporter were incubated with a panel of luciferase substrates. $N \geq 6$, where N equals the number of wells assessed over 3 trials.

Next, we determined if the NanoLuc substrates are also substrates for ABC transporters. Native coelenterazine and the 4 analogs that produced the largest bioluminescence signal (furimazine, coelenterazine-h, coelenterazine- hcp, coelenterazine-f) were screen in the panel of transfected cells. The bioluminescence

signal was measured every minute over a 5-minute period and the area under the curve was calculated (**Figure 8.4**). Native coelenterazine was a positive control as it was previously determined to be a substrate for both human ABCG2 and ABCB1. As seen in **Figure 8.4a**, native coelenterazine was a substrate for all 4 ABC transporters. The addition of an ABC inhibitor did not impact the bioluminescence signal produced by native coelenterazines within EV cells, but significantly increased the signal within all 4 transfected lines. Furimazine, which produced the largest bioluminescence signal in EV cells, was determined to be a substrate for both human ABCG2 and zebrafish Abcg2a, but not ABCB1 nor Abcb4 (**Figure 8.4b)**. Similarly, coelenterazine-h was only a substrate for ABCG2 and Abcg2a (**Figure 8.4c)**. Alternatively, coelenterazine-f was only a substrate for ABCG2 (**Figure 8.4d)**. Lastly, coelenterazine-hcp was only not a substate for ABCB1 (**Figure 8.4d)**. All NanoLuc substrates that screened were substrates for human Abcg2, while the majority were not substrates for human ABCB1. Similarly, the NanoLuc substrates were more likely to be a substate for zebrafish Abcg2a compared to Abcb4.

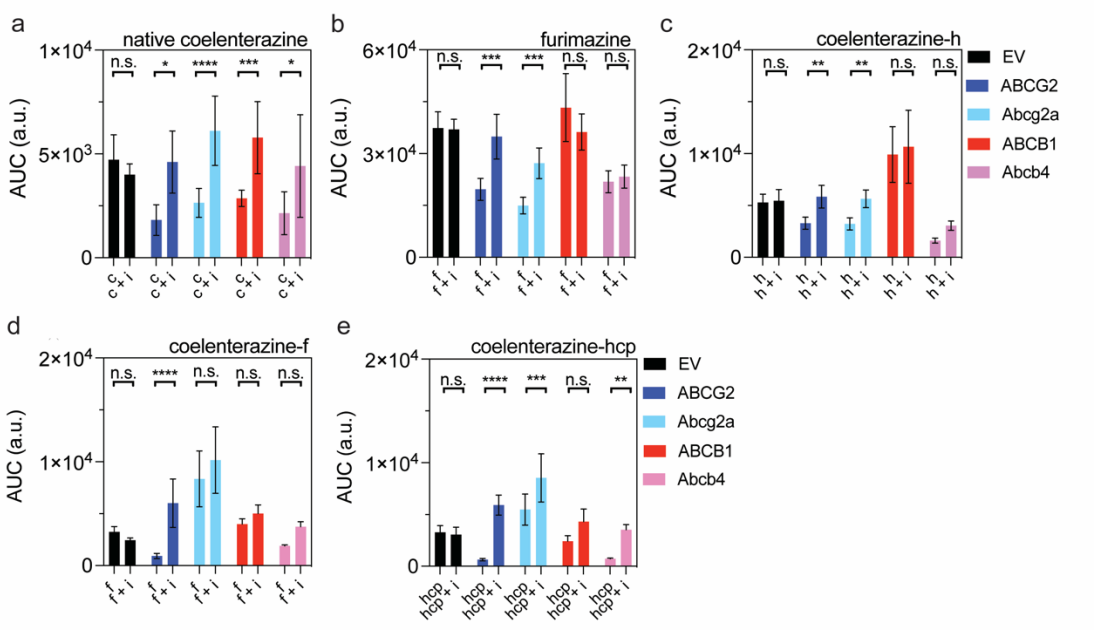

Figure 9.4 ABC Substrate Screening. A panel of transfected cells were incubated with (**a**) native coelenterazine and (**b-e**) coelenterazine analogs Substrates (c, f, h, f, or hcp) with and without ABC transporter inhibitors (+ i) were incubated with cells over expressing the 4 different ABC transporters for 5 minutes. The area under the curve of the bioluminescence signal was calculated from 5 different time points. $N \geq 6$, where N equals the number of wells assessed over 3 trials.

While it's important to determine which NanoLuc substrates are ABC transporter substrates, its equally important to determine the degree of which they are effluxed. Although a substate may produce a large bioluminescence, if it is a weak ABC substate, it can lower the specificity of the in vivo model. NanoLuc substrates that are not substrates for the ABC transporters will have a lower percent increase in bioluminescence near 0%, while strong substrates that are largely effluxed from the cell will have a percent increase in bioluminescence greater than 100% (**Figure 8.5**). EV cells incubated with all the NanoLuc substrates with or without an ABC inhibitor had a ~0% increase. The largest percent increase in bioluminescence occurred when coelenterazine-hcp was incubated with cells over expressing ABCG2 and the Ko143

inhibitor, at ~729.8±405.7% (**Figure 8.5e**). The largest percent increase for zebrafish Abcg2a and Abcb4 were coelenterazine-h at 97.3±45.7% (**Figure 8.5c**) and coelenterazine-hcp at 338.7±180.3%, respectively (**Figure 8.5e**).

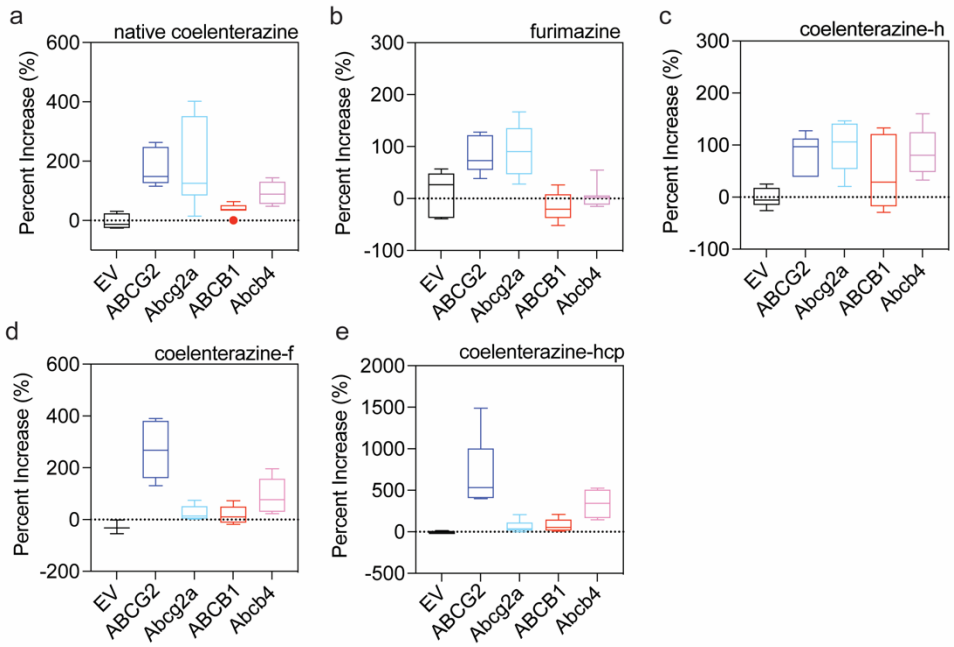

Figure 9.5 Bioluminescence Signal Percent Increase. Transfected HEK293 cells were incubated with (**a**) native coelenterazine or a (**b-e**) coelenterazine analog with and without an ABC transporter inhibitor (Ko143 for ABCG2 and Abcg2a; elacridar for ABCB1 and Abcb4). A single bioluminescence measurement at 5 minutes post incubation was used to calculate percent increase. N ≥ 6, where N equals the number of wells assessed over 3 trials.

8.4 Discussion and Conclusions

Treatment options for diseases of central nervous system remain limited [540]. Most therapeutics cannot effectively enter the brain on their own because of the intact BBB [541]. The endothelial cells of the BBB form tight junctions that restrict the passage of molecules [95]. Additionally, at the apical surface, the ABC transporters ABCB1 and ABCG2 work in concert to transport substrates back into the bloodstream and prevent access to the brain [542]. A number of chemotherapeutic agents are

substrates for one or both of the transporters. This includes traditional chemotherapies such as paclitaxel, vinblastine, etoposide, colchicine and doxorubicin but also targeted therapies such as erlotinib, lapatinib and vemurafenib that have been approved to treat metastatic cancers of the lung, breast or melanoma, respectively [543-545]. Despite the clear need to develop treatment modalities to increase brain penetration of approved therapies, little progress has been made.

Zebrafish offer a unique model to study transporter activity at the BBB. Our lab has recently discovered zebrafish Abcg2a and Abcb4 [534] transporters are present at the BBB and function similarly to their human homologs, ABCG2 and ABCB1, respectively. We are currently developing a transgenic zebrafish model that relies on NanoLuc luciferase luminescence to study the functions of these ABC transporters and BBB permeability. Once established, we see the potential for this model to be used for many applications that would impact public health by increasing our understanding of this critical physiological barrier and increasing brain penetration of cancer therapies. The transgenic fish could be used in high-throughput screens for inhibitors of ABCB1 and ABCG2 at the BBB and would directly measure brain penetration of a small molecule caused by transporter inhibition. To our knowledge, this would be the first high-throughput assay to measure BBB penetration in a living organism. One of the major advantages of this system is that the transgenic fish can be used to identify not only direct inhibitors of transporter proteins at the BBB, but any compounds that might increase permeability of the BBB to small molecules. For example, adenosine A2A receptor agonists have been shown to modulate transporter expression at the BBB without directly inhibiting the transporters [546]. The zebrafish model proposed here

would have utility in identifying similar compounds, unlike cell-based assays that can only measure direct inhibition. Additionally, this model could be used to assess the ability of novel methods—such as nanoparticles—to deliver chemotherapy to the brain. However, prior to a working zebrafish model, it is necessary to determine if NanoLuc luciferase substrates are also substrates for the zebrafish ABC transporters present at the BBB.

Native coelenterazine and its analogs contain an imidazopyrazinone core, a nitrogen-bearing heterocycle, and three side groups [547]. Although there are only slight differences within the side groups corresponding to different amino acid side chains, the panel of coelenterazine analogs produced bioluminescence signals that were up to 155.7-fold different from each other. The zebrafish larva brain at 5dpf is extremely small, limiting the number of astrocytes that would express Nanoluc luciferase. Foreseeing sensitivity problems within the in vivo model due to a small bioluminescence signal, we first tested a panel of NanoLuc substrates within EV cells. As expected, cells incubated with furimazine, a substrate engineered to react with NanoLuc, produced the largest luminescence. Cells incubated with native coelenterazine produced a luminescence that was 35.9-fold smaller than furimazine. High-throughput screening experiments revealed all the NanoLuc substrates tested were also substrates for human ABCG2. Only native coelenterazine was a substrate for human ABCB1. More importantly, we identified that native coelenterazine, furimazine, coelenterazine-h, and coelenterazine-hcp were substrates for zebrafish Abcg2a, while coelenterazine-f was not a substrate. Similarly, native coelenterazine and coelenterazine-hcp were substrates for zebrafish abcb4. Using different Nanoluc

substrates (which are also ABC transporter substrates) within the in vivo zebrafish model could lead to differences in sensitivity and specificity when screening unknown ABC inhibitors. The largest percent increase in bioluminescent for zebrafish Abcg2a and Abcb4 were coelenterazine-h at and coelenterazine-hcp. Although furimazine produced the largest bioluminescent signal, other coelenterazine analogs that are stronger ABC transporter substrates may be more helpful in understanding BBB permeability.

In Summary, the development of a transgenic zebrafish can increase our understanding of drug delivery to the brain. Identifying which luciferase substrates are effluxed by ABC transporters present at the zebrafish BBB is the first step to engineering this novel model.

Chapter 9. Conclusions and Contributions to Science

The invasive GBM cells that invade outwards into the healthy brain play a major role in disease recurrence. A vast amount of research has been dedicated to figuring out methods to eradicate these invasive cells. The fluorescence guided resection of the primary tumor has extended patient survival but does not adequately address the invasive nature of the disease. The intact BBB limits the ability of chemotherapy to accumulate in the invasive GBM cells and kill them. Numerous methods have been developed to open the BBB for the enhanced delivery of chemotherapy, but none are universally available in the clinic. Many of these BBB opening methods are lack specificity, have low efficacy, or can induce healthy tissue damage. PDT using the photosensitizer ALA-induced PpIX has shown promise in opening the BBB and treating GBM. However, the limited activation depth of PpIX in the brain stops the treatment from reaching the majority of the invasive cancer cells. In addition, large and non-optimized PDT doses within the brain can also result in healthy tissue damage. Here, we determined the activation depth of the clinically relevant VP photosensitizer in the rodent brain. We examined the mechanisms behind low dose PDT-mediated BBB opening in a transwell model. Furthermore, we engineered a novel pure-drug carrier-free nanoparticle of VP for improved cancer cell uptake and PDT treatment. We examined both PDT and PDP treatment within a subcutaneous GBM mouse model and intracranial rat model. Finally, we aided in the development of a high throughput zebrafish model that will allow us to study BBB integrity in mor detail.

9.1 Verteporfin can be Activated Up to 2 cm in the Rodent Brain

FGR of GBM is routinely utilized in clinical centers around the world, whereas PDT treatment for GBM has yet to reach universal clinical implementation and remains an active area of preclinical and translational investigations. One of the major challenges to clinical use of PDT for brain cancer is the limited light penetration depth in brain tissues. To address this shortcoming, in **Chapter 3**, we developed Liposomal protoporphyrin IX and Liposomal verteporfin and evaluated their photodynamic effects as a function of depth in tissue and light fluence using rat brains. Although red light penetration depth (defined as the depth at which the incident optical energy drops to 1/e, ~37%) is typically a few millimeters in most tissues, we show that the remaining optical energy could induce PDT effects up to 2cm into brain tissues. Photobleaching and singlet oxygen yield studies suggest that deep-tissue PDT (>1cm) is more effective when using Liposomal VP, compared to Liposomal PpIX. Together, these findings suggest that Liposomal VP based PDT is more likely to generate cytotoxic effects deep within the brain and offer the possibility of treating brain invading tumor cells centimeters away from the main, resectable tumor mass. Fluorescence imaging revealed ALA-induced PpIX remains the ideal choice for the FGS of GBM.

9.2 PDP-induced Blood-brain Barrier Opening Enhances Drug Delivery

The BBB remains a major obstacle for drug delivery to the central nervous system. In particular, the tight and adherens junctions that join the brain capillary endothelial cells limit the diffusion of various molecules from the bloodstream into the

brain. PDP is a non-cytotoxic modality that involves light activation of photosensitizers to photochemically modulate nearby molecules without killing the cells. In **Chapter 4**, we investigated the effects of sub-lethal photochemistry on junction phenotype (i.e., continuous, punctate, or perpendicular), as well as the BBB permeability in a transwell model of HBMECs. We showed that PDP decreases the mature continuous junction architecture by ~20%, increases the immature perpendicular junction architecture by ~40%, and has minimal impact on cell morphology in HBMECs. Furthermore, transwell permeability assay revealed that PDP improves the HBMEC permeability to dextran or nanoliposomes by up to 30-fold for 6-9 days. These results suggest that PDP could safely reverse the mature brain endothelial junctions without killing the HBMECs. This study not only emphasizes the critical roles of PDP in the modulation junction phenotype, but also highlights the opportunity to further develop PDP-based combinations that opens the cerebrum endothelium for enhanced drug transporter across the BBB.

9.3 Combinations of Photosensitizing Biomolecules may increase PDT Efficacy, but Limits Cellular Accumulation

Many photosensitizers including VP are hydrophobic and require a drug delivery vehicle for patient administration. Photosensitizing biomolecules (PSBM) represent a new generation of light-absorbing compounds that could improve optical and physicochemical properties for biomedical applications. Despite numerous advances in lipid-, polymer-, and protein-based PSBMs, their effective use requires a fundamental understanding of how macromolecular structure influences the physicochemical and biological properties of the photosensitizer. In **Chapter 5**, we

prepared and characterized three well-defined PSBMs based on the photosensitizer, VP. The PSBMs include 16:0 lysophosphocholine-VP (16:0 Lyso-PC-VP), *distearoylphosphoethanolamine-polyethylene-glycol*-VP (DSPE-PEG-VP), and anti-EGFR cetuximab-VP (Cetuximab-VP). In two glioma cell lines, DSPE-PEG-VP exhibited the highest singlet oxygen yield but was the least phototoxic due to low cellular uptake. 16:0 Lyso-PC-VP had the highest PDT efficacy but redirected VP's subcellular localization from mitochondria to lysosomes. At 24 hours after incubation, proteolysed Cetuximab-VP was localized to mitochondria and effectively disrupted the mitochondrial membrane potential upon light activation. Our results reveal the cellular uptake, variable trafficking, and end effects of PSBMs, provide valuable insights into methods of PSBM evaluation, as well as strategies to select PSBMs based on subcellular targets and cytotoxic mechanisms. We ultimately demonstrated that PSBMs reduced cancer cell uptake and PDT killing compared to free-form VP, however, biologically informed combinations that target different organelles, concurrently, may lead to enhanced therapeutic effects.

9.4 Pure-drug Carrier-free Nanoparticles of Verteporfin have Superior PDT Efficacy Compared to Liposomes

A variety of photosensitizers have been investigated and marketed for PDT of cancer. Since the FDA approved the first and only nanoformulation of photosensitizer—Liposomal VP—for PDT of macular degeneration 20 years ago, significant advancements have occurred in our understanding of photosensitizer delivery. While liposomes significantly increase the ability of water-insoluble photosensitizers to achieve a clinically relevant concentration in aqueous media,

liposomes enclosed by phospholipid bilayers could also hinder the uptake and photochemical activity of photosensitizers in cells. In **Chapter 7**, we report a facile surfactant-free method to prepare amorphous nanodrug of VP (NanoVP) with 100% active pharmaceutical ingredients and nearly 1,500-fold higher photosensitizer-loading capacity compared to standard Liposomal VP. Monodispersed NanoVP is self-quenched during storage in saline solution and can be de-quenched in cells, enabling PDT and fluorescence imaging of cancer cells. We demonstrate up to 10-fold enhancement in anti-tumor PDT efficacy of NanoVP compared to Liposomal VP in GBM cells and mouse models. Importantly, we also reported that low dose NanoVP-PDT priming can be used for safe, localized, and controlled BBB opening, increasing Evans Blue accumulation in rat brains by 5.5-fold, compared to using FDA-approved ALA-induced PpIX photosensitizer. Collectively, the NanoVP represents a next-generation versatile photosensitizer formulation and may facilitate treatment strategies for brain tumors and invasive central nervous system diseases that are protected by the intact BBB.

9.5 A High Throughput Zebrafish Model aids in the Study of BBB Integrity

The BBB represents a significant impediment to the treatment of brain cancers and cancers that have metastasized to the brain. Brain diseases are so intractable due to, in part, the expression of ABC transporters at the BBB. The ABC transporter family is comprised of 48 members that use ATP to transport substrates against a concentration gradient. Two transporters that are found at very high levels at the BBB are P-gp (or ABCB1, encoded by the *ABCB1* gene) and the ABCG2 (encoded by the *ABCG2* gene). Counted among the substrates of P-gp and ABCG2 are a number of traditional

chemotherapeutic agents including paclitaxel, vinblastine, vincristine, doxorubicin and daunorubicin as well as a number of targeted therapies such as erlotinib, lapatinib and vemurafenib [110].

Knockout mouse models have consistently demonstrated the major role ABC transporters play in keeping chemotherapeutic agents out of the brain. However, mouse models cannot be used to perform high-throughput studies. Recent reports have suggested that the Zebrafish (*Danio rerio)* BBB is a useful surrogate for the human BBB. The zebrafish BBB contains claudin-5 tight junction complexes and ABC transporter homologs that restrict many of the same chemotherapeutics from entering the brain. In **Chapter 8**, we develop a high throughput cell-based assay to study NanoLuc luciferase and ABC transporter substrates. Screening revealed that all coelenterazine analogs tested were substrates for human ABCG2 and the majority were substrates for zebrafish Abcg2a. Only 2 coelenterazine analogs were substrates for zebrafish Abcb4. Foreseeing sensitivity problems with the zebrafish model, we determined that furimazine produced a 35.9-fold larger bioluminescent signal than native coelenterazine. Determining if luciferase substrates are also ABC transporter substrates is a critical first step in the development of a transgenic zebrafish model. We see the potential for this model to be used for many applications that would impact public health by increasing our understanding of this critical physiological barrier and increasing brain penetration of cancer therapies.

9.6 Closing Remarks

Overall, this dissertation advocates for the addition of NanoVP-mediated PDP into the clinical workflow for GBM. Evidence suggests that NanoVP-mediated PDP

can open the BBB for the enhanced delivery of drugs to the brain. Incorporating this BBB opening method can allow for a dose reduction of TMZ as more will be able to reach the invasive cells. In addition, other chemotherapies that normally can't cross the BBB could then be used. NanoVP-mediated PDT can also be used for eradicating remaining GBM cells after surgery. Given that the feasibility of PDT has already been demonstrated in the clinic for the treatment of GBM and that fluorescence guided resection already relies on the necessary equipment, leveraging NanoVP for PDP and PDT treatments can help address the challenges associated with standard chemotherapy. Further investigations into multicycle treatments are warranted to fully exploit NanoVP as a PDT and PDP agent.

9.7 Contributions to the Field

9.7.1 Scientific Contributions

The work in this dissertation makes the following contributions to the understanding of drug delivery and PDT:

- Established that 690nm light activation of VP can occur at deeper depths, up to 2 cm, in the rat brain compared to 635nm light activation of PpIX (**Chapter 3**);
- Established that light activation of VP results in a ~1.7-2.5-fold higher production of $^1O_2$ than PpIX *in situ* (**Chapter 3**);
- Established that low dose VP-mediated PDT increases the permeability of 100nm liposomes in a transwell model without killing the endothelial cells (**Chapter 4**);

- Established that low dose VP-mediated PDT increases the amount of immature perpendicular cell-cell junction and simultaneously decreases the amount of mature continuous junction (**Chapter 4**);
- Established that covalent conjugation of VP to three different biomolecules decreases cellular uptake compared to free-form VP (**Chapter 5**);
- Established that total VP uptake better predicates PDT efficacy than in situ $^1O_2$ production (**Chapter 5**);
- Established that dual targeting mitochondria and lysosome during PDT treatment can result in enhanced cell killing (**Chapter 5**);
- Established that pure-drug nanoparticles of VP (NanoVP) have superior PDT efficacy than Liposomal VP as a direct result of increased cell accumulation (**Chapter 7**);
- Established that low dose NanoVP-mediated PDP can open the rat BBB without causing major healthy tissue damage (**Chapter 7**);
- Established that the majority of coelenterazine analogs were substrates for human ABCG2 and zebrafish Abcg2a while only one was a substrate for human ABCB1 and two were substrates for zebrafish Abcb4 (**Chapter 8**);

Table 10.1. Summary of Contributions to the field.

Chapter	Considerations	Current methods	Gaps in the field	Our current contribution
3	**Activation depth of photosensitizers**	Necrosis (histology staining after PDT treatment), photon detection	Labor and time intensive. Only focus on light not PS.	Comparing the activation depth of two PS's using an ex vivo model. (**Inglut C.**, Gaitan B., et al., Photochem. and Photobio. 2020)
4	**BBB modulation**	BBB opening (osmotic solutions, ultrasound, targeted nanoparticles), Convection-enhanced, Interstitial delivery	Low efficacy, invasive, healthy brain damage	Using low doses of PDT, known as priming, to modulate tight junctions. (**Inglut C.**, Gray K. et al, IEEE J Sel Top Quantum Electron. 2020)
5-7	**Photosensitizer delivery & PDT applications**	PDT for GBM relies on pro-drug, ALA. Gold standard to deliver VP is via liposomes	Long term GBM survival has not been achieved with either formulation.	Development of a pure drug nanoparticle & understanding liposome design parameters. **(Inglut C.**, Baglo Y., et al, J Clin Med. 2019) (**Inglut C.**, et at., Nanomaterials. 2020) **(Inglut C.**, et al., Submitted)
8	**BBB modeling**	Mouse model, cell culture model, organ on a chip	Mice are expensive and total variables are limited. Cell culture doesn't accurately represent BBB.	A zebrafish model to examine ABC transporter substrates and inhibitors. (**Inglut C.**, et al., In preparation)

9.7.2 Peer-Reviewed Journal Publications

Published manuscripts:

- **Inglut C.T**., Goodfriend (Gray) K.M., Vig S., Jung J.W., Stabile J., Zhang Y., Stroka K.M., Huang H.C. "Photodynamic Priming Modulates Endothelial Cell–Cell Junction Phenotype for Light-activated Remote Control of Drug Delivery" *IEEE JSTQE*. 2020.
- **Inglut C.T**., Sorrin A.J., Kuruppu T., Vig S., Cicalo J., Ahmad H., Huang HC. "Immunological and Toxicological Considerations for the Design of Liposomes" *Nanomaterials*. 2020.
- Gaitan B., **Inglut C.T**., Liu Y., Chen Y., Huang H.C. "Depth Resolved Imaging of Photosensitizer in the Rodent Brain using Fluorescence Laminar Optical Tomography" *J. Biomed. Opt.* 2020.
- Goodfriend (Gray) K.M., Jung J.W., **Inglut C.T**., Huang H.C., Stroka K.M. "Quantitatively Relating Brain Endothelial Cell-Cell Junction Phenotype to

Global and Local Barrier Properties Under Varied Culture Conditions via the Junctional Analyzer Program" *Fluids and Barriers of the CNS*. 2020.

- **Inglut C.T**.[+], Baglo Y. [+], Liang B.J., Cheema Y., Stabile J., Woodworth G.F., Huang H.C. "Systematic Evaluation of Light-Activatable Biohybrids for Anti-Glioma Photodynamic Therapy" *J. Clin. Med.* 2019. (+, equal contribution)
- **Inglut C.T.** [+], Gaitan B. [+], Najafali D., Lopez I.A., Connolly N.P., Orsila S., Perttilä R., Woodworth G.F., Chen Y., Huang H.C. "Predictors and Limitations of the Penetration Depth of Photodynamic Effects in the Rodent Brain" *Photochem Photobio*l. 2019. (+, equal contribution)
- Stabile J., Najafali D., Cheema Y., **Inglut C.T**., Liang B.J., Vaja S., Sorrin A.J., Huang H.C. "Engineering gold nanoparticles for photothermal therapy, surgery, and Imaging. In Nanoparticles for Biomedical Application - Fundamental Concepts, Biological Interactions and Clinical Applications" *Elsevier: Chapter 12. Chung EJ and Rinaldi C, editors*. 2019.

Submitted manuscripts:

- **Inglut C.T**., Quinlan J., Rahman I., Stable J., Gaitan B., Srivastava P., Chiou W., Karim B., Connolly N., Robey R., Woodworth G., Gottesman M., Huang H.C. "Carrier-free, amorphous verteporfin nanodrug for enhanced photodynamic cancer therapy and brain drug delivery" *Submitted to Advanced Materials*. 2022.
- Gaitan B., **Inglut C.T**., Kanniyappan U., Xu H., Li L., Huang H.C., Chen Y. "Development of an endoscopic auto-fluorescent sensing device to aid in the

detection of breast cancer and inform PDT treatment". *Submitted to IEEE Transactions on Biomedical Engineering*. 2022.

Manuscripts in preparation:

- **Inglut C.T**., Quinlan J., Robey R., Thomas J., Huang H.C., Gottesman M. "Development of a High-Throughput Screening Strategy for Discovery of Human and Zebrafish ABC Transporter Substrates". *In Preparation*. 2022

9.7.3 National and International Conference Presentations

(* denotes presenter)

- "Clinically Relevant Pure Porphyrin Nanoparticles for Photodynamic Therapy and Priming Applications". **Inglut C**[*], Quinlan J, Rahman I, Stable J, Gaitan B, Srivastava P., Chiou W, Karim B, Connolly N, Robey R, Woodworth G, Gottesman M, Huang HC. *SPIE Photonics Europe*, Strasbourg, France, April 2022.
- "Photodynamic Modulation of Bidirectional Drug Transport Across the Blood-Brain Barrier". **Inglut C**, Liang B**,** Huang HC[*]. *ASP 2021 Symposium - 20th Anniversary for Theresa Busch*. June 2021.
- "Photodynamic Therapy for Brain Cancer: Tissue Penetration and Blood Brain Barrier Modulation". **Inglut C**[*], Gaitan B, Gray K, Najafali D, Stabile J, Lopez IA, Jung J, Stroka K, Chen Y, Huang HC. *2019 BMES. Cancer Drug Delivery* (Cancer Technologies; Drug Delivery), Philadelphia, PA, October 2019.
- "Photosensitizing Biomolecules and Nanocrystals for Anti-Glioma Photodynamic Therapy". **Inglut C**[*], Baglo Y, Liang BJ, Stabile J, Cheema Y,

Najafali D, Woodworth GF, Huang HC*17th International Photodynamic Association World Congress*, Cambridge, MA, July 2019.

Chapter 10. Future Work and Outlook

The work in this dissertation has motivated several additional projects and new areas of research, many of which will contribute to a more comprehensive

understanding of drug delivery, BBB opening and modeling, and PDT treatment. For example, **Chapter 5** focused on the development and characterization of VP-biomolecules. While different combinations of VP-biomolecules have the potential to increase PDT efficacy, it was determined that covalent conjunction of VP to biomolecules decreased cellular uptake. Two additional research projects lead by fellow lab mates, Dr. Barry Liang and Dr. Yan Baglo, examined ways to overcome the downsides of the new VP-biomolecules. Their research focused on enhancing delivery of antibody-VP conjugates to cancer cells via the "carrier effect" [548] and escaping ABC transporter-mediated cellular efflux using lipid-VP conjugates [196]. Several of the future projects that were motivated by the results introduced in this dissertation are discussed below and preliminary results are presented.

10.1 The Treatment of Intracranial Brain Tumors

A logical extension of the work presented in this dissertation is the treatment of brain tumors with NanoVP-mediated interstitial PDT. For interstitial PDT one or more laser fibers can be inserted into the brain, through the primary tumor or near the invasive GBM cells. Light can be delivered through the end of the fiber or throughout a fiber with a cylindrical diffuser. Interstitial PDT could help overcome light penetration concerns as the light source is now at the center of the tumor instead of the resection cavity edge. Additionally, interstitial PDT could be more useful than surface illumination PDT if MRI imaging reveals the majority of the infiltrative cancer cells are localized to one area/path. In a small-scale clinical trial that examined interstitial PDT for recurrent GBM treatment, 4 out of 10 patients survived over 24, when the expected survival is only 6-8 months [549].

Preliminary studies of the treatment of intracranial brain tumors have been performed using NanoVP-mediated interstitial PDT. Here, U87 cells were implanted

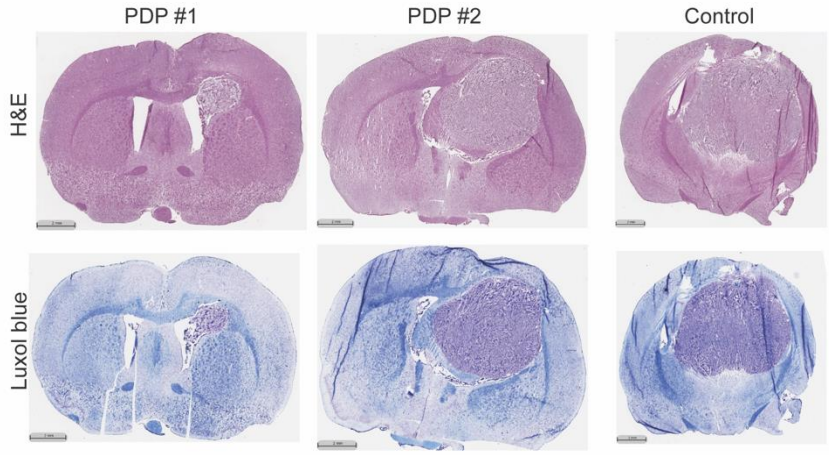

Figure 11.1 NanoVP-mediated Interstitial PDP Treatment does not Result in Healthy Tissue Damage. U87 cells were implanted into the rat brain and were treated with interstitial PDP 10 days later. 24 hours post treatment, brains were harvested and cryosection. N =1-2 mice.

into the brains of two rats. Approximately 10 days later when the tumor is expected to fill most of the right brain hemisphere, treatment was performed. Rats were administering a low dose of NanoVP (0.25 mg/kg) and 30 minutes later PDT (40 J, 100 mW) was performed using a single laser fiber that was inserted into the same burr hole used for tumor implantation. A single rat that had the laser fiber inserted into the brain but didn't receive PDT treatment was used as a control. After treatment, the incisions were closed, and rats were allowed to recover for 24 hours. The rats were then euthanized, and the brains harvested. Cryosections of the brain were stained with H&E or Luxol faster blue (methods described in *Section 7.2.15*). Results revealed the two treated animals had a tumor diameter of 5.4 mm^2 and 45.3 mm^2 while the control animal had a tumor diameter of 95.8 mm^2. More importantly, no signs of brain damage surrounding the tumor were present in the PDT treated animals.

Future work for this project includes combining PDP and PDT. First interstitial PDP can be performed to open the BBB and enhance the delivery of NanoVP to the tumor. After varying VP accumulation via fluorescence imaging, a second PDT does can be performed to kill the remaining cancer cells. Additionally, a larger dose of NanoVP can be administered to exploit VPs chemotherapeutic effects (discussed in *Section 7.3.3* and *10.4*)

10.2 PDP Synergizes with Irinotecan and Minocycline

Irinotecan is an effective salvage chemotherapy for GBM patients with a compromised BBB. Irinotecan functions as a topoisomerase I (Top1) inhibitor, trapping the Top1 DNA cleavage complex which causes double-stranded DNA breaks and cell death. However, the full potential of irinotecan remains to be hindered by the inability to cross the intact BBB, the overexpression of DNA damage repair enzymes (i.e., tyrosyl-DNA phosphodiesterase 1, Tdp1 [550]) and normal tissue toxicity. A two-prong strategy to overcome these challenges includes: (1) The selective and reversible opening of the BBB with non-cytotoxic PDP; and (2) The repurposing of minocycline, a Tdp1 inhibitor and a neuroprotective agent. Minocycline, a broad-spectrum antibiotic, has been shown to inhibit the expression of Tdp1, enhancing the potency of irinotecan [198]. The central hypothesis is that the photo-activatable delivery of mechanism-based combinations in a spatiotemporally controlled manner will supersede the blind administration of cytotoxic cocktails.

Previous studies have shown the ability of PDP to synergize with irinotecan for the treatment of pancreatic tumors [175]. In addition, studies have shown that irinotecan and minocycline synergize for the treatment of ovarian cancer [198]. Here,

we examine the effectiveness of the triple combination for the treatment of GBM *in vitro and in vivo*. First, the three free-form drugs were tested in cell culture. U87 cells were plated and allowed to adhere overnight. The next day 12 μM irinotecan, 30 μM minocycline, and/or 0.25 μM VP were added to the cell. On day 3, PDT (0.25 J/cm^2, 10 mW/cm^2) was performed and on day 5, cell viability was assessed via MTT assay. Results show all dual therapies deceased cell viability more than monotherapies and the triple therapy modestly decreases cell viability compared to dual therapies, although only significantly more than minocycline + PDT (**Figure 10.2**). This is unsurprising as the dual therapies have already shown to be synergistic in other cancer types. Differences in cell viability can be further increased by optimizing the treatment timeline, as pretreatments with minocycline might be necessary to decrease the expression of Tdp1.

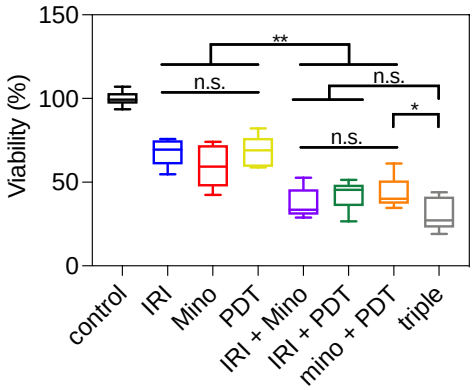

Figure 11.2 Triple Combination Treatment within U87 Cancer Cells. U87 cells were incubated with irionotecan (IRI), minocycline (mino), and/or VP (PDT) for 72 hours. n = 4, *P < 0.05, **P < 0.01, n.s.: nonsignificant.

Knowing the dual therapies can well manage tumor growth, we next test the triple combination in an aggressive subcutaneous mouse model. Here, GBM39 tumors

that were grown and continually passaged in the mouse flank were dissociated and implanted into new mice. Treatment began thirteen days after implantation, when tumors reached approximately 120 mm^3 (**Figure 10.3**), minocycline (40 mg/kg) was orally administered for 12 consecutive days (days 13-24). On days 17 and 24, Liposomal VP (0.25 mg/kg) and Liposomal irinotecan (20 mg/kg) were intravenously administered, and 2 hours later, PDT (50 J/cm^2, 50 mW/cm^2) was performed. Results from this study indicate that the addition of PDP to irinotecan and minocycline treatment modestly decreases tumor volume (**Figure 10.4**). Compared to the PDT treatment performed in *Section 7.3.4* that resulted in noticeable necrosis, PDP left no signs of damage. Due to the aggressive nature of this patient derived cell line and beginning the treatment regimen when tumors were already above 100 mm^3, it is not surprising the triple combination did not effectively manage tumor growth. Usually, PDT and chemotherapy treatments are administered when the tumor is 50-100 mm^3. Here, the fist cycle of PDT and irinotecan was administered when the tumors were ~200 mm^3.

Future work for this project, being conducted by Sumioa Pang and Dr. Payal Srivastava, includes identifying cancer types with a high Tdp1 and Top1 activity ratio and engineering a nanoparticle that contains all three active pharmaceuticals: VP, irinotecan, and minocycline.

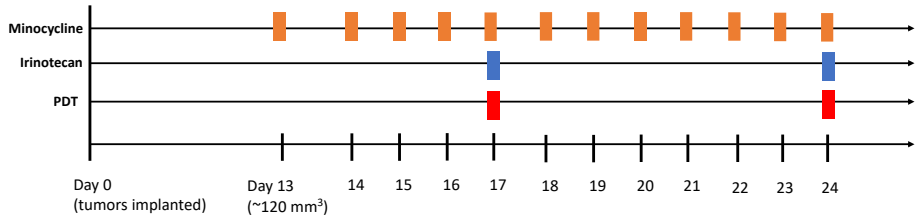

Figure 11.3 In Vivo Treatment Timeline. On day 13 post tumor cell implantation, animals received minocycline (40 mg/kg, oral), irinotecan (20 mg/kg, IV), and VP-mediated PDP (0.25 mg/kg, 50 J/cm^2, 50 mW/cm^2).

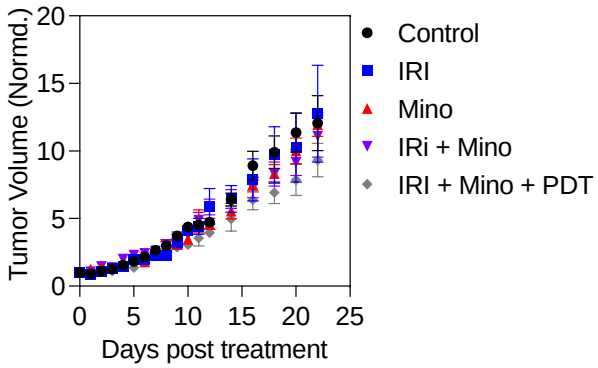

Figure 11.4 GBM39 Normalized Tumor Volume. Minocycline treatment began on day 0. PDT and irinotecan were administered on days 4 and 11. n=4-6 animals per group. *Performed with help from Sumiao Pang.*

10.3 A Second-generation Targeted Version of NanoVP

Active targeting of nanoparticles toward a desired site has been a main research topic in nanomedicine for decades. In 2021, Japan approved the first photoimmunoconjugate, Alluminox, which combines an anti-PD1 antibody with a photosensitizer for head and neck cancer. As mentioned in Chapter 5, targeted nanoformulations offer a unique solution to differentiate drug delivery between cancer cells and normal cells. Targeted nanoparticles can deliver toxic treatments preferentially to diseased cells. We previously reported the development of an EGFR antibody conjugated with VP (Cetuximab-VP) for GBM treatment. However, studies

revealed VP uptake and photokilling were severely hindered. This new project, overseen by Idrisa Rahman, entails engineering a targeted formulation of NanoVP. The central hypothesis is delivering a high payload of VP to cancer cells via active targeting will increase PDT efficacy while minimizing healthy tissue damage. As stated in *Section 7.3.1*, we have created a stable NanoVP suspension coated with neutral polymer poloxamer 407. One goal of this project is to conjugate an EGFR antibody to the PEG end caps of poloxamer 407. Additionally, efforts are underway in creating a NanoVP particle that is partially composed of VP-NHS (as described in *Section 5.2.1*) for ligand conjugation.

10.4 Exploring NanoVP as a Chemotherapeutic

As mentioned in *Section 7.3.3*, high doses of VP can act as a chemotherapy without light irradiation. Recent clinical and preclinical studies have reported high doses of VP (μM-mM) can induce 'dark' toxicity in cancer cells including GBM (NCT04590664) [506-508]. A 10-100-fold higher dose of VP, compared to the PDT dose, has been shown to downregulate Bcl-2, disrupt the YAP/TAZ-TEAD complex interaction, and induce cancer cell death without light activation [506, 507]. This dissertation revealed NanoVP can deliver high payloads of VP to cancer cells for effective cell killing. Alternatively, Liposomal VP stimulated cancer cell death. A future project includes designing a sequential treatment plan that includes NanoVP-mediated PDP followed by large doses of NanoVP without light. The goal of PDP is to modulate the BBB and inhibit ABC transporters for enhanced drug delivery to cancer cells. The second dose of NanoVP will act as a YAP/TAZ inhibitor. The central hypothesis of the project is NanoVP-mediated PDP will increase delivery of VP via

BBB permeabilization and ABC transporter inhibition, resulting in enhanced VP-mediated YAP sequestration effects in GBM cells. Preliminary experiments performed by John Quinlan show that this sequential treatment on GBM cells alone in vitro does not yield a synergistic or additive effect on cell killing (**Figure 10.5**). In this experiment, U87 cells are incubated with 0.25 μM nanoVP prior to PDT (0-7.5J/cm^2, 10 mW/cm^2). After light irradiation, fresh medium supplemented with 8-14 μM NanoVP is added to the cells. Cell viability is measured via MTT assay 2 days later. Results show cell death is either driven by YAP inhibition (PDT ≤ 0.1 J/cm^2) or by PDT (0.5 J/cm^2), but an enhancement effect in vitro is not seen. Work is ongoing to evaluate the combination of these modalities in vivo to leverage PDP-mediated vascular permeabilization and ABC transporter inhibition to enhance drug delivery, enhancing YAP/TAZ sequestration effects.

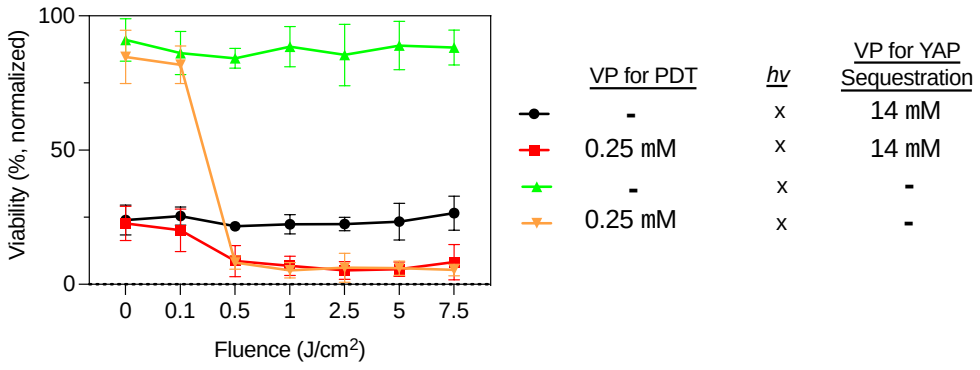

Figure 11.5 NanoVP-mediated PDP and YAP/TAZ Inhibition for GBM Cell Killing. U87 cells were incubated with 0.25 μM NanoVP prior to PDT, followed by 14 μM NanoVP for two days. N=3. *Conducted by John Quinlan.*

10.5 PDP can Modulate ABC Transporter Expression

Our lab has previously shown VP-mediated PDT can directly damage ABC transporters and decrease ATPase activity, thereby increasing the intracellular concertation of drugs [111, 175, 551]. Free-form VP is a substrate for human ABCG2 and ABCB1. When VP is within the ABC transporter binding pocket and PDT is performed, $^1O_2$ can covalently crosslink the protein [551]. After creating and validating our transgenic zebrafish model, mentioned in **Chapter 8**, one goal is to examine the effects of PDT on BBB integrity and ABC transporter function.

First, to determine if VP is also a substrate for zebrafish Abcg2a and Abcb4, transfected HEK 293 cells were incubated with VP, with and without an ABC transporter inhibitor, and the mean fluorescence intensity of VP was measured on FACs. As expected, the mean fluorescence ratio of VP to VP + inhibitor within EV cells (i.e., cells without a transporter) was 1.09, suggesting VP was not effluxed out of the cell. Similarly, the mean fluorescence ratio within ABCG2 and ABCB1 cells was 0.291 and 0.566, respectively, suggesting VP was effluxed by both proteins. Here, we show the mean fluorescence ratio of VP within Abcg2a and Abcb1 was 0.58 and 0.417, respectively, suggesting VP is a substrate for both zebrafish proteins.

Next, we examined the PDT efficacy within the transfected HEK 293 cells in order to determine a subtherapeutic dose for ABC transporter modulation experiments (**Figure 10.6**). Transfected cells were incubated with 0.25 μM VP for 24 hours prior to PDT (0-4 J/cm^2, 10 mW/cm^2). As expected, EV cells were the least resistant to PDT treatment, having an IC_{50} of 0.167 J/cm^2. Cells overexpressing ABCG2, Abcg2a, ABCB1, and Abcb4 had an IC_{50} of 0.41, 0.35, 0.39, and 0.23, respectively. The

subtherapeutic dose of 0.1 J/cm^2, which resulted in viability > 90%, was selected for modulation experiments.

Preliminary experiments suggest PDP can modulate ABC transporter expression in transfected HEK293 cells (**Figure 10.7**). Here, cells overexpressing human ABCG2 were incubated with 0.25 μM VP for 24 hours prior to PDP (0.1 J/cm^2, 10 mW/cm^2). Cell lysates were collected, and protein expression was examined. Compared to the no treatment control, PDP modestly decreased the expression of ABCG2 to 0.95, 0.81, and 0.80 at 1-, 6-, and 24-hours post treatment, respectively. Although PDP treatment can decrease transporter expression by > 50% within cancer cells, these HEK293 cells are non-cancerous and were transfected.

Future work for the project, being carried out by John Quinlan, includes using NanoVP-mediated PDP to modulate the ABC transporters at the zebrafish BBB and using coelenterazine analogs as permeability tracers to examine treatment outcomes.

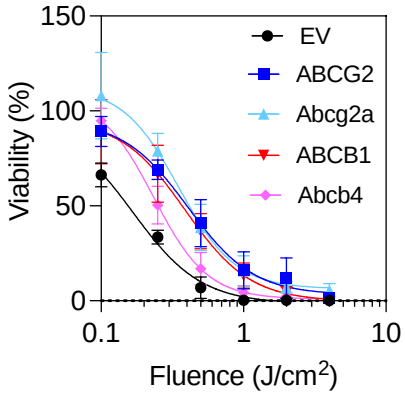

Figure 11.6 PDT Dose Viability Curves. PDT was performed on HEK 293 cells transfected with NanoLuc luciferase and ABCG2, Abcg2a, ABCB1, and Abcb4. EV cells without a transporter were used as a control. N ≥ 6, where N equals the number of wells assessed over 3 trials.

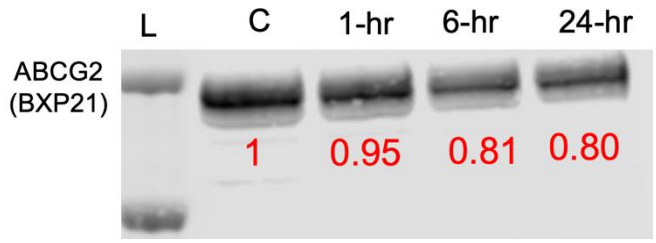

Figure 11.7 Immunoblots of ABCG2 within Transfected HEK293 cells. VP-mediated PDP modestly decreases ABCG2 expression with transfected HEK293 cells. N=2 gels.

10.6 A Zebrafish Model to Study Blood-brain Barrier Integrity

As mentioned in **Chapter 8**, our goal is to develop a transgenic zebrafish model to study BBB integrity and ABC transporter activity. This ongoing project is currently being conducted by Dr. Joanna Thomas. The transgenic zebrafish model consists of NanoLuc luciferase expression under the control of the glial fibrillary acidic protein promoter, leading to expression in the astrocytes behind the BBB. When the zebrafish BBB is disrupted either by inhibiting ABC transporters at the zebrafish BBB or otherwise increasing permeability, the luciferase substrates will cross the BBB and react with the luciferases, yielding a bioluminescent signal. We have already shown that coelenterazine-h, a NanoLuc substrate, is a substrate for zebrafish Abcg2a within transfected HEK293 cells. Similarly, native coelenterazine is a substrate for Abcg2a as well as Abcb4 in HEK293 cells. Here, we show coelenterazine-h is transported by Abcg2a at the zebrafish BBB and produces a bright luminescence signal within the brain (**Figure 10.8**). Zebrafish at 7 days post feralization were preincubated with 10 μM inhibitor for 2 hours prior to incubation with 3 μM native coelenterazine or

coelenterazine-h. Luminescence was recorded every 15 minutes for 90 minutes. Without the addition of inhibitors, native coelenterazine and coelenterazine-h do not reach the NanoLuc containing astrocytes and produced a minimal luminescence signal. As expected, when Abcb4 is inhibited by valspodar and Abcg2a is inhibited by Ko-143, native coelenterazine can interact with NanoLuc luciferase and produce luminescence, suggesting it is a substrate for both proteins. Similarly, when Abcg2a is inhibited by Ko-143, coelenterazine-h can cross the BBB and produce a significantly brighter luminescence, matching our *in vitro* data. Next steps for this project include examining wider concentration titrations of inhibitors to check dose response relationship and sensitivity of the assay. Our long-term goal is to test novel ABC transporter inhibitors and examine other ways to open the BBB within zebrafish.

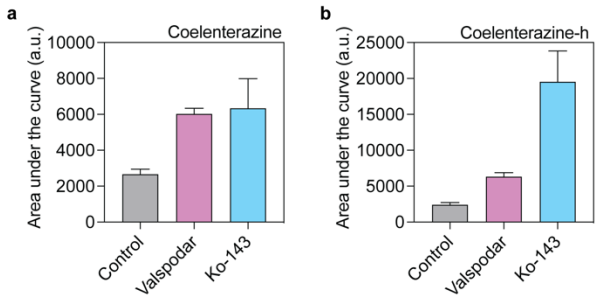

Figure 11.8 Native coelenterazine and coelenterazine-h are transported by Abcb4 or Abcg2a at the zebrafish BBB. Zebrafish (7 days post fertilization) were incubated with (**a**) native coelenterazine or (**b**) coelenterazine-h, with and without ABC inhibitors for 60 minutes. Native coelenterazine is a substrate for zebrafish Abcb4 or Abcg2a, and when the transporters are inhibited, it can cross the BBB and produce a luminescence signal. Coelenterazine-h is only a substrate for Abcg2a, and when it is inhibited by Ko-143, it can cross the BBB and react with NanoLuc luciferase. $N \geq 5$, where N equals the number of fish. Conducted by *Joanna Thomas.*

10.7 Outlook

It is seemingly clear the GBM cells 1-2 cm away from the primary tumor edge underlie the near 100% disease recurrence. The intact BBB plays a significant role in

hindering current GBM treatments. Combining the proposed treatment techniques, NanoVP-mediated PDP, NanoVP-mediated PDT, and/or NanoVP-mediated YAP/TAZ inhibition, with the current treatment options hold significant promise in effectively treating GBM. Using the established *ex vivo* rat brain model and the proposed zebrafish model offer ways to better understand PDT treatment outcomes in the brain and the mechanisms hindering drug delivery to the brain. Furthermore, the expanded studies on an active targeting NanoVP formulation, planning sequential treatment strategies around NanoVP, and inhibiting ABC drug efflux transporters are the first steps in expanding NanoVP use for other disease types. In addition, the work in this dissertation has motivated the development of a triple combination nanoparticle/therapy to treat ovarian cancer. The knowledge presented in this dissertation has the potential to improve treatments for a wide range of cancers.

Bibliography

1. Ostrom, Q.T., et al., *CBTRUS Statistical Report: Primary brain and other central nervous system tumors diagnosed in the United States in 2010-2014.* Neuro Oncol, 2017. **19**(suppl_5): p. v1-v88.
2. Tamimi, A.F. and M. Juweid, *Epidemiology and Outcome of Glioblastoma*, in *Glioblastoma*, S. De Vleeschouwer, Editor. 2017: Brisbane (AU).
3. Dhermain, F., *Radiotherapy of high-grade gliomas: current standards and new concepts, innovations in imaging and radiotherapy, and new therapeutic approaches.* Chinese journal of cancer, 2014. **33**(1): p. 16-24.
4. Sengupta, S., et al., *Impact of temozolomide on immune response during malignant glioma chemotherapy.* Clinical & developmental immunology, 2012. **2012**: p. 831090-831090.
5. Mrugala, M.M. and M.C. Chamberlain, *Mechanisms of Disease: temozolomide and glioblastoma—look to the future.* Nature Clinical Practice Oncology, 2008. **5**(8): p. 476-486.
6. Inglut, C.T., et al., *Immunological and Toxicological Considerations for the Design of Liposomes.* Nanomaterials (Basel), 2020. **10**(2).
7. Pardridge, W.M., *The blood-brain barrier: bottleneck in brain drug development.* NeuroRx : the journal of the American Society for Experimental NeuroTherapeutics, 2005. **2**(1): p. 3-14.
8. Hersh, D.S., et al., *Evolving Drug Delivery Strategies to Overcome the Blood Brain Barrier.* Curr Pharm Des, 2016. **22**(9): p. 1177-1193.
9. Neuwelt, E.A., et al., *Effects of adrenal cortical steroids and osmotic blood-brain barrier opening on methotrexate delivery to gliomas in the rodent: the factor of the blood-brain barrier.* Proceedings of the National Academy of Sciences of the United States of America, 1982. **79**(14): p. 4420-4423.
10. Tsai, H.-C., et al., *Safety evaluation of frequent application of microbubble-enhanced focused ultrasound blood-brain-barrier opening.* Scientific reports, 2018. **8**(1): p. 17720-17720.
11. Chu, P.-C., et al., *Neuromodulation accompanying focused ultrasound-induced blood-brain barrier opening.* Scientific reports, 2015. **5**: p. 15477-15477.
12. Kostron, H., A. Obwegeser, and R. Jakober, *Photodynamic therapy in neurosurgery: a review.* Journal of Photochemistry and Photobiology B: Biology, 1996. **36**(2): p. 157-168.
13. Dougherty, T.J., et al., *Photodynamic therapy.* Journal of the National Cancer Institute, 1998. **90**(12): p. 889-905.
14. Madsen, S.J. and H. Hirschberg, *Site-specific opening of the blood-brain barrier.* J Biophotonics, 2010. **3**(5-6): p. 356-67.
15. Hirschberg, H., et al., *Disruption of the blood-brain barrier following ALA-mediated photodynamic therapy.* Lasers Surg Med, 2008. **40**(8): p. 535-42.
16. Semyachkina-Glushkovskaya, O., et al., *Photodynamic opening of blood-brain barrier.* Biomedical optics express, 2017. **8**(11): p. 5040-5048.

17. Zhang, C., et al., *Photodynamic opening of the blood-brain barrier to high weight molecules and liposomes through an optical clearing skull window.* Biomedical optics express, 2018. **9**(10): p. 4850-4862.
18. Sorrin, A.J., et al., *Photodynamic Therapy and the Biophysics of the Tumor Microenvironment.* Photochem Photobiol, 2020. **2**(96): p. 232-259.
19. Huang, H.C., et al., *Photodynamic Therapy Synergizes with Irinotecan to Overcome Compensatory Mechanisms and Improve Treatment Outcomes in Pancreatic Cancer.* Cancer Res, 2016. **76**(5): p. 1066-77.
20. Luo, D., et al., *Vessel-Targeted Chemophototherapy with Cationic Porphyrin-Phospholipid Liposomes.* Molecular Cancer Therapeutics, 2017. **16**(11): p. 2452-2461.
21. Inglut, C.T., et al., *Systematic Evaluation of Light-Activatable Biohybrids for Anti-Glioma Photodynamic Therapy.* J Clin Med, 2019. **8**(9): p. 1269.
22. Inglut, C.T., et al., *Predictors and Limitations of the Penetration Depth of Photodynamic Effects in the Rodent Brain.* Photochemistry and Photobiology, 2019. **96**(2): p. 301-309.
23. Celli, J.P., et al., *Imaging and Photodynamic Therapy: Mechanisms, Monitoring, and Optimization.* Chemical Reviews, 2010. **110**(5): p. 2795-2838.
24. Fahr, A., et al., *Transfer of lipophilic drugs between liposomal membranes and biological interfaces: Consequences for drug delivery.* European Journal of Pharmaceutical Sciences, 2005. **26**(3): p. 251-265.
25. Bhakay, A., et al., *Bioavailability Enhancement of Poorly Water-Soluble Drugs via Nanocomposites: Formulation(-)Processing Aspects and Challenges.* Pharmaceutics, 2018. **10**(3).
26. Chow, T.H., et al., *Improvement of biodistribution and therapeutic index via increase of polyethylene glycol on drug-carrying liposomes in an HT-29/luc xenografted mouse model.* Anticancer Res, 2009. **29**(6): p. 2111-20.
27. Olusanya, T.O.B., et al., *Liposomal Drug Delivery Systems and Anticancer Drugs.* Molecules (Basel, Switzerland), 2018. **23**(4): p. 907.
28. Drummond, D.C., et al., *Optimizing liposomes for delivery of chemotherapeutic agents to solid tumors.* Pharmacol Rev, 1999. **51**(4): p. 691-743.
29. Immordino, M.L., F. Dosio, and L. Cattel, *Stealth liposomes: review of the basic science, rationale, and clinical applications, existing and potential.* International journal of nanomedicine, 2006. **1**(3): p. 297-315.
30. Dams, E.T.M., et al., *Accelerated Blood Clearance and Altered Biodistribution of Repeated Injections of Sterically Stabilized Liposomes.* Journal of Pharmacology and Experimental Therapeutics, 2000. **292**(3): p. 1071-1079.
31. Laverman, P., et al., *Factors Affecting the Accelerated Blood Clearance of Polyethylene Glycol-Liposomes upon Repeated Injection.* Journal of Pharmacology and Experimental Therapeutics, 2001. **298**(2): p. 607-612.
32. Ishida, T., et al., *Accelerated clearance of PEGylated liposomes in rats after repeated injections.* Journal of Controlled Release, 2003. **88**(1): p. 35-42.

33. Xu, H., et al., *Influence of phospholipid types and animal models on the accelerated blood clearance phenomenon of PEGylated liposomes upon repeated injection.* Drug Deliv, 2015. **22**(5): p. 598-607.
34. Ishida, T., et al., *Effect of the physicochemical properties of initially injected liposomes on the clearance of subsequently injected PEGylated liposomes in mice.* J Control Release, 2004. **95**(3): p. 403-12.
35. Semple, S.C., et al., *Immunogenicity and Rapid Blood Clearance of Liposomes Containing Polyethylene Glycol-Lipid Conjugates and Nucleic Acid.* Journal of Pharmacology and Experimental Therapeutics, 2005. **312**(3): p. 1020-1026.
36. Ishida, T., et al., *Accelerated blood clearance of PEGylated liposomes upon repeated injections: effect of doxorubicin-encapsulation and high-dose first injection.* J Control Release, 2006. **115**(3): p. 251-8.
37. Wang, X., T. Ishida, and H. Kiwada, *Anti-PEG IgM elicited by injection of liposomes is involved in the enhanced blood clearance of a subsequent dose of PEGylated liposomes.* J Control Release, 2007. **119**(2): p. 236-44.
38. Ishida, T., S. Kashima, and H. Kiwada, *The contribution of phagocytic activity of liver macrophages to the accelerated blood clearance (ABC) phenomenon of PEGylated liposomes in rats.* J Control Release, 2008. **126**(2): p. 162-5.
39. Koide, H., et al., *T cell-independent B cell response is responsible for ABC phenomenon induced by repeated injection of PEGylated liposomes.* Int J Pharm, 2010. **392**(1-2): p. 218-23.
40. Suzuki, T., et al., *Accelerated blood clearance of PEGylated liposomes containing doxorubicin upon repeated administration to dogs.* Int J Pharm, 2012. **436**(1-2): p. 636-43.
41. Lopes, T.C.M., et al., *Accelerated Blood Clearance (ABC) Phenomenon Favors the Accumulation of Tartar Emetic in Pegylated Liposomes in BALB/c Mice Liver.* Pathology Research International, 2018. **2018**: p. 7.
42. Wang, F.L., et al., *Activation of PXR-Cytochrome P450s axis: A Possible Reason for the Enhanced Accelerated Blood Clearance Phenomenon of PEGylated Liposomes in vivo.* Drug Metabolism and Disposition, 2019: p. dmd.119.086769.
43. Ishida, T. and H. Kiwada, *Accelerated blood clearance (ABC) phenomenon upon repeated injection of PEGylated liposomes.* International Journal of Pharmaceutics, 2008. **354**(1): p. 56-62.
44. Sherriff, J., et al., *Patterns of relapse in glioblastoma multiforme following concomitant chemoradiotherapy with temozolomide.* The British Journal of Radiology, 2013. **86**(1022): p. 20120414.
45. Wallner, K.E., et al., *Patterns of failure following treatment for glioblastoma multiforme and anaplastic astrocytoma.* Int J Radiat Oncol Biol Phys, 1989. **16**(6): p. 1405-9.
46. Hambardzumyan, D. and G. Bergers, *Glioblastoma: Defining Tumor Niches.* Trends in cancer, 2015. **1**(4): p. 252-265.
47. Giese, A. and M. Westphal, *Glioma invasion in the central nervous system.* Neurosurgery, 1996. **39**(2): p. 235-50; discussion 250-2.

48. Claes, A., A.J. Idema, and P. Wesseling, *Diffuse glioma growth: a guerilla war.* Acta neuropathologica, 2007. **114**(5): p. 443-458.
49. Olar, A. and K.D. Aldape, *Using the molecular classification of glioblastoma to inform personalized treatment.* The Journal of pathology, 2014. **232**(2): p. 165-177.
50. Simpson, J.R., et al., *Influence of location and extent of surgical resection on survival of patients with glioblastoma multiforme: results of three consecutive Radiation Therapy Oncology Group (RTOG) clinical trials.* Int J Radiat Oncol Biol Phys, 1993. **26**(2): p. 239-44.
51. Mickevicius, N.J., et al., *Location of brain tumor intersecting white matter tracts predicts patient prognosis.* Journal of neuro-oncology, 2015. **125**(2): p. 393-400.
52. Zhang, J., M.F. Stevens, and T.D. Bradshaw, *Temozolomide: mechanisms of action, repair and resistance.* Curr Mol Pharmacol, 2012. **5**(1): p. 102-14.
53. Fan, C.H., et al., *O6-methylguanine DNA methyltransferase as a promising target for the treatment of temozolomide-resistant gliomas.* Cell death & disease, 2013. **4**(10): p. e876-e876.
54. Silber, J.R., et al., *O(6)-methylguanine-DNA methyltransferase in glioma therapy: promise and problems.* Biochimica et biophysica acta, 2012. **1826**(1): p. 71-82.
55. Dréan, A., et al., *ATP binding cassette (ABC) transporters: expression and clinical value in glioblastoma.* J Neurooncol, 2018. **138**(3): p. 479-486.
56. Jensen, R.L., et al., *Preoperative dynamic contrast-enhanced MRI correlates with molecular markers of hypoxia and vascularity in specific areas of intratumoral microenvironment and is predictive of patient outcome.* Neuro-oncology, 2014. **16**(2): p. 280-291.
57. Portnow, J., et al., *The neuropharmacokinetics of temozolomide in patients with resectable brain tumors: potential implications for the current approach to chemoradiation.* Clinical cancer research : an official journal of the American Association for Cancer Research, 2009. **15**(22): p. 7092-7098.
58. Chinot, O.L., et al., *Correlation between O6-methylguanine-DNA methyltransferase and survival in inoperable newly diagnosed glioblastoma patients treated with neoadjuvant temozolomide.* J Clin Oncol, 2007. **25**(12): p. 1470-5.
59. Gerber, D.E., et al., *The impact of thrombocytopenia from temozolomide and radiation in newly diagnosed adults with high-grade gliomas.* Neuro-oncology, 2007. **9**(1): p. 47-52.
60. Blumenthal, D.T., et al., *Is more better? The impact of extended adjuvant temozolomide in newly diagnosed glioblastoma: a secondary analysis of EORTC and NRG Oncology/RTOG.* Neuro-Oncology, 2017. **19**(8): p. 1119-1126.
61. Nokia, M.S., M.L. Anderson, and T.J. Shors, *Chemotherapy disrupts learning, neurogenesis and theta activity in the adult brain.* European Journal of Neuroscience, 2012. **36**(11): p. 3521-3530.

62. Agarwala, S.S. and J.M. Kirkwood, *Temozolomide, a novel alkylating agent with activity in the central nervous system, may improve the treatment of advanced metastatic melanoma.* Oncologist, 2000. **5**(2): p. 144-51.
63. Brennan, P.M., et al., *Second surgery for progressive glioblastoma: a multi-centre questionnaire and cohort-based review of clinical decision-making and patient outcomes in current practice.* Journal of Neuro-Oncology, 2021. **153**(1): p. 99-107.
64. Weller, M., et al., *Standards of care for treatment of recurrent glioblastoma—are we there yet?* Neuro-Oncology, 2012. **15**(1): p. 4-27.
65. Chamberlain, M.C., *Bevacizumab for the treatment of recurrent glioblastoma.* Clinical Medicine Insights. Oncology, 2011. **5**: p. 117-129.
66. Kazmi, F., et al., *Re-irradiation for recurrent glioblastoma (GBM): a systematic review and meta-analysis.* J Neurooncol, 2019. **142**(1): p. 79-90.
67. Vredenburgh, J.J., et al., *Experience with irinotecan for the treatment of malignant glioma.* Neuro-oncology, 2009. **11**(1): p. 80-91.
68. Beauchesne, P., *Extra-neural metastases of malignant gliomas: myth or reality?* Cancers (Basel), 2011. **3**(1): p. 461-77.
69. Sarkaria, J.N., et al., *Is the blood–brain barrier really disrupted in all glioblastomas? A critical assessment of existing clinical data.* Neuro-Oncology, 2017. **20**(2): p. 184-191.
70. Minata, M., et al., *Phenotypic Plasticity of Invasive Edge Glioma Stem-like Cells in Response to Ionizing Radiation.* Cell Reports, 2019. **26**(7): p. 1893-1905.e7.
71. Armento, A., et al., *Molecular Mechanisms of Glioma Cell Motility*, in *Glioblastoma*, S. De Vleeschouwer, Editor. 2017, Codon Publications Copyright: The Authors.: Brisbane (AU).
72. Ulrich, T.A., E.M. de Juan Pardo, and S. Kumar, *The mechanical rigidity of the extracellular matrix regulates the structure, motility, and proliferation of glioma cells.* Cancer research, 2009. **69**(10): p. 4167-4174.
73. Velásquez, C., et al., *Molecular and Clinical Insights into the Invasive Capacity of Glioblastoma Cells.* Journal of Oncology, 2019. **2019**: p. 1740763.
74. Soubannier, V. and S. Stifani, *NF-κB Signalling in Glioblastoma.* Biomedicines, 2017. **5**(2): p. 29.
75. Choe, G., et al., *Active matrix metalloproteinase 9 expression is associated with primary glioblastoma subtype.* Clin Cancer Res, 2002. **8**(9): p. 2894-901.
76. Wick, W., M. Platten, and M. Weller, *Glioma cell invasion: regulation of metalloproteinase activity by TGF-beta.* J Neurooncol, 2001. **53**(2): p. 177-85.
77. Iwadate, Y., *Epithelial-mesenchymal transition in glioblastoma progression.* Oncology letters, 2016. **11**(3): p. 1615-1620.
78. Monteiro, A.R., et al., *The Role of Hypoxia in Glioblastoma Invasion.* Cells, 2017. **6**(4): p. 45.
79. Li, J., et al., *Prognostic significance of epidermal growth factor receptor expression in glioma patients.* OncoTargets and therapy, 2018. **11**: p. 731-742.
80. Stepp, H. and W. Stummer, *5-ALA in the management of malignant glioma.* Lasers Surg Med, 2018. **50**(5): p. 399-419.

81. Banks, W.A., *From blood–brain barrier to blood–brain interface: new opportunities for CNS drug delivery.* Nature Reviews Drug Discovery, 2016. **15**(4): p. 275-292.
82. Chen, Y. and L. Liu, *Modern methods for delivery of drugs across the blood–brain barrier.* Advanced Drug Delivery Reviews, 2012. **64**(7): p. 640-665.
83. Daneman, R. and A. Prat, *The blood-brain barrier.* Cold Spring Harbor perspectives in biology, 2015. **7**(1): p. a020412-a020412.
84. Iadecola, C., *Neurovascular regulation in the normal brain and in Alzheimer's disease.* Nat Rev Neurosci, 2004. **5**(5): p. 347-60.
85. Bell, A.H., et al., *The Neurovascular Unit: Effects of Brain Insults During the Perinatal Period.* Frontiers in Neuroscience, 2020. **13**(1452).
86. Takemiya, T. and K. Yamagata, *Intercellular signaling pathway among Endothelia, astrocytes and neurons in excitatory neuronal damage.* International journal of molecular sciences, 2013. **14**(4): p. 8345-8357.
87. Dong, X., *Current Strategies for Brain Drug Delivery.* Theranostics, 2018. **8**(6): p. 1481-1493.
88. Kadry, H., B. Noorani, and L. Cucullo, *A blood–brain barrier overview on structure, function, impairment, and biomarkers of integrity.* Fluids and Barriers of the CNS, 2020. **17**(1): p. 69.
89. Hladky, S.B. and M.A. Barrand, *Fluid and ion transfer across the blood-brain and blood-cerebrospinal fluid barriers; a comparative account of mechanisms and roles.* Fluids Barriers CNS, 2016. **13**(1): p. 19.
90. Attwell, D., et al., *What is a pericyte?* Journal of cerebral blood flow and metabolism : official journal of the International Society of Cerebral Blood Flow and Metabolism, 2016. **36**(2): p. 451-455.
91. Abbott, N.J., L. Rönnbäck, and E. Hansson, *Astrocyte–endothelial interactions at the blood–brain barrier.* Nature Reviews Neuroscience, 2006. **7**(1): p. 41-53.
92. Janzer, R.C. and M.C. Raff, *Astrocytes induce blood-brain barrier properties in endothelial cells.* Nature, 1987. **325**(6101): p. 253-7.
93. Zihni, C., et al., *Tight junctions: from simple barriers to multifunctional molecular gates.* Nature Reviews Molecular Cell Biology, 2016. **17**(9): p. 564-580.
94. Liebner, S., U. Cavallaro, and E. Dejana, *The Multiple Languages of Endothelial Cell-to-Cell Communication.* Arteriosclerosis, Thrombosis, and Vascular Biology, 2006. **26**(7): p. 1431-1438.
95. Luissint, A.C., et al., *Tight junctions at the blood brain barrier: physiological architecture and disease-associated dysregulation.* Fluids Barriers CNS, 2012. **9**(1): p. 23.
96. Vestweber, D., *VE-Cadherin.* Arteriosclerosis, Thrombosis, and Vascular Biology, 2008. **28**(2): p. 223-232.
97. Taddei, A., et al., *Endothelial adherens junctions control tight junctions by VE-cadherin-mediated upregulation of claudin-5.* Nature Cell Biology, 2008. **10**(8): p. 923-934.

98. Lampugnani, M.G., et al., *Vascular endothelial cadherin controls VEGFR-2 internalization and signaling from intracellular compartments.* The Journal of cell biology, 2006. **174**(4): p. 593-604.
99. Knipp, G.T., et al., *Paracellular diffusion in Caco-2 cell monolayers: effect of perturbation on the transport of hydrophilic compounds that vary in charge and size.* J Pharm Sci, 1997. **86**(10): p. 1105-10.
100. Günzel, D. and A.S.L. Yu, *Claudins and the modulation of tight junction permeability.* Physiological reviews, 2013. **93**(2): p. 525-569.
101. Greene, C., N. Hanley, and M. Campbell, *Claudin-5: gatekeeper of neurological function.* Fluids and Barriers of the CNS, 2019. **16**(1): p. 3.
102. Obermeier, B., R. Daneman, and R.M. Ransohoff, *Development, maintenance and disruption of the blood-brain barrier.* Nature medicine, 2013. **19**(12): p. 1584-1596.
103. Wevers, N.R. and H.E. de Vries, *Morphogens and blood-brain barrier function in health and disease.* Tissue barriers, 2015. **4**(1): p. e1090524-e1090524.
104. Ota, H., et al., *Photochemically induced increase in endothelial permeablity regulated by RhoA activation.* Photochemical & Photobiological Sciences, 2009. **8**(10): p. 1401-1407.
105. Gray, K.M., et al., *Quantitative Phenotyping of Cell–Cell Junctions to Evaluate ZO-1 Presentation in Brain Endothelial Cells.* Annals of Biomedical Engineering, 2019. **47**(7): p. 1675-1687.
106. Onken, M.D., et al., *Endothelial monolayers and transendothelial migration depend on mechanical properties of the substrate.* Cytoskeleton (Hoboken, N.J.), 2014. **71**(12): p. 695-706.
107. Huveneers, S., et al., *Vinculin associates with endothelial VE-cadherin junctions to control force-dependent remodeling.* The Journal of cell biology, 2012. **196**(5): p. 641-652.
108. Gray, K.M., et al., *Quantitatively relating brain endothelial cell-cell junction phenotype to global and local barrier properties under varied culture conditions via the Junction Analyzer Program.* Fluids Barriers CNS, 2020. **17**(1): p. 16.
109. Seebach, J., J. Cao, and H.J. Schnittler, *Quantitative dynamics of VE-cadherin at endothelial cell junctions at a glance: basic requirements and current concepts.* Discoveries, 2016. **4**(3): p. e63.
110. Basseville, A., et al., *The ABCG2 Multidrug Transporter*, in *ABC Transporters - 40 Years on*, A.M. George, Editor. 2016, Springer International Publishing: Cham. p. 195-226.
111. Liang, B.J., et al., *Use of photoimmunoconjugates to characterize ABCB1 in cancer cells.* Nanophotonics, 2021. **10**(12): p. 3049-3061.
112. Qosa, H., et al., *Regulation of ABC efflux transporters at blood-brain barrier in health and neurological disorders.* Brain research, 2015. **1628**(Pt B): p. 298-316.
113. Enerson, B.E. and L.R. Drewes, *The rat blood-brain barrier transcriptome.* J Cereb Blood Flow Metab, 2006. **26**(7): p. 959-73.

114. Robey, R.W., et al., *Revisiting the role of ABC transporters in multidrug-resistant cancer.* Nature reviews. Cancer, 2018. **18**(7): p. 452-464.
115. Rapoport, S.I., *Osmotic Opening of the Blood–Brain Barrier: Principles, Mechanism, and Therapeutic Applications.* Cellular and Molecular Neurobiology, 2000. **20**(2): p. 217-230.
116. Brown, R.C., R.D. Egleton, and T.P. Davis, *Mannitol opening of the blood-brain barrier: regional variation in the permeability of sucrose, but not 86Rb+ or albumin.* Brain Res, 2004. **1014**(1-2): p. 221-7.
117. Vykhodtseva, N.I., K. Hynynen, and C. Damianou, *Histologic effects of high intensity pulsed ultrasound exposure with subharmonic emission in rabbit brain in vivo.* Ultrasound Med Biol, 1995. **21**(7): p. 969-79.
118. Sheikov, N., et al., *Effect of focused ultrasound applied with an ultrasound contrast agent on the tight junctional integrity of the brain microvascular endothelium.* Ultrasound in medicine & biology, 2008. **34**(7): p. 1093-1104.
119. Salford, L.G., et al., *Permeability of the blood-brain barrier induced by 915 MHz electromagnetic radiation, continuous wave and modulated at 8, 16, 50, and 200 Hz.* Microsc Res Tech, 1994. **27**(6): p. 535-42.
120. Stam, R., *Electromagnetic fields and the blood–brain barrier.* Brain Research Reviews, 2010. **65**(1): p. 80-97.
121. Appelboom, G., et al., *Stereotactic modulation of blood-brain barrier permeability to enhance drug delivery.* Neuro-Oncology, 2016. **18**(12): p. 1601-1609.
122. Sandor, N., et al., *Low dose cranial irradiation-induced cerebrovascular damage is reversible in mice.* PLoS One, 2014. **9**(11): p. e112397.
123. Sarkaria, J.N., et al., *Is the blood-brain barrier really disrupted in all glioblastomas? A critical assessment of existing clinical data.* Neuro Oncol, 2018. **20**(2): p. 184-191.
124. Ackroyd, R., et al., *The History of Photodetection and Photodynamic Therapy.* Photochemistry and Photobiology, 2001. **74**(5): p. 656-669.
125. Yun, S.H. and S.J.J. Kwok, *Light in diagnosis, therapy and surgery.* Nature Biomedical Engineering, 2017. **1**: p. 0008.
126. Dolmans, D.E., D. Fukumura, and R.K. Jain, *Photodynamic therapy for cancer.* Nat Rev Cancer, 2003. **3**(5): p. 380-7.
127. H.C., H. and H. T., *The "Nano" World in Photodynamic Therapy* Austin J Nanomed Nanotechnol, 2014. **2**(3): p. 1020.
128. Obaid, G., et al., *Photonanomedicine: a convergence of photodynamic therapy and nanotechnology.* Nanoscale, 2016. **8**(25): p. 12471-12503.
129. Castano, A.P., T.N. Demidova, and M.R. Hamblin, *Mechanisms in photodynamic therapy: part one-photosensitizers, photochemistry and cellular localization.* Photodiagnosis and photodynamic therapy, 2004. **1**(4): p. 279-293.
130. Dougherty, T.J., et al., *Photoradiation in the treatment of recurrent breast carcinoma.* J Natl Cancer Inst, 1979. **62**(2): p. 231-7.
131. Hamblin, M.R., *Photodynamic Therapy for Cancer: What's Past is Prologue.* Photochemistry and photobiology, 2020. **96**(3): p. 506-516.

132. Wilson, B.C., M.S. Patterson, and L. Lilge, *Implicit and explicit dosimetry in photodynamic therapy: a New paradigm.* Lasers in Medical Science, 1997. **12**(3): p. 182-199.
133. MOAN, J. and K. BERG, *THE PHOTODEGRADATION OF PORPHYRINS IN CELLS CAN BE USED TO ESTIMATE THE LIFETIME OF SINGLET OXYGEN.* Photochemistry and Photobiology, 1991. **53**(4): p. 549-553.
134. Agostinis, P., et al., *Photodynamic therapy of cancer: an update.* CA: a cancer journal for clinicians, 2011. **61**(4): p. 250-281.
135. Zhu, T.C., et al., *In-vivo singlet oxygen threshold doses for PDT.* Photonics & lasers in medicine, 2015. **4**(1): p. 59-71.
136. Morgan, J. and A.R. Oseroff, *Mitochondria-based photodynamic anti-cancer therapy.* Adv Drug Deliv Rev, 2001. **49**(1-2): p. 71-86.
137. Elena-Real, C.A., et al., *Cytochrome c speeds up caspase cascade activation by blocking 14-3-3ε-dependent Apaf-1 inhibition.* Cell Death & Disease, 2018. **9**(3): p. 365.
138. Kessel, D. and Y. Luo, *Mitochondrial photodamage and PDT-induced apoptosis.* Journal of photochemistry and photobiology. B, Biology, 1998. **42**(2): p. 89-95.
139. Kessel, D. and M. Castelli, *Evidence that bcl-2 is the target of three photosensitizers that induce a rapid apoptotic response.* Photochem Photobiol, 2001. **74**(2): p. 318-22.
140. Zhao, B. and Y.-Y. He, *Recent advances in the prevention and treatment of skin cancer using photodynamic therapy.* Expert review of anticancer therapy, 2010. **10**(11): p. 1797-1809.
141. Dhillon, S.S., et al., *A Phase I Study of Light Dose for Photodynamic Therapy Using 2-[1-Hexyloxyethyl]-2 Devinyl Pyropheophorbide-a for the Treatment of Non-Small Cell Carcinoma In Situ or Non-Small Cell Microinvasive Bronchogenic Carcinoma: A Dose Ranging Study.* Journal of thoracic oncology : official publication of the International Association for the Study of Lung Cancer, 2016. **11**(2): p. 234-241.
142. Azzouzi, A.R., et al., *TOOKAD(R) Soluble focal therapy: pooled analysis of three phase II studies assessing the minimally invasive ablation of localized prostate cancer.* World J Urol, 2015. **33**(7): p. 945-53.
143. Mahmoudi, K., et al., *5-aminolevulinic acid photodynamic therapy for the treatment of high-grade gliomas.* Journal of neuro-oncology, 2019. **141**(3): p. 595-607.
144. Huang, Z., *A review of progress in clinical photodynamic therapy.* Technology in cancer research & treatment, 2005. **4**(3): p. 283-293.
145. Schmidt-Erfurth, U., et al., *Vascular targeting in photodynamic occlusion of subretinal vessels.* Ophthalmology, 1994. **101**(12): p. 1953-61.
146. Sordillo, L., et al., *Deep optical imaging of tissue using the second and third near-infrared spectral windows.* Journal of Biomedical Optics, 2014. **19**(5): p. 056004.
147. Dougherty, T.J., et al., *Photodynamic Therapy.* JNCI: Journal of the National Cancer Institute, 1998. **90**(12): p. 889-905.

148. Wachowska, M., et al., *Aminolevulinic Acid (ALA) as a Prodrug in Photodynamic Therapy of Cancer.* Molecules, 2011. **16**(5): p. 4140-4164.
149. Hadjipanayis, C.G. and W. Stummer, *5-ALA and FDA approval for glioma surgery.* J Neurooncol, 2019. **141**(3): p. 479-486.
150. Aveline, B.M., T. Hasan, and R.W. Redmond, *The effects of aggregation, protein binding and cellular incorporation on the photophysical properties of benzoporphyrin derivative monoacid ring A (BPDMA).* J Photochem Photobiol B, 1995. **30**(2-3): p. 161-9.
151. Redmond, R.W. and J.N. Gamlin, *A compilation of singlet oxygen yields from biologically relevant molecules.* Photochem Photobiol, 1999. **70**(4): p. 391-475.
152. Aveline, B., T. Hasan, and R.W. Redmond, *Photophysical and photosensitizing properties of benzoporphyrin derivative monoacid ring A (BPD-MA).* Photochem Photobiol, 1994. **59**(3): p. 328-35.
153. Lozovaya, G.I., Z. Masinovsky, and A.A. Sivash, *Protoporphyrin ix as a possible ancient photosensitizer: Spectral and photochemical studies.* Origins of life and evolution of the biosphere, 1990. **20**(3): p. 321-330.
154. Schmidt-Erfurth, U. and T. Hasan, *Mechanisms of Action of Photodynamic Therapy with Verteporfin for the Treatment of Age-Related Macular Degeneration.* Survey of Ophthalmology, 2000. **45**(3): p. 195-214.
155. Cruess, A.F., et al., *Photodynamic therapy with verteporfin in age-related macular degeneration: a systematic review of efficacy, safety, treatment modifications and pharmacoeconomic properties.* Acta Ophthalmologica, 2009. **87**(2): p. 118-132.
156. Christie, J.G. and U.B. Kompella, *Ophthalmic light sensitive nanocarrier systems.* Drug discovery today, 2008. **13**(3-4): p. 124-134.
157. Eljamel, M.S., *Brain photodiagnosis (PD), fluorescence guided resection (FGR) and photodynamic therapy (PDT): past, present and future.* Photodiagnosis Photodyn Ther, 2008. **5**(1): p. 29-35.
158. Nagaya, T., et al., *Fluorescence-Guided Surgery.* Frontiers in Oncology, 2017. **7**.
159. Gandhi, S., et al., *Survival Outcomes Among Patients With High-Grade Glioma Treated With 5-Aminolevulinic Acid-Guided Surgery: A Systematic Review and Meta-Analysis.* Front Oncol, 2019. **9**: p. 620.
160. Stummer, W., et al., *Intraoperative detection of malignant gliomas by 5-aminolevulinic acid-induced porphyrin fluorescence.* Neurosurgery, 1998. **42**(3): p. 518-25; discussion 525-6.
161. Cramer, S.W. and C.C. Chen, *Photodynamic Therapy for the Treatment of Glioblastoma.* Frontiers in surgery, 2020. **6**: p. 81-81.
162. Dolmans, D.E.J.G.J., D. Fukumura, and R.K. Jain, *Photodynamic therapy for cancer.* Nature Reviews Cancer, 2003. **3**(5): p. 380-387.
163. Yano, T., et al., *Photodynamic therapy for esophageal cancer.* Annals of translational medicine, 2014. **2**(3): p. 29-29.
164. Simone, C.B., 2nd, et al., *Photodynamic therapy for the treatment of non-small cell lung cancer.* Journal of thoracic disease, 2012. **4**(1): p. 63-75.

165. Worel, N. and G. Leitner, *Clinical Results of Extracorporeal Photopheresis.* Transfusion medicine and hemotherapy : offizielles Organ der Deutschen Gesellschaft fur Transfusionsmedizin und Immunhamatologie, 2012. **39**(4): p. 254-262.
166. Azzouzi, A.R., et al., *TOOKAD(®) Soluble vascular-targeted photodynamic (VTP) therapy: determination of optimal treatment conditions and assessment of effects in patients with localised prostate cancer.* BJU Int, 2013. **112**(6): p. 766-74.
167. Rizvi, I., et al., *A Combination of Visudyne and a Lipid-anchored Liposomal Formulation of Benzoporphyrin Derivative Enhances Photodynamic Therapy Efficacy in a 3D Model for Ovarian Cancer.* Photochemistry and Photobiology, 2019. **95**(1): p. 419-429.
168. Huggett, M.T., et al., *Phase I/II study of verteporfin photodynamic therapy in locally advanced pancreatic cancer.* Br J Cancer, 2014. **110**(7): p. 1698-704.
169. Bechet, D., et al., *Photodynamic therapy of malignant brain tumours: A complementary approach to conventional therapies.* Cancer Treatment Reviews, 2014. **40**(2): p. 229-241.
170. Ito, S., et al., *Oedema formation in experimental photo-irradiation therapy of brain tumours using 5-ALA.* Acta Neurochir (Wien), 2005. **147**(1): p. 57-65; discussion 65.
171. Henry Hirschberg, M.D., et al. *Increased brain edema following 5-aminolevulinic acid mediated photodynamic in normal and tumor bearing rats*. in *Proc.SPIE*. 2007.
172. Stummer, W., et al., *Kinetics of Photofrin II in perifocal brain edema.* Neurosurgery, 1993. **33**(6): p. 1075-81; discussion 1081-2.
173. Silva, Z.S., Jr., et al., *Animal models for photodynamic therapy (PDT).* Bioscience reports, 2015. **35**(6): p. e00265.
174. Fingar, V.H., et al., *Analysis of acute vascular damage after photodynamic therapy using benzoporphyrin derivative (BPD).* British journal of cancer, 1999. **79**(11-12): p. 1702-1708.
175. Huang, H.C., et al., *Photodynamic Priming Mitigates Chemotherapeutic Selection Pressures and Improves Drug Delivery.* Cancer Res, 2018. **78**(2): p. 558-571.
176. Eljamel, M.S., C. Goodman, and H. Moseley, *ALA and Photofrin fluorescence-guided resection and repetitive PDT in glioblastoma multiforme: a single centre Phase III randomised controlled trial.* Lasers Med Sci, 2008. **23**(4): p. 361-7.
177. Sandell, J.L. and T.C. Zhu, *A review of in-vivo optical properties of human tissues and its impact on PDT.* Journal of biophotonics, 2011. **4**(11-12): p. 773-787.
178. Wang, P. and T. Li, *Which wavelength is optimal for transcranial low-level laser stimulation?* J Biophotonics, 2019. **12**(2): p. e201800173.
179. Li, T., et al., *Photon penetration depth in human brain for light stimulation and treatment: A realistic Monte Carlo simulation study.* Journal of Innovative Optical Health Sciences, 2017. **10**(05): p. 1743002.

180. Haeussinger, F.B., et al., *Simulation of near-infrared light absorption considering individual head and prefrontal cortex anatomy: implications for optical neuroimaging.* PLoS One, 2011. **6**(10): p. e26377.
181. Pitzschke, A., et al., *Red and NIR light dosimetry in the human deep brain.* Phys Med Biol, 2015. **60**(7): p. 2921-37.
182. Tedford, C.E., et al., *Quantitative analysis of transcranial and intraparenchymal light penetration in human cadaver brain tissue.* Lasers Surg Med, 2015. **47**(4): p. 312-22.
183. Henderson, T.A. and L.D. Morries, *Near-infrared photonic energy penetration: can infrared phototherapy effectively reach the human brain?* Neuropsychiatr Dis Treat, 2015. **11**: p. 2191-208.
184. Hamblin, M.R., *Shining light on the head: Photobiomodulation for brain disorders.* BBA Clin, 2016. **6**: p. 113-124.
185. Perria, C., et al., *Fast attempts at the photodynamic treatment of human gliomas.* J Neurosurg Sci, 1980. **24**(3-4): p. 119-29.
186. Cheng, M., et al., *Effects of Photoradiation Therapy on Normal Rat Brian.* Neurosurgery, 1984. **15**(6): p. 804–810.
187. Wilson, B.C., P.J. Muller, and J.C. Yanch, *Instrumentation and light dosimetry for intra-operative photodynamic therapy (PDT) of malignant brain tumours.* Phys Med Biol, 1986. **31**(2): p. 125-33.
188. Olzowy, B., et al., *Photoirradiation therapy of experimental malignant glioma with 5-aminolevulinic acid.* J Neurosurg, 2002. **97**(4): p. 970-6.
189. Shackley, D.C., et al., *Light penetration in bladder tissue: implications for the intravesical photodynamic therapy of bladder tumours.* BJU Int, 2000. **86**(6): p. 638-43.
190. Huang, H.C., et al., *23 - Advancing photodynamic therapy with biochemically tuned liposomal nanotechnologies*, in *Applications of Nanoscience in Photomedicine*, M.R. Hamblin and P. Avci, Editors. 2015, Chandos Publishing: Oxford. p. 487-510.
191. Bressler, N.M., *Photodynamic therapy of subfoveal choroidal neovascularization in age-related macular degeneration with verteporfin: two-year results of 2 randomized clinical trials-tap report 2.* Arch Ophthalmol, 2001. **119**(2): p. 198-207.
192. Schmidt, M.H., et al., *Evaluation of photodynamic therapy near functional brain tissue in patients with recurrent brain tumors.* J Neurooncol, 2004. **67**(1-2): p. 201-7.
193. Tachikawa, S., et al., *Localization-dependent cell-killing effects of protoporphyrin (PPIX)-lipid micelles and liposomes in photodynamic therapy.* Bioorg Med Chem, 2015. **23**(24): p. 7578-84.
194. Zou, X., et al., *X-ray-induced nanoparticle-based photodynamic therapy of cancer.* Nanomedicine (Lond), 2014. **9**(15): p. 2339-51.
195. Yan, L., et al., *Protoporphyrin IX (PpIX)-Coated Superparamagnetic Iron Oxide Nanoparticle (SPION) Nanoclusters for Magnetic Resonance Imaging and Photodynamic Therapy.* Advanced functional materials, 2018. **28**(16): p. 1707030.

196. Baglo, Y., et al., *Porphyrin-lipid assemblies and nanovesicles overcome ABC transporter-mediated photodynamic therapy resistance in cancer cells.* Cancer Letters, 2019. **457**: p. 110-118.
197. Pigula, M., et al., *Size-dependent Tumor Response to Photodynamic Therapy and Irinotecan Monotherapies Revealed by Longitudinal Ultrasound Monitoring in an Orthotopic Pancreatic Cancer Model.* Photochem Photobiol, 2018.
198. Huang, H.C., et al., *Mechanism-informed Repurposing of Minocycline Overcomes Resistance to Topoisomerase Inhibition for Peritoneal Carcinomatosis.* Mol Cancer Ther, 2018. **17**(2): p. 508-520.
199. Chang, H.I. and M.K. Yeh, *Clinical development of liposome-based drugs: formulation, characterization, and therapeutic efficacy.* Int J Nanomedicine, 2012. **7**: p. 49-60.
200. Torchilin, V.P., *Recent advances with liposomes as pharmaceutical carriers.* Nat Rev Drug Discov, 2005. **4**(2): p. 145-60.
201. Chowdhary, R.K., I. Shariff, and D. Dolphin, *Drug release characteristics of lipid based benzoporphyrin derivative.* J Pharm Pharm Sci, 2003. **6**(1): p. 13-9.
202. Kachatkou, D., et al., *Unusual photoinduced response of mTHPC liposomal formulation (Foslip).* Photochem Photobiol, 2009. **85**(3): p. 719-24.
203. Lovell, J.F., et al., *Porphysome nanovesicles generated by porphyrin bilayers for use as multimodal biophotonic contrast agents.* Nat Mater, 2011. **10**(4): p. 324-32.
204. Jarvi, M.T., M.S. Patterson, and B.C. Wilson, *Insights into photodynamic therapy dosimetry: simultaneous singlet oxygen luminescence and photosensitizer photobleaching measurements.* Biophys J, 2012. **102**(3): p. 661-71.
205. Kim, M.M., J.C. Finlay, and T.C. Zhu, *Macroscopic singlet oxygen model incorporating photobleaching as an input parameter.* Proc SPIE Int Soc Opt Eng, 2015. **9308**: p. 93080v.
206. Finlay, J.C., S. Mitra, and T.H. Foster, *In vivo mTHPC photobleaching in normal rat skin exhibits unique irradiance-dependent features.* Photochem Photobiol, 2002. **75**(3): p. 282-8.
207. Finlay, J.C., et al., *Photobleaching kinetics of Photofrin in vivo and in multicell tumour spheroids indicate two simultaneous bleaching mechanisms.* Phys Med Biol, 2004. **49**(21): p. 4837-60.
208. Tyrrell, J.S., S.M. Campbell, and A. Curnow, *The relationship between protoporphyrin IX photobleaching during real-time dermatological methyl-aminolevulinate photodynamic therapy (MAL-PDT) and subsequent clinical outcome.* Lasers Surg Med, 2010. **42**(7): p. 613-9.
209. Dereski, M.O., et al., *Depth measurements and histopathological characterization of photodynamic therapy generated normal brain necrosis as a function of incident optical energy dose.* Photochem Photobiol, 1991. **54**(1): p. 109-12.

210. Ikuta, S., et al., *Penetration depth of the 664-nm semiconductor laser light with talaporfin sodium into human brain tissue with glioma.* Photodiagnosis and Photodynamic Therapy, 2015. **12**(3): p. 349.
211. Jacques, S.L., *Simple optical theory for light dosimetry during PDT (Invited Paper).* OE/LASE '92. Vol. 1645. 1992: SPIE.
212. Jacques, S.L., *Light distributions from point, line and plane sources for photochemical reactions and fluorescence in turbid biological tissues.* Photochem Photobiol, 1998. **67**(1): p. 23-32.
213. Jacques, S.L., *How tissue optics affect dosimetry of photodynamic therapy.* J Biomed Opt, 2010. **15**(5): p. 051608.
214. Ong, Y.H. and T.C. Zhu, *Analytic function for predicting light fluence rate of circular fields on a semi-infinite turbid medium.* Opt Express, 2016. **24**(23): p. 26261-26281.
215. Jacques, S.L., *Optical properties of biological tissues: a review.* Physics in Medicine and Biology, 2013. **58**(11): p. R37-R61.
216. Bevilacqua, F., et al., *In vivo local determination of tissue optical properties: applications to human brain.* Appl Opt, 1999. **38**(22): p. 4939-50.
217. Yona, G., et al., *Realistic Numerical and Analytical Modeling of Light Scattering in Brain Tissue for Optogenetic Applications.* eneuro, 2016. **3**(1): p. ENEURO.0059-15.2015.
218. Josefsen, L.B. and R.W. Boyle, *Photodynamic therapy and the development of metal-based photosensitisers.* Met Based Drugs, 2008. **2008**: p. 276109.
219. Hart, N.S. and M. Fitzgerald, *A new perspective on delivery of red-near-infrared light therapy for disorders of the brain.* Discov Med, 2016. **22**(120): p. 147-156.
220. Schnapf, J.L., T.W. Kraft, and D.A. Baylor, *Spectral sensitivity of human cone photoreceptors.* Nature, 1987. **325**(6103): p. 439-41.
221. Silbergeld, D.L. and M.R. Chicoine, *Isolation and characterization of human malignant glioma cells from histologically normal brain.* J Neurosurg, 1997. **86**(3): p. 525-31.
222. Anbil, S., et al., *Vitamin D receptor activation and photodynamic priming enable durable low-dose chemotherapy.* Mol Cancer Ther, 2020.
223. Pranda, M.A., et al., *Tumor Cell Mechanosensing During Incorporation into the Brain Microvascular Endothelium.* Cell Mol Bioeng, 2019. **12**(5): p. 455-480.
224. *GraphPad Prism version 8.0.0 for MacOS, GraphPad Software, San Diego, California USA.*
225. *PHOTOFRIN (porfimer sodium) INJECTION [package insert]. U.S. Food and Drug Administration. Revised 04/2011.*
226. Baeten, K.M. and K. Akassoglou, *Extracellular matrix and matrix receptors in blood-brain barrier formation and stroke.* Developmental neurobiology, 2011. **71**(11): p. 1018-1039.
227. Li, B., et al., *Involvement of Rho/ROCK signalling in small cell lung cancer migration through human brain microvascular endothelial cells.* FEBS Letters, 2006. **580**(17): p. 4252-4260.

228. Wilson, C. and C. González-Billault, *Regulation of cytoskeletal dynamics by redox signaling and oxidative stress: implications for neuronal development and trafficking.* Frontiers in Cellular Neuroscience, 2015. **9**(381).
229. Moldovan, L., et al., *Reactive oxygen species in vascular endothelial cell motility. Roles of NAD(P)H oxidase and Rac1.* Cardiovascular Research, 2006. **71**(2): p. 236-246.
230. Campbell, H.K., J.L. Maiers, and K.A. DeMali, *Interplay between tight junctions & adherens junctions.* Experimental cell research, 2017. **358**(1): p. 39-44.
231. Abu Taha, A. and H.-J. Schnittler, *Dynamics between actin and the VE-cadherin/catenin complex: novel aspects of the ARP2/3 complex in regulation of endothelial junctions.* Cell adhesion & migration, 2014. **8**(2): p. 125-135.
232. Gavard, J. and J.S. Gutkind, *VE-cadherin and claudin-5: it takes two to tango.* Nature cell biology, 2008. **10**(8): p. 883-885.
233. Rodgers, L.S., et al., *Epithelial barrier assembly requires coordinated activity of multiple domains of the tight junction protein ZO-1.* Journal of Cell Science, 2013. **126**(7): p. 1565-1575.
234. Seebach, J., et al., *The CellBorderTracker, a novel tool to quantitatively analyze spatiotemporal endothelial junction dynamics at the subcellular level.* Histochem Cell Biol, 2015. **144**(6): p. 517-32.
235. Rabiet, M.-J., et al., *Thrombin-Induced Increase in Endothelial Permeability Is Associated With Changes in Cell-to-Cell Junction Organization.* Arteriosclerosis, Thrombosis, and Vascular Biology, 1996. **16**(3): p. 488-496.
236. Lampugnani, M.G., et al., *The molecular organization of endothelial cell to cell junctions: differential association of plakoglobin, beta-catenin, and alpha-catenin with vascular endothelial cadherin (VE-cadherin).* J Cell Biol, 1995. **129**(1): p. 203-17.
237. Seebach, J., et al., *Regulation of endothelial barrier function during flow-induced conversion to an arterial phenotype.* Cardiovasc Res, 2007. **75**(3): p. 596-607.
238. Geyer, H., et al., *Characterization of human vascular endothelial cadherin glycans.* Glycobiology, 1999. **9**(9): p. 915-25.
239. Ferreri, D.M., et al., *N-cadherin levels in endothelial cells are regulated by monolayer maturity and p120 availability.* Cell communication & adhesion, 2008. **15**(4): p. 333-349.
240. Lampugnani, M.G., et al., *Cell confluence regulates tyrosine phosphorylation of adherens junction components in endothelial cells.* Journal of Cell Science, 1997. **110**(17): p. 2065-2077.
241. Abu Taha, A., et al., *ARP2/3-mediated junction-associated lamellipodia control VE-cadherin-based cell junction dynamics and maintain monolayer integrity.* Molecular biology of the cell, 2014. **25**(2): p. 245-256.
242. Gavard, J., *Endothelial permeability and VE-cadherin: a wacky comradeship.* Cell adhesion & migration, 2014. **8**(2): p. 158-164.
243. Biemans, E.A.L.M., et al., *Limitations of the hCMEC/D3 cell line as a model for Aβ clearance by the human blood-brain barrier.* Journal of neuroscience research, 2017. **95**(7): p. 1513-1522.

244. Thomas, A., et al., *Characterization of vascular permeability using a biomimetic microfluidic blood vessel model.* Biomicrofluidics, 2017. **11**(2): p. 024102-024102.
245. Perrot, C.Y., J. Sawada, and M. Komatsu, *Prolonged activation of cAMP signaling leads to endothelial barrier disruption via transcriptional repression of RRAS.* Faseb j, 2018: p. fj201700818RRR.
246. Bulbake, U., et al., *Liposomal Formulations in Clinical Use: An Updated Review.* Pharmaceutics, 2017. **9**(2): p. 12.
247. Gabizon, A., H. Shmeeda, and Y. Barenholz, *Pharmacokinetics of pegylated liposomal Doxorubicin: review of animal and human studies.* Clin Pharmacokinet, 2003. **42**(5): p. 419-36.
248. Dai, T., K. Jiang, and W. Lu, *Liposomes and lipid disks traverse the BBB and BBTB as intact forms as revealed by two-step Förster resonance energy transfer imaging.* Acta pharmaceutica Sinica. B, 2018. **8**(2): p. 261-271.
249. Huwyler, J., D. Wu, and W.M. Pardridge, *Brain drug delivery of small molecules using immunoliposomes.* Proceedings of the National Academy of Sciences of the United States of America, 1996. **93**(24): p. 14164-14169.
250. Johnsen, K.B., et al., *Targeting transferrin receptors at the blood-brain barrier improves the uptake of immunoliposomes and subsequent cargo transport into the brain parenchyma.* Scientific Reports, 2017. **7**(1): p. 10396.
251. Kang, Y.-S., et al., *Use of PEGylated Immunoliposomes to Deliver Dopamine Across the Blood–Brain Barrier in a Rat Model of Parkinson's Disease.* CNS Neuroscience & Therapeutics, 2016. **22**(10): p. 817-823.
252. Schnyder, A., et al., *Targeting of daunomycin using biotinylated immunoliposomes: pharmacokinetics, tissue distribution and in vitro pharmacological effects.* J Drug Target, 2005. **13**(5): p. 325-35.
253. Afergan, E., et al., *Delivery of serotonin to the brain by monocytes following phagocytosis of liposomes.* Journal of Controlled Release, 2008. **132**(2): p. 84-90.
254. Lélu, S., et al., *Primary Porcine Brain Endothelial Cells as In Vitro Model to Study Effects of Ultrasound and Microbubbles on Blood–Brain Barrier Function.* IEEE Transactions on Ultrasonics, Ferroelectrics, and Frequency Control, 2017. **64**(1): p. 281-290.
255. Fan, L., et al., *Increasing of Blood-tumor Barrier Permeability through Paracellular Pathway by Low-frequency Ultrasound Irradiation In Vitro.* Journal of Molecular Neuroscience, 2011. **43**(3): p. 541-548.
256. Stepp, H. and W. Stummer, *Light can treat inoperable brain tumours.* Nature, 2019. **565**(7738): p. 161.
257. Salem, U., et al., *Neurosurgical applications of MRI guided laser interstitial thermal therapy (LITT).* Cancer Imaging, 2019. **19**(1): p. 65.
258. Ashraf, O., et al., *Laser-Induced Thermal Therapy in Neuro-Oncology: A Review.* World Neurosurg, 2018. **112**: p. 166-177.
259. Silva, D., et al., *Magnetic Resonance Thermometry and Laser Interstitial Thermal Therapy for Brain Tumors.* Neurosurg Clin N Am, 2017. **28**(4): p. 525-533.

260. Lovell, J.F., et al., *Activatable Photosensitizers for Imaging and Therapy.* Chemical Reviews, 2010. **110**(5): p. 2839-2857.
261. Anand, S., et al., *Fluorouracil Enhances Photodynamic Therapy of Squamous Cell Carcinoma via a p53-Independent Mechanism that Increases Protoporphyrin IX levels and Tumor Cell Death.* Mol Cancer Ther, 2017. **16**(6): p. 1092-1101.
262. Almeida-Marrero, V., et al., *Porphyrinoid biohybrid materials as an emerging toolbox for biomedical light management.* Chemical Society Reviews, 2018. **47**(19): p. 7369-7400.
263. Castano, A.P., P. Mroz, and M.R. Hamblin, *Photodynamic therapy and anti-tumour immunity.* Nat Rev Cancer, 2006. **6**(7): p. 535-545.
264. Spring, B.Q., et al., *A photoactivable multi-inhibitor nanoliposome for tumour control and simultaneous inhibition of treatment escape pathways.* Nat Nanotechnol, 2016. **11**(4): p. 378-87.
265. Spring, B.Q., et al., *The role of photodynamic therapy in overcoming cancer drug resistance.* Photochemical & Photobiological Sciences, 2015. **14**(8): p. 1476-1491.
266. Gallagher-Colombo, S.M., et al., *Erlotinib Pretreatment Improves Photodynamic Therapy of Non-Small Cell Lung Carcinoma Xenografts via Multiple Mechanisms.* Cancer Res, 2015. **75**(15): p. 3118-26.
267. Bown, S.G., et al., *Photodynamic therapy for cancer of the pancreas.* Gut, 2002. **50**(4): p. 549-557.
268. Moore, C.M., et al., *Determination of optimal drug dose and light dose index to achieve minimally invasive focal ablation of localised prostate cancer using WST11-vascular-targeted photodynamic (VTP) therapy.* BJU Int., 2015. **116**(6): p. 888-96.
269. Schmidt, S., et al., *[Clinical use of photodynamic therapy in gynecologic tumor patients--antibody-targeted photodynamic laser therapy as a new oncologic treatment procedure].* Zentralbl Gynakol, 1992. **114**(6): p. 307-11.
270. Mitsunaga, M., et al., *Cancer cell-selective in vivo near infrared photoimmunotherapy targeting specific membrane molecules.* Nat Med, 2011. **17**(12): p. 1685-91.
271. Komatsu, T., et al., *Self-organized lipid-porphyrin bilayer membranes in vesicular form: nanostructure, photophysical properties, and dioxygen coordination.* Chemistry, 2002. **8**(23): p. 5469-80.
272. Shao, S., et al., *Functionalization of cobalt porphyrin-phospholipid bilayers with his-tagged ligands and antigens.* Nat Chem, 2015. **7**(5): p. 438-46.
273. Hamblin, M.R., et al., *Pegylation of a chlorin(e6) polymer conjugate increases tumor targeting of photosensitizer.* Cancer Res, 2001. **61**(19): p. 7155-62.
274. Hamblin, M.R., et al., *Pegylation of charged polymer-photosensitiser conjugates: effects on photodynamic efficacy.* Br J Cancer, 2003. **89**(5): p. 937-43.
275. Savellano, M.D. and T. Hasan, *Targeting cells that overexpress the epidermal growth factor receptor with polyethylene glycolated BPD verteporfin*

photosensitizer immunoconjugates. Photochem Photobiol, 2003. **77**(4): p. 431-9.
276. Spring, B.Q., et al., *Selective treatment and monitoring of disseminated cancer micrometastases in vivo using dual-function, activatable immunoconjugates.* Proceedings of the National Academy of Sciences, 2014. **111**(10): p. E933-E942.
277. Savellano, M.D. and T. Hasan, *Photochemical targeting of epidermal growth factor receptor: a mechanistic study.* Clin Cancer Res, 2005. **11**(4): p. 1658-68.
278. Huang, H.C., et al., *Immobilization of Photo-Immunoconjugates on Nanoparticles Leads to Enhanced Light-Activated Biological Effects.* Small, 2018: p. e1800236.
279. Obaid, G., et al., *Nanolipid Formulations of Benzoporphyrin Derivative: Exploring the Dependence of Nanoconstruct Photophysics and Photochemistry on Their Therapeutic Index in Ovarian Cancer Cells.* Photochem Photobiol, 2018.
280. Sarkaria, J.N., et al., *Use of an orthotopic xenograft model for assessing the effect of epidermal growth factor receptor amplification on glioblastoma radiation response.* Clin Cancer Res, 2006. **12**(7 Pt 1): p. 2264-71.
281. Schneider, C.A., W.S. Rasband, and K.W. Eliceiri, *NIH Image to ImageJ: 25 years of image analysis.* Nat Methods, 2012. **9**(7): p. 671-5.
282. Jin, C.S., et al., *Targeting-triggered porphysome nanostructure disruption for activatable photodynamic therapy.* Adv Healthc Mater, 2014. **3**(8): p. 1240-9.
283. Abrahamse, H. and M.R. Hamblin, *New photosensitizers for photodynamic therapy.* Biochem J, 2016. **473**(4): p. 347-64.
284. Nunes, S.S., et al., *Influence of PEG coating on the biodistribution and tumor accumulation of pH-sensitive liposomes.* Drug delivery and translational research, 2019. **9**(1): p. 123-130.
285. Kaufman, M.B., *Pharmaceutical Approval Update.* P t, 2017. **42**(11): p. 673-683.
286. Stepp, H., et al., *ALA and malignant glioma: fluorescence-guided resection and photodynamic treatment.* J Environ Pathol Toxicol Oncol, 2007. **26**(2): p. 157-64.
287. Han, J. and K. Burgess, *Fluorescent indicators for intracellular pH.* Chem Rev, 2010. **110**(5): p. 2709-28.
288. Zhu, H., et al., *Fluorescent Probes for Sensing and Imaging within Specific Cellular Organelles.* Acc Chem Res, 2016. **49**(10): p. 2115-2126.
289. Bacellar, I.O., et al., *Photodynamic Efficiency: From Molecular Photochemistry to Cell Death.* Int J Mol Sci, 2015. **16**(9): p. 20523-59.
290. Kessel, D. and J.J. Reiners, Jr., *Promotion of Proapoptotic Signals by Lysosomal Photodamage.* Photochem Photobiol, 2015. **91**(4): p. 931-6.
291. Tsubone, T.M., et al., *Enhanced efficiency of cell death by lysosome-specific photodamage.* Sci Rep, 2017. **7**(1): p. 6734.
292. Dos Santos, A.F., et al., *Methylene blue photodynamic therapy induces selective and massive cell death in human breast cancer cells.* BMC Cancer, 2017. **17**(1): p. 194.

293. Mizushima, N. and T. Yoshimori, *How to interpret LC3 immunoblotting.* Autophagy, 2007. **3**(6): p. 542-5.
294. To, M.S., et al., *Mitochondrial uncoupler FCCP activates proton conductance but does not block store-operated Ca(2+) current in liver cells.* Arch Biochem Biophys, 2010. **495**(2): p. 152-8.
295. Martins, W.K., et al., *Parallel damage in mitochondria and lysosomes is an efficient way to photoinduce cell death.* Autophagy, 2018: p. 1-21.
296. Cincotta, L., et al., *Benzophenothiazine and benzoporphyrin derivative combination phototherapy effectively eradicates large murine sarcomas.* Photochem Photobiol, 1996. **63**(2): p. 229-37.
297. Kessel, D., *Photodynamic therapy: Promotion of efficacy by a sequential protocol.* J Porphyr Phthalocyanines, 2016. **20**(1-4): p. 302-306.
298. Martins, W.K., et al., *Parallel damage in mitochondrial and lysosomal compartments promotes efficient cell death with autophagy: The case of the pentacyclic triterpenoids.* Sci Rep, 2015. **5**: p. 12425.
299. Rizvi, I., et al., *Photodynamic therapy: Promoting in vitro efficacy of photodynamic therapy by liposomal formulations of a photosensitizing agent.* Lasers Surg Med, 2018. **50**(5): p. 499-505.
300. Moor, A.C., *Signaling pathways in cell death and survival after photodynamic therapy.* J Photochem Photobiol B, 2000. **57**(1): p. 1-13.
301. Akbarzadeh, A., et al., *Liposome: classification, preparation, and applications.* Nanoscale research letters, 2013. **8**(1): p. 102-102.
302. Bozzuto, G. and A. Molinari, *Liposomes as nanomedical devices.* International journal of nanomedicine, 2015. **10**: p. 975-999.
303. Szoka, F., Jr. and D. Papahadjopoulos, *Procedure for preparation of liposomes with large internal aqueous space and high capture by reverse-phase evaporation.* Proceedings of the National Academy of Sciences of the United States of America, 1978. **75**(9): p. 4194-4198.
304. Bangham, A.D. and R.W. Horne, *NEGATIVE STAINING OF PHOSPHOLIPIDS AND THEIR STRUCTURAL MODIFICATION BY SURFACE-ACTIVE AGENTS AS OBSERVED IN THE ELECTRON MICROSCOPE.* J Mol Biol, 1964. **8**: p. 660-8.
305. Bangham, A.D., M.M. Standish, and J.C. Watkins, *Diffusion of univalent ions across the lamellae of swollen phospholipids.* Journal of Molecular Biology, 1965. **13**(1): p. 238-IN27.
306. Barenholz, Y., *Doxil® — The first FDA-approved nano-drug: Lessons learned.* Journal of Controlled Release, 2012. **160**(2): p. 117-134.
307. Chrai, S.S., R. Murari, and I. Ahmad, *Liposomes (a review)-Part one: Manufacturing issues.* Biopharm-the Applied Technologies of Biopharmaceutical Development, 2001. **14**(11): p. 10-+.
308. Dua, J., A. Rana, and A. Bhandari, *Liposome: methods of preparation and applications.* Int J Pharm Stud Res, 2012. **3**(2): p. 14-20.
309. Powers, D. and N. Nosoudi, *Liposomes; from synthesis to targeting macrophages.* Biomed Res, 2019. **30**(1): p. 288.

310. Gubernator, J., *Active methods of drug loading into liposomes: recent strategies for stable drug entrapment and increased in vivo activity.* Expert Opin Drug Deliv, 2011. **8**(5): p. 565-80.
311. Sur, S., et al., *Remote loading of preencapsulated drugs into stealth liposomes.* Proceedings of the National Academy of Sciences of the United States of America, 2014. **111**(6): p. 2283-2288.
312. Yu, L.X. and B.V. Li, *FDA Bioequivalence Standards*. 2014: Springer New York.
313. Richter, A.M., et al., *Biodistribution of tritiated benzoporphyrin derivative (3H-BPD-MA), a new potent photosensitizer, in normal and tumor-bearing mice.* J Photochem Photobiol B, 1990. **5**(2): p. 231-44.
314. Sercombe, L., et al., *Advances and Challenges of Liposome Assisted Drug Delivery.* Frontiers in pharmacology, 2015. **6**: p. 286-286.
315. Vieira, D.B. and L.F. Gamarra, *Getting into the brain: liposome-based strategies for effective drug delivery across the blood-brain barrier.* Int J Nanomedicine, 2016. **11**: p. 5381-5414.
316. Rahman, A.M., S.W. Yusuf, and M.S. Ewer, *Anthracycline-induced cardiotoxicity and the cardiac-sparing effect of liposomal formulation.* International journal of nanomedicine, 2007. **2**(4): p. 567-583.
317. Xing, M., et al., *Efficacy and Cardiotoxicity of Liposomal Doxorubicin-Based Chemotherapy in Advanced Breast Cancer: A Meta-Analysis of Ten Randomized Controlled Trials.* PloS one, 2015. **10**(7): p. e0133569-e0133569.
318. Kanter, P.M., et al., *Preclinical toxicology study of liposome encapsulated doxorubicin (TLC D-99): comparison with doxorubicin and empty liposomes in mice and dogs.* In Vivo, 1993. **7**(1): p. 85-95.
319. Drummond, D.C., et al., *Development of a Highly Active Nanoliposomal Irinotecan Using a Novel Intraliposomal Stabilization Strategy.* Cancer Research, 2006. **66**(6): p. 3271-3277.
320. Wilhelm, S., et al., *Analysis of nanoparticle delivery to tumours.* Nature Reviews Materials, 2016. **1**: p. 16014.
321. Daemen, T., et al., *Liposomal doxorubicin-induced toxicity: Depletion and impairment of phagocytic activity of liver macrophages.* International Journal of Cancer, 1995. **61**(5): p. 716-721.
322. Filion, M.C. and N.C. Phillips, *Toxicity and immunomodulatory activity of liposomal vectors formulated with cationic lipids toward immune effector cells.* Biochim Biophys Acta, 1997. **1329**(2): p. 345-56.
323. Takano, S., Y. Aramaki, and S. Tsuchiya, *Physicochemical properties of liposomes affecting apoptosis induced by cationic liposomes in macrophages.* Pharm Res, 2003. **20**(7): p. 962-8.
324. Aramaki, Y., S. Takano, and S. Tsuchiya, *Induction of apoptosis in macrophages by cationic liposomes.* FEBS Letters, 1999. **460**(3): p. 472-476.
325. Watson, D.S., A.N. Endsley, and L. Huang, *Design considerations for liposomal vaccines: influence of formulation parameters on antibody and cell-mediated immune responses to liposome associated antigens.* Vaccine, 2012. **30**(13): p. 2256-2272.

326. Ishida, T., et al., *Injection of PEGylated liposomes in rats elicits PEG-specific IgM, which is responsible for rapid elimination of a second dose of PEGylated liposomes.* Journal of Controlled Release, 2006. **112**(1): p. 15-25.
327. Landesman-Milo, D. and D. Peer, *Altering the immune response with lipid-based nanoparticles.* J Control Release, 2012. **161**(2): p. 600-8.
328. Li, J., et al., *A review on phospholipids and their main applications in drug delivery systems.* Asian Journal of Pharmaceutical Sciences, 2015. **10**(2): p. 81-98.
329. Miranda, D. and J.F. Lovell, *Mechanisms of light-induced liposome permeabilization.* Bioengineering & Translational Medicine, 2016. **1**(3): p. 267-276.
330. Luo, D., et al., *Rapid Light-Triggered Drug Release in Liposomes Containing Small Amounts of Unsaturated and Porphyrin-Phospholipids.* Small (Weinheim an der Bergstrasse, Germany), 2016. **12**(22): p. 3039-3047.
331. Kohli, A.G., et al., *Designer lipids for drug delivery: from heads to tails.* Journal of controlled release : official journal of the Controlled Release Society, 2014. **190**: p. 274-287.
332. Tsui, F.C., D.M. Ojcius, and W.L. Hubbell, *The intrinsic pKa values for phosphatidylserine and phosphatidylethanolamine in phosphatidylcholine host bilayers.* Biophysical journal, 1986. **49**(2): p. 459-468.
333. Irby, D., C. Du, and F. Li, *Lipid-Drug Conjugate for Enhancing Drug Delivery.* Molecular pharmaceutics, 2017. **14**(5): p. 1325-1338.
334. Signorell, R.D., et al., *Pharmacokinetics of lipid-drug conjugates loaded into liposomes.* Eur J Pharm Biopharm, 2018. **128**: p. 188-199.
335. Swenson, C.E., et al., *Pharmacokinetics of doxorubicin administered i.v. as Myocet (TLC D-99; liposome-encapsulated doxorubicin citrate) compared with conventional doxorubicin when given in combination with cyclophosphamide in patients with metastatic breast cancer.* Anti-Cancer Drugs, 2003. **14**(3): p. 239-246.
336. Hamilton, A., et al., *EORTC 10968: a phase I clinical and pharmacokinetic study of polyethylene glycol liposomal doxorubicin (Caelyx®, Doxil®) at a 6-week interval in patients with metastatic breast cancer.* Annals of Oncology, 2002. **13**(6): p. 910-918.
337. Corbo, C., et al., *Effects of the protein corona on liposome-liposome and liposome-cell interactions.* Int J Nanomedicine, 2016. **11**: p. 3049-63.
338. Corbo, C., et al., *The impact of nanoparticle protein corona on cytotoxicity, immunotoxicity and target drug delivery.* Nanomedicine (London, England), 2016. **11**(1): p. 81-100.
339. Barbero, F., et al., *Formation of the Protein Corona: The Interface between Nanoparticles and the Immune System.* Seminars in Immunology, 2017. **34**: p. 52-60.
340. Caracciolo, G., *Liposome-protein corona in a physiological environment: challenges and opportunities for targeted delivery of nanomedicines.* Nanomedicine, 2015. **11**(3): p. 543-57.

341. Hadjidemetriou, M., et al., *In Vivo Biomolecule Corona around Blood-Circulating, Clinically Used and Antibody-Targeted Lipid Bilayer Nanoscale Vesicles.* ACS Nano, 2015. **9**(8): p. 8142-8156.
342. Gessner, A., et al., *Functional groups on polystyrene model nanoparticles: Influence on protein adsorption.* Journal of Biomedical Materials Research Part A, 2003. **65A**(3): p. 319-326.
343. Gessner, A., et al., *Nanoparticles with decreasing surface hydrophobicities: influence on plasma protein adsorption.* International Journal of Pharmaceutics, 2000. **196**(2): p. 245-249.
344. Papahadjopoulos, D., G. Poste, and B.E. Schaeffer, *Fusion of mammalian cells by unilamellar lipid vesicles: Influence of lipid surface charge, fluidity and cholesterol.* Biochimica et Biophysica Acta (BBA) - Biomembranes, 1973. **323**(1): p. 23-42.
345. Pagano, R.E., L. Huang, and C. Wey, *Interaction of phospholipid vesicles with cultured mammalian cells.* Nature, 1974. **252**(5479): p. 166-167.
346. Adams, D.H., et al., *Liposome toxicity in the mouse central nervous system.* J Neurol Sci, 1977. **31**(2): p. 173-9.
347. Shi, M., et al., *Liposomal formulations of carboplatin injected by convection-enhanced delivery increases the median survival time of F98 glioma bearing rats.* Journal of Nanobiotechnology, 2018. **16**(1): p. 77.
348. Fan, Y., et al., *Cationic liposome-hyaluronic acid hybrid nanoparticles for intranasal vaccination with subunit antigens.* J Control Release, 2015. **208**: p. 121-129.
349. Hernandez-Caselles, T., J. Villalain, and J.C. Gomez-Fernandez, *Influence of liposome charge and composition on their interaction with human blood serum proteins.* Mol Cell Biochem, 1993. **120**(2): p. 119-26.
350. Heath, T.D., N.G. Lopez, and D. Papahadjopoulos, *The effects of liposome size and surface charge on liposome-mediated delivery of methotrexate-gamma-aspartate to cells in vitro.* Biochim Biophys Acta, 1985. **820**(1): p. 74-84.
351. Parnham, M.J. and H. Wetzig, *Toxicity screening of liposomes.* Chem Phys Lipids, 1993. **64**(1-3): p. 263-74.
352. Lappalainen, K., et al., *Comparison of Cell Proliferation and Toxicity Assays Using Two Cationic Liposomes.* Pharmaceutical Research, 1994. **11**(8): p. 1127-1131.
353. Lentz, B.R., *Exposure of platelet membrane phosphatidylserine regulates blood coagulation.* Progress in Lipid Research, 2003. **42**(5): p. 423-438.
354. Zbinden, G., H. Wunderli-Allenspach, and L. Grimm, *Assessment of thrombogenic potential of liposomes.* Toxicology, 1989. **54**(3): p. 273-80.
355. Ishiwata, H., et al., *Characteristics and biodistribution of cationic liposomes and their DNA complexes.* Journal of Controlled Release, 2000. **69**(1): p. 139-148.
356. (CDER), U.S.D.o.H.a.H.S.F.a.D.A.C.f.D.E.a.R., *Liposome Drug Products: Chemistry, Manufacturing, and Controls; Human Pharmacokinetics and Bioavailability; and Labeling Documentation. Guidance for Industry.* 2018.

357. White, R.E., et al., *Radiolabeled mass-balance excretion and metabolism studies in laboratory animals: a commentary on why they are still necessary.* Xenobiotica, 2013. **43**(2): p. 219-25; discussion 226-7.
358. Simoes, S., et al., *Cationic liposomes for gene delivery.* Expert Opin Drug Deliv, 2005. **2**(2): p. 237-54.
359. Balazs, D.A. and W. Godbey, *Liposomes for use in gene delivery.* Journal of drug delivery, 2011. **2011**: p. 326497-326497.
360. Tabernero, J., et al., *First-in-Humans Trial of an RNA Interference Therapeutic Targeting VEGF and KSP in Cancer Patients with Liver Involvement.* Cancer Discovery, 2013. **3**(4): p. 406-417.
361. Zhou, J., et al., *Nanoparticle-Based Delivery of RNAi Therapeutics: Progress and Challenges.* Pharmaceuticals (Basel, Switzerland), 2013. **6**(1): p. 85-107.
362. Akhtar, S. and I.F. Benter, *Nonviral delivery of synthetic siRNAs in vivo.* The Journal of clinical investigation, 2007. **117**(12): p. 3623-3632.
363. Li, W. and F.C. Szoka, *Lipid-based Nanoparticles for Nucleic Acid Delivery.* Pharmaceutical Research, 2007. **24**(3): p. 438-449.
364. Lv, H., et al., *Toxicity of cationic lipids and cationic polymers in gene delivery.* J Control Release, 2006. **114**(1): p. 100-9.
365. Kedmi, R., N. Ben-Arie, and D. Peer, *The systemic toxicity of positively charged lipid nanoparticles and the role of Toll-like receptor 4 in immune activation.* Biomaterials, 2010. **31**(26): p. 6867-75.
366. Knudsen, K.B., et al., *In vivo toxicity of cationic micelles and liposomes.* Nanomedicine, 2015. **11**(2): p. 467-77.
367. Hattori, Y., et al., *Effect of Cationic Lipid Type in Folate-PEG-Modified Cationic Liposomes on Folate Receptor-Mediated siRNA Transfection in Tumor Cells.* Pharmaceutics, 2019. **11**(4).
368. Zelphati, O. and F.C. Szoka, *Intracellular Distribution and Mechanism of Delivery of Oligonucleotides Mediated by Cationic Lipids.* Pharmaceutical Research, 1996. **13**(9): p. 1367-1372.
369. Romøren, K., et al., *Transfection efficiency and cytotoxicity of cationic liposomes in salmonid cell lines of hepatocyte and macrophage origin.* Biochimica et Biophysica Acta (BBA) - Biomembranes, 2004. **1663**(1): p. 127-134.
370. Cui, S., et al., *Correlation of the cytotoxic effects of cationic lipids with their headgroups.* Toxicology Research, 2018. **7**(3): p. 473-479.
371. Yang, K., et al., *Cationic liposomes induce cell necrosis through lysosomal dysfunction and late-stage autophagic flux inhibition.* Nanomedicine, 2016. **11**(23): p. 3117-3137.
372. Soenen, S.J.H., A.R. Brisson, and M. De Cuyper, *Addressing the problem of cationic lipid-mediated toxicity: The magnetoliposome model.* Biomaterials, 2009. **30**(22): p. 3691-3701.
373. Wei, X., et al., *Cationic nanocarriers induce cell necrosis through impairment of Na+/K+-ATPase and cause subsequent inflammatory response.* Cell Research, 2015. **25**(2): p. 237-253.

374. Aramaki, Y., S. Takano, and S. Tsuchiya, *Cationic Liposomes Induce Macrophage Apoptosis through Mitochondrial Pathway.* Archives of Biochemistry and Biophysics, 2001. **392**(2): p. 245-250.
375. Iwaoka, S., et al., *Cationic liposomes induce apoptosis through p38 MAP kinase–caspase-8–Bid pathway in macrophage-like RAW264.7 cells.* Journal of Leukocyte Biology, 2006. **79**(1): p. 184-191.
376. Chrai, S.S., R. Murari, and I. Ahmad, *Liposomes (a review): Part two: Drug delivery systems.* BioPharm, 2002. **15**: p. 40-43+49.
377. Senior, J.H., *Fate and behavior of liposomes in vivo: a review of controlling factors.* Critical reviews in therapeutic drug carrier systems, 1987. **3**(2): p. 123-93.
378. Kimelberg, H.K., et al., *The Effect of Entrapment in Liposomes on the in Vivo Distribution of [3H]Methotrexate in a Primate.* Cancer Research, 1976. **36**(8): p. 2949-2957.
379. Yona, S. and S. Gordon, *From the Reticuloendothelial to Mononuclear Phagocyte System - The Unaccounted Years.* Frontiers in immunology, 2015. **6**: p. 328-328.
380. Guilliams, M., et al., *Dendritic cells, monocytes and macrophages: a unified nomenclature based on ontogeny.* Nature Reviews Immunology, 2014. **14**(8): p. 571-578.
381. Soundararajan, A., et al., *[(186)Re]Liposomal doxorubicin (Doxil): in vitro stability, pharmacokinetics, imaging and biodistribution in a head and neck squamous cell carcinoma xenograft model.* Nuclear medicine and biology, 2009. **36**(5): p. 515-524.
382. Beyer, I., et al., *Coadministration of epithelial junction opener JO-1 improves the efficacy and safety of chemotherapeutic drugs.* Clinical cancer research : an official journal of the American Association for Cancer Research, 2012. **18**(12): p. 3340-3351.
383. Arnold, R.D., et al., *Effect of repetitive administration of Doxorubicin-containing liposomes on plasma pharmacokinetics and drug biodistribution in a rat brain tumor model.* Clinical cancer research : an official journal of the American Association for Cancer Research, 2005. **11**(24 Pt 1): p. 8856-8865.
384. Lu, W.L., et al., *A pegylated liposomal platform: pharmacokinetics, pharmacodynamics, and toxicity in mice using doxorubicin as a model drug.* J Pharmacol Sci, 2004. **95**(3): p. 381-9.
385. Luo, R., et al., *Distinct biodistribution of doxorubicin and the altered dispositions mediated by different liposomal formulations.* International Journal of Pharmaceutics, 2017. **519**(1): p. 1-10.
386. Allen, T.M., et al., *Chronic liposome administration in mice: effects on reticuloendothelial function and tissue distribution.* Journal of Pharmacology and Experimental Therapeutics, 1984. **229**(1): p. 267.
387. Ellens, H., E. Mayhew, and Y.M. Rustum, *Reversible depression of the reticuloendothelial system by liposomes.* Biochimica et Biophysica Acta (BBA) - General Subjects, 1982. **714**(3): p. 479-485.

388. Van Rooijen, N. and A. Sanders, *Kupffer cell depletion by liposome-delivered drugs: comparative activity of intracellular clodronate, propamidine, and ethylenediaminetetraacetic acid.* Hepatology, 1996. **23**(5): p. 1239-43.
389. Storm, G., et al., *Doxorubicin entrapped in sterically stabilized liposomes: effects on bacterial blood clearance capacity of the mononuclear phagocyte system.* Clin Cancer Res, 1998. **4**(1): p. 111-5.
390. Rooijen, N.v. and E.v. Kesteren-Hendrikx, *"In Vivo" Depletion of Macrophages by Liposome-Mediated "Suicide"*, in *Methods in Enzymology*. 2003, Academic Press. p. 3-16.
391. Daemen, T., et al., *Toxicity of doxorubicin entrapped within long-circulating liposomes.* Journal of Controlled Release, 1997. **44**(1): p. 1-9.
392. La-Beck, N.M., X. Liu, and L.M. Wood, *Harnessing Liposome Interactions With the Immune System for the Next Breakthrough in Cancer Drug Delivery.* Frontiers in Pharmacology, 2019. **10**(220).
393. Cruz-Leal, Y., et al., *Liposomes of phosphatidylcholine and cholesterol induce an M2-like macrophage phenotype reprogrammable to M1 pattern with the involvement of B-1 cells.* Immunobiology, 2014. **219**(6): p. 403-15.
394. Rajan, R., et al., *Liposome-induced immunosuppression and tumor growth is mediated by macrophages and mitigated by liposome-encapsulated alendronate.* Journal of controlled release : official journal of the Controlled Release Society, 2018. **271**: p. 139-148.
395. Mantovani, A., et al., *Macrophage polarization: tumor-associated macrophages as a paradigm for polarized M2 mononuclear phagocytes.* Trends in Immunology, 2002. **23**(11): p. 549-555.
396. Miao, X., X. Leng, and Q. Zhang, *The Current State of Nanoparticle-Induced Macrophage Polarization and Reprogramming Research.* International journal of molecular sciences, 2017. **18**(2): p. 336.
397. Sabnani, M.K., et al., *Liposome promotion of tumor growth is associated with angiogenesis and inhibition of antitumor immune responses.* Nanomedicine: Nanotechnology, Biology and Medicine, 2015. **11**(2): p. 259-262.
398. Batenjany, M.M., et al., *The effect of cholesterol in a liposomal Muc1 vaccine.* Biochimica et Biophysica Acta (BBA) - Biomembranes, 2001. **1514**(2): p. 280-290.
399. Demel, R.A., et al., *Effects of temperature and cholesterol on the glucose permeability of liposomes prepared with natural and synthetic lecithins.* Biochimica et Biophysica Acta (BBA) - Biomembranes, 1968. **150**(4): p. 655-665.
400. Papahadjopoulos, D., M. Cowden, and H. Kimelberg, *Role of cholesterol in membranes. Effects on phospholipid-protein interactions, membrane permeability and enzymatic activity.* Biochim Biophys Acta, 1973. **330**(1): p. 8-26.
401. Briuglia, M.L., et al., *Influence of cholesterol on liposome stability and on in vitro drug release.* Drug Deliv Transl Res, 2015. **5**(3): p. 231-42.
402. Kirby, C., J. Clarke, and G. Gregoriadis, *Effect of the cholesterol content of small unilamellar liposomes on their stability in vivo and in vitro.* Biochem J, 1980. **186**(2): p. 591-8.

403. Lopez-Pinto, J.M., M.L. Gonzalez-Rodriguez, and A.M. Rabasco, *Effect of cholesterol and ethanol on dermal delivery from DPPC liposomes.* Int J Pharm, 2005. **298**(1): p. 1-12.
404. Smaby, J.M., et al., *Phosphatidylcholine acyl unsaturation modulates the decrease in interfacial elasticity induced by cholesterol.* Biophys J, 1997. **73**(3): p. 1492-505.
405. Magarkar, A., et al., *Cholesterol level affects surface charge of lipid membranes in saline solution.* Scientific Reports, 2014. **4**: p. 5005.
406. Papahadjopoulos, D., S. Nir, and S. Ohki, *Permeability properties of phospholipid membranes: Effect of cholesterol and temperature.* Biochimica et Biophysica Acta (BBA) - Biomembranes, 1972. **266**(3): p. 561-583.
407. Li, Y., et al., *Enrichment of endoplasmic reticulum with cholesterol inhibits sarcoplasmic-endoplasmic reticulum calcium ATPase-2b activity in parallel with increased order of membrane lipids: implications for depletion of endoplasmic reticulum calcium stores and apoptosis in cholesterol-loaded macrophages.* J Biol Chem, 2004. **279**(35): p. 37030-9.
408. Li, Y., et al., *Free cholesterol-loaded macrophages are an abundant source of tumor necrosis factor-alpha and interleukin-6: model of NF-kappaB- and map kinase-dependent inflammation in advanced atherosclerosis.* J Biol Chem, 2005. **280**(23): p. 21763-72.
409. Roerdink, F.H., et al., *Effect of cholesterol on the uptake and intracellular degradation of liposomes by liver and spleen; a combined biochemical and γ-ray perturbed angular correlation study.* Biochimica et Biophysica Acta (BBA) - Biomembranes, 1989. **980**(2): p. 234-240.
410. Kaur, R., et al., *Effect of incorporating cholesterol into DDA:TDB liposomal adjuvants on bilayer properties, biodistribution, and immune responses.* Mol Pharm, 2014. **11**(1): p. 197-207.
411. Nakano, Y., et al., *Cholesterol inclusion in liposomes affects induction of antigen-specific IgG and IgE antibody production in mice by a surface-linked liposomal antigen.* Bioconjug Chem, 2002. **13**(4): p. 744-9.
412. Ganapathi, R., et al., *Effect of cholesterol content on antitumor activity and toxicity of liposome-encapsulated 1-beta-D-arabinofuranosylcytosine in vivo.* Cancer Res, 1980. **40**(3): p. 630-3.
413. Ishida, T., et al., *Biodistribution of liposomes and C3 fragments associated with liposomes: evaluation of their relationship.* International Journal of Pharmaceutics, 2000. **205**(1): p. 183-193.
414. Cunningham, C.M., et al., *Activation of Human Complement by Liposomes: A Model for Membrane Activation of the Alternative Pathway.* The Journal of Immunology, 1979. **122**(4): p. 1237-1242.
415. Chonn, A., P.R. Cullis, and D.V. Devine, *The role of surface charge in the activation of the classical and alternative pathways of complement by liposomes.* The Journal of Immunology, 1991. **146**(12): p. 4234-4241.
416. Remes, A. and D.F. Williams, *Immune response in biocompatibility.* Biomaterials, 1992. **13**(11): p. 731-43.

417. Lynn, A.D., et al., *Temporal progression of the host response to implanted poly(ethylene glycol)-based hydrogels.* J Biomed Mater Res A, 2011. **96**(4): p. 621-31.
418. Szebeni, J. and S.M. Moghimi, *Liposome triggering of innate immune responses: a perspective on benefits and adverse reactions.* J Liposome Res, 2009. **19**(2): p. 85-90.
419. Dobrovolskaia, M.A., et al., *Preclinical studies to understand nanoparticle interaction with the immune system and its potential effects on nanoparticle biodistribution.* Molecular pharmaceutics, 2008. **5**(4): p. 487-495.
420. Dobrovolskaia, M.A. and S.E. McNeil, *Immunological properties of engineered nanomaterials.* Nature Nanotechnology, 2007. **2**(8): p. 469-478.
421. Lee, Y.K., et al., *Effect of the protein corona on nanoparticles for modulating cytotoxicity and immunotoxicity.* International journal of nanomedicine, 2014. **10**: p. 97-113.
422. Kinsky, S.C., et al., *Complement-dependent damage to liposomes prepared from pure lipids and Forssman hapten.* Biochemistry, 1969. **8**(10): p. 4149-4158.
423. Alving, C.R., et al., *Liposomes containing lipid A: an effective, safe, generic adjuvant system for synthetic vaccines.* Expert Rev Vaccines, 2012. **11**(6): p. 733-44.
424. Alving, C.R., *Liposomes as carriers of antigens and adjuvants.* Journal of Immunological Methods, 1991. **140**(1): p. 1-13.
425. Perrie, Y., et al., *Designing liposomal adjuvants for the next generation of vaccines.* Advanced Drug Delivery Reviews, 2016. **99**: p. 85-96.
426. Didierlaurent, A.M., et al., *Adjuvant system AS01: helping to overcome the challenges of modern vaccines.* Expert Rev Vaccines, 2017. **16**(1): p. 55-63.
427. Badiee, A., et al., *The role of liposome charge on immune response generated in BALB/c mice immunized with recombinant major surface glycoprotein of Leishmania (rgp63).* Exp Parasitol, 2009. **121**(4): p. 362-9.
428. Badiee, A., et al., *The role of liposome size on the type of immune response induced in BALB/c mice against leishmaniasis: rgp63 as a model antigen.* Experimental Parasitology, 2012. **132**(4): p. 403-409.
429. Henriksen-Lacey, M., A. Devitt, and Y. Perrie, *The vesicle size of DDA:TDB liposomal adjuvants plays a role in the cell-mediated immune response but has no significant effect on antibody production.* J Control Release, 2011. **154**(2): p. 131-7.
430. Yamamoto, S., et al., *HEPC-based liposomes trigger cytokine release from peripheral blood cells: effects of liposomal size, dose and lipid composition.* International Journal of Pharmaceutics, 2002. **236**(1): p. 125-133.
431. Niwa, K., et al., *Inflammatory cytokine production in whole blood modified by liposome-encapsulated hemoglobin.* Artif Cells Blood Substit Immobil Biotechnol, 1998. **26**(5-6): p. 559-70.
432. Noris, M. and G. Remuzzi, *Overview of complement activation and regulation.* Seminars in nephrology, 2013. **33**(6): p. 479-492.
433. van den Berg, R.H., et al., *The First Subcomponent of Complement, C1q, Triggers the Production of IL-8, IL-6, and Monocyte Chemoattractant*

Peptide-1 by Human Umbilical Vein Endothelial Cells. The Journal of Immunology, 1998. **161**(12): p. 6924-6930.
434. Wagner, H., *Bacterial CpG DNA Activates Immune Cells to Signal Infectious Danger*, in *Advances in Immunology*, F.J. Dixon, Editor. 1999, Academic Press. p. 329-368.
435. Ahmad-Nejad, P., et al., *Bacterial CpG-DNA and lipopolysaccharides activate Toll-like receptors at distinct cellular compartments.* Eur J Immunol, 2002. **32**(7): p. 1958-68.
436. Sellins, K., et al., *Type I interferons potently suppress gene expression following gene delivery using liposome(-)DNA complexes.* Mol Ther, 2005. **12**(3): p. 451-9.
437. Yasuda, S., et al., *Comparison of the type of liposome involving cytokine production induced by non-CpG Lipoplex in macrophages.* Mol Pharm, 2010. **7**(2): p. 533-42.
438. Pusztai, L., et al., *Changes in plasma levels of inflammatory cytokines in response to paclitaxel chemotherapy.* Cytokine, 2004. **25**(3): p. 94-102.
439. Szebeni, J., *The interaction of liposomes with the complement system.* Crit Rev Ther Drug Carrier Syst, 1998. **15**(1): p. 57-88.
440. Cullis, P.R., A. Chonn, and S.C. Semple, *Interactions of liposomes and lipid-based carrier systems with blood proteins: Relation to clearance behaviour in vivo.* Adv Drug Deliv Rev, 1998. **32**(1-2): p. 3-17.
441. Bradley, A.J., et al., *C1q Binding to liposomes is surface charge dependent and is inhibited by peptides consisting of residues 14–26 of the human C1qA chain in a sequence independent manner.* Biochimica et Biophysica Acta (BBA) - Biomembranes, 1999. **1418**(1): p. 19-30.
442. Harashima, H., et al., *Enhanced Hepatic Uptake of Liposomes Through Complement Activation Depending on the Size of Liposomes.* Pharmaceutical Research, 1994. **11**(3): p. 402-406.
443. Liu, Z.Y., R. Solow, and V.W. Hu, *Fluorescence analysis of size distribution and mode of dye release from carboxyfluorescein-loaded vesicles: application to the study of complement-membrane interactions.* Biochim Biophys Acta, 1988. **945**(2): p. 253-62.
444. Alving, C.R., R.L. Richards, and A.A. Guirguis, *Cholesterol-Dependent Human Complement Activation Resulting in Damage to Liposomal Model Membranes.* The Journal of Immunology, 1977. **118**(1): p. 342-347.
445. Szebeni, J., et al., *Role of complement activation in hypersensitivity reactions to doxil and hynic PEG liposomes: experimental and clinical studies.* J Liposome Res, 2002. **12**(1-2): p. 165-72.
446. Chanan-Khan, A., et al., *Complement activation following first exposure to pegylated liposomal doxorubicin (Doxil®): possible role in hypersensitivity reactions.* Annals of Oncology, 2003. **14**(9): p. 1430-1437.
447. van den Hoven, J.M., et al., *Complement activation by PEGylated liposomes containing prednisolone.* European Journal of Pharmaceutical Sciences, 2013. **49**(2): p. 265-271.

448. Fülöp, T., et al., *Liposome-induced hypersensitivity reactions: Risk reduction by design of safe infusion protocols in pigs.* Journal of Controlled Release, 2019. **309**: p. 333-338.
449. Szebeni, J., et al., *Liposome-induced pulmonary hypertension: properties and mechanism of a complement-mediated pseudoallergic reaction.* Am J Physiol Heart Circ Physiol, 2000. **279**(3): p. H1319-28.
450. Ingen-Housz-Oro, S., et al., *Immediate hypersensitivity reaction to pegylated liposomal doxorubicin: management and outcome in four patients.* Eur J Dermatol, 2017. **27**(3): p. 271-274.
451. Arning, M., et al., *Pulmonary toxicity during infusion of liposomal amphotericin B in two patients with acute leukemia.* Eur J Clin Microbiol Infect Dis, 1995. **14**(1): p. 41-3.
452. Judge, A., et al., *Hypersensitivity and loss of disease site targeting caused by antibody responses to PEGylated liposomes.* Mol Ther, 2006. **13**(2): p. 328-37.
453. Ringden, O., et al., *Allergic reactions and other rare side-effects of liposomal amphotericin.* Lancet, 1994. **344**(8930): p. 1156-7.
454. Alberts, D.S. and D.J. Garcia, *Safety Aspects of Pegylated Liposomal Doxorubicin in Patients with Cancer.* Drugs, 1997. **54**(4): p. 30-35.
455. Szebeni, J., et al., *Hemodynamic changes induced by liposomes and liposome-encapsulated hemoglobin in pigs: a model for pseudoallergic cardiopulmonary reactions to liposomes. Role of complement and inhibition by soluble CR1 and anti-C5a antibody.* Circulation, 1999. **99**(17): p. 2302-9.
456. Hammerschmidt, D., et al., *ASSOCIATION OF COMPLEMENT ACTIVATION AND ELEVATED PLASMA-C5a WITH ADULT RESPIRATORY DISTRESS SYNDROME: Pathophysiological Relevance and Possible Prognostic Value.* The Lancet, 1980. **315**(8175): p. 947-949.
457. Marceau, F., C. Lundberg, and T.E. Hugli, *Effects of the anaphylatoxins on circulation.* Immunopharmacology, 1987. **14**(2): p. 67-84.
458. Kozma, G.T., et al., *Pseudo-anaphylaxis to Polyethylene Glycol (PEG)-Coated Liposomes: Roles of Anti-PEG IgM and Complement Activation in a Porcine Model of Human Infusion Reactions.* ACS Nano, 2019. **13**(8): p. 9315-9324.
459. Szebeni, J., et al., *Activation of complement by therapeutic liposomes and other lipid excipient-based therapeutic products: Prediction and prevention.* Advanced Drug Delivery Reviews, 2011. **63**(12): p. 1020-1030.
460. Weiss, R.B., et al., *Hypersensitivity reactions from taxol.* J Clin Oncol, 1990. **8**(7): p. 1263-8.
461. Castells, M.C., et al., *Hypersensitivity reactions to chemotherapy: outcomes and safety of rapid desensitization in 413 cases.* J Allergy Clin Immunol, 2008. **122**(3): p. 574-80.
462. Szebeni, J., et al., *Liposome-induced complement activation and related cardiopulmonary distress in pigs: factors promoting reactogenicity of Doxil and AmBisome.* Nanomedicine: Nanotechnology, Biology and Medicine, 2012. **8**(2): p. 176-184.
463. *ALZA Pharmaceuticals, I. Doxil Package Insert. Mountain View, CA,*

USA 2000.
464. Szebeni, J., et al., *Roadmap and strategy for overcoming infusion reactions to nanomedicines.* Nature Nanotechnology, 2018. **13**(12): p. 1100-1108.
465. Ishida, T., et al., *PEGylated liposomes elicit an anti-PEG IgM response in a T cell-independent manner.* J Control Release, 2007. **122**(3): p. 349-55.
466. Verhoef, J.J.F. and T.J. Anchordoquy, *Questioning the Use of PEGylation for Drug Delivery.* Drug delivery and translational research, 2013. **3**(6): p. 499-503.
467. Ichihara, M., et al., *Anti-PEG IgM Response against PEGylated Liposomes in Mice and Rats.* Pharmaceutics, 2010. **3**(1): p. 1-11.
468. Mohamed, M., et al., *PEGylated liposomes: immunological responses.* Science and technology of advanced materials, 2019. **20**(1): p. 710-724.
469. Yang, Q. and S.K. Lai, *Anti-PEG immunity: emergence, characteristics, and unaddressed questions.* Wiley interdisciplinary reviews. Nanomedicine and nanobiotechnology, 2015. **7**(5): p. 655-677.
470. Mond, J.J., et al., *T cell independent antigens.* Current Opinion in Immunology, 1995. **7**(3): p. 349-354.
471. Boes, M., *Role of natural and immune IgM antibodies in immune responses.* Mol Immunol, 2000. **37**(18): p. 1141-9.
472. Ishida, T., et al., *Spleen plays an important role in the induction of accelerated blood clearance of PEGylated liposomes.* Journal of Controlled Release, 2006. **115**(3): p. 243-250.
473. Bucke, W.E., et al., *Surface-Modified Amikacin-Liposomes: Organ Distribution and Interaction with Plasma Proteins.* Journal of Drug Targeting, 1998. **5**(2): p. 99-108.
474. Cheng, T.-L., et al., *Accelerated Clearance of Polyethylene Glycol-Modified Proteins by Anti-Polyethylene Glycol IgM.* Bioconjugate Chemistry, 1999. **10**(3): p. 520-528.
475. Hauet, T. and M. Eugene, *A new approach in organ preservation: potential role of new polymers.* Kidney Int, 2008. **74**(8): p. 998-1003.
476. Gabizon, A., et al., *An open-label study to evaluate dose and cycle dependence of the pharmacokinetics of pegylated liposomal doxorubicin.* Cancer Chemother Pharmacol, 2008. **61**(4): p. 695-702.
477. Yang, Q., et al., *Analysis of Pre-existing IgG and IgM Antibodies against Polyethylene Glycol (PEG) in the General Population.* Anal Chem, 2016. **88**(23): p. 11804-11812.
478. Wang, F., et al., *Time Interval of Two Injections and First-Dose Dependent of Accelerated Blood Clearance Phenomenon Induced by PEGylated Liposomal Gambogenic Acid: The Contribution of PEG-Specific IgM.* J Pharm Sci, 2019. **108**(1): p. 641-651.
479. Calori, I.R., et al., *Self-aggregation of the proteolytic forms of Verteporfin: An in silico and in vitro study.*
480. Richter, A.M., et al., *Liposomal delivery of a photosensitizer, benzoporphyrin derivative monoacid ring A (BPD), to tumor tissue in a mouse tumor model.* Photochem Photobiol, 1993. **57**(6): p. 1000-6.

481. Kramer, M., et al., *Liposomal benzoporphyrin derivative verteporfin photodynamic therapy. Selective treatment of choroidal neovascularization in monkeys.* Ophthalmology, 1996. **103**(3): p. 427-38.
482. Participants, V.R., *Guidelines for using verteporfin (Visudyne) in photodynamic therapy for choroidal neovascularization due to age-related macular degeneration and other causes: update.* Retina, 2005. **25**(2): p. 119-34.
483. Participants, V.R.a., T.o.a.-r.m.d.w.p.t.T.s.g.p. investigators, and V.i.p.t.V.s.g.p. investigators, *Guidelines for using verteporfin (visudyne) in photodynamic therapy to treat choroidal neovascularization due to age-related macular degeneration and other causes.* Retina, 2002. **22**(1): p. 6-18.
484. van Dijk, E.H.C., et al., *Photodynamic Therapy for Chorioretinal Diseases: A Practical Approach.* Ophthalmol Ther, 2020. **9**(2): p. 329-342.
485. Hanada, Y., et al., *EUS-guided verteporfin photodynamic therapy for pancreatic cancer.* Gastrointest Endosc, 2021.
486. Isakoff, S.J., et al., *An open label, phase II trial of continuous low-irradiance photodynamic therapy (CLIPT) using verteporfin for the treatment of cutaneous breast cancer metastases.* Journal of Clinical Oncology, 2017. **35**(15_suppl): p. TPS1121.
487. Ghosh, S., K.A. Carter, and J.F. Lovell, *Liposomal formulations of photosensitizers.* Biomaterials, 2019. **218**: p. 119341.
488. Guirguis, M., et al., *Membrane composition is a functional determinant of NIR-activable liposomes in orthotopic head and neck cancer.* Nanophotonics, 2021. **10**(12): p. 3169-3185.
489. Michy, T., et al., *Verteporfin-Loaded Lipid Nanoparticles Improve Ovarian Cancer Photodynamic Therapy In Vitro and In Vivo.* Cancers, 2019. **11**(11): p. 1760.
490. Mullin, J.W., *5. Nucleation*, in *Crystallization (4th Edition)*. Elsevier.
491. Kulkarni, T.A., et al., *A year-long extended release nanoformulated cabotegravir prodrug.* Nature Materials, 2020. **19**(8): p. 910-920.
492. Gautam, N., et al., *Lipophilic nanocrystal prodrug-release defines the extended pharmacokinetic profiles of a year-long cabotegravir.* Nature Communications, 2021. **12**(1): p. 3453.
493. Sillman, B., et al., *Creation of a long-acting nanoformulated dolutegravir.* Nat Commun, 2018. **9**(1): p. 443.
494. Liu, Y., L. Huang, and F. Liu, *Paclitaxel nanocrystals for overcoming multidrug resistance in cancer.* Mol Pharm, 2010. **7**(3): p. 863-9.
495. Harrison, M.R., et al., *A phase II study of 2-methoxyestradiol (2ME2) NanoCrystal® dispersion (NCD) in patients with taxane-refractory, metastatic castrate-resistant prostate cancer (CRPC).* Invest New Drugs, 2011. **29**(6): p. 1465-74.
496. Jarvis, M., V. Krishnan, and S. Mitragotri, *Nanocrystals: A perspective on translational research and clinical studies.* Bioeng Transl Med, 2019. **4**(1): p. 5-16.

497. Junghanns, J.-U.A.H. and R.H. Müller, *Nanocrystal technology, drug delivery and clinical applications.* International journal of nanomedicine, 2008. **3**(3): p. 295-309.
498. Radu, M. and J. Chernoff, *An in vivo assay to test blood vessel permeability.* Journal of visualized experiments : JoVE, 2013(73): p. e50062-e50062.
499. Kessel, D. and J.J. Reiners, Jr., *Enhanced efficacy of photodynamic therapy via a sequential targeting protocol.* Photochemistry and photobiology, 2014. **90**(4): p. 889-895.
500. Buytaert, E., M. Dewaele, and P. Agostinis, *Molecular effectors of multiple cell death pathways initiated by photodynamic therapy.* Biochimica et Biophysica Acta (BBA) - Reviews on Cancer, 2007. **1776**(1): p. 86-107.
501. Kessel, D., *Death pathways associated with photodynamic therapy.* Medical laser application : international journal for laser treatment and research, 2006. **21**(4): p. 219-224.
502. Matsubara, A., et al., *Photodynamic Therapy Induces Caspase-Dependent Apoptosis in Rat CNV Model.* Investigative Ophthalmology & Visual Science, 2007. **48**(10): p. 4741-4747.
503. Ali, S.M., et al., *Photodynamic therapy induced Fas-mediated apoptosis in human carcinoma cells.* Int J Mol Med, 2002. **9**(3): p. 257-70.
504. Srivastava, M., et al., *Involvement of Bcl-2 and Bax in Photodynamic Therapy-mediated Apoptosis: ANTISENSE Bcl-2 OLIGONUCLEOTIDE SENSITIZES RIF 1 CELLS TO PHOTODYNAMIC THERAPY APOPTOSIS *.* Journal of Biological Chemistry, 2001. **276**(18): p. 15481-15488.
505. Robey, R.W., et al., *Pheophorbide a Is a Specific Probe for ABCG2 Function and Inhibition.* Cancer Research, 2004. **64**(4): p. 1242-1246.
506. Baglo, Y., et al., *Harnessing the Potential Synergistic Interplay Between Photosensitizer Dark Toxicity and Chemotherapy.* Photochemistry and Photobiology, 2020. **96**(3): p. 636-645.
507. Vigneswaran, K., et al., *YAP/TAZ Transcriptional Coactivators Create Therapeutic Vulnerability to Verteporfin in EGFR-mutant Glioblastoma.* Clinical Cancer Research, 2021. **27**(5): p. 1553-1569.
508. Barrette, A.M., et al., *Anti-invasive efficacy and survival benefit of the YAP-TEAD inhibitor Verteporfin in preclinical glioblastoma models.* Neuro-Oncology, 2021.
509. Ventola, C.L., *Progress in Nanomedicine: Approved and Investigational Nanodrugs.* P & T : a peer-reviewed journal for formulary management, 2017. **42**(12): p. 742-755.
510. Lu, Y., et al., *Development and evaluation of transferrin-stabilized paclitaxel nanocrystal formulation.* Journal of controlled release : official journal of the Controlled Release Society, 2014. **176**: p. 76-85.
511. Zhang, Q., et al., *The anticancer efficacy of paclitaxel liposomes modified with low-toxicity hydrophobic cell-penetrating peptides in breast cancer: an in vitro and in vivo evaluation.* RSC Advances, 2018. **8**(43): p. 24084-24093.
512. Chen, Y. and T. Li, *Cellular Uptake Mechanism of Paclitaxel Nanocrystals Determined by Confocal Imaging and Kinetic Measurement.* The AAPS journal, 2015. **17**(5): p. 1126-1134.

513. Seynhaeve, A.L.B., et al., *Intact Doxil is taken up intracellularly and released doxorubicin sequesters in the lysosome: Evaluated by in vitro/in vivo live cell imaging.* Journal of Controlled Release, 2013. **172**(1): p. 330-340.
514. Chen, B., et al., *Combining vascular and cellular targeting regimens enhances the efficacy of photodynamic therapy.* International Journal of Radiation Oncology*Biology*Physics, 2005. **61**(4): p. 1216-1226.
515. Richter, A.M., et al., *Photosensitising potency of structural analogues of benzoporphyrin derivative (BPD) in a mouse tumour model.* British Journal of Cancer, 1991. **63**(1): p. 87-93.
516. Miller, C.R., et al., *Liposome-cell interactions in vitro: effect of liposome surface charge on the binding and endocytosis of conventional and sterically stabilized liposomes.* Biochemistry, 1998. **37**(37): p. 12875-83.
517. Semyachkina-Glushkovskaya, O.V., et al., *Blood–brain barrier and laser technology for drug brain delivery.* Journal of Innovative Optical Health Sciences, 2017. **10**(05): p. 1730011.
518. Inglut, C.T., et al., *Photodynamic Priming Modulates Endothelial Cell Cell Junction Phenotype for Light-activated Remote Control of Drug Delivery.* IEEE Journal of Selected Topics in Quantum Electronics, 2020: p. 1-11.
519. Kovacs, Z.I., et al., *Disrupting the blood–brain barrier by focused ultrasound induces sterile inflammation.* Proceedings of the National Academy of Sciences, 2017. **114**(1): p. E75-E84.
520. Ji, Y., et al., *Toxicity of photodynamic therapy with photofrin in the normal rat brain.* Lasers Surg Med, 1994. **14**(3): p. 219-28.
521. Winkelman, J.W. and G.H. Collins, *Neurotoxicity of tetraphenylporphinesulfonate TPPS4 and its relation to photodynamic therapy.* Photochem Photobiol, 1987. **46**(5): p. 801-7.
522. Rapp, M., et al., *Recurrence Pattern Analysis of Primary Glioblastoma.* World Neurosurgery, 2017. **103**: p. 733-740.
523. Durmus, S., J.J. Hendrikx, and A.H. Schinkel, *Apical ABC transporters and cancer chemotherapeutic drug disposition.* Adv Cancer Res, 2015. **125**: p. 1-41.
524. Schinkel, A.H., et al., *Disruption of mouse mdr-1a p-glycoprotein gene leads to a deficiency in the blood-brain barrier and to increased sensitivity to drugs.* Cell, 1994. **77**: p. 491-502.
525. Kodaira, H., et al., *Kinetic analysis of the cooperation of P-glycoprotein (P-gp/Abcb1) and breast cancer resistance protein (Bcrp/Abcg2) in limiting the brain and testis penetration of erlotinib, flavopiridol, and mitoxantrone.* J Pharmacol Exp Ther, 2010. **333**(3): p. 788-96.
526. Wang, J., et al., *P-glycoprotein (MDR1/ABCB1) and Breast Cancer Resistance Protein (BCRP/ABCG2) affect brain accumulation and intestinal disposition of encorafenib in mice.* Pharmacol Res, 2018. **129**: p. 414-423.
527. Durmus, S., et al., *Oral availability and brain penetration of the B-RAFV600E inhibitor vemurafenib can be enhanced by the P-GLYCOprotein (ABCB1) and breast cancer resistance protein (ABCG2) inhibitor elacridar.* Mol Pharm, 2012. **9**(11): p. 3236-45.

528. Umans, R.A. and M.R. Taylor, *Zebrafish as a model to study drug transporters at the blood-brain barrier.* Clin Pharmacol Ther, 2012. **92**(5): p. 567-70.
529. Kim, S.S., et al., *Zebrafish as a Screening Model for Testing the Permeability of Blood-Brain Barrier to Small Molecules.* Zebrafish, 2017. **14**(4): p. 322-330.
530. Jeong, J.Y., et al., *Functional and developmental analysis of the blood-brain barrier in zebrafish.* Brain Res Bull, 2008. **75**(5): p. 619-28.
531. O'Brown, N.M., S.G. Megason, and C. Gu, *Suppression of transcytosis regulates zebrafish blood-brain barrier function.* Elife, 2019. **8**.
532. Fischer, S., et al., *Abcb4 acts as multixenobiotic transporter and active barrier against chemical uptake in zebrafish (Danio rerio) embryos.* BMC Biol, 2013. **11**: p. 69.
533. Kobayashi, I., et al., *Characterization and localization of side population (SP) cells in zebrafish kidney hematopoietic tissue.* Blood, 2008. **111**(3): p. 1131-7.
534. Robey, R.W., et al., *Characterization and tissue localization of zebrafish homologs of the human ABCB1 multidrug transporter.* bioRxiv, 2021: p. 2021.02.18.431829.
535. Heise, K., et al., *Dual luciferase assay for secreted luciferases based on Gaussia and NanoLuc.* Assay Drug Dev Technol, 2013. **11**(4): p. 244-52.
536. Huang, R., et al., *ATP-binding cassette transporters modulate both coelenterazine- and D-luciferin-based bioluminescence imaging.* Mol Imaging, 2011. **10**(3): p. 215-26.
537. England, C.G., E.B. Ehlerding, and W. Cai, *NanoLuc: A Small Luciferase Is Brightening Up the Field of Bioluminescence.* Bioconjugate chemistry, 2016. **27**(5): p. 1175-1187.
538. Robey, R.W., et al., *Inhibition of P-glycoprotein (ABCB1)- and multidrug resistance-associated protein 1 (ABCC1)-mediated transport by the orally administered inhibitor, CBT-1((R)).* Biochemical pharmacology, 2008. **75**(6): p. 1302-1312.
539. Basnet, R.M., et al., *Zebrafish Larvae as a Behavioral Model in Neuropharmacology.* Biomedicines, 2019. **7**(1): p. 23.
540. Gosselet, F., et al., *Central nervous system delivery of molecules across the blood-brain barrier.* Neurochemistry International, 2021. **144**: p. 104952.
541. Bhowmik, A., R. Khan, and M.K. Ghosh, *Blood brain barrier: a challenge for effectual therapy of brain tumors.* BioMed research international, 2015. **2015**: p. 320941-320941.
542. Begley, D.J., *ABC transporters and the blood-brain barrier.* Curr Pharm Des, 2004. **10**(12): p. 1295-312.
543. Choi, C.-H., *ABC transporters as multidrug resistance mechanisms and the development of chemosensitizers for their reversal.* Cancer cell international, 2005. **5**: p. 30-30.
544. Shukla, S., S. Ohnuma, and S.V. Ambudkar, *Improving cancer chemotherapy with modulators of ABC drug transporters.* Current drug targets, 2011. **12**(5): p. 621-630.

545. Anreddy, N., et al., *Tyrosine kinase inhibitors as reversal agents for ABC transporter mediated drug resistance.* Molecules (Basel, Switzerland), 2014. **19**(9): p. 13848-13877.
546. Kim, D.-G. and M.S. Bynoe, *A2A adenosine receptor modulates drug efflux transporter P-glycoprotein at the blood-brain barrier.* The Journal of clinical investigation, 2016. **126**(5): p. 1717-1733.
547. Francis, W.R., et al., *Occurrence of Isopenicillin-N-Synthase Homologs in Bioluminescent Ctenophores and Implications for Coelenterazine Biosynthesis.* PloS one, 2015. **10**(6): p. e0128742-e0128742.
548. Liang, B.J., et al., *Breaking the selectivity-uptake trade-off of photoimmunoconjugates with nanoliposomal irinotecan for synergistic multi-tier cancer targeting.* J Nanobiotechnology, 2020. **18**(1): p. 1.
549. Shafirstein, G., et al., *Interstitial Photodynamic Therapy-A Focused Review.* Cancers (Basel), 2017. **9**(2).
550. Wang, W., et al., *Tyrosyl-DNA Phosphodiesterase 1 and Topoisomerase I Activities as Predictive Indicators for Glioblastoma Susceptibility to Genotoxic Agents.* Cancers, 2019. **11**(10): p. 1416.
551. Liang, B.J., et al., *Mechanistic Insights into Photodynamic Regulation of Adenosine 5′-Triphosphate-Binding Cassette Drug Transporters.* ACS Pharmacology & Translational Science, 2021. **4**(5): p. 1578-1587.